





Universitat Autònoma de Barcelona

ADVERTIMENT. L'accés als continguts d'aquesta tesi queda condicionat a l'acceptació de les condicions d'ús establertes per la següent llicència Creative Commons:  http://cat.creativecommons.org/?page_id=184

ADVERTENCIA. El acceso a los contenidos de esta tesis queda condicionado a la aceptación de las condiciones de uso establecidas por la siguiente licencia Creative Commons:  <http://es.creativecommons.org/blog/licencias/>

WARNING. The access to the contents of this doctoral thesis it is limited to the acceptance of the use conditions set by the following Creative Commons license:  <https://creativecommons.org/licenses/?lang=en>

Ph.D THESIS

Hybrid Electrode Materials Based on
Polyoxometalates for Their First-Time Application in
Organic Electrolyte Supercapacitors

A thesis presented by

Junjie Zhu

For the Degree of *Doctor of Philosophy*
In Materials Science programme of
Universitat Autònoma de Barcelona (UAB)

Director & Tutor
Prof. Dr. Pedro Gómez-Romero, CSIC

Institut Català de Nanociència i Nanotecnologia (ICN2)
Bellaterra-08193, Barcelona, Spain
June, 2022

Memòria presentada per aspirar al Grau de Doctor per

Junjie Zhu

Vist i plau

Prof. Dr. Pedro Gómez-Romero

CSIC Full Professor & Group Leader

Novel Energy-Oriented Materials Group

Institut Català de Nanociència i Nanotecnologia (ICN2)

Acknowledgements

First and foremost, I would like to express my sincere gratitude to my supervisor, Prof. Pedro Gomez-Romero, for his consistently patient guidance and trust in my ideas throughout my PhD study. I appreciate the opportunity he provided for me to explore the scientific mysteries, which in turn trained me to be an independent researcher.

It is a wonderful and unforgettable experience for the four-year study in ICN2, thanks to my colleagues in the NEO-Energy group. I am grateful to Dr. Daniel Rueda-Garcia, who acquainted me with everything in the lab on the first day, and kept helping me throughout the four years. I would like to thank Veronica Fabian and Anukriti Pokhriyal. The two lovely girls make my life in ICN2 vivid. I want to express my gratitude to Dr. Rosa Maria González Gil for providing various resources. Moreover, I want to thank the former members in our group, Dr. Raúl Benages, Dr. Sara Goberna, Dr. Victor Fuentes, Dr. Sergio Mollá and Luis Javier Martinez-Soria, for their valuable help and generous support during the time we worked together.

I want to show my profound gratitude to Dr. Avireddy Hemesh, for his collaboration in research, participation in discussion, assistance and advice in problem-solving,

I would like to thank the China Scholarship Council for supporting me to carry out the doctoral program through the fellowship.

My heartfelt gratitude goes out to my parents, without whose support I would not be where I am now. Their endless love, unfailing support, and encouragement have always been there for me.

Ultimately, I would like to continue expressing my appreciation to the friends around me or thousands of miles away, on another continent. I would like to thank Sen Du, Ze Wang, Yunhui Yang, Chen Gao and Yakun Zhao for their arranging and participating in various entertaining activities. I would like to thank Huan Tan, Ming Liu and Ashwin for founding and managing badminton group, which for sure help me keep healthy and even become stronger day by day. I would also like to thank my best friends in China, Singapore, Italy and the United States, who share happiness and sorrow with me.

Abstract

Supercapacitors, also known as electrochemical capacitors, are fascinating energy storage devices, featuring high power density and long cycle life. Their energy density is yet to be improved. Hybrid electrodes which combine electrical double-layer capacitance and redox reactions provide an approach to enhancing the energy density. Polyoxometalates (POMs) are nanoscale metal oxide clusters (typically of V, Mo or W) and can carry out fast reversible redox reactions. They are well suited for fabricating hybrid materials, providing enhanced capacity. On the other hand, the use of organic electrolytes and ionic liquids allows for an increased working voltage and therefore a greater energy density.

This thesis focuses on developing POM-based hybrid materials for organic-electrolyte supercapacitors, a goal that is successfully reached here for the first time. W and Mo POMs with the well-known Keggin structure were used. Chapter 3 presents the efforts to integrate inorganic POM salts or acids as well as organic POM-derivatives in activated carbon (AC) as hybrid materials for the setting up of symmetric organic-electrolyte supercapacitors. Contrary to the acids or inorganic salts, the organic-inorganic POMs-derivatives (with tetraalkylammonium salts) show enhanced capacitance (+36% volumetric capacitance), proving that POMs can also enhance the capacitive performance of other materials in organic electrolytes. Then, efforts were steered to develop other novel POM-based hybrid materials. Chapter 4 shows various attempts to incorporate POMs into $Ti_3C_2T_x$ (MXene). The sonication-assisted direct anchoring can only load very little amounts (<1 at%) of POMs on MXene. The quaternary ammonium cations expand the interlayer distance of MXene, and also serve as the anchoring sites for POMs, which allows for in-situ growth of MXene/POMs hybrid materials with high POMs concentration. The small quaternary ammonium cations which cannot expand the interlayer distance enough will lead to an aggregation of POMs crystals out of MXene nanosheets. This kind of MXene/POMs hybrid materials shows poor electrochemical stability (<20 % after 20 cycles). On the other hand, the cetyltrimethylammonium cations (CTA) expanded the interlayer distance to around 2 nm and induced the POMs intercalation in between atomic MXene layers, exhibiting superior

electrochemical stability (>98% after 100 cycles). However, the capacitive performance of these MXene/POMs binary hybrid materials does not get much improvement due to the high molecular weight of POMs ($[\text{PW}_{12}\text{O}_{40}]^{3-}$). Thus, a new hybridization strategy was developed. Chapter 5 describes our work on a rational design of MXene/AC/POMs triple hybrid materials, which combine the merits of each component and show synergic effects. Well-balanced MXene/AC/POMs triple hybrid materials with improved gravimetric and volumetric capacitance were obtained. Finally, chapter 6 deals with the integration of gel polymer electrolytes with POMs and POM-based hybrid electrodes. Symmetric supercapacitors with AC/POMs hybrid electrodes and the organic gel polymer electrolyte (1 M TEABF₄ in acetonitrile/PVDF-HFP) were fabricated, outperforming the organic-electrolyte supercapacitors with conventional configuration (liquid electrolyte and commercial separators). This improved performance (3 times energy density at higher power density) was assigned to the combination of extra capacity from the hybrid electrode and proper integration of the gel electrolyte forming a coherent pathway throughout the electrodes and the gel polymer electrolyte/separator.

Resumen

Los supercondensadores, también conocidos como condensadores electroquímicos, son dispositivos de almacenamiento de energía que presentan una alta densidad de potencia y un ciclo de vida prolongado. No obstante, su densidad de energía es relativamente baja y necesita ser mejorada. Los electrodos híbridos que combinan materiales capacitivos de doble capa eléctrica y materiales con reacciones redox brindan un enfoque útil para mejorar la densidad de energía. Los polioxometalatos (POM) son agregados moleculares de óxidos metálicos de tamaño nanométrico (normalmente de V, Mo o W) y pueden llevar a cabo reacciones redox reversibles y rápidas. Son muy adecuados para la fabricación de materiales híbridos, proporcionando una mayor capacidad. Por otro lado, el uso de electrolitos orgánicos y líquidos iónicos permite un mayor voltaje de trabajo y por tanto una mayor densidad energética.

Esta tesis se centra en el desarrollo de materiales híbridos basados en POMs (de W o Mo, con la estructura de Keggin) como electrodos de supercondensadores con electrolitos orgánicos, un objetivo que se alcanza con éxito por primera vez con este trabajo. El Capítulo 3 presenta los esfuerzos para integrar sales o ácidos inorgánicos de POM, así como derivados orgánicos de POM en carbón activado (AC) como materiales híbridos para la creación de supercondensadores de electrolitos orgánicos simétricos. A diferencia de los ácidos o las sales inorgánicas, los derivados de POM orgánico-inorgánicos (con sales de tetraalquilamonio) muestran una capacitancia mejorada (+36 % de capacitancia volumétrica), lo que demuestra que los POMs también pueden mejorar el rendimiento capacitivo de materiales carbonosos en electrolitos orgánicos. En una segunda etapa de la tesis hemos desarrollado otros nuevos materiales híbridos basados en POM de complejidad creciente. Así, el Capítulo 4 muestra varios intentos de incorporar POM en $Ti_3C_2T_x$ (MXene). El anclaje directo asistido por sonicación solo puede cargar cantidades muy pequeñas (<1 at%) de POM en MXene. Los cationes de amonio cuaternario amplían la distancia entre capas de MXene y también sirven como sitios de anclaje para los POM, lo que permite el crecimiento in situ de materiales híbridos MXene/POM con una alta concentración de POMs. Los cationes de amonio cuaternario más

pequeños, que no pueden expandir lo suficiente la distancia entre capas de MXene dieron lugar al crecimiento de cristales de POM fuera de la estructura laminar del MXene. Este tipo de materiales híbridos MXene/POM muestra una estabilidad electroquímica deficiente (<20 % después de 20 ciclos). Por otro lado, los cationes de cetiltrimetilamonio (CTA) expandieron la distancia entre capas a alrededor de 2 nm y permitieron la intercalación de POM entre las capas atómicas de MXene, exhibiendo una estabilidad electroquímica superior (> 98% después de 100 ciclos). Sin embargo, el rendimiento capacitivo de estos materiales híbridos binarios MXene/POM no mejora mucho debido al alto peso molecular de los POMs utilizados ($[PW_{12}O_{40}]^{3-}$). En consecuencia, se desarrolló una nueva estrategia de hibridación. El capítulo 5 describe nuestro trabajo sobre un diseño racional de materiales híbridos triples MXene/AC/POM, que combinan las ventajas de cada componente y muestran efectos sinérgicos. Se obtuvieron materiales híbridos triples MXene/AC/POM bien equilibrados, con capacitancia gravimétrica y volumétrica mejorada. Finalmente, el capítulo 6 trata sobre la integración de electrolitos en forma de geles poliméricos con POMs y con electrodos híbridos basados en POMs. Se fabricaron supercondensadores simétricos con electrodos híbridos AC/POM y electrolito de gel polimérico orgánico (TEABF₄ 1 M en acetonitrilo/PVDF-HFP), superando a los supercondensadores de electrolito orgánico con configuración convencional (electrolito líquido y separadores comerciales). Este rendimiento mejorado (3 veces la densidad de energía a mayor densidad de potencia) se asignó a la combinación de capacidad adicional del electrodo híbrido y la integración adecuada del electrolito de gel que forma una ruta coherente a lo largo de los electrodos y el electrolito/separador de polímero de gel.

Table of contents

Acknowledgements	i
Abstract	iii
Resumen	v
Table of contents	vii
List of acronyms	xi
List of publications	xiii
Chapter 1 Introduction	1
1.1 Energy storage	1
1.2 Electrochemical energy storage	1
1.3 Active materials	3
1.3.1 EDLC materials	3
1.3.2 Redox-active materials	4
1.3.3 Polyoxometalates	9
1.3.4 POM-based Hybrid materials.....	12
1.4 Electrolytes	13
1.4.1 Liquid electrolytes.....	13
1.4.2 Quasi-solid electrolytes	14
1.5 Motivation and Objectives	17
Chapter 2 Experimental and Characterization Procedures	23
2.1 Materials Preparation.....	23
2.1.1 Preparation of alkylammonium POM salts.....	24
2.1.2 Preparation of AC/POM hybrid materials.....	24
2.1.3 Preparation of MXene ($\text{Ti}_3\text{C}_2\text{T}_x$) through delamination with fluorine.....	25
2.1.4 Preparation of MXene through delamination with alkylammonium hydroxide ..	25
2.1.5 Preparation of MXene/alkylammonium phosphotungstate	25
2.1.6 Preparation of MXene/HPW12.....	26

2.1.7 Preparation of MXene/AC/HPW12 triple hybrids	26
2.1.8 Preparation of MXene/AC/TEAPW12 triple hybrids.....	26
2.1.9 Preparation of gel electrolyte.....	26
2.2 Basic Characterization Techniques	27
2.2.1 X-ray diffraction (XRD)	27
2.2.2 Fourier-transform infrared spectroscopy (FT-IR).....	28
2.2.3 Thermogravimetric Analysis (TGA)	28
2.2.4 Specific Surface Area and Pore Size Distribution.....	28
2.2.5 Scanning Electron Microscopy (SEM)	30
2.2.6 Transmission Electron Microscopy (TEM)	30
2.2.7 High-Angle Annular Dark-Field Scanning Transmission Electron Microscopy (HAADF-STEM).....	31
2.2.8 Energy Dispersive X-ray Spectroscopy (EDX)	31
2.2.9 X-ray photoelectron spectroscopy (XPS)	32
2.3 Electrochemical Characterization and Energy storage Tests	33
2.3.1 Preparation of the electrodes.....	33
2.3.2 Cyclic Voltammetry (CV)	33
2.3.3 Galvanostatic Charge-Discharge (GCD).....	36
2.3.4 Electrochemical Impedance Spectroscopy (EIS)	37
Chapter 3 Activated Carbon/Polyoxometalates Hybrid Materials for Organic- Electrolyte Supercapacitors	41
3.1 Context	41
3.2 Activated carbon/polyoxometallic acid materials.....	42
3.2.1 Characterizations	42
3.2.2 Electrochemical characterization	45
3.3 Activated carbon/organic polyoxometalate salts hybrid materials (Article 1)	48
Chapter 4 MXene/POM hybrid materials	77
4.1 Context	77

4.2 Direct anchoring: MXene/HPW12	78
4.3 Cation-assisted in-situ growth (Article 2)	81
4.4 Capacitive performance of the POMs intercalated MXene	116
4.5 Conclusion	116
Chapter 5 MXene/AC/POM triple hybrid materials	119
5.1 Context	119
5.2 Rational Design of MXene/Activated Carbon/Polyoxometalate Triple Hybrid Electrodes with Enhanced Capacitance for Organic-Electrolyte Supercapacitors (Article 3)	119
Chapter 6 Gel polymer Electrolytes integrated with POM electrodes	151
6.1 Context	151
6.2 Aqueous POM gel polymer electrolytes	151
6.2.1 Synthesis	152
6.2.2 Electrochemical behaviour of the electrolytes	153
6.2.3 Capacitive properties of AC in PVA/SiW12/H ₃ PO ₄ GPE	154
6.3 Hybrid electrodes with organic GPE (Article 4)	155
Chapter 7 Conclusions and perspectives	179
7.1 Thesis overview and final conclusions	179
7.2 Perspective	182

List of acronyms

AC	activated carbon
ACN	acetonitrile
BET	Brunauer–Emmett–Teller method
CNP	carbon nanopipes
CNT	carbon nanotubes
CP	cyclic polarization
CV	cyclic voltammetry
EC	ethylene carbonate
EDLC	electric double layer capacitor
EDX	energy dispersive X-ray spectroscopy
EIS	electrochemical impedance spectroscopy
EMC	ethyl methyl carbonate
EMIMTFSI	1-ethyl-3-methylimidazolium bis(trifluoromethylsulfonyl)imide
FT-IR	Fourier-transform infrared spectroscopy
GCD	galvanostatic charge-discharge
GPE	gel polymer electrolyte
HAADF-STEM	high-angle annular dark-field scanning transmission electron microscopy
HPMo ₁₂	phosphomolybdic acid (H ₃ PMo ₁₂ O ₄₀)
HPW ₁₂	phosphotungstic acid (H ₃ PW ₁₂ O ₄₀)
HSiW ₁₂	silicotungstic (H ₄ SiW ₁₂ O ₄₀)
LiTFSI	lithium bis(trifluoromethanesulfonyl)imide
PAN	polyacrylonitrile

PC	propylene carbonate
PEG	polyethylene glycol
PEO	polyethylene oxide
PMMA	polymethyl methacrylate
PMo12	phosphomolybdate
POM	polyoxometalate
PPy	polypyrrole
PVA	polyvinyl alcohol
PVDF	poly(vinylidene fluoride)
PVDF-HFP	poly(vinylidene fluoride-co-hexafluoro propene)
PW12	phosphotungstate
rGO	reduced graphene oxide
SEM	scanning electron microscopy
SiW12	silicotungstate
TEA	tetraethylammonium
TEABF ₄	tetraethylammonium tetrafluoroborate
TEM	transmission electron microscopy
TGA	thermogravimetric Analysis
XRD	X-ray diffraction

List of publications

1. Can polyoxometalates enhance the capacitance and energy density of activated carbon in organic electrolyte supercapacitors? Jun-Jie Zhu, Raul Benages-Vilau, Pedro Gomez-Romero*, Electrochimica Acta, 2020, 362, 137007
2. Coherent Integration of Organic Gel Polymer Electrolyte and Ambipolar Polyoxometalate Hybrid Nanocomposite Electrode in a Compact High-Performance Supercapacitor. Jun-Jie Zhu*, Luis Martinez-Soria, Pedro Gomez-Romero*, Nanomaterials, 2022, 12, 514
3. Rational design of MXene/activated carbon/polyoxometalate triple hybrid electrodes with enhanced capacitance for organic-electrolyte supercapacitors, Jun-Jie Zhu*, Avireddy Hemesh, Jordi Jacas Biendicho, Luis Martinez-Soria, Daniel Rueda-Garcia, Joan Ramon Morante, Belen Ballesteros, Pedro Gomez-Romero*, Journal of Colloid and Interface Science 2022, 623, 947-961
4. Polyoxometalate Intercalated MXene with Enhanced Electrochemical Stability. Jun-Jie Zhu, Pedro Gomez-Romero*, under review

Chapter 1 Introduction

1.1 Energy storage

Fossil fuels are non-renewable resources and are being depleted. Their utilization causes several issues: combustion produces tiny particles that pollute the air, as well as large amounts of greenhouse gas (CO₂) that contribute to global warming and the climate emergency - the most challenging issue of this century. As a result, various types of energy storage are being developed with the aim of reducing the use of fossil fuels and facilitating clean energy.

The major advantages of energy storage devices are that they can compensate for the variability of renewable energy sources, provide power to portable devices that cannot be permanently connected to a power grid, and mitigate fluctuations in consumption.

For these reasons, the energy storage device is seen as a key complementary piece in sustainable electricity production.

1.2 Electrochemical energy storage

Among the various energy storage types, electrochemical energy storage prevails due to its high reliability, scalability, high energy density, high conversion efficiency, portability, and installability.

According to the energy storage mechanism, electrochemical energy storage devices can be classified into two main types: supercapacitors, and batteries that can be further classified as primary (non-rechargeable) and rechargeable systems.

The rechargeable battery family has been formed by many different chemistries over the years, from the oldest lead-acid battery invented in 1859, to the obsolete nickel-cadmium batteries, nickel-metal hydride and finally, lithium-ion batteries, introduced by Sony in 1991. During the last two decades, R&D of a wide variety of chemistries alternative to Li have been developed, including sodium, potassium, magnesium, calcium, zinc and aluminium. However, all these batteries store energy through redox reactions involving a variety of active materials. These redox reactions tend to be sluggish because they normally

involve ion transport and diffusion to compensate the charge involved in electron transfer within the lattice of the active phases [1, 2]. As a result, batteries provide relatively low power densities, but high energy densities. Moreover, batteries are burdened by several other issues, including heat generation due to internal resistance and dendrite formation, both frequently leading to failure before the expected lifespan, which in terms of the number of cycles is, at best, of a few thousand.

In contrast, supercapacitors also known as ultracapacitors or electrochemical capacitors can complement, or even replace batteries in some fields as they store energy through surface or subsurface electrochemical processes. These processes can be redox reactions (pseudocapacitance) or the formation of electric double layers (electrochemical double layer capacitors, EDLC). With EDLCs, an electric double layer forms spontaneously by arranging charges (cations and anions) at the electrode-electrolyte interface when an electrode immersed in an electrolyte is charged. The charging and discharging processes are associated with the rearrangement of ions instead of any Faradaic process. Although this storage process is quite similar to conventional dielectric capacitors, EDLCs can deliver capacitance several orders of magnitude higher than dielectric capacitors. This is due to the fact that capacitance is proportional to the area and inversely proportional to the charge separation distance. In the EDLCs, the active materials have a high specific surface area ($>1000 \text{ m}^2 \text{ g}^{-1}$), whereas the electrical double layers with thicknesses of a few nanometers provide a short separation distance, and both factors combine to lead to high capacitance in EDLCs (see equation 1.1 below).

In contrast to EDLCs, pseudocapacitors store charge through fast, reversible redox reactions at the surface or subsurface of the active materials. This mechanism involves valence state change of the active material, and a charge transfer that occurs at the interfaces of electrodes and electrolytes. Due to the involvement of redox reactions, pseudocapacitors can deliver higher capacitance than EDLCs, but the charge storage process is slower. The energy storage mechanisms of supercapacitor devices can be EDLC, redox-active, or hybrid according to the active materials.

1.3 Active materials

A variety of materials can serve as active materials for supercapacitors. They can be classified into three main groups: carbon-based materials, transition metal oxides (or nitrides, carbides, sulphides), and conductive polymers.

1.3.1 EDLC materials

EDLCs are the first invented type of supercapacitors, which date back to 1957. The EDLCs mainly store charge through the adsorption of electrolyte ions on the surface, as shown in Fig. 1.1.

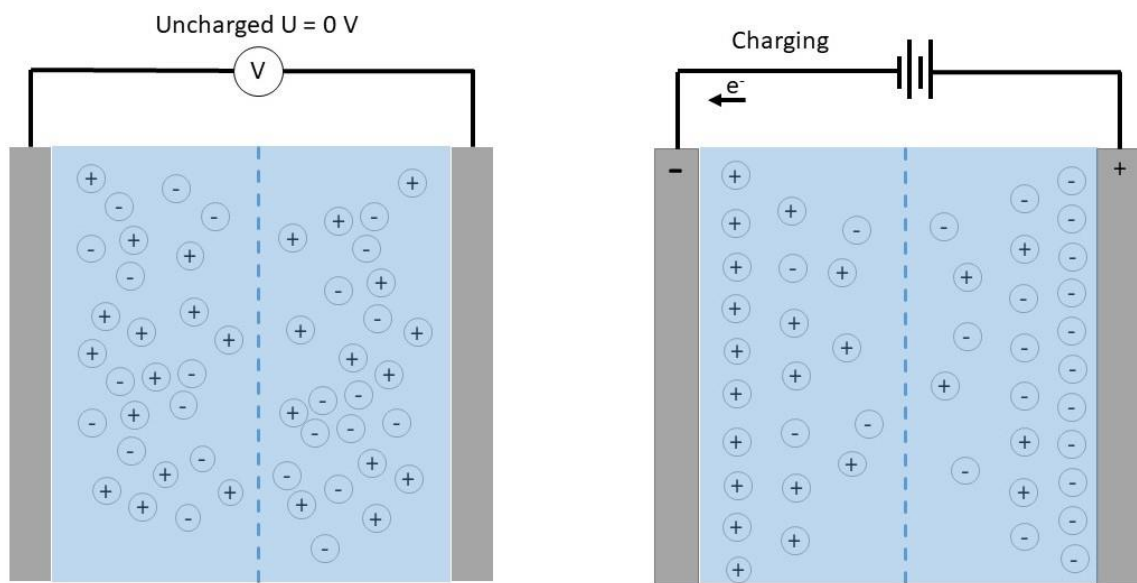


Fig. 1.1 Schematic of the charge-storage mechanism for EDLCs.

The specific capacitance of EDLCs is directly proportional to the accessible surface area and the surface properties of active materials. The capacitance of an EDLC can be estimated through the following equation[3]:

$$C = \frac{\epsilon_r \epsilon_0}{d} A, \quad \text{Eq. 1.1}$$

where ϵ_r is the electrolyte relative permittivity (or dielectric constant), ϵ_0 is the permittivity in vacuum, d is the effective thickness of the double layer (charge separation distance) and A is the electrode surface area.

Carbon-based materials are the most commonly used and commercialized materials for EDLCs due to their low cost, conductivity, stability, and capability to

Other characteristic features of redox active materials are related to the voltage-specific nature of the redox process which leads to well-defined (and characteristic) redox waves in their cyclic voltammograms and the corresponding plateaus in the charge-discharge curves.

Supercapacitors that store energy through redox reactions are also referred to as pseudocapacitors. In pseudocapacitors, redox reactions happen only on the surface or subsurface. The ions in the electrolyte can reach the external active sites without bulk diffusion and therefore the overall redox reaction can take place at a faster rate. In CVs, these redox reactions exhibit widely extended bulges, in some cases, they cannot even be distinguished from the rectangle (e.g. in the case of heteroatoms-doped carbon).

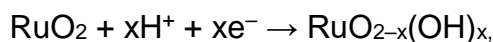
Transition metal compounds (oxides, nitrides, carbides, sulfides), conductive polymers and even noble metals can be pseudocapacitive. These pseudocapacitive behaviours can be intrinsic or extrinsic. According to the energy storage mechanism, we can categorize pseudocapacitance into three types: underpotential deposition, redox pseudocapacitance and intercalation pseudocapacitance.

Underpotential deposition happens when ions are deposited on an electrode(metal)-electrolyte interface at potentials positive to their reversible redox potential[13]. The first idea of pseudocapacitive charge storage can be traced back to 1962. Conway and Gileadi explained the underpotential deposition of hydrogen atoms on noble-metal surfaces[14]. However, the working potential window is usually small, only 0.3–0.6 V, and the capacitance values are potential-dependent for the underpotential deposition process. Thus, the energy density is relatively low compared to other pseudocapacitive systems and this mechanism has provided little practical application.

Redox pseudocapacitance is the most widely studied and applied pseudocapacitance mechanism. It stores charge through the fast redox reaction between the electrochemically absorbed species (e.g., protons in aqueous electrolytes) and active materials on the surface or subsurface. Most pseudocapacitive materials (e.g., RuO₂, MnO₂ and conducting polymers) store charge through this mechanism.

The first applied pseudocapacitive material, ruthenium dioxide (RuO₂), was discovered in the 1970s. Since then, many researchers have carried out studies

to exploit its capacitance and RuO₂ has become the benchmark for an ultrafast-response, high-capacitance material for energy storage. RuO₂ store charges through the following redox reaction:



where $0 \leq x \leq 2$, The following equation can estimate the theoretical specific capacitance of pseudocapacitive material:

$$C = \frac{Q}{V} = \left(\frac{nF}{m}\right) \frac{X}{V}, \quad \text{Eq. 1.2}$$

where X is the fractional coverage of active sites, m is the molecular weight of the active material, n is the number of electrons and F is the Faraday constant.

The theoretical specific capacitance of RuO₂ is as high as 1609 F g⁻¹, derived from a voltage window of 0.9 V in 1 M sulfuric acid electrolyte. However, RuO₂ can seldom achieve such high specific capacitance, and its high price further hinders its application.

Manganese dioxide (MnO₂) is a promising candidate for pseudocapacitors due to its high theoretical capacitance (1370 F g⁻¹, 0.9 V voltage windows), low cost, natural abundance and environmental friendliness. However, its specific capacitance is still far from the theoretical value. Various methods, such as preparing mesoporous MnO₂, have been applied to enhance its specific capacitance[15, 16]. The enhancement is not as significant as for RuO₂. The pristine nanostructured MnO₂ can deliver a specific capacitance around 250 F g⁻¹ in a neutral aqueous electrolyte[17].

Functional groups on the electrode surface can be another source of pseudocapacitance. Some carbon-based materials show pseudocapacitive behaviours and gain extra capacitance in this way[18]. For example, N and P dual-doped hierarchically porous carbon can deliver a gravimetric specific capacitance of 373 F g⁻¹ at 1 A g⁻¹ in KOH electrolyte[19]. Similarly, nitrogen and sulfur co-doped porous carbon can deliver a specific capacitance of 308 F g⁻¹ at 1 A g⁻¹ in 6 M KOH electrolyte[20], while N-doped graphene has a gravimetric capacitance of 280 F g⁻¹ at 20 A g⁻¹ in 1 M TEABF₄ in acetonitrile[21]. These surface-functionalized carbon-based materials deliver significantly higher capacitance than pristine carbon, indicating that combining two energy storage mechanisms could be an alternative to high-performance capacitive materials.

In the past decade, a new family of two-dimension materials, MXene, was discovered and exploited for supercapacitors. MXene is usually synthesized through the selective etching of particular metal atomic layers from their layered precursors, MAX phases (Fig. 1.2). MAX phases are a collection of ternary carbides and nitrides, which contain layers of transition metal carbides or nitrides (MX) interleaved with layers of A-element atoms (most commonly, group 13th or 14th elements of the periodic table). Once the A-element layers are etched, the created surface ends with termination groups (hydroxyl, oxygen or fluorine). Thus, MXene has a general formula $M_{n+1}X_nT_x$, where M is a transition metal, X is carbon and/or nitrogen, n is an integer between 1 and 3, and T_x represents surface termination groups. The pseudocapacitance of MXenes mostly stems from the surface termination groups[22]. $Ti_3C_2T_x$ was the first synthesized MXene in 2011[23], followed by numerous studies. The most outstanding merit of $Ti_3C_2T_x$ as a supercapacitor electrode is its high volumetric capacitance[24, 25]. The $Ti_3C_2T_x$ clay can deliver a volumetric capacitance of 1500 F cm^{-3} in 1 M sulfuric acid, four times larger than activated carbon, and even better than the best result of RuO_2 [22]. Meanwhile, numerous efforts have been made to improve the gravimetric capacitance of $Ti_3C_2T_x$. Strategies similar to those used for other pseudocapacitive materials, such as expanding the interlayer distance or designing porous MXene to promote the exposure of active sites to the electrolyte, have been pursued[26-29].

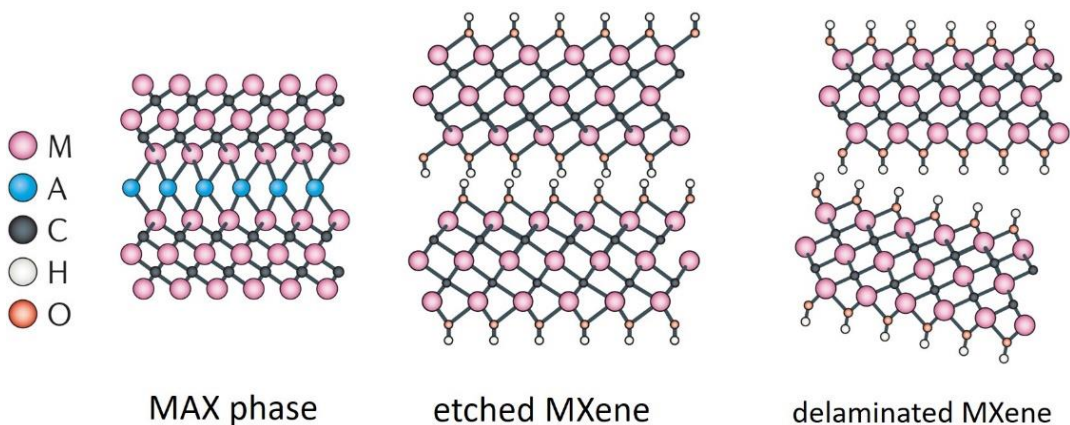


Fig. 1.2 Schematic diagram of the atomic structure of M_3X_2A MAX phase, etched $M_3X_2T_x$ MXene and delaminated $M_3X_2T_x$ MXene[30]

Besides pseudocapacitance from the surface termination groups, MXene can also store charge through cation intercalation. That is, intercalation pseudocapacitance, which benefits from an effectively open layered structure.

Intercalation pseudocapacitance stores charges through the intercalation of ions (usually cations) into the layered crystalline materials along with a change of metal valence to maintain electric neutrality. The most common case is the intercalation of Li^+ in a process reminiscent of Li-ion batteries (LIB). The main difference is that the intercalation pseudocapacitance shows capacitor-like characteristics, such as fast response, high rate capability and long cycle life. Most importantly, this pseudocapacitance does not show any voltage-specific charge transfer process (in CVs or GCD) but a flat CV and linear GCD profiles typical of supercapacitors.

$\text{Ti}_3\text{C}_2\text{T}_x$ can deliver a gravimetric capacitance of 195 F g^{-1} at 2 mV s^{-1} in 1 M LiTFSI in a three-electrode cell with propylene carbonate electrolyte[31]. An expansion and contraction of $\text{Ti}_3\text{C}_2\text{T}_x$ interlayer distance during charge-discharge was observed and intercalation pseudocapacitance was the main energy storage mechanism for MXene in aprotic electrolytes with small cations (e.g. Li^+ , Na^+)[32-34].

Besides MXene, some LIB cathode materials (e.g. LiCoO_2 [35], LiMn_2O_4 [35]) also exhibit intercalation and marginally pseudocapacitive behaviours when they are in particular morphologies (ultrathin films) or nanoscale forms where diffusion occurs through very limited timescale. On the other hand, the same materials with slightly different morphologies or under different conditions show charge-discharge inclined plateaus reminiscent of batteries. These materials are defined as "extrinsic" pseudocapacitive materials[1]. In addition, many other metal oxides (e.g. V_2O_5 [36], TiO_2 [37], Nb_2O_5 [38], etc.) show extrinsic pseudocapacitive behaviours when nano-sized, proving that size effects play a vital role in determining energy storage mechanism.

Ni and Co-based compounds were used to be defined as pseudocapacitive in the past decades. However, they are different from intrinsic pseudocapacitive materials (MnO_2 and RuO_2). Their CVs exhibit well-defined redox peaks, and their galvanostatic charge-discharge profiles show clear plateaus, which means the stored charge has no linear dependence on potential – contrary to the definition

of capacitance. In such cases, capacity is more appropriate to describe the energy storage capability of these materials.

1.3.3 Polyoxometalates

Polyoxometalates (POMs) are a class of discrete transition metal-oxide clusters with sizes ranging from 1 to a few nanometres. They are inherent nanoclusters, with a well-defined composition and structure. POMs are generally characterized by fast reversible redox reactions and they have been described as perfect models for quantum-sized metal oxide nanoparticles[39]. These characteristics endow POMs with a variety of applications, including catalysis, sensor, energy conversion and energy storage[40].

The history of POMs dates back to two centuries ago[41]. However, due to the underdeveloped characterization techniques, the structure of POMs was a mystery. This situation changed in 1934, when J. F. Keggin interpreted the structure of 12-phosphotungstic acid through X-ray diffraction. Subsequently, many other POMs conforming to that same molecular structure were found and fully characterized and are generally referred to as the Keggin structure. They are anions of chemical formula $[XM_{12}O_{40}]^{n-}$, in which X represents a heteroatom, M represents transition metal addenda atoms (generally W, Mo, but also V or Nb). They can be protonated in which case they can crystallize as solid acids or be accompanied by a variety of cations.

Up to now, a variety of POMs have been synthesized. According to the features of their structure, they can be classified into different types, such as Keggin, Dawson, Anderson, Lindqvist, and others. Fig. 1.3 presents the structure of various POMs clusters. Among them, Keggin-type and Dawson-type are the most widely studied for energy storage[42, 43].

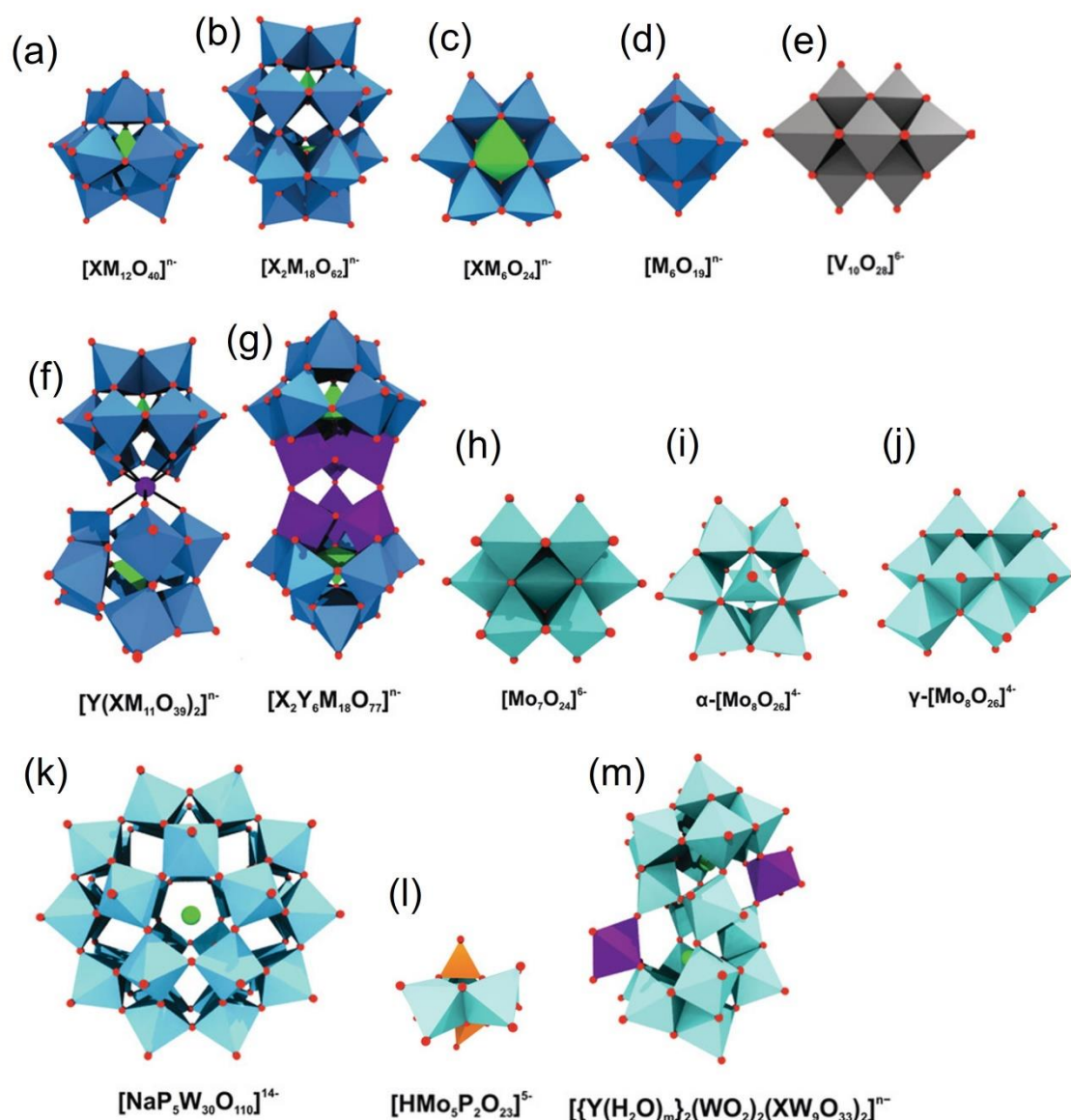


Fig. 1.3 Overview of common POM archetypes. a) Keggin, b) Wells–Dawson, c) Anderson, d) Lindqvist, e) decavanadate, f) sandwich Keggin, g) double Keggin, h) heptamolybdate, i) α - and j) γ -octamolybdate, k) Preyssler, l) Strandberg, and m) Krebs-type structure. Blue polyhedra are $[MO_6]$ (M =any addenda atom), light green polyhedra $[XO_n]$ (X =heteroatom), light green spheres sodium, light blue polyhedra $[WO_6]$, light cyan polyhedra $[MoO_6]$, gray polyhedra $[VO_6]$, purple polyhedra and spheres $[YOn]$ and Y (Y =second heteroatom), orange polyhedra $[PO_4]$, red spheres oxygen[44].

POMs are candidates in both batteries and supercapacitors thanks to their multi reversible redox reactions. The first study on applying POMs in energy

storage dates back to the 1990s[45]. Since then, POM-based materials have been flourishing in electrochemical energy storage applications. POMs can serve as either cathode or anode materials in batteries thanks to their redox reactions in a wide potential range. For instance, phosphomolybdate (PMo12) derivatives can deliver a capacity of 260 mAh g⁻¹ as the cathode[46], or 1500 mAh g⁻¹ as the anode[47] in LIBs. However, the specific capacity of POM cathodes is relatively low due to the high molecular weight of POMs and few electrons being involved per metal atom. The POM anode can deliver high specific capacity because more redox processes take place, but the cycle stability is poor, most likely because the over-reduction reactions are not 100% reversible[48]. Actually, pure isolated POMs are unsuitable as active materials for energy storage. Their electrical conductivities are very poor, since they do not provide extended lattices for electron delocalization, and their multi-electron reactions cannot be fully utilized in a compact crystallized state formed by pure POM clusters. Therefore, most efforts have been devoted to developing POM-based composites. The goals are apparent: increasing conductivity and exposing more active sites. In order to do this, POMs can be anchored in a variety of ways to a variety of conductive materials, from conductive polymers[45, 49, 50] to activated carbon[51], carbon nanotubes [50], nanopipes[52], graphene [51] etc. Our group has done various pioneering work in this direction. We found it critical to get the clusters dispersed at a molecular level for optimal performance step by step. Otherwise, when the fabrication procedure led to growing tiny POM crystals on a conductive framework, such as carbon nanotubes[53], conductive polymers[45, 49, 50, 54-56], graphene[54], etc., not all the clusters were in direct contact with the electrolyte. In these POM-based composites, POMs are crystallized, and their redox reactions are diffusion-controlled. The best merits of POMs (e.g., numerous active sites in direct contact with an electrolyte and fast reversible redox reactions) are not properly exploited in crystallized POM materials and only nano-dispersed POMs can make full use of these merits.

Contrary to crystallized POMs, nano-dispersed individual POM clusters have been shown to be excellent active components for supercapacitors owing to their fast reversible redox reactions[48]. The key to exploiting the fast reversible redox reactions is selecting or designing a matrix that can anchor the POMs clusters discretely. That is, to prepare hybrid materials.

1.3.4 POM-based Hybrid materials

Conventional capacitive materials deliver high power densities but low energy densities, whereas redox-active materials deliver high energy densities. Hybrid materials integrate these two kinds of active materials, which offers opportunities for synergic behaviours and improved properties with respect to their individual components. Transition metal oxides (or carbides, sulphides, phosphates etc.) and carbon-based materials are the two primary types of components. The former store energy through redox reactions, usually are capable of delivering higher energy density, but have poor conductivity, whereas the latter feature EDLC and good conductivity, ensuring a high power density.

As indicated by our above-mentioned study, POMs are intrinsic nanoscale metal oxide clusters that are easy to disperse and very well suited as a component for hybrid materials. The key to taking advantage of POMs is keeping good dispersion or preventing agglomeration. Various nanomaterials can serve as the matrix to disperse POMs, from 1D nanomaterials, like carbon nanotubes[57, 58], to 2D materials, like graphene[59], MXene[60], and to 3D nanomaterials, like, metal–organic frameworks(MOFs)[61] or microporous activated carbons[51].

Our group has carried out some pioneering work in this respect. At first, some conductive polymers (polypyrrole[45], polyaniline[49, 50, 62], poly(3,4-ethylenedioxythiophene)[63] etc.) were combined with POMs to synthesize organic-inorganic hybrid materials. They demonstrated that the addition of POMs could provide extra capacitance (or capacity). However, these organic-inorganic hybrid materials seldom retained high capacitance after 1000 cycles, limited by the intrinsic poor cycle stability. Carbon-based materials usually have better cycle stability than conducting polymers since they do not suffer crystal lattice expansion during charge-discharge while conducting polymers do. Consequently, a new line of work incorporating POMs into a variety of carbon materials, including carbon nanotubes[64], activated carbon[51], graphene[59, 65] and carbon nanotubes was pursued. These hybrid materials could deliver enhanced capacitance and even work in an extended potential window for long term. For instance, activated carbon/phosphotungstic acid hybrid material could provide a specific capacitance of 254 F g^{-1} (130 F cm^{-3}) in sulfuric acid at a working voltage

window of 1.6 V for 30,000 cycles with 98% retention of the initial capacitance[51]. In comparison, the pristine AC only delivered 186 F g⁻¹ (96 F cm⁻³) in the same electrolyte, and the maximum voltage window is 1 V.

Meanwhile, some other groups have also shown interest in developing POM-based materials. Most of them were carried out in the same direction: conducting polymers[66, 67] and/or nanostructured carbon materials[68, 69] were incorporated with POMs. Besides conducting polymers and nanostructured carbons, metal-organic frameworks were also integrated with POMs and several 3D polyoxometallate-based metal organic frameworks (POMOFs) were obtained. Due to MOFs' 3D porous structure and pseudocapacitance, these POMOFs hybrid materials showed very high specific capacitance (up to 900 F g⁻¹ at a current density of 3 A g⁻¹[64, 65]), excellent rate ability and long cycle stability.

Until now, various POM-based hybrid materials have been developed and have shown enhanced capacitive performance. However, as far as we know, all these studies were carried out in aqueous electrolytes. The maximum working voltage was only 1.6 V. Considering that the energy densities are proportional to the voltage window, electrolytes of high potential windows are always favoured.

1.4 Electrolytes

1.4.1 Liquid electrolytes

Electrolytes are another critical component in electrochemical energy storage devices. For supercapacitors, their energy densities are calculated by the following equation:

$$E = CV^2, \quad \text{Eq. 1.3}$$

where C is the capacitance, V is the voltage window. The voltage window of a device strongly depends on the stable potential window of the electrolyte. Due to water splitting, aqueous electrolytes usually have a stable potential window narrower than 1.23 V.

Since POMs tend to decompose in basic conditions, only acidic or neutral aqueous electrolytes are compatible with POM-based hybrid materials. Sulfuric acids are the most commonly used aqueous electrolyte for POMs. Various POM-based hybrid materials, including AC/POMs[70], rGO/POM[59], CNTs/POMs[57],

have shown enhanced capacitive performance in this electrolyte. And in some cases, the voltage window of the device is improved because POMs repress hydrogen evolution. For instance, AC/phosphotungstic acid symmetric supercapacitor can work steadily in 1 M sulfuric acid with a potential window of 1.6 V[51].

Compared with aqueous electrolytes, organic electrolytes and ionic liquids, which have stable potential windows wider than 2.7 V, make supercapacitors with high energy densities. Indeed, a few organic electrolytes, such as 1 M TEABF₄ in acetonitrile (ACN) or propylene carbonate (PC), have been commercialized in electrical double layer supercapacitors for wide application as they outperform aqueous-electrolyte supercapacitors.

However, metal oxides are mostly incompatible with these organic electrolytes and ionic liquids because their redox behaviours are proton-involved and the organic cations do not actively participate in the redox reactions of metal oxides. For instance, MnO₂ and RuO₂, the two typical pseudocapacitive materials, show inferior performance in the commercial organic electrolyte for supercapacitors. However, several studies in which POMs were dissolved in the electrolytes instead of serving as active species on electrodes have proven that POMs are still redox-active in organic electrolytes[71, 72].

To improve the energy densities of POM-based hybrid materials, besides getting larger capacitance, it is more promising to integrate them into the electrode materials for organic electrolytes.

1.4.2 Quasi-solid electrolytes

Along with the demand for and development of wearable electronics, quasi-solid electrolytes (also called gel polymer electrolytes, GPEs) have attracted considerable attention. They have several advantages over conventional liquid electrolytes, including easy and inexpensive packaging, no leakage of toxic electrolytes, and mechanical stability, which allows for fabricating flexible and bendable supercapacitors[73]. Compared with real solid electrolytes (ceramic electrolytes, polyelectrolytes), GPEs usually have relatively high ionic conductivity and better mechanical stability.

Generally, GPEs have three components: a polymer host, a conducting salt, and a solvent which serves as a plasticizer for the polymer and the diffusion path for the conducting salt. Various polymers are used to prepare GPEs, including polyvinyl alcohol (PVA), polymethyl methacrylate (PMMA), polyethylene glycol (PEO), poly(vinylidene fluoride) (PVDF), poly(vinylidene fluoride-cohexafluoropropylene) (PVDF-HFP), etc. Depending on the hydrophilicity of the polymer host, they are suitable for both aqueous and non-aqueous electrolytes.

Aqueous GPEs have been widely studied for their high ionic conductivity, low cost and nontoxicity. Water acts as a plasticizer and the hydrophilic polymers, such as PVA, PMMA, PEO etc., can serve as the polymer matrix, while acids, alkalis and neutral salts can serve as the conducting salts. PVA has dominated the polymer matrix for aqueous GPEs as it is compatible with various conducting salts, and the resultant aqueous GPEs, such as PVA/H₂SO₄, PVA/KOH, PVA/LiCl, which show excellent properties: good ionic conductivity comparable with the liquid electrolytes of the similar composition, wider potential window, and good machinability.

POMs and POM-based hybrid materials have already been incorporated with PVA-based GPEs. Xie et al. integrated phosphomolybdic acid (HPMo12) with PVA/H₃PO₄ GPE, and enhanced the ionic conductivity from 3.85 mS cm⁻¹ (PVA/H₃PO₄) to 5.45 mS cm⁻¹ (PVA/H₃PO₄/HPMo12)[74]. The capacitance of the flexible device based on the PVA/H₃PO₄/HPMo12 GPE doubled thanks to the extra redox activities from HPMo12. Lian et al. developed a PVA/phosphotungstic acid (HPW12) aqueous GEP and applied it in the graphite/RuO₂ asymmetric supercapacitor[75]. This device could work steadily in a voltage window of 1.5 V, wider than the stable potential window of water, which was ascribed to POMs' ability to alter the hydrogen and oxygen evolution potential. Their group has also applied POMs as additives in normal aqueous acid GPEs. For example, silicotungstic acid (HSiW12) was integrated with PVA/H₃PO₄ GPE. As-prepared PVA/H₃PO₄/HSiW12 GPE presented an ionic conductivity of 8 mS cm⁻¹ at the ambient conditions[76]. They added extra SiO₂ as a plasticizer, cross-linker and water-retaining agent and the ionic conductivity was further enhanced to 16 mS cm⁻¹. Furthermore, they prepared PVA/H₅BW₁₂O₄₀ (HBW12) GPE and PVA/H₄SiW₁₂O₄₀ (HSiW12) GPE. PVA/HBW12 outperformed PVA/HSiW12 in

both ionic conductivity and stable potential window[77] and the PVA/HBW12 GPE flexible devices could work in a voltage window of 1.6V.

POM-based hybrid electrodes are also compatible with PVA GPEs. For instance, our group applied rGO/HPMo12 hybrid electrodes in PVA/H₂SO₄ GPE and obtained a high-performance symmetric supercapacitor[59]. Recently, Cheng et al. applied HPMo12 and HSiW12 to incorporate with polyaniline to prepare hybrid electrode and incorporate with PVA/POMs GPEs[78]. The flexible device showed a greatly improved areal capacitance.

Although these devices with aqueous GPEs showed considerably improved capacitive performance, the highest voltage they could reach was only 1.6 V, much lower than organic electrolytes and ionic liquid. As a result, since the device's energy density is proportional to the operating voltage window, electrolytes of a wider stable potential window are always favored in high-performance supercapacitors.

Although non-aqueous GPEs are promising, some issues, such as low ionic conductivity and poor interfacial conductance between the electrolyte-electrode interface, hinder their practical application[79]. Moreover, the compatibility between the polymer and the solvent affects the electrolyte-electrode interfacial conductance. PVDF-HFP is one of the most widely studied polymers for non-aqueous GPEs, thanks to its good compatibility with a variety of organic solvents, including ethylene carbonate (EC), propylene carbonate (PC), acetonitrile (ACN), ethyl methyl carbonate (EMC), etc. Osaka et al.[80] first attempted to apply PVDF-HFP as the binder in the electrode and the polymer matrix in the electrolyte. The GPE contained PC/EC as the solvent and TEABF₄ as the salt. It had an ionic conductivity of 5 mS cm⁻¹, comparable with some organic electrolytes and the activated carbon electrode delivered a specific capacitance of 120 F g⁻¹. Besides activated carbon, other carbon materials, including rGO[81], CNT[82, 83], porous carbon[84], are also integrated with PVDF-HFP GPEs and these devices feature high flexibility, high operating voltage and long cycle life.

POMs have been successfully integrated with aqueous GPEs, or to serve as the electrode to couple with aqueous GPEs. However, as far as we know, no studies have combined POMs with non-aqueous GPEs for supercapacitors because the fast reversible redox activities of POMs are believed to involve protons, that is, in aqueous electrolytes. However, the development of POMs that

can carry out fast reversible redox reactions in aprotic electrolytes, integrating POMs with non-aqueous GPEs could be an effective way to improve capacitive performance.

1.5 Motivation and Objectives

Accordingly, the motivation of this thesis is to develop high-performance POM-based hybrid supercapacitors.

Several studies have proved that some POMs are also redox-active in organic electrolytes. However, they have either applied the crystallized POM electrodes in battery electrolytes[47, 53, 56], or dissolved POMs in some organic solvents[85, 86]. But none of them have applied POM-based hybrid materials in the electrolytes for supercapacitors to fully use the fast reversible redox activities of POMs.

This thesis therefore aims to integrate POMs or POM-based hybrid materials with organic electrolytes to develop high-performance hybrid supercapacitors and has the following objectives:

1. To investigate the electrochemical activities of POMs in conventional organic electrolytes.
2. To integrate these POMs with activated carbon to test the hypothesis that POM-based hybrid materials are compatible with organic electrolytes.
3. To develop novel POM-based hybrid materials for the organic electrolyte.
4. To integrate organic GPE with POMs or POM-based hybrid electrodes to fabricate high-performance organic-electrolyte supercapacitors.

References

- [1] Y.L. Shao, M.F. El-Kady, J.Y. Sun, Y.G. Li, Q.H. Zhang, M.F. Zhu, H.Z. Wang, B. Dunn, R.B. Kaner, *Chemical Reviews*, 118 (2018) 9233-9280.
- [2] C. Choi, D.S. Ashby, D.M. Butts, R.H. DeBlock, Q. Wei, J. Lau, B. Dunn, *Nature Reviews Materials*, (2019).
- [3] P. Simon, Y. Gogotsi, *Nature materials*, 7 (2008) 845-854.
- [4] P.L. Taberna, P. Simon, J.F. Fauvarque, *Journal of The Electrochemical Society*, 150 (2003).
- [5] B. Xu, Y. Chen, G. Wei, G. Cao, H. Zhang, Y. Yang, *Materials Chemistry and Physics*, 124 (2010) 504-509.
- [6] C. Coughon, E. Lebègue, G. Pognon, *Journal of Power Sources*, 274 (2015) 551-559.
- [7] E. Frackowiak, K. Metenier, V. Bertagna, F. Beguin, *Applied Physics Letters*, 77 (2000) 2421-2423.
- [8] Y. Wang, Z. Shi, Y. Huang, Y. Ma, C. Wang, M. Chen, Y. Chen, *The Journal of Physical Chemistry C*, 113 (2009) 13103-13107.
- [9] D. Dubal, A. Jagadale, N. Chodankar, D.-H. Kim, P. Gomez-Romero, R. Holze, *Energy Technology*, (2018).
- [10] C. Vix-Guterl, E. Frackowiak, K. Jurewicz, M. Friebe, J. Parmentier, F. Béguin, *Carbon*, 43 (2005) 1293-1302.
- [11] F. Beguin, V. Presser, A. Balducci, E. Frackowiak, *Adv Mater*, 26 (2014) 2219-2251, 2283.
- [12] T. Brousse, O. Crosnier, D. Bélanger, J.W. Long, 1 - Capacitive and Pseudocapacitive Electrodes for Electrochemical Capacitors and Hybrid Devices, in: D.P. Dubal, P. Gomez-Romero (Eds.) *Metal Oxides in Supercapacitors*, Elsevier, 2017, pp. 1-24.
- [13] E. Herrero, L.J. Buller, H.D. Abruña, *Chemical Reviews*, 101 (2001) 1897-1930.
- [14] B.E. Conway, E. Gileadi, *Transactions of the Faraday Society*, 58 (1962) 2493-2509.
- [15] J.-J. Zhu, L.-L. Yu, J.-T. Zhao, *Journal of Power Sources*, 270 (2014) 411-417.
- [16] L.-L. Yu, J.-J. Zhu, J.-T. Zhao, *Journal of Materials Chemistry A*, 2 (2014).

- [17] W. Wei, X. Cui, W. Chen, D.G. Ivey, *Chemical society reviews*, 40 (2011) 1697-1721.
- [18] X. Chen, R. Paul, L. Dai, *National Science Review*, 4 (2017) 453-489.
- [19] S. Huo, Y. Zhao, M. Zong, B. Liang, X. Zhang, I.U. Khan, X. Song, K. Li, *Journal of Materials Chemistry A*, 8 (2020) 2505-2517.
- [20] L. Chen, Z. Wen, L. Chen, W. Wang, Q. Ai, G. Hou, Y. Li, J. Lou, L. Ci, *Carbon*, 158 (2020) 456-464.
- [21] H.M. Jeong, J.W. Lee, W.H. Shin, Y.J. Choi, H.J. Shin, J.K. Kang, J.W. Choi, *Nano Lett.*, 11 (2011) 2472-2477.
- [22] M.R. Lukatskaya, S. Kota, Z. Lin, M.-Q. Zhao, N. Shpigel, M.D. Levi, J. Halim, P.-L. Taberna, M.W. Barsoum, P. Simon, Y. Gogotsi, *Nature Energy*, 2 (2017).
- [23] M. Naguib, M. Kurtoglu, V. Presser, J. Lu, J. Niu, M. Heon, L. Hultman, Y. Gogotsi, M.W. Barsoum, *Advanced Materials*, 23 (2011) 4248-4253.
- [24] M.R. Lukatskaya, O. Mashtalir, C.E. Ren, Y. Dall'Agnese, P. Rozier, P.L. Taberna, M. Naguib, P. Simon, M.W. Barsoum, Y. Gogotsi, *Science*, 341 (2013) 1502-1505.
- [25] M. Ghidui, M.R. Lukatskaya, M.Q. Zhao, Y. Gogotsi, M.W. Barsoum, *Nature*, 516 (2014) 78-81.
- [26] J. Li, X. Yuan, C. Lin, Y. Yang, L. Xu, X. Du, J. Xie, J. Lin, J. Sun, *Advanced Energy Materials*, 7 (2017).
- [27] Y. Zhu, K. Rajouâ, S. Le Vot, O. Fontaine, P. Simon, F. Favier, *Nano Energy*, 73 (2020).
- [28] F. Bu, M.M. Zagho, Y. Ibrahim, B. Ma, A. Elzatahry, D. Zhao, *Nano Today*, 30 (2020).
- [29] X. Yang, Q. Wang, K. Zhu, K. Ye, G. Wang, D. Cao, J. Yan, *Advanced Functional Materials*, (2021).
- [30] B. Anasori, M.R. Lukatskaya, Y. Gogotsi, *Nature Reviews Materials*, 2 (2017).
- [31] X. Wang, T.S. Mathis, K. Li, Z. Lin, L. Vlcek, T. Torita, N.C. Osti, C. Hatter, P. Urbankowski, A. Sarycheva, M. Tyagi, E. Mamontov, P. Simon, Y. Gogotsi, *Nature Energy*, 4 (2019) 241-248.
- [32] W. Zheng, P. Zhang, J. Chen, W.B. Tian, Y.M. Zhang, Z.M. Sun, *Journal of Materials Chemistry A*, 6 (2018) 3543-3551.
- [33] S. Niu, Z. Wang, M. Yu, M. Yu, L. Xiu, S. Wang, X. Wu, J. Qiu, *ACS nano*, 12 (2018) 3928-3937.

- [34] J. Luo, C. Fang, C. Jin, H. Yuan, O. Sheng, R. Fang, W. Zhang, H. Huang, Y. Gan, Y. Xia, C. Liang, J. Zhang, W. Li, X. Tao, *Journal of Materials Chemistry A*, 6 (2018) 7794-7806.
- [35] J. Lu, H. Ran, J. Li, J. Wan, C. Wang, P. Ji, X. Wang, G. Liu, C. Hu, *Electrochimica Acta*, 331 (2020) 135426.
- [36] B. Saravanakumar, K.K. Purushothaman, G. Muralidharan, *ACS Applied Materials & Interfaces*, 4 (2012) 4484-4490.
- [37] X. Lu, G. Wang, T. Zhai, M. Yu, J. Gan, Y. Tong, Y. Li, *Nano Letters*, 12 (2012) 1690-1696.
- [38] H. Yang, H. Xu, L. Wang, L. Zhang, Y. Huang, X. Hu, *Chemistry*, 23 (2017) 4203-4209.
- [39] P. Gómez-Romero, *Solid State Ionics*, 101-103 (1997) 243-248.
- [40] Y.C. Ji, L.J. Huang, J. Hu, C. Streb, Y.F. Song, *Energy & Environmental Science*, 8 (2015) 776-789.
- [41] L.C.W. Baker, D.C. Glick, *Chemical Reviews*, 98 (1998) 3-50.
- [42] R. Zhong, L. Cui, K. Yu, J. Lv, Y. Guo, E. Zhang, B. Zhou, *Inorg Chem*, 60 (2021) 9869-9879.
- [43] J. Gao, L. Gong, X. Fan, K. Yu, Z. Zheng, B. Zhou, *ACS Appl. Nano Mater.*, 3 (2020) 1497-1507.
- [44] A. Bijelic, M. Aureliano, A. Rompel, *Angew. Chem. Int. Ed. Engl.*, 58 (2019) 2980-2999.
- [45] P. Gómez-Romero, M. Lira-Cantú, *Advanced Materials*, 9 (1997) 144-147.
- [46] H. Wang, S. Hamanaka, Y. Nishimoto, S. Irle, T. Yokoyama, H. Yoshikawa, K. Awaga, *Journal of the American Chemical Society*, 134 (2012) 4918-4924.
- [47] T. Wei, M. Zhang, P. Wu, Y.-J. Tang, S.-L. Li, F.-C. Shen, X.-L. Wang, X.-P. Zhou, Y.-Q. Lan, *Nano Energy*, 34 (2017) 205-214.
- [48] M.R. Horn, A. Singh, S. Alomari, S. Goberna-Ferrón, R. Benages-Vilau, N. Chodankar, N. Motta, K. Ostrikov, J. MacLeod, P. Sonar, P. Gomez-Romero, D. Dubal, *Energy & Environmental Science*, 14 (2021) 1652-1700.
- [49] P. Gómez-Romero, M. Chojak, K. Cuentas-Gallegos, J.A. Asensio, P.J. Kulesza, N. Casañ-Pastor, M. Lira-Cantú, *Electrochemistry Communications*, 5 (2003) 149-153.
- [50] M. Lira-Cantú, P. Gómez-Romero, *Chemistry of materials*, 10 (1998) 698-704.

- [51] J. Suárez-Guevara, V. Ruiz, P. Gomez-Romero, *Journal of Materials Chemistry A*, 2 (2014) 1014-1021.
- [52] D.P. Dubal, B. Ballesteros, A.A. Mohite, P. Gomez-Romero, *ChemSusChem*, 10 (2017) 731-737.
- [53] J. Hu, Y. Ji, W. Chen, C. Streb, Y.-F. Song, *Energy & Environmental Science*, 9 (2016) 1095-1101.
- [54] M. Zhang, T. Wei, A.M. Zhang, S.-L. Li, F.-C. Shen, L.-Z. Dong, D.-S. Li, Y.-Q. Lan, *ACS Omega*, 2 (2017) 5684-5690.
- [55] H. Yang, T. Song, L. Liu, A. Devadoss, F. Xia, H. Han, H. Park, W. Sigmund, K. Kwon, U. Paik, *The Journal of Physical Chemistry C*, 117 (2013) 17376-17381.
- [56] E. Ni, T. Tsukada, Q. Wen, N. Sonoyama, *Journal of the Electrochemical Society*, 166 (2018) A5226-A5230.
- [57] M. Genovese, K. Lian, *Electrochemistry Communications*, 43 (2014) 60-62.
- [58] A. Guillen-Lopez, N.D. Espinosa-Torres, A.K. Cuentas-Gallegos, M. Robles, J. Muniz, *Carbon*, 130 (2018) 623-635.
- [59] D.P. Dubal, J. Suarez-Guevara, D. Tonti, E. Enciso, P. Gomez-Romero, *Journal of Materials Chemistry A*, 3 (2015) 23483-23492.
- [60] H. Chao, H. Qin, M. Zhang, Y. Huang, L. Cao, H. Guo, K. Wang, X. Teng, J. Cheng, Y. Lu, H. Hu, M. Wu, *Advanced Functional Materials*, (2021).
- [61] N.N. Du, L.G. Gong, L.Y. Fan, K. Yu, H. Luo, S.J. Pang, J.Q. Gao, Z.W. Zheng, J.H. Lv, B.B. Zhou, *ACS Appl. Nano Mater.*, 2 (2019) 3039-3049.
- [62] A.K. Cuentas-Gallegos, M. Lira-Cantú, N. Casañ-Pastor, P. Gómez-Romero, *Advanced Functional Materials*, 15 (2005) 1125-1133.
- [63] J. Vaillant, M. Lira-Cantu, K. Cuentas-Gallegos, N. Casañ-Pastor, P. Gómez-Romero, *Progress in Solid State Chemistry*, 34 (2006) 147-159.
- [64] A.K. Cuentas-Gallegos, R. Martínez-Rosales, M. Baibarac, P. Gómez-Romero, M.E. Rincón, *Electrochemistry Communications*, 9 (2007) 2088-2092.
- [65] J. Suarez-Guevara, V. Ruiz, P. Gomez-Romero, *Physical chemistry chemical physics : PCCP*, 16 (2014) 20411-20414.
- [66] M. Wang, Y. Zhang, T. Zhang, Y. Li, M. Cui, X. Cao, Y. Lu, D. Peng, W. Liu, X. Liu, T. Wang, Y. Huang, *Nanoscale*, (2020).
- [67] S. Herrmann, N. Aydemir, F. Nagele, D. Fantauzzi, T. Jacob, J. Travas-Sejdic, C. Streb, *Advanced Functional Materials*, 27 (2017).
- [68] M. Genovese, K. Lian, *Journal of Materials Chemistry A*, 5 (2017) 3939-3947.

- [69] H.Y. Chen, R. Al-Oweini, J. Friedl, C.Y. Lee, L.L. Li, U. Kortz, U. Stimming, M. Srinivasan, *Nanoscale*, 7 (2015) 7934-7941.
- [70] V. Ruiz, J. Suarez-Guevara, P. Gomez-Romero, *Electrochemistry Communications*, 24 (2012) 35-38.
- [71] M.H. Chiang, J.A. Dzielawa, M.L. Dietz, M.R. Antonio, *Journal of Electroanalytical Chemistry*, 567 (2004) 77-84.
- [72] J. Zhang, A.M. Bond, D.R. MacFarlane, S.A. Forsyth, J.M. Pringle, A.W.A. Mariotti, A.F. Glowinski, A.G. Wedd, *Inorganic Chemistry*, 44 (2005) 5123-5132.
- [73] D.P. Dubal, N.R. Chodankar, D.H. Kim, P. Gomez-Romero, *Chem Soc Rev*, 47 (2018) 2065-2129.
- [74] Y. Xie, J. Wang, *Journal of Sol-Gel Science and Technology*, 86 (2018) 760-772.
- [75] K. Lian, Q. Tian, *Electrochemistry Communications*, 12 (2010) 517-519.
- [76] H. Gao, K. Lian, *J. Electrochem. Soc.*, 160 (2013) A505-A510.
- [77] H. Gao, A. Virya, K. Lian, *J. Mater. Chem. A*, 3 (2015) 21511-21517.
- [78] D. Cheng, B. Li, S. Sun, L.-J. Zhu, Y. Li, X.-L. Wu, H.-Y. Zang, *CCS Chemistry*, 3 (2021) 1649-1658.
- [79] H. Dai, G. Zhang, D. Rawach, C. Fu, C. Wang, X. Liu, M. Dubois, C. Lai, S. Sun, *Energy Storage Materials*, 34 (2021) 320-355.
- [80] T. Osaka, X. Liu, M. Nojima, T. Momma, *Journal of The Electrochemical Society*, 146 (1999) 1724-1729.
- [81] O. Okhay, A. Tkach, P. Staiti, F. Lufrano, *Electrochimica Acta*, 353 (2020).
- [82] Y. Kumar, G.P. Pandey, S.A. Hashmi, *The Journal of Physical Chemistry C*, 116 (2012) 26118-26127.
- [83] L.-Q. Fan, Q.-M. Tu, C.-L. Geng, Y.-L. Wang, S.-J. Sun, Y.-F. Huang, J.-H. Wu, *International Journal of Hydrogen Energy*, 45 (2020) 17131-17139.
- [84] S.N. Syahidah, S.R. Majid, *Electrochimica Acta*, 112 (2013) 678-685.
- [85] B. Chen, R. Neumann, *Physical chemistry chemical physics : PCCP*, 18 (2016) 22487-22493.
- [86] M. Sadakane, E. Steckhan, *Chemical Reviews*, 98 (1998) 219-238.

Chapter 2 Experimental and Characterization Procedures

2.1 Materials Preparation

All the chemicals were used as received. Table 2.1 presents the information of the main chemicals.

Table 2.1 Specification of the main chemicals

Name	Chemical formula	Grade	Supplier
Activated carbon	C	≥99%	Norit
Tetramethylammonium hydroxide solution	(CH ₃) ₄ N(OH)	25 wt. % in water	Sigma-Aldrich
Tetraethylammonium hydroxide solution	(C ₂ H ₅) ₄ N(OH)	35 wt. % in water	Sigma-Aldrich
Tetrabutylammonium hydroxide solution	(CH ₃ CH ₂ CH ₂ CH ₂) ₄ N(OH)	40 wt. % in water	Sigma-Aldrich
Dodecyltrimethylammonium bromide	CH ₃ (CH ₂) ₁₁ N(CH ₃) ₃ Br	≥98%	Sigma-Aldrich
Hexadecyltrimethylammonium bromide	CH ₃ (CH ₂) ₁₅ N(Br)(CH ₃) ₃	≥98%	Sigma-Aldrich
Tetraethylammonium chloride	(C ₂ H ₅) ₄ N(Cl)	≥99%	Sigma-Aldrich
Tetrabutylammonium chloride	[CH ₃ (CH ₂) ₃] ₄ NCl	≥99%	Sigma-Aldrich
Tetramethylammonium chloride	(CH ₃) ₄ N(Cl)	≥99%	Sigma-Aldrich
Lithium fluoride	LiF	≥99%	Sigma-Aldrich
Poly(vinyl alcohol) averageMw 89,000-98,000	[-CH ₂ CHOH-] _n	≥99%	Sigma-Aldrich
Polyvinylidene fluoride (Kynar 1810)	(CH ₂ CF ₂) _n	≥99%	Arkema
Phosphomolybdic acid hydrate	H ₃ [P(Mo ₃ O ₁₀) ₄] · xH ₂ O	≥99.9%	Sigma-Aldrich
Phosphotungstic acid hydrate	H ₃ [P(W ₃ O ₁₀) ₄] · xH ₂ O	reagent grade	Sigma-Aldrich
Tungstosilicic acid hydrate	H ₄ [Si(W ₃ O ₁₀) ₄] · xH ₂ O	≥99.9%	Sigma-Aldrich

Tetraethylammonium tetrafluoroborate	$(C_2H_5)_4N(BF_4)$	$\geq 99\%$	Sigma-Aldrich
<i>Table 2.1 continue</i>			
Acetonitrile	CH_3CN	electronic grade	Sigma-Aldrich
N,N-Dimethylformamide (DMF)	$HCON(CH_3)_2$	$\geq 99.8\%$	Sigma-Aldrich
1-Ethyl-3-methylimidazolium bis(trifluoromethylsulfonyl)imide	$C_8H_{11}F_6N_3O_4S_2$	$\geq 97.0\%$	Sigma-Aldrich
Poly(vinylidene fluoride-co-hexafluoropropylene)(average Mn ~130,000)	$(-CH_2CF_2-)_x[-CF_2CF(CF_3)-]_y$	reagent grade	Sigma-Aldrich
Carbon SuperP	C	$\geq 99\%$	Thermo Fisher Scientific
Ti_3AlC_2 MAX phase	Ti_3AlC_2	$\geq 99\%$	Y-Carbon

2.1.1 Preparation of alkylammonium POM salts

All the alkylammonium POM salts were synthesized through metathesis reaction in the light of the literature method[1]. Typically, 200 mL of a 20 mM aqueous solution of polyoxometalic acids was added to 200 mL of a 70 mM aqueous solution of alkylammonium salts. A considerable amount of white precipitate appeared immediately. The suspension was kept stirring for 6 h, then filtered-off. The precipitate was washed with deionized water and dried overnight in air at 80 °C. A variety of alkylammonium POMs salts were prepared, both with tetraethylammonium ($[C_2H_5]_4N$), (TEA)) and tetrabutylammonium ($[C_4H_9]_4N$), (TBA)) cations ($([C_2H_5]_4N)_3PW_{12}O_{40}$ (TEAPW12), $([C_4H_9]_4N)_3PW_{12}O_{40}$ (TBAPW12), and $([C_2H_5]_4N)_3Mo_{12}O_{40}$ (TEAPMo12)).

2.1.2 Preparation of AC/POM hybrid materials

An activated carbon (AC) suspension was prepared by sonicating 0.5 g AC in 100 mL solvent (Milli-Q water for AC/POMs acids, or DMF for AC/alkylammonium POMs salts) for 1 h. Variable volumes of 20 mM POMs acids

solutions (or alkylammonium POMs salts solutions) were added to the suspension, which was kept it 5 h in a bath sonicator and stirred overnight. Finally, the sample was collected by filtration, and dried at 80 °C for 12 h in vacuum oven.

2.1.3 Preparation of MXene ($\text{Ti}_3\text{C}_2\text{T}_x$) through delamination with fluorine

MXene ($\text{Ti}_3\text{C}_2\text{T}_x$) was synthesized through a fluorine (LiF/HCl) etching method. Namely, 0.5 g MAX phase (Ti_3AlC_2) was added slowly to a mixture of 0.5 g LiF and 10 mL 9 M HCl solution. The etching process was carried out in a Teflon-lined autoclave for 24 h at 35°C. For washing and delamination, the mixture was poured into a 50 mL centrifugation tube and washed with deionized water by centrifugation at 3500 rpm for 5 minutes. The supernatant was discarded. This step was repeated for several cycles until the pH of the dark-green supernatant was >6. The grey sediment at the bottom got swollen upon washing, which indicates the delamination. Finally, the sediment was dispersed in water by hand-shaking and deaerated with Ar for 20 minutes, stored in the fridge for future use. A measured amount of the colloid was filtered-off onto a Celgard 3501 membrane (25 μm Microporous Monolayer Membrane (PP), Surfactant-Coated) to determine the concentration, and for further use.

2.1.4 Preparation of MXene trough delamination with alkylammonium hydroxide

$\text{Ti}_3\text{C}_2\text{T}_x$ was treated with alkylammonium hydroxide to replace Li^+ with alkylammonium cation. Typically, 5 mL 40% alkylammonium hydroxide was mixed with 50 mL $\text{Ti}_3\text{C}_2\text{T}$ colloid(around 1 mg mL^{-1}), which was shaken overnight. A certain amount of this mixture was filtered off, washed with water until the filtrate was neutral and dried at 60 °C under vacuum for further characterization.

2.1.5 Preparation of MXene/alkylammonium phosphotungstate

After the washing process of preparing MXene/TEAOH (i.e., until the pH of filtrate < 8.5), 20 mL of 20 mM phosphotungstic acid was added on the residue, that was left to rest for 3 h, then filtered again and washed until the filtrate was neutral (pH>5.5), thereby obtaining the MXene/POMs hybrid (MXene/TEAPW12).

2.1.6 Preparation of MXene/HPW12

20 mL $\text{Ti}_3\text{C}_2\text{T}_x$ colloid (around 1 mg mL^{-1}) was mixed with 20 mL 10 mM phosphotungstic acid ($\text{H}_3\text{PW}_{12}\text{O}_{40}$, HPW12) solution, and probe-sonicated for 1 h under circulating cooling water at $10 \text{ }^\circ\text{C}$. The mixture was filtered-off and washed with Milli-Q water until the filtrate was neutral. The product was peeled off from the membrane, dried in a vacuum oven at $60 \text{ }^\circ\text{C}$ and stored in an argon-filled glovebox. As-prepared sample (MXene/HPW12) could serve as a free-standing electrode.

2.1.7 Preparation of MXene/AC/HPW12 triple hybrids

0.5 g activated carbon and 2.88 g phosphotungstic acid (HPW12) were added into 50 mL MXene colloid (1 mg mL^{-1}) and kept under probe-sonication for 1 h under circulating cooling water to keep the temperature below 10°C . Subsequently, the mixture was filtered-off on a Celgard 3501 membrane (thickness=25 μm) to obtain a free-standing electrode.

2.1.8 Preparation of MXene/AC/TEAPW12 triple hybrids

AC/TEAPW12 was prepared following the previously reported method. Then, 0.1 g AC/TEAPW12 was added into 100 mL MXene colloid (1 mg mL^{-1}) and kept in probe-sonication for 1 h under circulating cooling water to keep the temperature below $10 \text{ }^\circ\text{C}$. The mixture was filtered-off on a Celgard 3501 membrane to get a free-standing electrode.

2.1.9 Preparation of gel electrolyte

Typically, 2 g of Poly(vinylidene fluoride)-co-hexafluoropropylene (PVDF-HFP) was added to 10 mL acetone under vigorous stirring at $50 \text{ }^\circ\text{C}$ until a transparent viscous solution formed. Subsequently, the solution was cast on a glass plate using the doctor-blade method. After a few minutes, the acetone evaporated, and a white, half-transparent film was obtained. With this method, the film can be easily peeled off by a spatula, stored in the argon-filled glove box for further use. PVDF-HFP films of different thicknesses can be obtained by selecting separate doctor-blade bars, ranging from 2 μm to 36 μm . The film needs to be soaked in the liquid electrolyte just before assembling the devices.

2.2 Basic Characterization Techniques

2.2.1 X-ray diffraction (XRD)

XRD is a powerful technique for characterizing the crystal structure of the sample, or perform quantitative analysis on a sample composed of different phases. It relies on Bragg's law (Eq 2.1), proposed by William Henry and William Lawrence Bragg in 1912. As shown in Fig. 2.1, when the X-ray beam interacts with the sample at a specific angle, a set of lattice planes, whose interplanar distances meet Bragg's law, diffract the X-ray and give the signal to the detector. The intensity of this signal relates to the atoms and their location, which is another characteristic of the crystal structure. Therefore, by scanning a powder sample in a range of angles, we can detect the diffracted signals from all possible planes. The position and the intensity of the diffraction peaks are characteristic of a crystal structure.

$$n\lambda = 2d\sin\theta \quad \text{Eq 2.1}$$

The powder XRD patterns were collected on a PANalytical X'pert Pro-MRD diffractometer with Cu K α radiation (wavelength=1.5406 Å), a Ge(440) monochromator and PIXel detector, with a scan rate of 0.03 ° s⁻¹ from 3° to 80°.

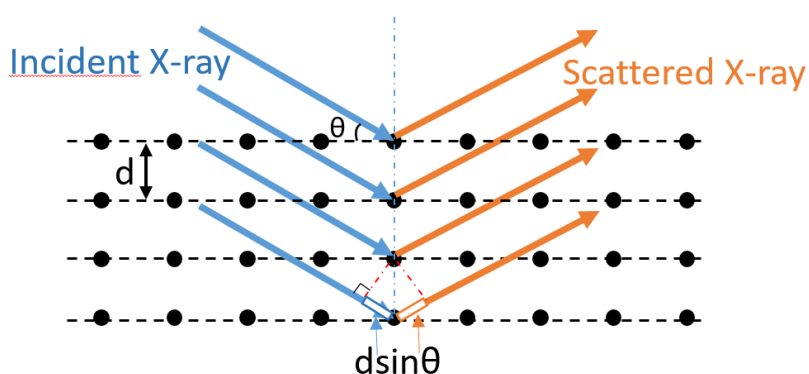


Fig. 2.1 Representation on how the incident X-ray meet the Bragg's law to produce a scattered beam.

2.2.2 Fourier-transform infrared spectroscopy (FT-IR)

Fourier transform infrared spectroscopy is a vibrational spectroscopy which constitutes an effective tool for determining bonding characters of samples. Infrared spectroscopy exploits the detection of characteristic absorbed frequencies corresponding to vibrational modes, which can be associated to specific bonds or functional groups in molecules or solids. These frequencies match the frequency of the bond or group vibration, called resonant frequencies. The resonant frequencies relate to the strength of the bond, and the mass of the atoms at either end of it. Therefore, the frequency of the vibrations is associated with a particular bond type.

The Fourier Transform nature of this technique means that instead of using a monochromatic beam and scanning its frequency, the sample is irradiated with an infrared beam of constant wavelength. The computer can then perform the Fourier transform to convert the raw data (light absorption for each mirror position) into the desired result (light absorption for each wavelength).

In this study, the FT-IR spectra were performed on Bruker Tensor 27 FTIR spectrometer in attenuated total reflectance mode. The resultant spectrum was a combination of 32 scans, with a data spacing of 1.928 cm^{-1}

2.2.3 Thermogravimetric Analysis (TGA)

In thermogravimetric analysis, the mass of the sample is recorded over time as the temperature increases. Many physical process, including phase transitions, absorption, and desorption as well as chemical process, such as pyrolysis, chemisorption, and solid-gas reaction can be detected and studied.

In this study, the thermogravimetric analysis were carried out by NETZSCH-STA 449 F1 Jupiter thermal analysis system with the heating rate of $10\text{ }^{\circ}\text{C min}^{-1}$ under dry air or nitrogen flow.

2.2.4 Specific Surface Area and Pore Size Distribution

Specific surface area was analysed through nitrogen adsorption isotherm measurements at 77 K on the basis of the Brunauer-Emmett-Teller (BET) method. This method continues to be widely used for the evaluation of surface areas of

micro- and mesoporous adsorbents. Usually, two stages are involved in the evaluation of the BET area. First, it is necessary to transform a physisorption isotherm into the “BET plot” and use it to derive the value of the BET monolayer capacity, n_m . The second stage is the calculation of the specific surface area, S , which requires knowledge of the molecular cross-sectional area. The monolayer capacity, n_m , is calculated from the adsorption isotherm using the BET equation:

$$\frac{1}{n\left(\frac{P_0}{P} - 1\right)} = \frac{1}{n_m C} + \frac{C - 1}{n_m C} \left(\frac{P_0}{P}\right), \quad \text{Eq 2.2}$$

where n is the adsorbed amount, n_m is the monolayer capacity and C a constant which gives an indication of the order of magnitude of the attractive adsorbent–adsorbate interactions, P and P_0 are the equilibrium and the saturation pressure of adsorbates at the temperature of adsorption, respectively.

From the BET equation, we can obtain a linear plot with $1/(n(P_0/P - 1))$ on y-axis and P_0/P on x-axis in the range of P_0/P to determine the slope $(C - 1)/(n_m C)$ and the y-intercept $(1/(n_m C))$.

$$S_{BET} = \frac{n_m N s}{V a} \quad \text{Eq 2.3}$$

Where N is the Avogadro number, s is the adsorption cross section of the adsorbate, V is the molar volume of the adsorbate gas, and a the mass of the sample.

The microporous volume was calculated using the Dubinin–Radushkevich equation (Eq 2.5):

$$A = -RT \ln\left(\frac{P_0}{P}\right) \quad \text{Eq 2.4}$$

$$w = w_0 \exp\left[-\left(\frac{A}{E}\right)^2\right], \quad \text{Eq 2.5}$$

where w_0 ($\text{cm}^3 \text{ kg}^{-1}$) presents the maximum sorbate adsorption loading, E (kJ mol^{-1}) is the characteristic energy associated to the given working.

Since activated carbon contains a lot of micropores, we have to use density functional theory to evaluate the pore size distribution. Accordingly, volumetric N_2

sorption isotherms were collected at 77 K (N₂) using an ASAP 2020 HD (Micromeritics). Temperature was controlled by using a liquid nitrogen bath and total pore volume (V_{total}) was calculated at $P/P_0 = 0.95$, and microporous volume (V_{micro}) was calculated using the Dubinin–Radushkevich equation. Pore size distribution was estimated using a density functional theory (DFT) model (N₂–cylindrical pores–oxide surface) implemented in the Microactive 4.00 software with a regularization factor of 0.01.

2.2.5 Scanning Electron Microscopy (SEM)

Scanning electron microscopy is an ideal technique for studying the overall microstructure and morphology of samples. In SEM, an electron beam scans the sample and the scattered electrons are collected to produce the image. Two kinds of scattered electrons are mainly used in SEM: secondary electrons and back-scattered electrons. Secondary electrons originate from the surface or the near-surface regions of the sample. They are a result of inelastic interactions between the primary electron beam and the sample and have lower energy than the backscattered electrons. Secondary electrons are very useful for the inspection of the topography of the sample's surface. In contrast, back-scattered electrons are a result of elastic collisions of electrons with atoms, which results in a change in the electrons' trajectory. Larger atoms are much stronger scatterers of electrons than light atoms, and therefore produce a higher signal. The brightness of the image depicts the atomic number Z of the element.

In this study, Quante 650 Field-Emission-Gun microscopy was used and the electron energy was selected from 2 kV to 20 kV depending on the conductivities, crystallinities, thicknesses of samples, etc. in order to obtain clear images.

2.2.6 Transmission Electron Microscopy (TEM)

Transmission electron microscopy takes images by making use of the interactions between the electrons and the atoms and recording electrons going through the sample. A high-energy electron beam is shone on a very thin sample and the electrons collide with the atoms and change their directions. The scattering angle contains a lot of information related, for example, to thickness, and density, which can be used for imaging.

The De Broglie wavelength of electrons can be 0.1 – 0.2 nm, while the wavelength of visible light is 400 – 760 nm. The resolution of any optical system is defined by the Abbe's equation:

$$d = \frac{\lambda}{2n \sin\theta}, \quad \text{Eq 2.6}$$

where d is the minimum resolvable distance, λ is the wavelength, n is the refractive index and θ is the aperture angle of the objective lens. Thus, TEM can provide much higher resolution than optical microscopy.

2.2.7 High-Angle Annular Dark-Field Scanning Transmission Electron Microscopy (HAADF-STEM)

A scanning transmission electron microscope (STEM) is a type of transmission electron microscope (TEM). Unlike conventional TEM in which the electron beam is shone on the whole plane, in STEM, the electron beam is focused to a fine spot and then scanned over the sample in a raster illumination system.

The high-angle annular dark-field detector is the most commonly used detector for STEM. It produces an annular dark field image formed by very high angle, incoherently scattered electrons (Rutherford scattered from the nucleus of the atoms) - as opposed to Bragg scattered electrons. This technique is highly sensitive to variations in the atomic number of atoms in the sample (Z-contrast images). For elements of high Z, their nuclei scatter more electrons at higher angles due to greater electrostatic interactions between the nucleus and electron beam. Thus, they appear to be brighter in HAADF-STEM images.

2.2.8 Energy Dispersive X-ray Spectroscopy (EDX)

EDX is a method for chemical analytical characterization of materials. EDX is generally affiliated to an electron microscopy instrument such as transmission electron microscopy (TEM) or scanning electron microscopy (SEM).

Energy dispersive X-ray spectroscopy is usually affiliated with SEM or TEM. It records the energy and intensity of the x-rays generated by the excitation of

atoms in the sample by the electron beam of the electrons on the sample, which could provide a qualitative and quantitative elemental analysis.

When the core electrons from the atoms in the sample are excited by the electron beam, an electron from a higher binding energy electron level falls into the core hole and emit an X-ray with the energy of the difference of the electron level binding energies. The energy between different electronic levels is a characteristic of an element. Therefore, by analyzing the energy and intensity of the X-rays, we can collect the type and quantity information of elements in the sample. We can perform mapping and linear scan to see the distribution of various elements.

In this study, EDX were performed on both Quante 650 Field-Emission-Gun microscopy and FEI Tecnai G2 F20 microscopy.

2.2.9 X-ray photoelectron spectroscopy (XPS)

X-ray photoelectron spectroscopy (XPS) is a powerful surface-probing technique for quantitative analysis of the elemental composition of a material and determining the binding states of the elements.

XPS is based on the photoelectric effect. A soft X-ray irradiates the sample and some photoelectrons are emitted, whose kinetic energy is associated with the binding energy of the electron and the energy of the x-ray, as shown in Eq2.7,

$$BE = hv - KE - \Phi \quad , \quad \text{Eq 2.7}$$

where BE is the binding energy, hv is the energy of X-ray, KE is the kinetic energy of emitted electron and Φ is the work function (a constant). Thus, any electron with a binding energy less than the X-ray source energy is emitted from the sample, observed with the XPS technique and recorded as spectra. Since the nearest neighbours and the oxidation state of the elements affect the binding energy of the photoelectron, XPS reveal the chemical environment and the composition of the elements on the surface of materials.

In this thesis, XPS was collected on Phoibos 150 probe from SPECS. Peak fitting for the high-resolution spectra was performed using CasaXPS Version

2.3.1. Before the peak fitting, the background was subtracted using a Shirley function.

2.3 Electrochemical Characterization and Energy storage Tests

2.3.1 Preparation of the electrodes

Two kinds of electrodes were prepared: a conventional one for the use with liquid electrolytes and a special one for gel polymer electrolyte.

The conventional working electrodes were fabricated by mixing the active material, carbon black and polyvinylidene fluoride (PVDF) at a weight ratio of 85:5:10. Typically, the mixture was first formed as a slurry by adding a few drops of N-methyl-2-pyrrolidinone, then coated onto aluminum foil using the doctor-blade method, and dried under vacuum at 120 °C for 12 h.

The special working electrodes for GPE were prepared by dispersing the active materials, carbon black and PVDF-HFP (pre-dissolved in NMP) at a weight ratio of 85:5:10. The slurry was stirred for 6 h, then coated onto aluminium foil, and dried under vacuum at 120 °C for 12 h.

The characterization of electrodes and devices were performed with BioLogic VMP3 multichannel potentiostat.

2.3.2 Cyclic Voltammetry (CV)

Cyclic Voltammetry, which measures the current's variation of potential, is one of the most useful techniques in electrochemistry. The potential applied to the working electrode with respect to a reference electrode is cyclically swept at a given scan rate and the resulting current passing through the working electrode and counter electrode is measured and plotted as a function of potential. The key of CV is that the potential measured at the WE is measured in the absence of any ohmic drop associated with the passing current (no current between WE and RE). If the counter electrode is also used as the reference electrode, this current versus voltage plot should not be considered a CV; instead it could be called a "cyclic polarization" experiment (CP). Fig. 2.2 illustrates the difference between three-electrode and two-electrode setups. CV is an effective method to explore

the electrochemical behaviors of the working electrode in a three-electrode configuration, and CP is widely used to characterize the capacitance (or capacity) of the device in two electrode systems.

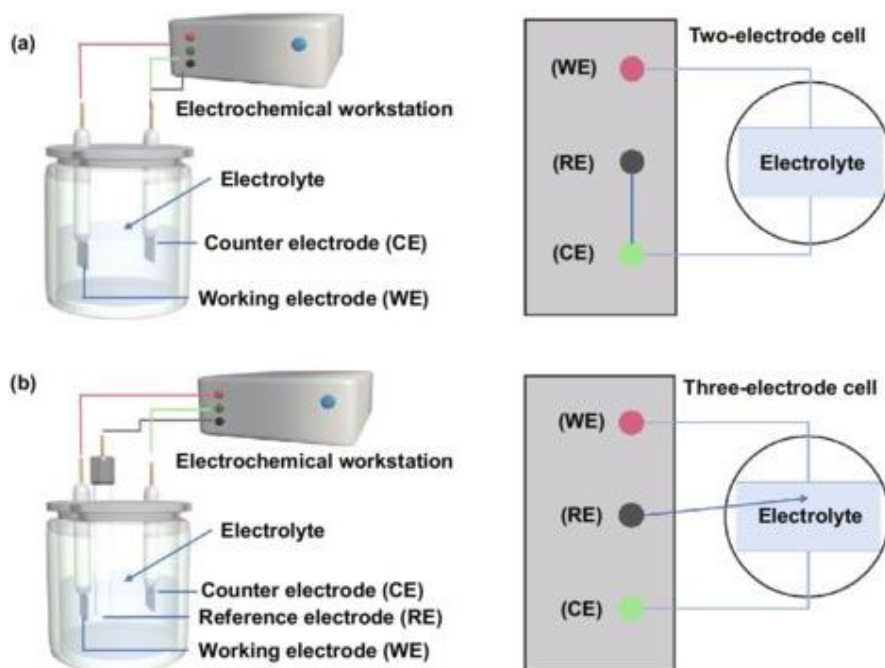


Fig. 2.2 Schemes illustrating the experimental setups of (a) two-electrode and (b) three-electrode cells[2]

For pure capacitive electrodes (or devices), the CV (or CP) exhibits a rectangular profile because no voltage-specific redox reaction happens which leads to current increases at a specific potential (or voltage). Otherwise, if the energy process involves any redox reactions, the CV (or CP) present peaks or waves at potentials characteristic of the redox processes.

Both CV and CP can be utilized to calculate the capacitance of the electrode or the device (only for CP). The capacitance of the electrode in the three-electrode configuration, or the capacitance of the device in the two-electrode system can be calculated as follows:

$$C = \frac{\int I(V) \cdot dV}{2v\Delta V}, \quad \text{Eq 2.8}$$

where $\int I(V) \cdot dV$ is the integration area of CV (or CP), v is the scan rate and ΔV is voltage window.

In a symmetric supercapacitor, two identical electrodes are connected in series and the capacitance of the device C and the capacitance of the electrode C_e obey the following equation:

$$\frac{1}{C} = \frac{1}{C_e} + \frac{1}{C_e} \quad \text{Eq 2.9}$$

Thus, the capacitance of one electrode is two times the capacitance of the device.

Bruce Dunn et al.,[3] developed a method to estimate the surface capacitive and diffusion-controlled charge contributions to the total charge stored by analyzing the CVs at various scan rates. The dependence of the current on the scan rate can provide insights into the charge-storage mechanism according to

$$i = av^b, \quad \text{Eq 2.10}$$

where i is the maximum peak current obtained at a specific scan rate v , and a and b are adjustable parameters.

For a diffusion-controlled process, the voltammetric current i is expected to be proportional to the square root of the scan rate v ($b=0.5$). By contrast, the surface capacitive response follows a linear dependence on the scan rate ($b=1$). The following equation Eq 2.11 can be derived from Eq 2.10,

$$\log i = \log a + b \log v, \quad \text{Eq 2.11}$$

so the value of b for different potentials can be determined from the slope of the straight line of $\log i$ vs $\log v$. This equation is usually used to analyse whether the energy storage process is diffusion-controlled or not at a specific potential.

To analyse the contribution of different energy storage mechanisms to the total capacitance (or capacity) in the whole potential range, we can formally divide the voltammetric current into two parts by the following equation:

$$i(V) = k_1v + k_2v^{0.5}, \quad \text{Eq 2.12}$$

where $i(V)$ is the voltammetric current at the potential V , k_1v is the current contributions from the capacitive process and $k_2v^{0.5}$ is the current contributions from the diffusion-controlled process. This equation can be rearranged to

$$\frac{i(V)}{v^{0.5}} = k_1v^{0.5} + k_2. \quad \text{Eq 2.13}$$

Since we can run CVs at various scan rates and collect voltammetric current at any potentials, then we can obtain the k_1 and k_2 values from the slope and the y axis intercept by linear fitting of $i(V)/v^{0.5}$ vs $v^{0.5}$ at any potential. With the assistance of programming, we can obtain k_1 and k_2 values at different potentials and plot surface capacitive current vs potential and diffusion-controlled current vs potential, whose integrated areas relate to contributions from surface capacitive process and diffusion-controlled process, respectively.

2.3.3 Galvanostatic Charge-Discharge (GCD)

Galvanostatic charge-discharge is an electrochemical technique which consists of applying a constant current for charging or discharging a cell while recording the potential (or voltage) over time. The potential is bound by the upper limit and lower limit. Once the potential reaches these limits, the inverse current is applied.

For energy storage processes involving redox reactions, the potential remains almost constant until the redox process related to the charge or the discharge finishes. For the surface capacitive processes, the potential increases or decreases almost linearly during the charging or discharging.

A Galvanostatic discharge curve is the most common way to calculate the capacitance (or capacity), using the following equation for a pure capacitive device:

$$C = \frac{I\Delta t}{\Delta V}, \quad \text{Eq 2.14}$$

where I is the current, Δt is the discharge time and ΔV is the voltage window.

While for a device involving redox reactions (i.e. hybrid capacitors), the capacitance should be calculated in another way:

$$C = \frac{I \int V(t) \cdot dt}{\Delta V^2}, \quad Eq\ 2.15$$

where $\int V(t) \cdot dt$ is the integrated area of discharge curve.

For a symmetric capacitor, the capacitance of the electrode C_e is two times of the capacitance of the device C .

The gravimetric capacitance is calculated according to

$$C_g = \frac{C_e}{m} = \frac{2C}{m}, \quad Eq\ 2.16$$

where m is the mass of the active material on one electrode.

The volumetric capacitance is calculated according to

$$C_v = \frac{C_e}{V_e} = \frac{2C}{V_e}, \quad Eq\ 2.17$$

where V_e is the volume of the electrode

The energy density normalized by volume is calculated according to

$$E = \frac{C \Delta V^2}{8 V_e}; \quad Eq\ 2.18$$

normalized by mass

$$E = \frac{C \Delta V^2}{8 m}; \quad Eq\ 2.19$$

and the power density

$$P = \frac{E}{\Delta t}. \quad Eq\ 2.20$$

2.3.4 Electrochemical Impedance Spectroscopy (EIS)

Electrochemical impedance spectroscopy is an alternating current technique. During the measurement, the alternating voltages at various frequencies serve as the exciting signals, and cause alternating current signals that can be considered a Fourier series. These are then processed into frequency ω and phase shift φ , where impedance is expressed as the complex number:

$$Z(\omega) = Z_0 \exp(j\varphi) = Z_0(\cos\varphi - j\sin\varphi). \quad Eq\ 2.21$$

$Z(\omega)$ has the real and imaginary parts and the plot of $-Z''(\omega)$ vs $-Z'(\omega)$ is called the Nyquist plot.

EIS data are commonly analyzed by fitting to an equivalent electrical circuit model. Most of the circuit elements in the model are common electrical elements such as resistors, capacitors, and inductors. The impedance of a resistor is independent of frequency and has no imaginary component. The impedance of an inductor increases as frequency increases. Inductors have only an imaginary impedance component. A capacitor's impedance decreases as the frequency is raised. Capacitors also have only an imaginary impedance component. The current through a capacitor is phase shifted 90 degrees with respect to the voltage.

The Randles circuit is the simplest equivalent circuit to express the electrochemical process on the electrode. It consists of an active electrolyte resistance R_s in series with the parallel combination of the double-layer capacitance C_{dl} and an impedance of a faradaic (charge-transfer) reaction R_{ct} in series with a specific electrochemical element of diffusion Z_w , as shown in Fig. 2.2

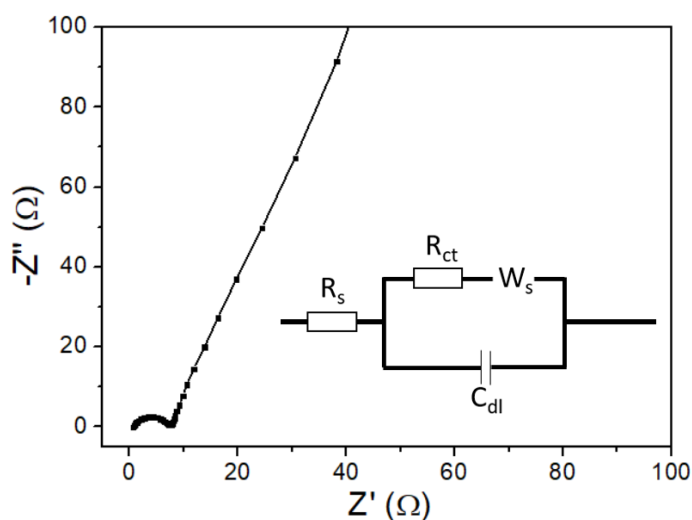


Fig. 2.2 Nyquist plot of a supercapacitor electrode. The inset is the Randles circuit for fitting.

In the Nyquist plot, R_s is represented as the intercept at the high frequency, R_{ct} is represented as the diameter of the semicircle at the medium frequency, and

Z_W relates to the final linear part. The infinite diffusion will present a 45°-slope line, and the finite diffusion will present a vertical line. In real electrochemical process, the diffusion can hardly be 100% infinite nor finite. Therefore, a modified restricted diffusion element is applied to fit the final linear part. Its impedance is calculated according to Eq 2.21. Z_W has three parameters. R_1 is the diffusion impedance; a_1 is an exponential factor: the number 0.5 means the infinite Warburg diffusion, and 1.0 means finite Warburg diffusion; τ_1 represents diffusion time. It relates to the effective diffusion thickness (L) and the diffusion coefficient (D) as Eq. 2.22 shows:

$$Z(f) = \frac{R_1 \coth(\tau_1 i 2\pi f)^{\frac{a_1}{2}}}{(\tau_1 i 2\pi f)^{\frac{a_1}{2}}} \quad \text{Eq 2.22}$$

$$\tau_1 = \frac{L^2}{D} \quad \text{Eq 2.23}$$

References

- [1] L. Ouahab, M. Bencharif, A. Mhanni, D. Pelloquin, J. Halet, O. Pena, J. Padiou, D. Grandjean, C. Garrigou-Lagrange, *Chemistry of materials*, 4 (1992) 666-674.
- [2] H. Lv, Q. Pan, Y. Song, X.X. Liu, T. Liu, *Nano-micro letters*, 12 (2020) 118.
- [3] J. Wang, J. Polleux, J. Lim, B. Dunn, *The Journal of Physical Chemistry C*, 111 (2007) 14925-14931.

Chapter 3 Activated Carbon/Polyoxometalates Hybrid

Materials for Organic-Electrolyte Supercapacitors

3.1 Context

Carbon-based materials are non-faradaic materials used from the beginning to develop Electrochemical Double Layer Capacitors (EDLC) (supercapacitors). However, their capacitance is lower than those of transition metal oxides and conducting polymers whose capacitance arises from faradaic processes (pseudocapacitance). Integration of electric double-layer capacitance and faradaic processes in a hybrid electrode material could improve the capacitive performance of carbon-based materials.

Polyoxometalates (POMs) have proved to be able to enhance the capacitive performance of carbon-based materials in aqueous electrolytes. This is consistent with their rich reversible electrochemistry in the aqueous acidic medium in which they are stable, with protons compensating for the negative charge of injected electrons. The question remains as to whether polyoxometalate clusters could be put to work as supercapacitor electrodes in organic electrolytes. This would result in a combined advantage of a greater working voltage and increased capacity due to their redox activity, both leading to an increased energy density.

This chapter will first explore the potential of AC/POM acid hybrid materials for organic electrolyte supercapacitors. Subsequently, we developed novel hybrid electrode material made of organic POM salts and activated carbon. As it will be shown, this material exhibits a combination of two charge storage mechanisms:

electrical double-layer from activated carbon and faradaic process from TEAPW12, thanks to the anchoring of the organic POMs clusters onto the carbon microporous surface, effectively leading to increased electrochemical behaviour of the hybrid electrodes and enhanced performance of symmetrical supercapacitor devices. Notably, it is the first time that POMs can be utilized to boost the capacitance as well as the energy density of carbon-based materials in organic electrolytes.

3.2 Activated carbon/polyoxometalic acid materials

3.2.1 Characterizations

The preparation of activated carbon/polyoxometalic acid materials is presented in section 2.1.2, Chapter 2. We estimate the loading mass of POMs on AC by comparing the initial mass of AC and the mass for as-prepared hybrid materials, as listed in Table 3.1. The loading masses of various POMs acids on AC are relatively high, at approximately 40-44%.

Table 3.1 Loading masses of POMs acids on the hybrid materials

	Total mass	AC	POMs
AC/HPW12	0.83	0.50	0.33
AC/HPMo12	0.89	0.50	0.39
AC/HSiW12	0.83	0.50	0.33

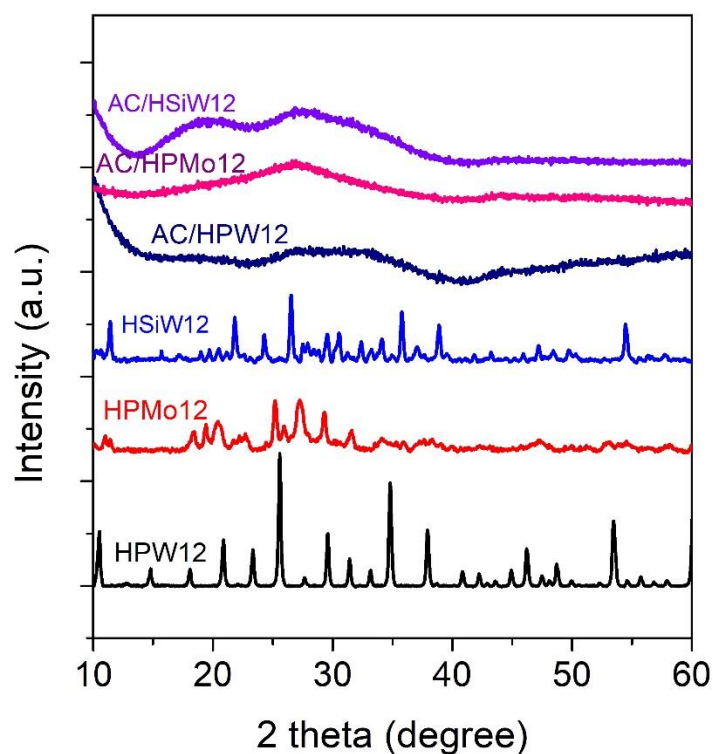


Fig. 3.1 XRD patterns of HPW12, HPMo12, HSiW12, AC/HPW12, AC/HPMo12 and AC/HSiW12.

Fig 3.1 presents the powder XRD patterns of the POM acids and the hybrid materials. All the samples were dried at 120 °C under vacuum overnight to remove some crystal water. The XRD patterns of POM acids show intense and well-defined diffraction peaks, while all the XRD patterns of hybrid materials exhibit no sharp diffraction peaks but only some broad bumps, which is the characteristic of AC samples. The loading masses of POMs in the hybrid materials are remarkable, more than enough to produce diffraction patterns if POMs were crystallized. Thus, the most likely explanation is that the POM molecules are well-dispersed as individual nanoscale clusters, not crystallized in extended phases. Actually, this hypothesis has been proven in our previous study.

Even though the XRD patterns cannot confirm the existence of POMs in the hybrid materials, we can use FT-IR for this purpose because POM clusters still

show characteristic vibrational frequencies even if nano-dispersed . As show in Fig. 3.2, HPW12 shows the following characteristic vibrational frequencies: 767 cm^{-1} (ν_{as} , W–O–W), 883 cm^{-1} (ν_{as} , W–O–W), 968 cm^{-1} (ν_{as} , W=O(t)) and 1078 cm^{-1} (ν_{as} , P–O(br))[1]. We can find all the corresponding peaks in the spectrum of AC/HPW12. HPMo12 shows similar characteristic vibrational frequencies, and the same are found in the hybrid AC/HPMo12[2]. HSiW12 exhibits different characteristic vibrational frequencies: 759 cm^{-1} (ν_{as} , W–O–W), 871 cm^{-1} (ν , W–O–W, ν_{as} , Si–O), 908 cm^{-1} (ν_{as} , W=O(t)) and 970 cm^{-1} (ν_{as} , W=O(br))[3]. The spectrum of AC/HSiW12 shows weaker peaks but at the same position. It confirms that all the hybrid materials contain the corresponding POM clusters.

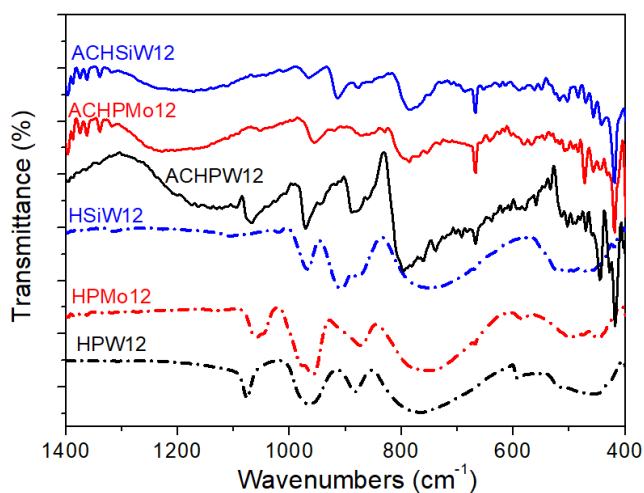


Fig. 3.2 FT-IR spectra of HPW12, HPMo12, HSiW12, AC/HPW12, AC/HPMo12 and AC/HSiW12.

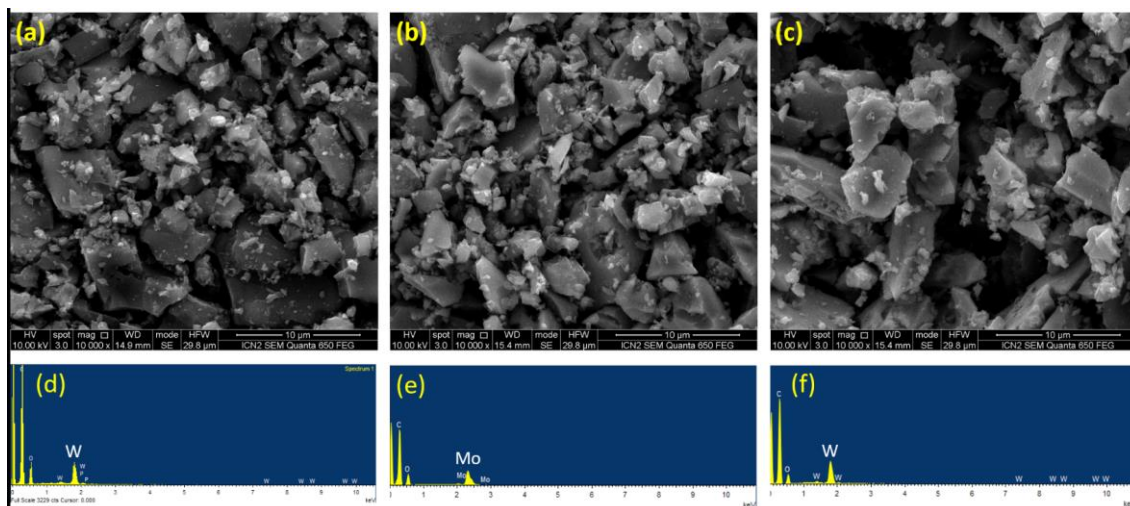


Fig. 3.3 SEM images of (a) AC/HPW12, (b) AC/HPMo12 and (c) AC/HSiW12. EDX spectra of (d) AC/HPW12, (e) AC/HPMo12 and (f) AC/HSiW12.

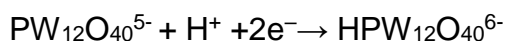
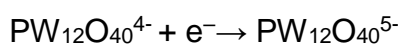
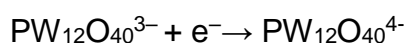
We attempted to use SEM to discern POMs in the hybrid materials AC/HPW12, AC/HPMo12 and AC/HSiW12, as show in Fig. 3.3 (a)-(c). All the three images are similar, we can only see large AC particles of different sizes but generally measuring a few microns. No crystals or agglomerates of POMs are apparent. Furthermore, we recorded EDX spectra (Fig. 3.3 (d)-(f)) on these samples. We detect significant amounts of heavy metal elements from POM: 27 wt% of W in AC/HPW12, 24 wt% of Mo in AC/HPMo12 and 28 wt% of W in AC/HSiW12, which are slightly lower than the estimated compositions from the loading masses (Table 3.1). Since we used the adhesive carbon tape to bind powders on the SEM sample stage, the detected percentage of carbon increases.

3.2.2 Electrochemical characterization

We studied the electrochemical behaviours of the hybrid materials in one of the most commonly used organic electrolytes: 1 M TEABF₄ in acetonitrile, as shown in Fig. 3.4. It's not surprising that all the hybrid materials exhibit redox activities in this organic electrolyte, but their current densities are lower than those

found for pristine AC. This implies that the addition of POMs acids might not be able to enhance the capacitive performance.

AC/HPW12 and AC/HPMo12 show three pairs of redox peaks, and AC/HSiW12 show two pairs of redox peaks. According to the literature, these three pairs of redox peaks of AC/HPW12 (or AC HPMo12) are associated with two one-electron redox reactions and one two-electron redox reaction[4], as shown below:



By contrast, AC/HSiW12 only exhibits two pairs of redox peaks. Both of them appear at the more negative potential. We speculate the third redox pair is out of the available potential range of our experiments.

The CV of AC is approximately rectangular in the potential range studied (Fig 3.4(a)). Its current density is significantly larger than those of the hybrid materials, indicating the hybrid materials have lower specific capacitance.

We assembled symmetric cells to evaluate the capacitive performance of the hybrid materials in real devices. Fig. 3.4(b) compares the CP curves of pristine AC and these hybrid materials. The CP curves of the hybrid materials show one or two pairs of redox wave, less than those in CV, because some redox waves overlap (details will be explained in next section 3.3). The capacitance of the hybrid materials in two-electrode device is remarkably lower than that of AC, as show in Table 3.2.

Table 3.2 Specific capacitance of AC, AC/HPW12, AC/HPMo12 and AC/HSiW12 at 20 mV s⁻¹

Specific capacitance at 20 mV s ⁻¹	
AC	78
AC/HPW12	27
AC/HPMo12	30
AC/HSiW12	40

The addition of POM acids does not improve the capacitance of AC in the organic electrolyte, and even makes it worse. The reason is multifaceted. First, the POMs have very large molecule weight, which would affect the gravimetric capacitance. Second, the redox reactions of POM acids usually involve protons, but the organic electrolyte is aprotic. This might impede the redox activities of POMs. Therefore, we decided to seek other derivatives of POMs compatible with aprotic electrolytes.

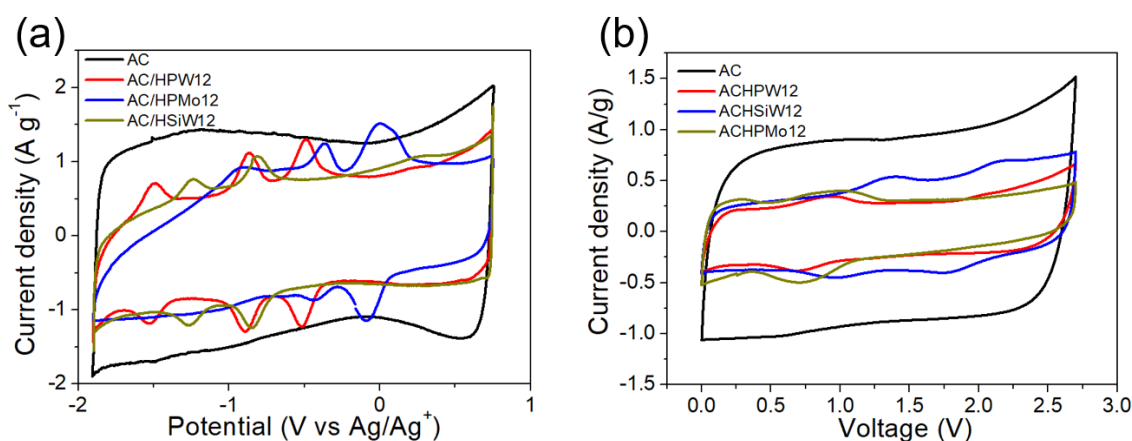


Fig. 3.4 (a) Cyclic voltammetry and (b) cyclic polarization curves of AC, AC/HPW12, AC/HPMo12 and AC/HSiW12 at 20 mV s⁻¹ in 1 M TEABF₄ in acetonitrile.

3.3 Activated carbon/organic polyoxometalate salts hybrid materials

(Article 1)

The activated carbon/polyoxometalic acid hybrid materials showed inferior capacitive performance compared to the parent activated carbon in the organic electrolyte. This phenomenon is expected to be associated with the fact that the redox reaction of polyoxometalic acids involves protons, which are absent in the organic electrolyte. Therefore, in this section several quaternary ammonium polyoxometalate salts were synthesized and incorporated to AC to study whether and how these POM salts could enhance the capacitive performance of AC.

Table 3.3 Capacitance of various AC/POM hybrid materials at 10 mV

s^{-1}

Sample	Gravimetric capacitance (F g ⁻¹)	Volumetric capacitance (F cm ⁻³)
AC/TEAPW12	72	64
AC/TEAPMo12	79	68
AC/TEASiW12	70	62
AC/TMAPW12	74	65
AC/TBAPW12	72	63
AC	78	39

A variety of quaternary ammonium cations (TMA, TEA and TBA) can be coupled with POM anions (PW12, PMo12 and SiW12). A series of AC/POM hybrid materials were obtained and all of them showed enhanced capacitance with respect to pristine AC, as shown in Table 3.3. The phosphotungstates with various quaternary ammonium cations have approximately the same capacitance, because all of them are compatible with the organic electrolyte. The

phosphomolybdate slightly outperforms the other two POMs with respect to gravimetric capacitance, since it has a smaller molecular weight.

Since the organic electrolyte contains TEA cations, and PW12 is the first discovered and most widely characterized Keggin POM, TEAPW12 was selected as a representative case study to show that AC/POM hybrid materials can enhance the capacitive performance of AC in a conventional organic electrolyte in the following research article (<https://doi.org/10.1016/j.electacta.2020.137007>).



Contents lists available at ScienceDirect

Electrochimica Acta

journal homepage: www.elsevier.com/locate/electacta



Can polyoxometalates enhance the capacitance and energy density of activated carbon in organic electrolyte supercapacitors?



Jun-Jie Zhu^a, Raul Benages-Vilau^a, Pedro Gomez-Romero^{a,b,*}

^a Catalan Institute of Nanoscience and Nanotechnology, ICN2 (CSIC-BIST), Campus UAB, 08193 Bellaterra, Barcelona, Spain

^b Consejo Superior de Investigaciones Científicas (CSIC), Spain

ARTICLE INFO

Article history:

Received 8 April 2020

Revised 3 August 2020

Accepted 23 August 2020

Available online 8 September 2020

Keywords:

Supercapacitor
Polyoxometalate
Organic electrolyte
Hybrid electrode

ABSTRACT

Polyoxometalates (POMs) have been shown to work as faradaic additives

to activated carbon (AC) in acidic aqueous electrolytes. Yet, their use in organic media allows not only for added capacity but also higher voltage. Here we show that the tetraethylammonium derivative of phosphotungstate [PW₁₂O₄₀]³⁻ (PW12) can be homogeneously distributed throughout the pores of activated carbon (AC) in organic solvents such as N,N-dimethylformamide (DMF) and demonstrate the use of this hybrid electrode material in an organic electrolyte (1 M TEABF₄ in acetonitrile) supercapacitor. Our results show the efficient electroactivity of the PW12 cluster even in the absence of protons, providing a higher voltage than aqueous electrolytes and fast and reversible redox activity. The hybrid material shows a combination of double-layer (AC) and redox (PW12) capacities leading to an increase (36%) in volumetric capacitance with respect to pristine AC in the same organic electrolyte (1 M TEABF₄ in acetonitrile). Remarkably, we were able to quantify this increase as coming predominantly from non-diffusion-limited processes thanks to the utterly dispersed nature of POMs. Moreover, the hybrid material delivers a good rate capability and excellent cycle stability (93% retention of the initial capacitance after 10,000 cycles). This study has a profound significance on improving capacitance of carbon-based materials in organic electrolytes.

© 2020 Elsevier Ltd. All rights reserved.

1. Introduction

In the field of energy storage, supercapacitors stand out thanks to their high power density and long cycle life, but at the expense of low energy densities because charges are stored on the electrode-electrolyte interphase through electric double layer capacitance, (EDLC) and/or surface redox reactions (pseudocapacitance) [1].

Combining high energy density, power density and long cycle life in a single device or material at low cost is the Holy Grail in energy storage. Active electrode materials determine the intrinsic energy density and power density of a certain device. Thus, most efforts have been made to explore novel electrode materials. A most promising approach is to design hybrid materials which combine both the merits of faradaic and non-faradaic materials to deliver both high energy density and power density [2–4]. The challenge lies here in the development of synergic active materials.

Carbon-based materials are non-faradaic materials used from the beginning in the development of supercapacitors (SCs), owing to their natural abundance, good electrical conductivity, and considerable capacitance related to their high specific surface area. Although carbon-based materials can deliver electric double layer capacitance, their capacitance is lower than those of transition metal oxides and conducting polymers whose capacitance arises from faradaic processes (pseudocapacitance) [5]. Numerous methods have been utilized to furnish carbon-based materials with pseudocapacitive behavior, including heteroatom-doping or making composites [6].

Polyoxometalates (POMs) are transition metal oxide clusters typically 1 nm in size that can be easily anchored to other materials. POMs-based materials have been applied in various fields, including catalysis, electrochromic, magnetic, and energy storage [7,8]. In a variety of energy storage devices, including supercapacitors [7–10], lithium ion batteries [11–13], flow cells [14,15], fuel cells [16] we can see the great potential of POMs stemming from their multi-electron redox activities. And POMs not only can deliver superior energy but also they are structurally best suited to do it at a fast rate since all of their active moieties are at the surface of the cluster. Reduced graphene oxides [17], conducting poly-

* Corresponding author at: Catalan Institute of Nanoscience and Nanotechnology, ICN2 (CSIC-BIST), Campus UAB, 08193 Bellaterra, Barcelona, Spain.
E-mail address: pedro.gomez@icn2.cat (P. Gomez-Romero).

mers [8–12,18–20], carbon nanotubes [21,22], carbon nanotubes [23], micro-mesoporous carbons [24,25] or activated carbons [26–28] have already been studied as the substrates for supporting POMs and all of them present some kind of enhanced capacitive performance, such as larger gravimetric specific capacitance [27], larger cell voltage window and/or longer cycle life [25,26].

However, as it is well known, the redox chemistry of POMs is most effectively displayed in aqueous acidic media. This is undoubtedly the reason why the vast majority of the studies carried out for POMs in supercapacitors were made in (acidic) aqueous electrolytes. Under these conditions thermodynamics limits the potential window to 1.2 V due to water splitting. And although some hybrid materials can extend the potential window up to 1.6 V [26], this value is still much lower than those attainable in organic electrolytes (2.7–3.5 V) or ionic liquids (ILs) (> 3.0 V) [3].

Since the energy density of a supercapacitor is proportional to the square of the operating voltage window for the cell, it comes as no surprise that organic or IL electrolytes are generally preferred for the design of high-energy systems. Yet, organic electrolytes are not problem-free, their greater viscosity, lower ionic conductivity which could produce a large amount of heat at high rate, and also the larger size of the ions dissolved tend to decrease their performance [29]. Thus, the capacitance of carbon-based materials is smaller in organic than in aqueous electrolytes. For instance, the specific capacitance of commercial activated carbon is around 100 F g^{-1} in organic electrolytes but close to 200 F g^{-1} in aqueous sulphuric acid [30]. Hybrid materials offer a path to break through this bottleneck as they introduce an alternative energy storage mechanism. Most achievements until now have resorted to inorganic salts of POMs (or their acids) to construct hybrid materials in order to boost capacitance in aqueous electrolytes. Recently, a few studies have been carried out on organic-inorganic POMs-based hybrid materials, but they are still applied for supercapacitors with aqueous electrolytes [31,32], or for lithium ion batteries [33].

The question remains as to whether polyoxometalate clusters could be put to work as supercapacitor electrodes in organic electrolytes with the combined advantage of the superior voltage and increased capacity due to their redox activity.

We report here for the first time such a system, based on a novel hybrid electrode material made of an organic phosphotungstate salt (tetraethylammonium phosphotungstate, TEAPW12) and activated carbon. As it will be shown, this material exhibits a combination of two charge storage mechanisms: electrical double layer from activated carbon and faradaic process from TEAPW12, thanks to the anchoring of the organic phosphotungstate clusters onto the carbon microporous surface effectively leads to increased electrochemical behavior of the hybrid electrodes and to enhanced performance of symmetrical supercapacitor devices. Notably, this study explores an alternative strategy to boost the capacitance as well as the energy density of carbon-based materials in organic electrolytes.

2. Experimental

2.1. Materials and synthetic procedures

2.1.1. Materials

All raw chemicals were obtained commercially and used without additional purification. Tetraethylammonium chloride ($\geq 98\%$), phosphotungstic acid hydrate, tetraethylammonium tetrafluoroborate ($\geq 99\%$), dimethylformamide (anhydrous, $\geq 99.8\%$), acetonitrile (anhydrous, $\geq 99.8\%$), N-Methyl-2-pyrrolidone ($\geq 99.5\%$) and poly(vinylidene fluoride) (average molecule weight ≈ 534000) were purchased from Sigma Aldrich. Carbon black Super P ($\geq 99\%$) was purchased from Alfa Aesar. Activated carbon DLC Su-

per 30, specially produced for supercapacitor applications by Norit Chemical, was used. Nitrocellulose filter membranes (pore size=0.025 mm) purchased from MF-Milipore, Merck were used as separators.

2.1.2. Synthesis of TEAPW12

The organic-inorganic POM salt was synthesized through metathesis reaction in the light of the literature method [34]. Typically, 200 mL of a 20 mM aqueous solution of phosphotungstic acid was added to 200 mL of a 70 mM aqueous solution of tetraethylammonium chloride. A considerable amount of white precipitate appeared immediately. The suspension was kept stirring for 6 h, then filtered. The precipitate was washed with deionized water and dried overnight in air at 80°C . Tetraethylammonium phosphotungstate ($[(\text{C}_2\text{H}_5)_4\text{N}]_3\text{PW}_{12}\text{O}_{40}$) was obtained.

2.1.3. Synthesis of AC/TEAPW12

An AC suspension was prepared by sonicating AC (0.5 g) in DMF (100 ml) for 1 h. 6.6 g of TEAPW12 was added to the suspension. Then we kept it 5 h in a bath sonicator and stirred overnight. Finally, the sample was collected by filtration, and dried at 80°C for 12 h in vacuum oven, around 0.63 g of the AC/TEAPW12 was obtained in each batch.

2.1.4. Synthesis of AC/HPW12

For comparison, inorganic hybrid material (activated carbon with phosphotungstic acid, named as AC/HPW12) was prepared following the previous literature methodology reported [26].

2.2. Material characterization

All the samples were dried at 120°C under vacuum overnight before the following material characterization. The thermal properties of the sample were studied by thermogravimetric analysis using NETZSCH-STA 449 F1 Jupiter thermal analysis system under air flow with a heating rate of $10^\circ\text{C min}^{-1}$ from room temperature to 900°C . The powder XRD patterns were collected on a PANalytical X'pert Pro-MRD diffractometer with $\text{Cu K}\alpha$ radiation and PIXel detector. Volumetric N_2 sorption isotherms were collected at 77 K (N_2) using an ASAP 2020 HD (Micromeritics). Temperature was controlled by using a liquid nitrogen bath. Total pore volume (V_{total}) was calculated at $P/P_0 = 0.95$, and microporous volume (V_{micro}) was calculated using the Dubinin–Radushkevich equation. Pore size distribution was estimated using a density functional theory (DFT) model (N_2 -cylindrical pores-oxide surface) implemented in the Microactive 4.00 software with a regularization factor of 0.01. High angle annular dark field scanning transmission electron microscopy (HAADF-STEM) images were taken on FEI Tecnai G2 F20 microscopy. Scanning electron microscopy images were taken on Quante 650 FEG microscopy.

2.3. Electrochemical characterization

The working electrodes were fabricated by mixing the active material, carbon black and poly(vinylidene fluoride) at a weight ratio of 85:5:10. Typically, the mixture was first formed as a slurry by adding a few drops of N-methyl-2-pyrrolidone, then coated onto aluminum foil ($>99\%$, with the thickness of 0.05 mm) with doctor-blade method (RK PrintCoat, with the gap of 60 μm), and dried under vacuum at 120°C for 12 h. The loading mass of each electrode is in the range of 1.5–2 mg cm^{-2} . Three-way stainless steel Swagelok® cells were used to characterize the materials in three-electrode configuration. Ag/Ag^+ (0.01 M AgNO_3) was used as reference electrode. An electrode loaded with double weight of the same active material was used as counter electrode. Symmetrical supercapacitors formed by two identical electrodes were assembled in CR2032 coin cells with a coin-cell crimper (TMAXCN).

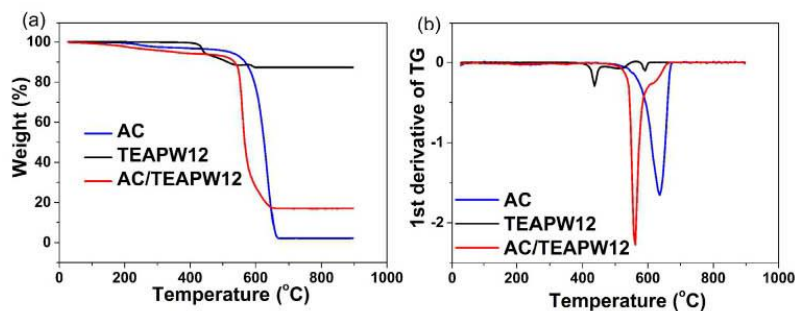


Fig. 1. (a) Thermogravimetric and (b) corresponding derivative (dw/dT) curves of AC/TEAPW12, TEAPW12 and pristine AC with the heating rate of $10\text{ }^{\circ}\text{C min}^{-1}$ under dry air flow.

All the electrodes were cut in the diameter of 14 mm and pressed at 3 MPa before assembling. 1 M tetraethylammonium tetrafluoroborate (TEABF₄) in acetonitrile was used as the electrolyte. All the cells were assembled in an argon-filled glovebox (Jacomex GP with $\text{O}_2 < 5\text{ ppm}$ and $\text{H}_2\text{O} < 5\text{ ppm}$). Cyclic voltammetry (CV) was performed in a three-electrode configuration at the various scan rates to investigate the capacitive behavior of individual electrodes. Cyclic polarization (CP) and galvanostatic charge-discharge (GCD) was performed in two-electrode cell to evaluate the capacitive performance in devices, and cycling stability. All the electrochemical tests were conducted on Biologic VMP3 multi-channel potentiostat.

3. Result and discussion

Fig. 1 presents the thermogravimetric curves and their corresponding derivative (dw/dT) curves of AC/TEAPW12, TEAPW12 and pristine AC. The pristine AC undergoes a slight weight loss (3.2%) before 400 °C, corresponding to the removal of adsorbates. Subsequently, a drastic drop of weight refers to the combustion of carbon in air. Finally, 2.18% of its initial weight remains as ashes. On its dw/dT curve, only one sharp peak can be discerned, corresponding to the combustion. Pure TEAPW12 exhibits a more complicated decomposition process. Its weight suffers a negligible loss (0.39%) when heating up to 400 °C, indicating that there is scarcely any crystal water in this salt (0.7 H_2O per TEAPW12 molecule). Afterwards, a remarkable weight loss, ranging from 400 °C to 600 °C, can be discerned, which should be assigned to the decomposition of tetraethylammonium moieties. The weight loss in this stage is 12.2%, in good agreement with the expected proportion of tetraethylammonium moieties (11.9%) in TEAPW12. The dw/dT curve presents three peaks, revealing that in this stage the decomposition involves several steps. The step-by-step decomposition process of tetraethylammonium has been verified in thermal decomposition study on tetraethylammonium in zeolites [35]. At the end, the weight stays relatively stable above 650 °C. Concerning the decomposition of phosphotungstate, Kalpakli et al. [36], reported that after 360 °C, anhydrous phosphotungstate starts to transform into a new tetragonal phase, a light-green colored phosphotungstate of empirical formula $\text{P}_2\text{O}_5 \cdot 24\text{WO}_3$ which is stable up to 1000 °C, and then decomposes gradually and some phosphorus oxides vaporize. In our case, a residue of $\text{P}_2\text{O}_5 \cdot 24\text{WO}_3$ would account for 87.2 wt% of TEAPW12, in very good agreement with the experimentally found residual weight (87.3% at 800 °C). The thermogravimetric curve of AC/TEAPW12 is similar to that of pristine AC, as AC makes up most of the hybrid material. On the other hand, the temperature of decomposition of activated carbon is ca. 50 °C lower in the presence of phosphotungstate clusters (PW12),

most likely due to the catalytic activity of this cluster at high temperature.

Finally, the residual weight after AC/TEAPW12 decomposition is 17%, from which we can estimate that the hybrid material contains a 17.5 wt% of TEAPW12.

Microstructural analyses were performed by a variety of methods in order to confirm the dispersion of TEAPW12 on AC. SEM images of the pristine AC (Fig. S1a) and the hybrid material AC/TEAPW12 (Fig. S1b) present no apparent difference, both exhibiting a blocky morphology. No apparent agglomeration nor crystallization of TEAPW12 can be detected in SEM images. On the other hand, the energy dispersive X-ray (EDX) spectra (see Fig. S1d) show a definitive difference between AC and the hybrid. The EDX spectrum of AC/TEAPW12 presents one extra peak at 1.78 eV, corresponding to W.

In order to study the distribution characteristics of TEAPW12, samples were observed under scanning transmission electron microscopy in high angle annular dark field (HAADF-STEM). HAADF-STEM images show the difference apparently. The image of AC (Fig. 2a) reveals its inhomogeneous nature. Plenty of micropores (pore size $< 2\text{ nm}$) and mesopores (pore size from 2 to 50 nm), corresponding to the dark areas in the image, can be discerned. In contrast, the image of AC/TEAPW12 (Fig. 2b) does not present similar dark area, but uniformly-distributed sparkly dots, which correspond to tungsten in TEAPW12 (confirmed by line scan of EDX, see Fig. S2b). The disappearance of the dark area in AC/TEAPW12 can be explained in two ways. Firstly, the TEAPW12 molecules in the pores leads to a slight fall of both surface area and pore volume [25]; secondly, the strong contrast between sparkly dots and dark pore makes the dark area less visible.

Even though TEAPW12 accounts for ca. 17.5 wt% in AC/TEAPW12, the XRD pattern of AC/TEAPW12 (see Fig. S2c) only presents a broad bump, similar to that found for pristine AC. This confirms that TEAPW12 clusters spread on the AC substrate homogeneously in the form of isolated clusters instead of well-crystallized extended solid particles.

The influence of the absorption of TEAPW12 on the porous properties of AC was evaluated by volumetric N_2 sorption experiments. Fig. 2c shows the N_2 sorption isotherms of AC and AC/TEAPW12. Both of them can be classified as Type I isotherm according to the IUPAC classification, revealing their microporous nature. Moreover, these two samples share the same pore size distribution, in which most pores fall within or close to the micropore range. The similar N_2 sorption isotherms and pore size distribution curves confirm that absorption of TEAPW12 on AC does not affect significantly its porous nature. However, the specific surface area and micropore volume (Table 1) are reduced from $1603\text{ m}^2\text{ g}^{-1}$ (AC) to $1007\text{ m}^2\text{ g}^{-1}$ (AC/TEAPW12), and from $0.344\text{ cm}^3\text{ g}^{-1}$

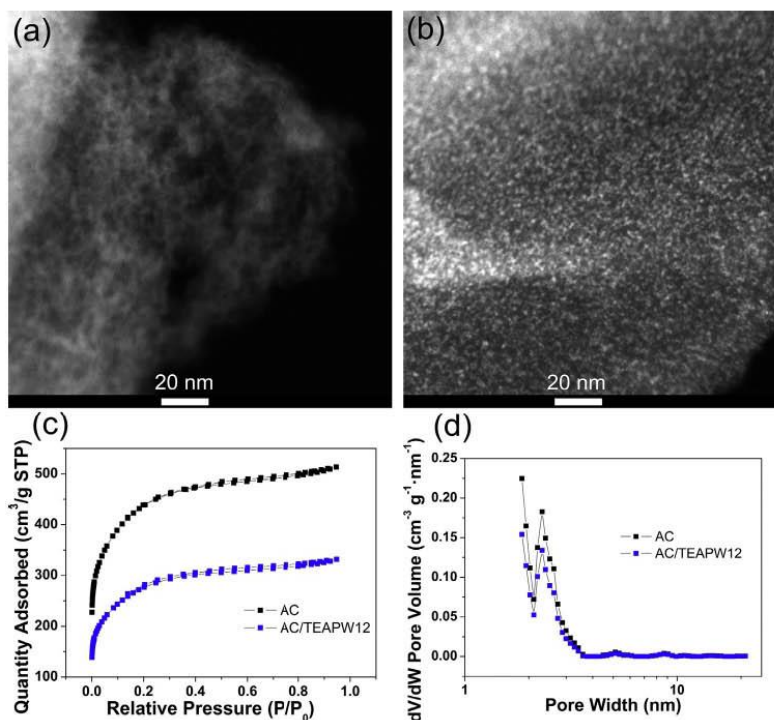


Fig. 2. HAADF-STEM images of (a) AC and (b) AC/TEAPW12. (c) N_2 sorption isotherms and (d) Pore size distribution curves of AC and AC/TEAPW12.

Table 1.

Porosity properties of samples AC and AC/TEAPW12.

Sample	S_{BET}^a ($m^2 g^{-1}$)	V_{Total}^b ($cm^3 g^{-1}$)	V_{Micro}^c ($cm^3 g^{-1}$)
AC	1603	0.712	0.344
AC/TEAPW12 ^d	1007	0.453	0.191
AC/TEAPW12 ^e	1220	0.549	0.232

^a Specific surface area determined according to BET method.

^b Total pore volume.

^c Micropore volume.

^d all the data in this line are normalized by the total weight.

^e all the data in this line are normalized by the weight of AC.

(AC) to $0.191 \text{ cm}^3 \text{ g}^{-1}$ (AC/TEAPW12), respectively. In principle this should be expected since the PW12 cluster is formed by heavy metals. However, the same trend is detected when normalizing per mass of AC (Table 1). Furthermore, the drop of micropore volume (-44.5%) is larger than that of specific surface area (-37.2%) or total pore volume (-36.3%). This leads us to speculate that the TEAPW12 clusters are mainly absorbed in the micropores of AC.

Based on the weight percentage, specific surface area and micropore volume, we can estimate if the surface of AC is large enough to spread TEAPW12 in a single layer and the micropore of AC is enough to accommodate all TEAPW12 clusters. We assume the projected area and occupied volume per TEAPW12 cluster is 1 nm^2 and 1 nm^3 , respectively. The area to spread TEAPW12 cluster in monolayer is 32.2 m^2 per gram of AC/TEAPW12. This is much lower than its specific surface area. The volume to accommodate TEAPW12 in 1 g of AC/TEAPW12 is 0.03 cm^3 , much less than the total micropore volume. Therefore, AC can provide enough area to

spread TEAPW12 clusters as monolayer, and enough micropores to accommodate all the TEAPW12 clusters.

Since TEAPW12 is composed of twelve WO_6 octahedra, all of them on the surface of the cluster and exposed to the electrolyte, the adsorption of these clusters on carbon affords the possibility to harness their faradaic redox activity without the sluggish ion diffusion found in extended phases. Besides, in this case AC acts not only as the substrate for immobilizing POM clusters, but also as a conducting matrix facilitating electron transport and transfer during the faradaic process.

Fig. 3a presents the cyclic voltammograms of AC and AC/TEAPW12 at the scan rate of 20 mV s^{-1} . Its y axis is the current normalized per volume of electrode. The CV of AC is nearly a rectangle, indicating ideal capacitive behavior. On the other hand, four pairs of redox peaks, which have the $E_{1/2}$ of -0.492 , -0.851 , -1.469 and -2.02 V vs. Ag/Ag^+ ($E_{1/2}$ refers to the mid-point potential between oxidation peak and reduction peak), can be distinguished on the CV of AC/TEAPW12. In the previous studies on phosphotungstic acid/carbon-based hybrid materials in acidic electrolytes, only three redox pairs could be discerned and the most negative one which involved two electrons was pH-dependent [26]. It should be stressed that protons are crucial in aqueous electrolytes for keeping the overall charge of the POM clusters at a low 3-/4- by concomitant protonation during reduction. Thus, in the absence of protons in the present organic electrolytes, we consider that the TEA counterions must fulfill a similar role most likely through the formation of ion pairs, as it has been previously reported in other organic solvents with a variety of cations [37–39].

Furthermore, we postulate that due to the absence of protons in the organic electrolyte and the formation of ion pairs with the TEA cations, the most negative pH-dependent redox wave has split

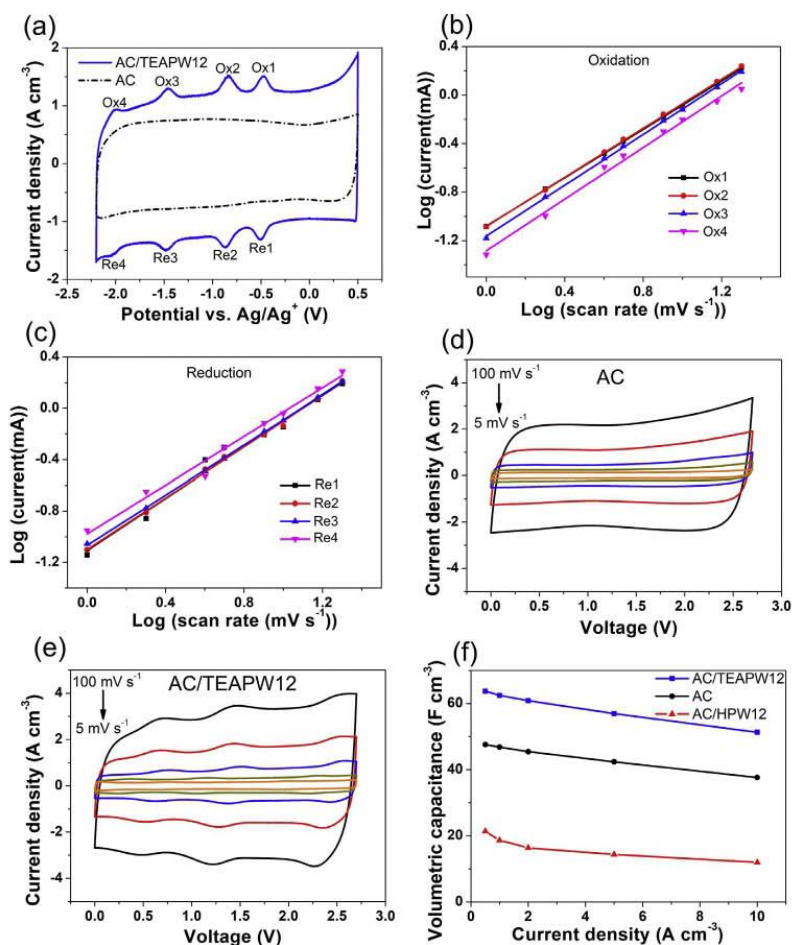


Fig. 3. (a) Cyclic voltammograms of AC and AC/TEAPW12 at 20 mV s^{-1} in three-electrode configuration, the y axis is the current normalized per volume of electrode. b-value determination for (b) oxidation peaks and (c) reduction peaks of CVs of AC/TEAPW12. Cyclic polarization curves of (d) AC and (e) AC/TEAPW12 in two-electrode cell at 5, 10, 20, 50 and 100 mV s^{-1} . (f) Volumetric capacitance of AC, AC/TEAPW12 and AC/HPW12 at various current densities. In all cases the electrolyte was 1 M TEABF_4 in CH_3CN .

in two. Indeed, this behavior is similar to a previously reported splitting in organic media [40].

We have estimated the contribution from TEAPW12 to the total stored charge in AC/TEAPW12 electrode with the assumption that hybridization does not affect the capacitive performance of AC (details are presented in supporting information S5). We find all the TEAPW12 clusters are utilized, which would account for 93.8% for the increased stored charge. Apart from the contribution from TEAPW12, the remaining slight increase could be due to the modification of the structure or the changed surface state of activated carbon after the hybridization. In other words, we can now state that the expected theoretical contribution of POM to reversible charge storage and the measured charge are compatible with all the 17.5 wt% of POM in the hybrid reversibly exchanging four electrons per cluster.

On the other hand, we note that the voltage specific activity associated to these redox processes shows in the CVs (Fig. 3a) as relatively weak peaks, whereas a rectangular-shaped capacitive component seems to dominate. This is expected for the purely capacitive AC but somewhat surprising for the hybrid.

Thus, the charge-storage mechanism was further analyzed by estimating the surface capacitive and ion-diffusion controlled charge contribution to the total charges stored by AC/TEAPW12 electrodes. Since the redox reaction of TEAPW12 in $\text{TEABF}_4/\text{acetonitrile}$ involves formation of ion pairs, it could be limited by the slow diffusion of cations. For this analysis, the CV curves at various scan rates were measured and presented in Fig. S3a. The dependence of the current response on the scan rate can provide insights into the charge-storage mechanism according to Eq. (1) [41]:

$$i = av^b \quad (1)$$

where i is the maximum peak current obtained at a specific scan rate v , and a and b are adjustable parameters. The current response of a linear dependence on scan rate ($b = 1$) usually means charge is stored by a fast response mechanism, such as surface capacitive mechanism and redox reactions which could perform at fast rate [31]. Otherwise, if any slow diffusion of ion or electron transfer

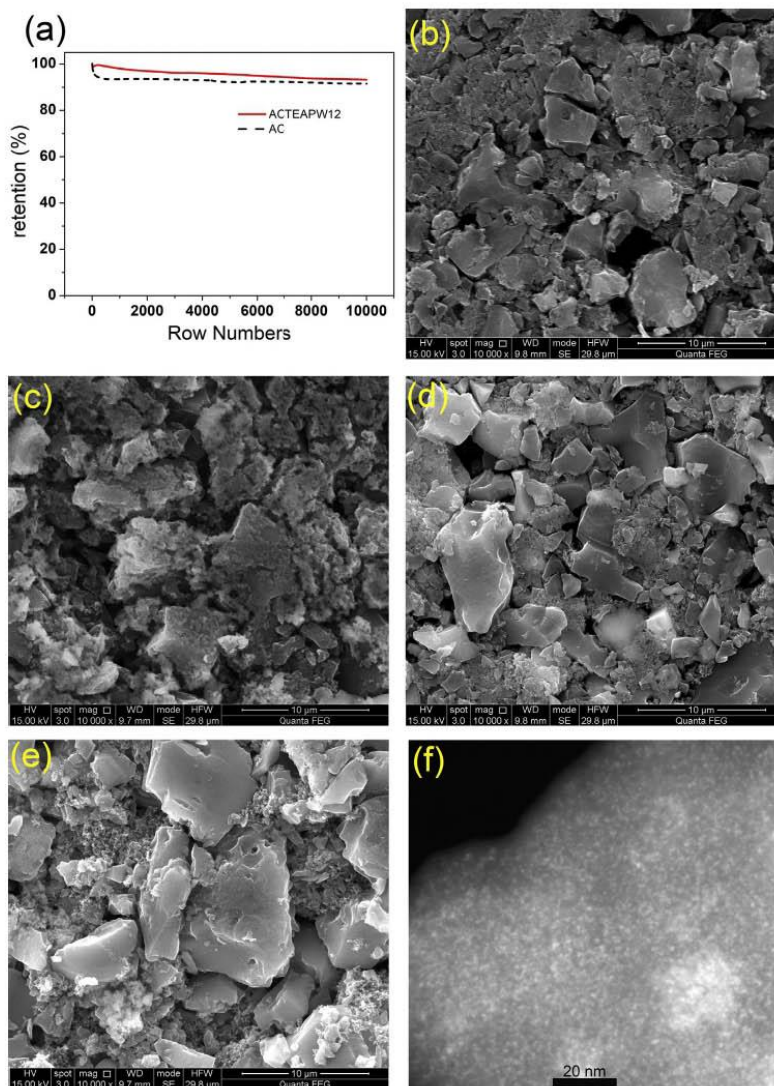


Fig. 4. (a) Capacitance retention upon cycling for AC and AC/TEAPW12 at the current density of 8 A g^{-1} . SEM images of AC (b) before and (c) after cycling. SEM images of AC/TEAPW12 (d) before and (e) after cycling. (f) HAADF-STEM images of AC/TEAPW12 electrode washed with acetonitrile after 10,000 cycles.

limits the reaction, the dependence could deviate from linearity ($b < 1$). The following equation

$$\log i = \log a + b \log v \quad (2)$$

can be derived from Eq. (1), so that the value of b for different potentials can be determined from the slope of the straight line of $\log i$ vs $\log v$, as shown in Fig. 3b and c. Herein, we mainly evaluate the b value for the four pairs of redox peaks. Table 2 presents the fitting results. All R^2 values are close to 1, confirming proper fittings. More importantly, all the b values are very close to 1, within experimental error, which means that the charge-storage process is not limited by any diffusion of cations nor interfacial electron transfer, even around the redox potentials charac-

teristic of the PW12 clusters. At first sight this might seem surprising for redox-active clusters such as POMs. Indeed, bulky POM-containing materials frequently exhibit ion-diffusion-controlled responses as detected from their CVs [13,42]. In our case, however, the fast current response ascertained must be associated to the fact that all electroactive moieties (WO₆) are directly available at the electrode-electrolyte interface for electron injection with simultaneous ion-pair formation. This is only possible by the proper dispersion and homogeneous distribution of POM clusters at the molecular nanoscale level, and it is at the heart of the working of these electrodes at fast rates, effectively working as pseudocapacitors. A similar instance of this behavior was reported by Ma et al. in the study on silicotungstate in an open 3D framework of [Cu(1,4-bis(triazol-1-ylmethyl)benzene)₄] [31]. Finally, it could be

Table 2.

Values of b Eqs. (1) and ((2)) and regression coefficients (R^2) derived from fitting current of reduction peaks (Re) and oxidation peaks (Ox) at various scan rates.

	Re1	Ox1	Re2	Ox2	Re3	Ox3	Re4	Ox4
b	0.99	1.0	1.0	1.0	1.0	0.98	1.0	0.95
R^2	0.9996	0.9787	0.999	0.9978	0.9994	0.9996	0.9924	0.9819

noted that a size effect on charge-storage mechanism is also observed for other common nanoparticulate redox active materials, such as TiO_2 , LiCoO_2 and V_2O_5 [41]. Thus, our result is perfectly compatible with PW12 clusters being distributed on AC substrate at a molecular level.

To evaluate the capacitive performance of the hybrid materials in real devices, symmetrical capacitors were assembled in coin cells. The shape of cyclic polarization curves of the AC symmetric cell (Fig. 3d) is ideally rectangular confirming its capacitance is mainly derived from a double layer mechanism. In contrast, the CP curves of AC/TEAPW12 (Fig. 3e) symmetric cell present three pairs of waves added to the rectangular shape, revealing its hybrid nature. The volumetric capacitance of AC/TEAPW12 derived from the CP at 5 mV s^{-1} is 66 F cm^{-3} (Fig. S3b), 35% higher than that of AC. When the scan rates rise to 100 mV s^{-1} , the contours of the waves remain, verifying the good rate capability of the faradaic process. 93% of the capacitance at 5 mV s^{-1} remains when the scan rate rises to 100 mV s^{-1} , indicating the excellent rate capability of AC/TEAPW12. This should be assigned to the homogeneous distribution of TEAPW12 on AC as we have confirmed in HAADF-STEM images, to the electronic conductivity provided by the carbon matrix and to the direct contact of all the electroactive centers with the electrolyte which precludes the need of any bulk ion diffusion.

The CV of an AC/TEAPW12 electrode in a three-electrode cell shows four pairs of redox waves as discussed above. On the other hand, the CP curves of two identical AC/TEAPW12 electrodes in two-electrode cell shows just three pairs of waves. This is perfectly compatible with the CV and it can be explained by the fact that the initial potential of each of the two identical AC/TEAPW12 electrodes is -0.7 V vs. Ag/Ag^+ , which is nearly in between the first two redox pairs of the CV (Ox1/Re1 and Ox2/Re2). Once the symmetric supercapacitor begins to charge, both the positive and negative electrode suffer redox reactions simultaneously (the positive Ox1, the negative Re2) thus leading to the first wave on the CP curves of the symmetric supercapacitor. After this, only the negative electrode will suffer redox reactions corresponding to Ox3/Re3 and Ox4/Re4 and leading to the other two pairs of waves in the CP curves. The variation of the potential of both positive and negative electrodes, as well as the symmetric capacitor voltage during GCD can be seen in Fig. S3c. Moreover, symmetrical supercapacitor based on inorganic hybrid material (AC/HPW12) were also characterized for comparison. The CP curves of AC/HPW12 (Fig. S3d) also exhibit polarization waves deriving from redox activity. However, both their specific capacitance and rate performance were poorer than for AC/TEAPW12 devices.

Galvanostatic charge-discharge was tested to evaluate the performance of symmetric supercapacitor under working conditions. The GCD curves are presented in Fig. S4a and b. Fig. 3f presents the volumetric capacitance at different current densities. AC/TEAPW12 exhibits a considerably higher volumetric capacitance, with a gain of ca. 36% enhancement, compared to AC. The improvement of capacitance can be attributed to the added activity of TEAPW12. It is currently understood that the origin of pseudocapacitance lies on the fast reversible faradaic processes taking place on the surface or near-surface of active phases [43]. In our case all the electroactive centers of all the clusters are surface-active. Therefore,

the homogeneous distribution of TEAPW12 provides numerous active sites on surface, allowing for the optimal harnessing of the clusters redox activity. In contrast, the capacitance of AC/HPW12 is lower, contrary to the trend in aqueous electrolytes [26]. What is the reason for the drastic underperformance of $\text{H}_3\text{PW}_{12}\text{O}_{40}$ in the present organic electrolyte? This different behavior must be associated to different reaction mechanisms. For instance, the deprotonation of acidic PW12 must be hindered in acetonitrile, probably due to the lack of a proton-accepting base such as H_2O . Thus, in addition to the important effect of cations in POM chemistry, we believe this underperformance could be due to the dispersion of a solid acid such as $\text{H}_3\text{PW}_{12}\text{O}_{40}$ in a non-aqueous electrolyte impeding the very effective Grotthuss mechanism taking place in protonated water.

Thus, contrary to the acidic derivative, TEAPW12 can effectively carry on the redox reaction in organic electrolytes without protons and contribute its redox activity to the total capacitance of the hybrid material. Gravimetric specific capacitance is also characterized by galvanostatic charge-discharge technique (Fig. S4c). AC/TEAPW12 exhibits nearly equivalent gravimetric specific capacitance with respect to AC in the whole range (around 82 F g^{-1} at 0.5 A g^{-1} and around 67 F g^{-1} at 20 A g^{-1}). This is not surprising given the very large molecular weight of TEAPW12 (ca. 3270 g/mol), which, when normalizing per mass, compensates for the increased capacitance provided by the cluster. On the other hand, when the key is compactness, that is, when volume normalization prevails, the AC/TEAPW12 electrode is a winner, since compact, 1 nm PW12 molecular clusters are directly attached to the porous surface of AC with no addition to the volume of the carbon material.

We tested the rate performance of our materials by measuring capacitances as a function of discharge current density (Fig. 3d). It should be noted that AC/TEAPW12 supercapacitors are superior to AC in the whole range. Furthermore, the drop in capacitance at fast rates is relatively small. Thus, by increasing the current density from 0.5 A cm^{-2} to 10 A cm^{-2} the capacitance values drop to 80.1% (AC/TEAPW12) and 79.9% (AC), suggesting good rate capability. As both the AC and hybrid electrodes are mainly composed of activated carbon (85 wt% for AC electrode, 66 wt% for AC/TEAPW12 electrode with carbon black and poly(vinylidene fluoride) accounting for 15%) and since the activated carbon acts as both substrate and conductor for TEAPW12, it is reasonable to ascribe the limitation on the rate capability to activated carbon.

In addition, the energy and power densities of these supercapacitors are compared and presented in the Ragone plot (see Fig. S4d). The maximum energy density for AC/TEAPW12 cell is found to be 16 mWh cm^{-3} at the power density of 1.35 W cm^{-3} , which is 36% higher than that of AC. The energy density of AC/TEAPW12 outperforms that of AC in the same power density range thanks to the improved volumetric capacitance and the superior cell voltage. Moreover, with respect to recently reported activated carbon-based supercapacitors, the AC/TEAPW12 surpass those both in aqueous electrolytes and organic electrolytes [44–47]. This behavior is similar to some previously reported materials made from activated carbon with redox active additives [48] or heteroatom doping [49,50]. Yet, it represents an alternative way to introduce pseudocapacitance without doping the carbon or adding redox active species to the electrolyte (which normally leads to faster self-

discharge), just by adsorbing electroactive molecular clusters onto AC.

Finally, we are presenting our cycle stability. Fig. 4a shows the retention of the initial capacitance values for AC and AC/TEAPW12 symmetric capacitors as a function of the cycle number. The capacitance of AC/TEAPW12 increases a little bit due to the activation process in the first cycles, which is normal for materials with pseudocapacitance [51]. In contrast, the capacitance of AC decreases from the beginning at a low but steady rate. After 10,000 cycles, the retention of both cells is higher than 91%, and owing to the increase of capacitance at the first stage, the retention of AC/TEAPW12 is even higher (93%). Fig. 4b–e shows the morphologies of AC and AC/TEAPW12 electrodes before and after cycling. Even after 10000 cycles, both AC and AC/TEAPW12 electrodes present no apparent difference except for a small amount of electrolyte residue. HAADF-STEM was performed to investigate the effective anchoring of TEAPW12 on AC after cycling (Fig. 4f). The bright dots associated to PW12 clusters spread on the AC substrate uniformly, demonstrating that even after 10000 charge-discharge cycles and acetonitrile washing, PW12 clusters are still anchored on AC. EDX spectra of cycled and washed AC/TEAPW12 is present in Fig. S6b. The existence of W is clearly verified. Moreover, a coin cell with the AC electrodes and the used electrolytes collected from AC/TEAPW12 cell is assembled to testify that TEAPW12 has not been dissolved in the electrolyte, at least not enough to present any redox waves (Fig. S6a). Thus, we could conclude that TEAPW12 clusters are anchoring on AC tightly, even after 10,000 cycles and acetonitrile washing. This should be attributed to the fact that the PW12 are mainly anchored in the micropores of similar size. Thanks to the stability of AC substrate and the tight anchoring of TEAPW12, the hybrid electrodes could deliver an excellent cycle stability in organic electrolytes

4. Conclusion

In this work an organic-inorganic polyoxometalate salt (TEAPW12) was exploited to hybridize with activated carbon in a facile way in order to enhance the capacitive performance of activated carbon in organic electrolytes. The as-prepared hybrid material was characterized by TGA and HAADF-STEM, showing a homogeneous distribution of TEAPW12 clusters anchored in the pores of AC with a final mass percentage of 17.5% of TEAPW12. The hybrid material was tested in a conventional organic electrolyte (1 M TEABF₄ in acetonitrile) in both three-electrode cell and two-electrode cell (as symmetric supercapacitors). The organic-inorganic hybrid material exhibits superior performance as compared with the parent AC supercapacitor system. But also, very remarkably, in this organic media the AC/TEAPW12 hybrid electrode shows better performance than the hybrid material based on the phosphotungstic acid derivative (AC/HPW12). Our work shows that the fast reversible redox reactions of PW12 can proceed in the absence of protons, provided by the use of a suitable salt. Owing to the faradaic process of TEAPW12 in the organic electrolyte, the symmetrical capacitors of the hybrid material show an increment of 36% in volumetric capacitance with respect to that of AC, good rate capability and good cycle stability (93% of initial capacitance retained after 10,000 cycles). Therefore, applying organic POMs salts, instead of inorganic POMs acids or salts, to construct hybrid materials has been proven to be an effective route to enhance the capacitance of carbon-based materials in organic electrolytes.

Declaration of Competing Interest

The authors declare that they have no known competing financial interests or personal relationships that could have appeared to influence the work reported in this paper.

CRediT authorship contribution statement

Jun-jie Zhu: Data curation, Investigation, Formal analysis, Methodology, Visualization, Writing - original draft. **Raul Benages-Vilau:** Formal analysis, Project administration, Supervision, Validation. **Pedro Gomez-Romero:** Conceptualization, Funding acquisition, Methodology, Supervision, Writing - review & editing.

Acknowledgments

Partial funding from Ministry of Science, Innovation and Universities (MCIU), the State Research Agency (AEI) and the European Regional Development Fund (FEDER) (grant RTI2018-099826-B-I00) and AGAUR (2017 SGR 00870) are gratefully acknowledged. ICN2 is funded by the CERCA programme / Generalitat de Catalunya, and it is supported by the Severo Ochoa Centres of Excellence programme, funded by the Spanish Research Agency (AEI), grant no. SEV-2017-0706. J.J.Z. acknowledges his scholarship (No. 201806370211) under China Scholarship Council. This work has been carried out within the framework of doctoral program (PhD) of Material Science (Department of Physics) of Universitat Autònoma de Barcelona (UAB).

Supplementary materials

Supplementary material associated with this article can be found, in the online version, at doi:10.1016/j.electacta.2020.137007.

References

- [1] D.P. Dubal, N.R. Chodankar, D.H. Kim, P. Gomez-Romero, *Chem. Soc. Rev.* 47 (2018) 2065–2129, doi:10.1039/c7cs00505a.
- [2] C. Choi, D.S. Ashby, D.M. Butts, R.H. DeBlock, Q. Wei, J. Lau, B. Dunn, *Nat. Rev. Mater.* (2019), doi:10.1038/s41578-019-0142-z.
- [3] Z. Lin, E. Goikolea, A. Balducci, K. Naoi, P.L. Taberna, M. Salanne, G. Yushin, P. Simon, *Mater. Today* 21 (2018) 419–436, doi:10.1016/j.mattod.2018.01.035.
- [4] S. Li, L.L. Yu, Y.T. Shi, J. Fan, R.B. Li, G.D. Fan, W.L. Xu, J.T. Zhao, *ACS Appl. Mater. Interfaces* 11 (2019) 10178–10188, doi:10.1021/acsami.8b21063.
- [5] X. Chen, R. Paul, L. Dai, *Natl. Sci. Rev.* 4 (2017) 453–489, doi:10.1093/nsr/nwx009.
- [6] F. Beguin, V. Presser, A. Balducci, E. Frackowiak, *Adv. Mater.* 26 (2014) 2219–2251, doi:10.1002/adma.201304137.
- [7] M. Skunik-Nuckowska, S. Dyjak, K. Grzejszczyk, N.H. Wisinska, F. Beguin, P.J. Kulesza, *Electrochim. Acta* 282 (2018) 533–543, doi:10.1016/j.electacta.2018.06.070.
- [8] D.P. Dubal, B. Ballesteros, A.A. Mohite, P. Gomez-Romero, *ChemSusChem* 10 (2017) 731–737, doi:10.1002/cssc.201601610.
- [9] P. Gómez-Romero, M. Chojak, K. Cuentas-Gallegos, J.A. Asensio, P.J. Kulesza, N. Casañ-Pastor, M. Lira-Cantú, *Electrochem. Commun.* 5 (2003) 149–153, doi:10.1016/S1388-2481(03)00010-9.
- [10] A.K. Cuentas-Gallegos, M. Lira-Cantú, N. Casañ-Pastor, P. Gómez-Romero, *Adv. Funct. Mater.* 15 (2005) 1125–1133, doi:10.1002/adfm.200400326.
- [11] P. Gómez-Romero, M. Lira-Cantú, *Adv. Mater.* 9 (1997) 144–147, doi:10.1002/adma.19970090210.
- [12] M. Lira-Cantú, P. Gómez-Romero, *Chem. Mater.* 10 (1998) 698–704, doi:10.1021/cm970107u.
- [13] S.-C. Huang, C.-C. Lin, C.-W. Hu, Y.-F. Liao, T.-Y. Chen, H.-Y. Chen, *J. Power Sources* 435 (2019) 226702, doi:10.1016/j.jpowsour.2019.226702.
- [14] J. Friedl, M.V. Holland-Cunz, F. Cording, F.L. Pfanschilling, C. Wills, W. McFarlane, B. Schrickler, R. Fleck, H. Wolfschmidt, U. Stimming, *Energy Environ. Sci.* 11 (2018) 3010–3018, doi:10.1039/c8ee00422f.
- [15] D.P. Dubal, D. Rueda-García, C. Marchante, R. Benages, P. Gomez-Romero, *Chem. Rec.* 18 (2018) 1076–1084, doi:10.1002/tcr.201700116.
- [16] N.L.O. Gunn, D.B. Ward, C. Menelaou, M.A. Herbert, T.J. Davies, *J. Power Sources* 348 (2017) 107–117, doi:10.1016/j.jpowsour.2017.02.048.
- [17] F.C. Shen, Y.R. Wang, S.L. Li, J. Liu, L.Z. Dong, T. Wei, Y.C. Cui, X.L. Wu, Y. Xu, Y.Q. Lan, *J. Mater. Chem. A* 6 (2018) 1743–1750, doi:10.1039/c7ta09810c.
- [18] H.N. Wang, M. Zhang, A.M. Zhang, F.C. Shen, X.K. Wang, S.N. Sun, Y.J. Chen, Y.Q. Lan, *ACS Appl. Mater. Interfaces* 10 (2018) 32265–32270, doi:10.1021/acsami.8b12194.
- [19] S. Herrmann, N. Aydemir, F. Nagele, D. Fantauzzi, T. Jacob, J. Travas-Sejdic, C. Streb, *Adv. Funct. Mater.* 27 (2017), doi:10.1002/adfm.201700881.
- [20] J. Vaillant, M. Lira-Cantu, K. Cuentas-Gallegos, N. Casañ-Pastor, P. Gómez-Romero, *Prog. Solid State Chem.* 34 (2006) 147–159, doi:10.1016/j.progsolidstchem.2005.11.015.
- [21] M. Genovese, K. Lian, *Electrochem. Commun.* 43 (2014) 60–62, doi:10.1016/j.elecom.2014.03.014.

- [22] A.K. Cuentas-Gallegos, R. Martínez-Rosales, M. Baibarac, P. Gómez-Romero, M.E. Rincón, *Electrochem. Commun.* 9 (2007) 2088–2092, doi:10.1016/j.elecom.2007.06.003.
- [23] D.P. Dubal, P. Gomez-Romero, *Mater. Today Energy* 8 (2018) 109–117, doi:10.1016/j.mtener.2018.03.005.
- [24] M. Genovese, K. Lian, *J. Mater. Chem. A* 5 (2017) 3939–3947, doi:10.1039/c6ta10382k.
- [25] C.C. Hu, E.B. Zhao, N. Nitta, A. Magasinski, G. Berdichevsky, G. Yushin, *J. Power Sources* 326 (2016) 569–574, doi:10.1016/j.jpowsour.2016.04.036.
- [26] J. Suárez-Guevara, V. Ruiz, P. Gomez-Romero, *J. Mater. Chem. A* 2 (2014) 1014–1021, doi:10.1039/c3ta14455k.
- [27] J. Suarez-Guevara, V. Ruiz, P. Gomez-Romero, *Phys. Chem. Chem. Phys.* 16 (2014) 20411–20414, doi:10.1039/c4cp03321c.
- [28] V. Ruiz, J. Suarez-Guevara, P. Gomez-Romero, *Electrochem. Commun.* 24 (2012) 35–38, doi:10.1016/j.elecom.2012.08.003.
- [29] D.E. Jiang, Z. Jin, D. Henderson, J. Wu, *J. Phys. Chem. Lett.* 3 (2012) 1727–1731, doi:10.1021/jz3004624.
- [30] L.L. Zhang, X.S. Zhao, *Chem. Soc. Rev.* 38 (2009) 2520–2531, doi:10.1039/b813846j.
- [31] D. Chai, Y. Hou, K.P. O'Halloran, H. Pang, H. Ma, G. Wang, X. Wang, *ChemElectroChem* 5 (2018) 3443–3450, doi:10.1002/celec.201801081.
- [32] N.N. Du, L.G. Gong, L.Y. Fan, K. Yu, H. Luo, S.J. Pang, J.Q. Gao, Z.W. Zheng, J.H. Lv, B.B. Zhou, *ACS Appl. Nano Mater.* 2 (2019) 3039–3049, doi:10.1021/acsnm.9b00409.
- [33] K. Kume, N. Kawasaki, H. Wang, T. Yamada, H. Yoshikawa, K. Awaga, *J. Mater. Chem. A* 2 (2014) 3801–3807, doi:10.1039/c3ta14569g.
- [34] L. Ouahab, M. Bencharif, A. Mhanni, D. Pelloquin, J. Halet, O. Pena, J. Padiou, D. Grandjean, C. Garrigou-Lagrange, *Chem. Mater.* 4 (1992) 666–674, doi:10.1021/cm00021a032.
- [35] E. Bourgeat-Lami, F. Di Renzo, F. Fajula, P.H. Mutin, T. Des Courieres, *J. Phys. Chem.* 96 (1992) 3807–3811, doi:10.1021/j100188a044.
- [36] A.O. Kalpakli, S. Ilhan, C. Kahruman, I. Yusufoglu, *Int. J. Refract. Metals Hard Mater.* 31 (2012) 14–20, doi:10.1016/j.jrmhm.2011.08.007.
- [37] B. Chen, R. Neumann, *Phys. Chem. Chem. Phys.* 18 (2016) 22487–22493, doi:10.1039/c6cp03315f.
- [38] J. Cao, C. Li, Z. Zhang, C. Xu, J. Yan, F. Cui, C. Hu, *J. Am. Soc. Mass Spectrom.* 23 (2012) 366–374, doi:10.1007/s13361-011-0296-4.
- [39] V.A. Grigoriev, C.L. Hill, I.A. Weinstock, *J. Am. Chem. Soc.* 122 (2000) 3544–3545, doi:10.1021/ja993862c.
- [40] T. Ueda, K. Kodani, H. Ota, M. Shiro, S.X. Guo, J.F. Boas, A.M. Bond, *Inorg. Chem.* 56 (2017) 3990–4001, doi:10.1021/acs.inorgchem.6b03046.
- [41] Y.L. Shao, M.F. El-Kady, J.Y. Sun, Y.G. Li, Q.H. Zhang, M.F. Zhu, H.Z. Wang, B. Dunn, R.B. Kaner, *Chem. Rev.* 118 (2018) 9233–9280, doi:10.1021/acs.chemrev.8b00252.
- [42] M. Zhang, A.M. Zhang, X.X. Wang, Q. Huang, X.S. Zhu, X.L. Wang, L.Z. Dong, S.L. Li, Y.Q. Lan, *J. Mater. Chem. A* 6 (2018) 8735–8741, doi:10.1039/c8ta01062e.
- [43] S. Li, L.-L. Yu, R.-B. Li, J. Fan, J.-T. Zhao, *Energy Storage Mater.* 11 (2018) 176–183, doi:10.1016/j.ensm.2017.07.011.
- [44] X. Liu, C. Ma, J. Li, B. Zielinska, R.J. Kalenczuk, X. Chen, P.K. Chu, T. Tang, E. Mirowska, *J. Power Sources* 412 (2019) 1–9, doi:10.1016/j.jpowsour.2018.11.032.
- [45] X. Yu, J. Lu, C. Zhan, R. Lv, Q. Liang, Z.-H. Huang, W. Shen, F. Kang, *Electrochim. Acta* 182 (2015) 908–916, doi:10.1016/j.electacta.2015.10.016.
- [46] Q. Xie, R. Bao, A. Zheng, Y. Zhang, S. Wu, C. Xie, P. Zhao, *ACS Sustain. Chem. Eng.* 4 (2016) 1422–1430, doi:10.1021/acssuschemeng.5b01417.
- [47] J. Niu, M. Liu, F. Xu, Z. Zhang, M. Dou, F. Wang, *Carbon* 140 (2018) 664–672, doi:10.1016/j.carbon.2018.08.036.
- [48] J.Y. Hwang, M. Li, M.F. El-Kady, R.B. Kaner, *Adv. Funct. Mater.* 27 (2017) 1605745, doi:10.1002/adfm.201605745.
- [49] Y. Wang, M. Zhang, Y. Dai, H.-Q. Wang, H. Zhang, Q. Wang, W. Hou, H. Yan, W. Li, J.-C. Zheng, *J. Power Sources* 438 (2019) 227045, doi:10.1016/j.jpowsour.2019.227045.
- [50] J. Zhou, J. Lian, L. Hou, J. Zhang, H. Gou, M. Xia, Y. Zhao, T.A. Strobel, L. Tao, F. Gao, *Nat. Commun.* 6 (2015) 8503, doi:10.1038/ncomms9503.
- [51] J.-J. Zhu, L.-L. Yu, J.-T. Zhao, *J. Power Sources* 270 (2014) 411–417, doi:10.1016/j.jpowsour.2014.07.093.

Supplementary materials

Can polyoxometalates enhance the capacitance and energy density of activated carbon in organic electrolyte supercapacitors?

Jun-Jie Zhu^a, Raul Benages-Vilau^a, Pedro Gomez-Romero^{a,b*}

^a Catalan Institute of Nanoscience and Nanotechnology (ICN2), CSIC and BIST,
Campus UAB, Bellaterra, 08193 Barcelona, Spain.

^b Consejo Superior de Investigaciones Científicas (CSIC), Spain

* Corresponding author. E-mail address: pedro.gomez@icn2.cat (P. Gomez-Romero) Tel: +34 937373608, Fax: +34 936917640

ICN2, Campus UAB, 08193 Bellaterra (Barcelona) Spain

Supporting information S1

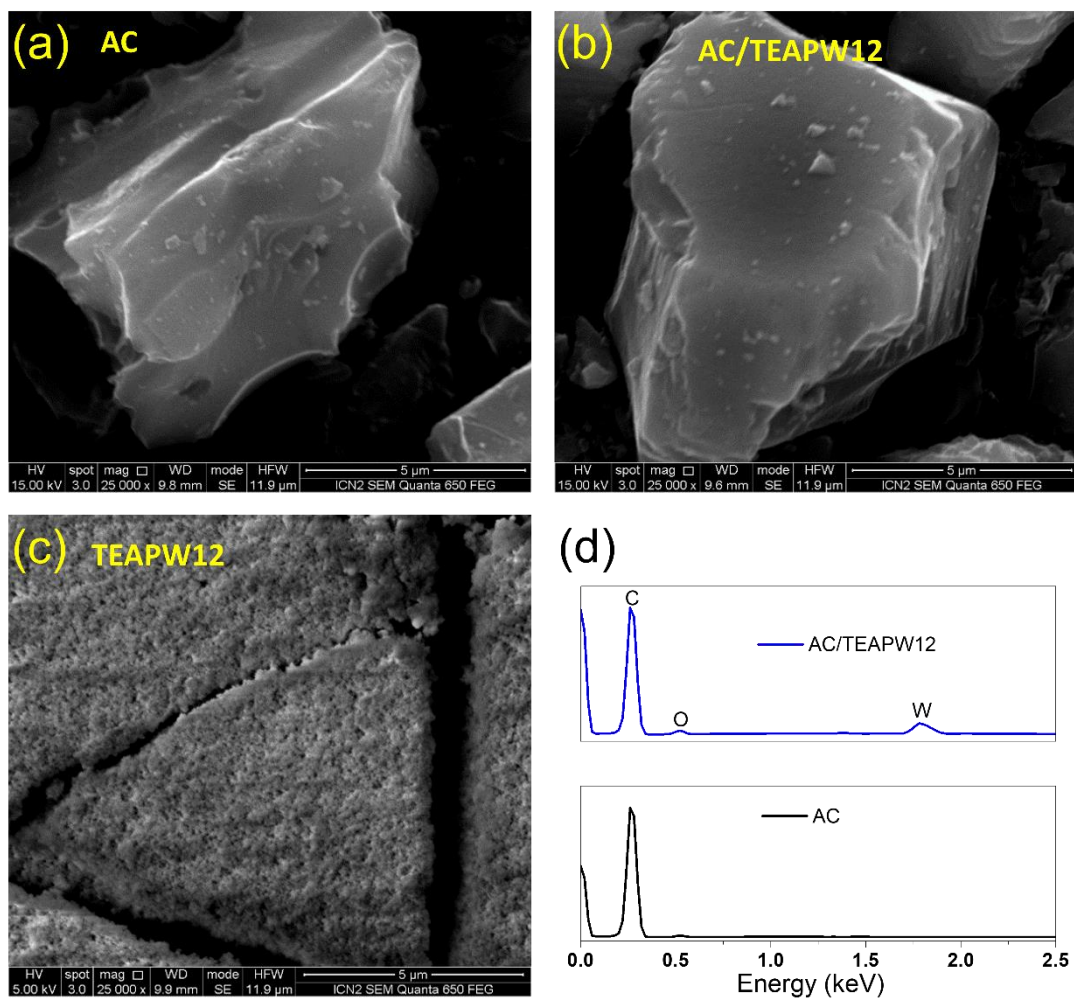


Fig. S1. (a-c)SEM images of AC, AC/TEAPW12 and TEAPW12. (d) EDX spectrum of AC and AC/TEAPW12.

Supporting information S2

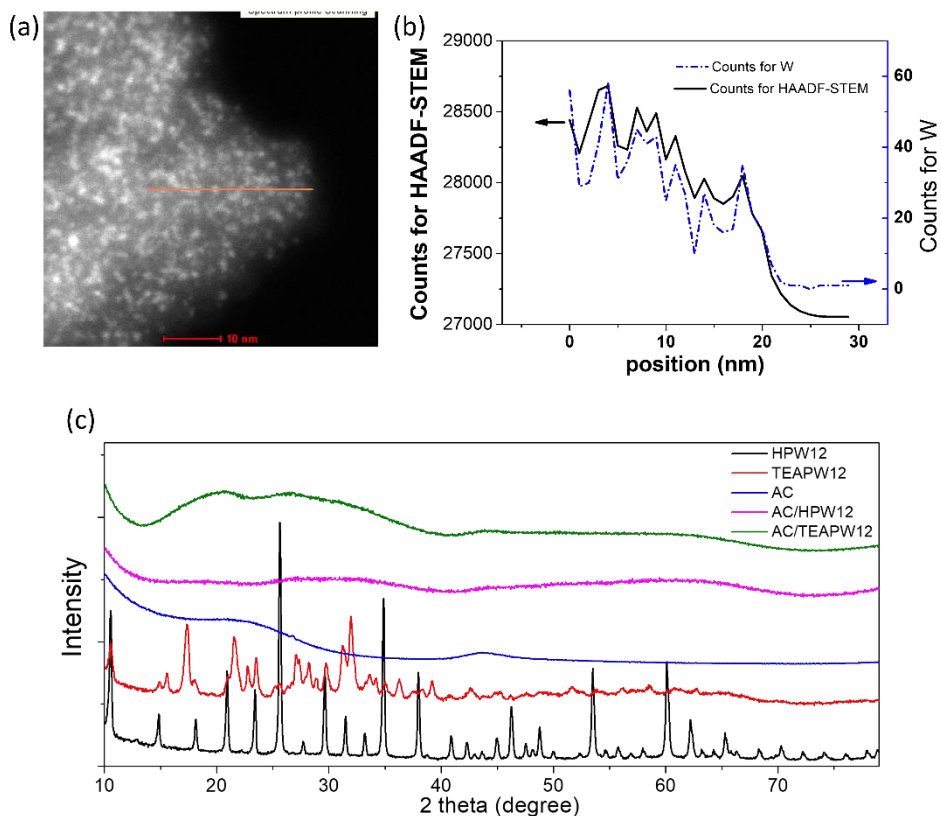


Fig. S2. (a and b) High angle annular dark field scanning transmission electron microscopy (HAADF-STEM) image of AC/TEAPW12 with corresponding EDX line scan which confirm that the fluctuation of brightness is consistent with the fluctuation of W concentration. Scale bar (bottom) 10nm. (c) XRD patterns of AC, TEAPW12, AC/TEAPW12, phosphotungstic acid (HPW12) and AC/HPW12.

Supporting information S3

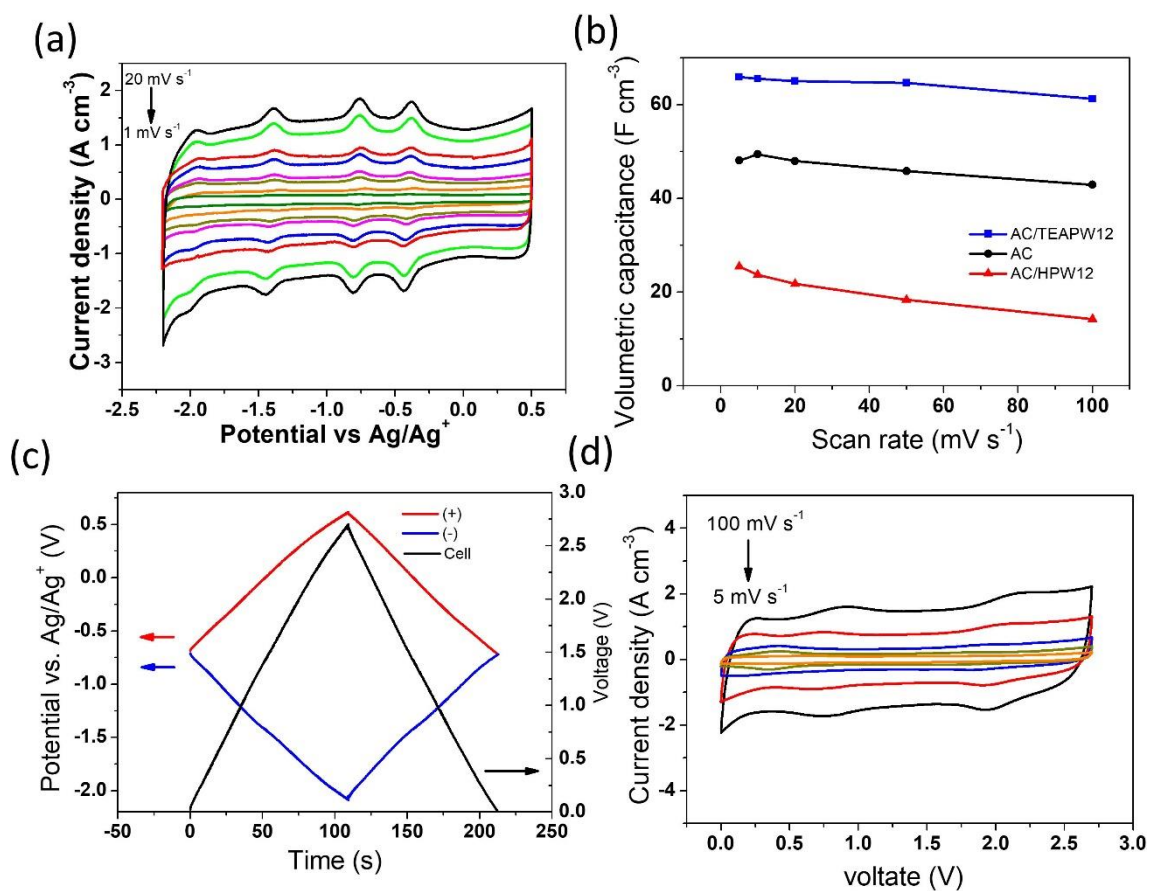


Fig. S3. (a) Cyclic voltammograms of AC/TEAPW12 at 1, 2, 4, 5, 8, 10, 15 and 20 mV s^{-1} . (b) Volumetric capacitance of AC, AC/TEAPW12 and AC/HPW12 at various scan rates. (c) The variation of the potential of both positive and negative electrodes, as well as the symmetric supercapacitor voltage during galvanostatic charging and discharging at 0.8 mA . (d) Cyclic polarization traces of AC/HPW12 in two-electrode configuration at 5, 10, 20, 50 and 100 mV s^{-1} .

Supporting information S4

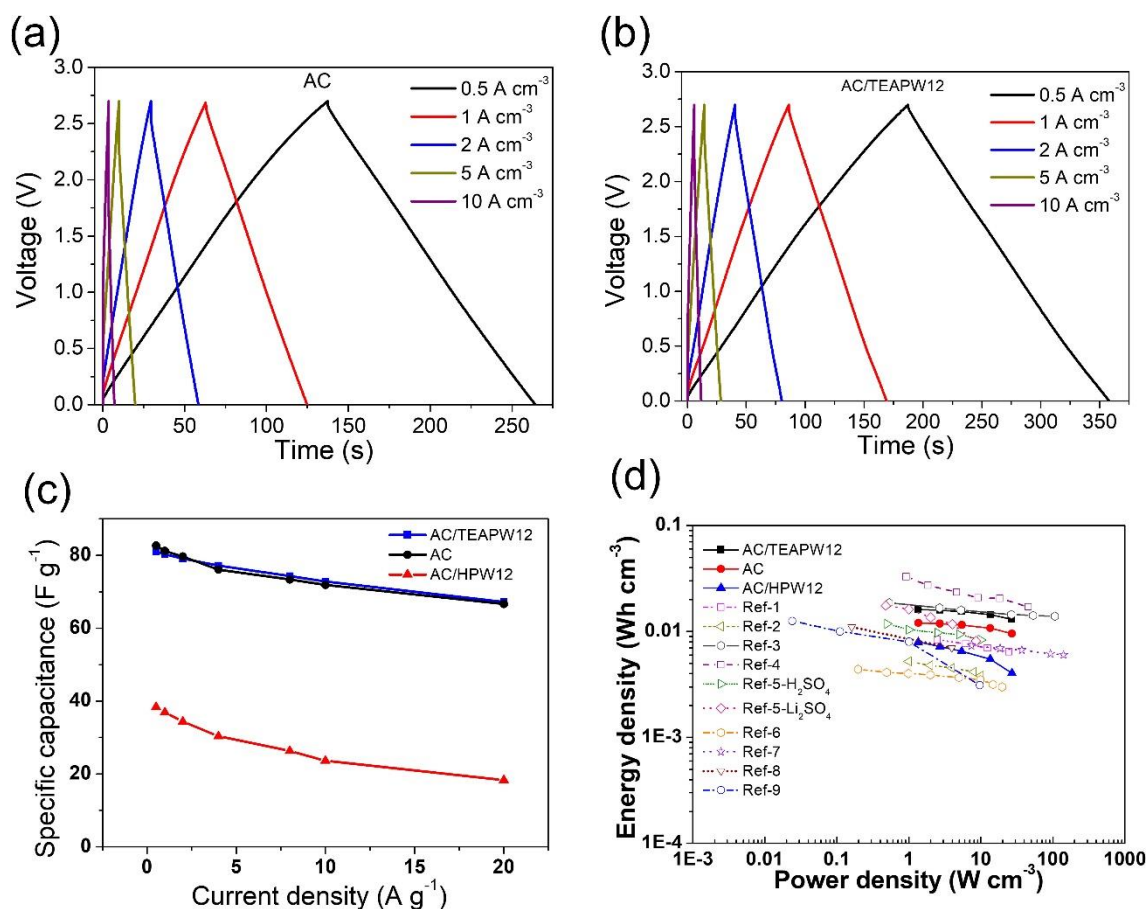


Fig. S4. Galvanostatic charging and discharging curves at various current density of (a) AC and (b) AC/TEAPW12. (c) Specific capacitance of AC, AC/TEAPW12 and AC/HPW12 at various current density. (d) Power density vs. energy density of AC, AC/TEAPW12, AC/HPW12 and latest reported activated carbon-based material.

Supporting information S5

Estimating the contribution of TEAPW12 to the capacitance of AC/TEAPW12

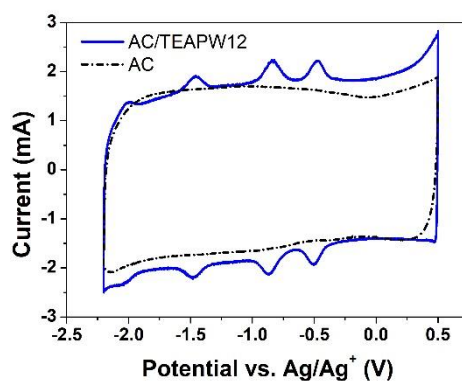


Fig. S5 Cyclic voltammograms of AC and AC/TEAPW12 at 20 mV s⁻¹

Fig. S5 present the same data of Fig. 3a without normalization for calculation.

The mass of active materials on these two working electrodes:

$$m_{AC} = 1.20 \text{ mg}$$

$$m_{AC/TEAPW12} = 1.45 \text{ mg}$$

Reversible stored charge (Q) can be calculated as following:

$$Q = \frac{\int i dV}{2v}$$

Where $\int i dV$ is the integral area of cyclic voltammograms (not normalized by mass nor volume), v is the scan rate (20 mV s⁻¹)

The reversible stored charge on these two working electrodes:

$$Q_{AC} = 0.210 \text{ C}$$

$$Q_{AC/TEAPW12} = 0.241 \text{ C}$$

If we assume that the anchoring of TEAPW12 does not substantially affect the capacitance of activated carbon, the charge stored by activated carbon in AC/TEAPW12 ($Q_{AC \text{ in } AC/TEAPW12}$) can be derived as follows:

$$Q_{AC \text{ in } AC/TEAPW12} = 82.5\% m_{AC/TEAPW12} Q_{AC} / m_{AC} = 0.209 \text{ C}$$

The stored charge after deducting the contribution from AC:

$$Q_{AC/TEAPW12} - Q_{AC \text{ in } AC/TEAPW12} = 0.032 \text{ C}$$

We assume TEAPW12 can only (reversibly) store charges associated to the total exchange of four electrons, then we can estimate the theoretical charge stored by TEAPW12 in AC/TEAPW12 ($Q_{TEAPW12 \text{ in } AC/TEAPW12}$) as follows:

$$Q_{TEAPW12 \text{ in } AC/TEAPW12} = 17.5\% m_{AC/TEAPW12} N_A / M_{TEAPW12} \times 4e = 0.030 \text{ C}$$

The theoretical charge ($Q_{TEAPW12 \text{ in } AC/TEAPW12}$) is just a little bit smaller than the charge after deducting the contribution from AC ($Q_{AC/TEAPW12} - Q_{AC \text{ in } AC/TEAPW12}$). Since all TEAPW12 clusters are able to spread on AC as a monolayer, we expect that all the TEAPW12 clusters make a contribution to the whole capacitance. $Q_{TEAPW12 \text{ in } AC/TEAPW12}$ could account 93.8% for ($Q_{AC/TEAPW12} - Q_{AC \text{ in } AC/TEAPW12}$). Thus, most of the increased stored charge is from TEAPW12. Apart from the contribution from TEAPW12, the remaining slight increase of stored charge (about 0.002 C) might be ascribed to the modification on the structure or changed surface state of activated carbon during the hybridization.

In other words, we can now state that the expected theoretical contribution of POM to reversible charge storage and the measured charge are compatible with all the 17.5 wt% of POM in the hybrid reversibly exchanging four electrons per cluster.

Supporting information S6

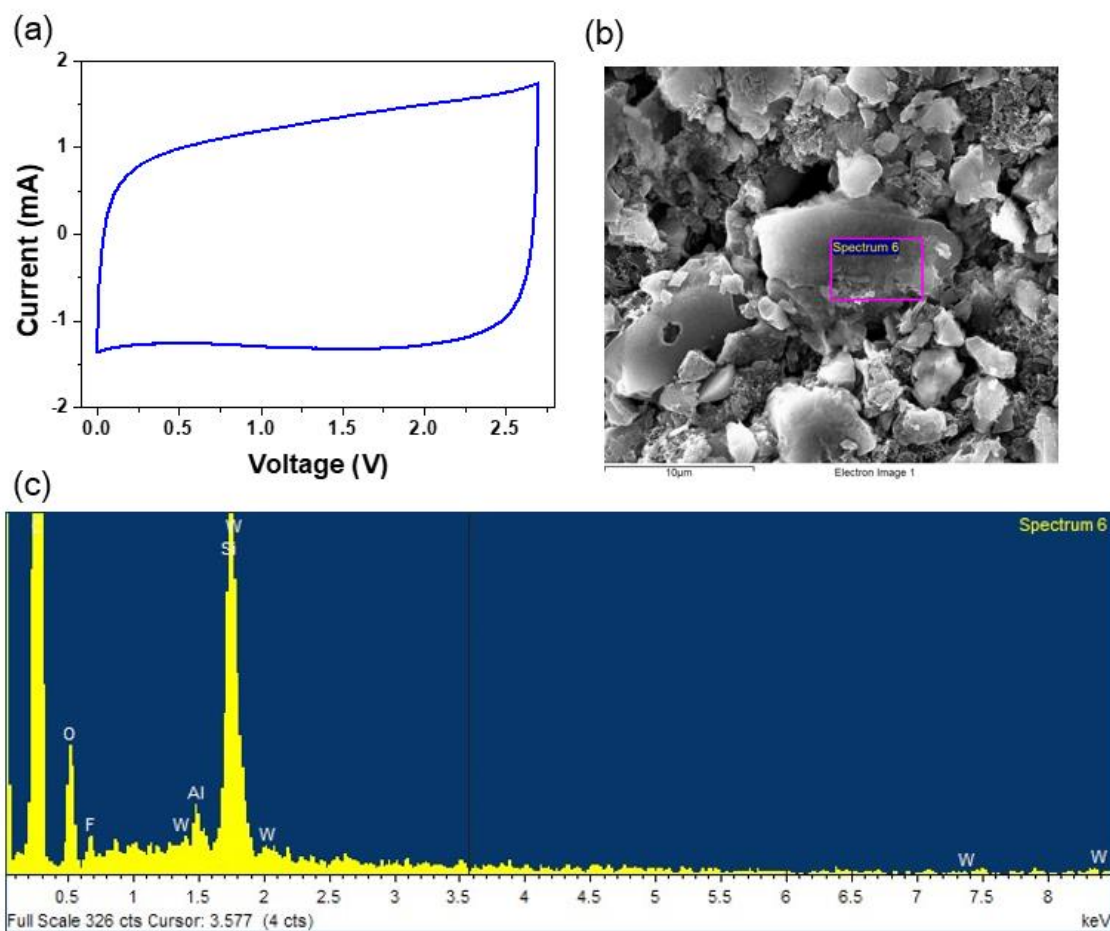


Fig.S6 (a) CP of AC coin cell using the electrolyte collected from cycled AC/TEAPW12 cell, at 20 mV s^{-1} . (b) SEM image of cycled, acetonitrile-washed AC/TEAPW12 electrode (pink rectangle: the interested area for EDX spectrum). (c) EDX spectrum of the area

Table S6 Quantitative analysis report for the EDX spectrum

Element	C	O	F	Al	Si	W	Total
Weight%	80.14	9.51	1.82	0.4	3.71	4.42	100

Note: Since the cycled AC/TEAPW12 electrode is highly contaminated by the electrolyte and other parts of the cell (separators, spacers, springs etc.) and washed by acetonitrile, the percentage of W here cannot represent the real amount of W in the cycled AC/TEAPW12 electrode. We speculate AC/TEAPW12 lose little TEAPW12 into the electrolyte, and its concentration is too low to yield a redox signal.

Supporting information S7

Table S7 Capacitive performance of latest reported activated carbon supercapacitors.

Ref	Volumetric capacitance	Current Density	Electrolyte	Voltage window
1	239 F cm ⁻³	0.1 A g ⁻¹	6M KOH	1 V
2	171 F cm ⁻³	0.05 A g ⁻¹	6M KOH	1 V
3	90 F cm ⁻³	0.6 A/g	1M TEABF ₄ ACN	2.3 V
4	482 F cm ⁻³	1 A g ⁻¹	1 M H ₂ SO ₄	1 V
5	63.6 F cm ⁻³	1 A g ⁻¹	1 M Li ₂ SO ₄	1.8 V
6	198 F cm ⁻³	0.2 A g ⁻¹	6M KOH	0.8 V
7	52.3 F cm ⁻³	1.7 mA cm ⁻²	1M TEABF ₄ ACN	2 V
8	257.7 F cm ⁻³	0.05 A g ⁻¹	6 M KOH	1 V
9	381 F cm ⁻³	0.1 A g ⁻¹	6 M KOH	1 V
this work (AC/TEAPW12)	66 F cm ⁻³	0.5 A cm ⁻³	1M TEABF ₄ ACN	2.7 V

Supporting information S8

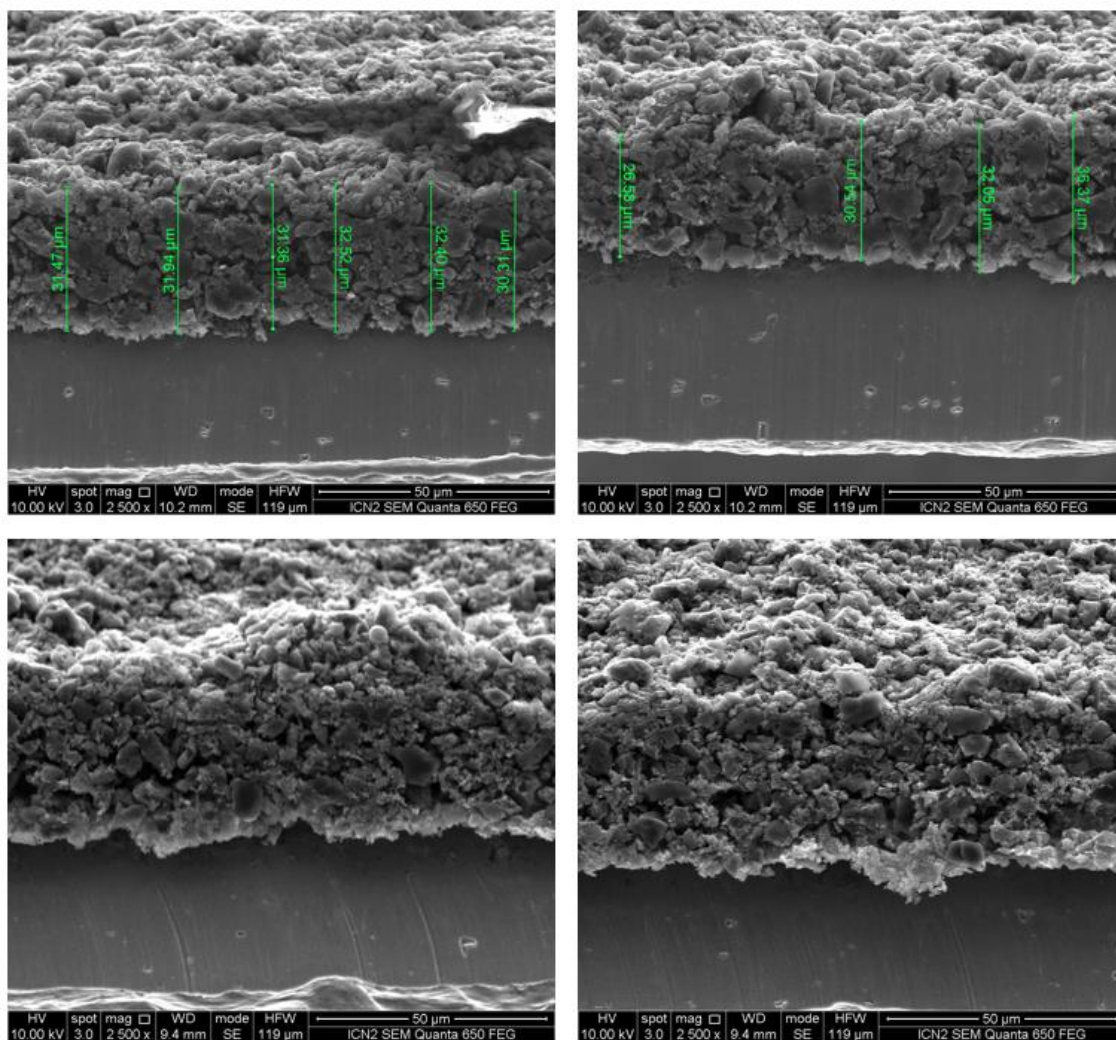


Fig. S8. SEM images of AC electrodes to measure the thickness. Images were taken by mounting the electrodes 70° to the horizontal.

Supporting information S9

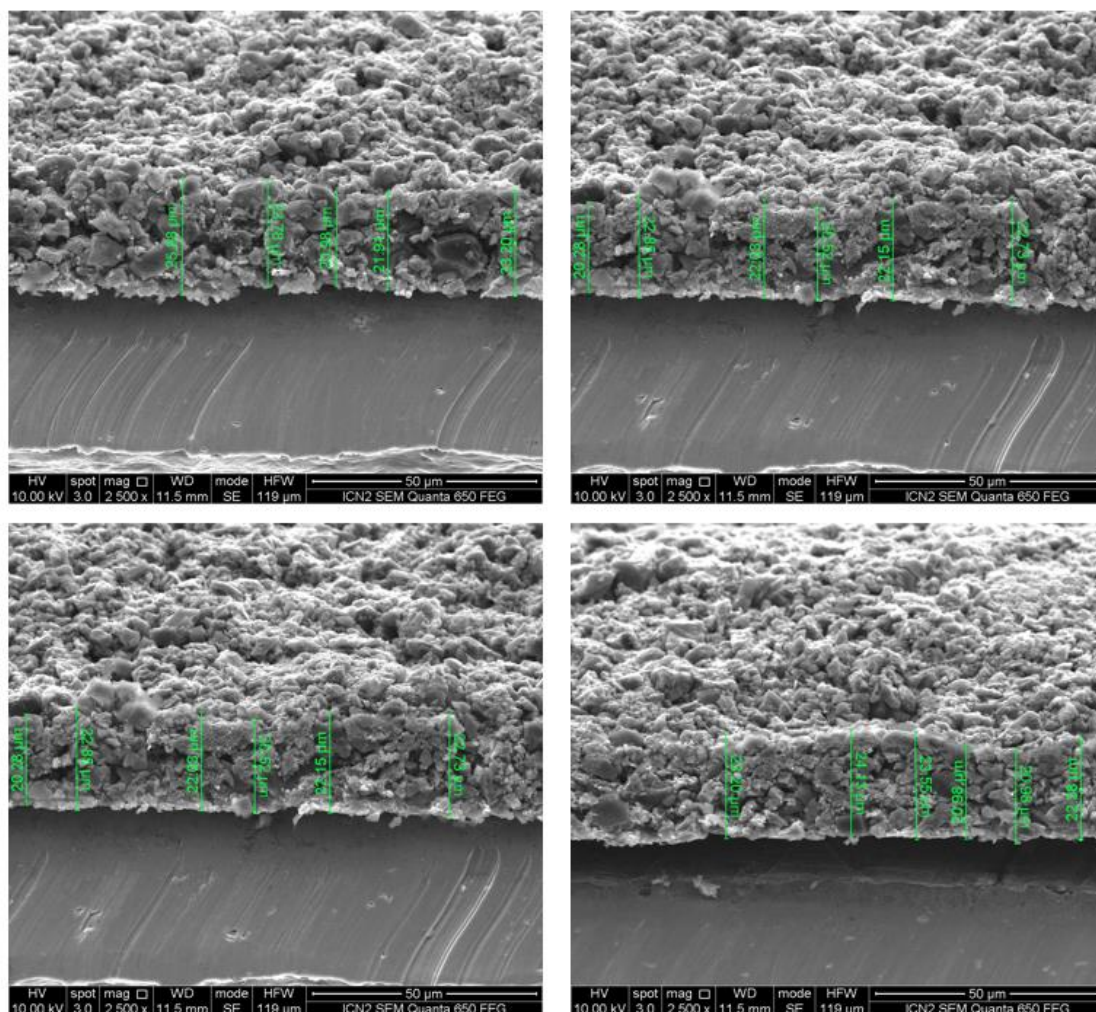


Fig. S9. SEM images of AC/TEAPW12 electrodes to measure the thickness. Images were taken by mounting the electrodes 70° to the horizontal.

Supporting information S10

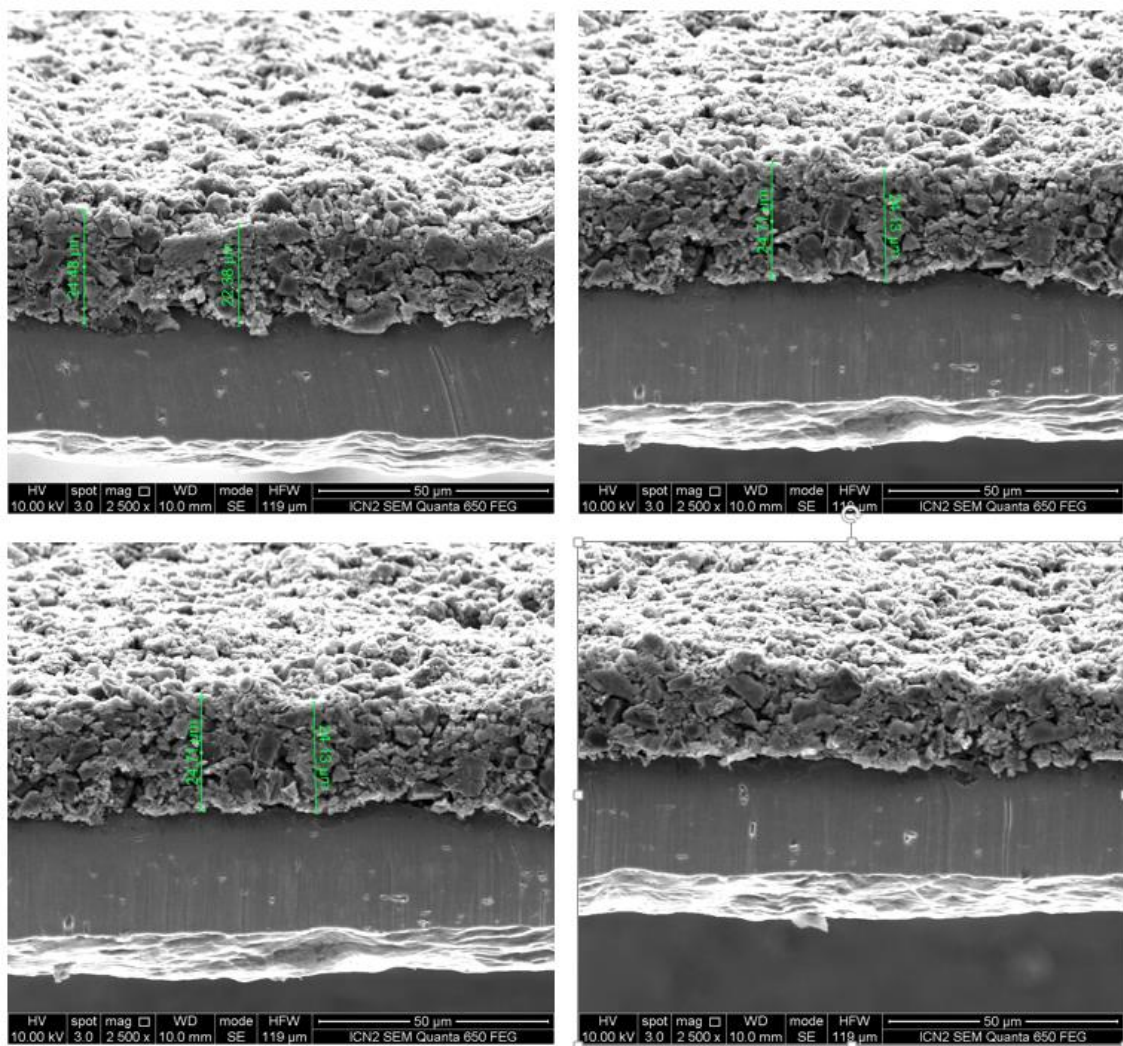


Fig. S10. SEM images of AC/HPW12 electrodes to measure the thickness. Images were taken by mounting the electrodes 70° to the horizontal.

Supporting information S11

Calculation methods for capacitance, energy density and power density

The capacitance of the devices (C), the volumetric capacitance (C_v), energy density (E) and power density (P) of the electrodes, the specific capacitance of active materials (C_m) were calculated from their galvanostatic charging and discharging (GCD) curves or cyclic voltammograms (CVs) according to the following equation:

$$C = \frac{I \int V(t) \cdot dt}{\Delta V^2} \quad \text{Eq S1}$$

$$C = \frac{\int I(V) \cdot dV}{2\nu\Delta V} \quad \text{Eq S2}$$

$$C_v = \frac{2C}{V_e} \quad \text{Eq S3}$$

$$E = \frac{C\Delta V^2}{8V_e} \quad \text{Eq S4}$$

$$P = \frac{E}{\Delta t_d} \quad \text{Eq S5}$$

$$C_m = \frac{2C}{m} \quad \text{Eq S6}$$

Where I is the discharge current of GCD, and ΔV is voltage window (excluding the iR drop for GCD curves), ν is the scan rate of CVs, V_e is the volume (cm^3) of the electrode after subtracting Al foil, m is the mass of active materials on one electrode. Δt_d is the discharge time.

Herein, the diameters of electrodes used for two-electrode cells (symmetric supercapacitors in CR2032 coin cells) and three-electrode cells (T-type Swagelok cells) are 14 mm and 10 mm, respectively. The thickness of the electrodes was measured in the SEM images using ImageJ software as well as the affiliated software of SEM. Four images were taken and 32 measurements were performed for each

sample. The thicknesses of materials on the electrodes of AC, AC/HPW12 and AC/TEAPW12 are 0.030 ± 0.002 , 0.020 ± 0.002 and 0.021 ± 0.002 mm, respectively. The volume of each electrode was calculated by regarding the electrode as a cylinder. The mass loadings of AC, AC/HPW12 and AC/TEAPW12 on 14 mm electrodes are around 2.4, 2.1 and 2.8 mg, respectively.

References to supplementary materials

- [1] C. Zhan, X. Yu, Q. Liang, W. Liu, Y. Wang, R. Lv, Z.-H. Huang, F. Kang, *RSC Advances*, 6 (2016) 89391-89396.
- [2] B. Xu, Y. Chen, G. Wei, G. Cao, H. Zhang, Y. Yang, *Materials Chemistry and Physics*, 124 (2010) 504-509.
- [3] L. Wei, M. Sevilla, A.B. Fuertes, R. Mokaya, G. Yushin, *Advanced Energy Materials*, 1 (2011) 356-361.
- [4] Y. Wang, M. Zhang, Y. Dai, H.-Q. Wang, H. Zhang, Q. Wang, W. Hou, H. Yan, W. Li, J.-C. Zheng, *Journal of Power Sources*, 438 (2019) 227045.
- [5] X. Liu, C. Ma, J. Li, B. Zielinska, R.J. Kalenczuk, X. Chen, P.K. Chu, T. Tang, E. Mijowska, *Journal of Power Sources*, 412 (2019) 1-9.
- [6] X. Yu, J. Lu, C. Zhan, R. Lv, Q. Liang, Z.-H. Huang, W. Shen, F. Kang, *Electrochimica Acta*, 182 (2015) 908-916.
- [7] J.Y. Hwang, M. Li, M.F. El-Kady, R.B. Kaner, *Advanced Functional Materials*, 27 (2017) 1605745.
- [8] Q. Xie, R. Bao, A. Zheng, Y. Zhang, S. Wu, C. Xie, P. Zhao, *ACS Sustainable Chemistry & Engineering*, 4 (2016) 1422-1430.
- [9] J. Niu, M. Liu, F. Xu, Z. Zhang, M. Dou, F. Wang, *Carbon*, 140 (2018) 664-672.

References to the maintext

- [1] M. Liu, F. Yu, B. Yuan, C. Xie, S. Yu, *BMC chemistry*, 15 (2021) 23.
- [2] A. Aouissi, Z.A. Al-Othman, H. Al-Anezi, *Molecules*, 15 (2010) 3319-3328.
- [3] P.F. Pinheiro, D.M. Chaves, M.J. da Silva, *Cellulose*, 26 (2019) 7953-7969.
- [4] J. Suárez-Guevara, V. Ruiz, P. Gomez-Romero, *Journal of Materials Chemistry A*, 2 (2014) 1014-1021.

Chapter 4 MXene/POM hybrid materials

4.1 Context

In the last chapter we presented our groundbreaking work proving how a series of tetraalkylammonium salts of POMs can enhance the capacitive performance of AC in a conventional organic electrolyte. In the corresponding paper we showed in detail the case study of AC/TEAPW12 and demonstrated that the charge storage mechanism of these hybrids are not limited by diffusion.

In this chapter we will describe our efforts to incorporate POMs to a more sophisticated and novel nanoscale pseudocapacitive material—MXene.

The application fields of MXene are partly overlapped with those of POMs. Both have reversible redox activity and have been used in supercapacitors, but MXene is an extended crystalline phase whereas POMs can be dispersed as nanoclusters. It would be interesting to integrate these two materials together. Several studies have been done along this direction. Chen et al. anchored POMs on the surface of $Ti_3C_2T_x$ with (ionic liquid) linkers; this hybrid material can deliver high specific capacitance for a long term in an aqueous electrolyte[1]. Chao et al. in-situ grew 10-20 nm Mo and Fe-based POM nanoparticles on $Ti_3C_2T_x$ nanosheets; this hybrid material shows excellent pseudocapacitive performance in lithium-ion capacitors and sodium-ion capacitors[2]. Zhou et al. embedded phosphomolybdic acid and $Ti_3C_2T_x$ in polypyrrole and constructed an impedimetric aptamer biosensor for osteopontin with extremely low detection limit, high selectivity and stability[3]. MXene/POM hybrid materials not only show great potential in their common fields, but also expand their application. Zong et al. developed GdW_{10} -based polyoxometalates/ $Ti_3C_2T_x$ composite for contrast-

enhanced computed tomography and magnetic resonance imaging[4]. Thus the study of MXene/POM hybrid materials presents a double interest, to strengthen the properties and create synergies in their common application fields and to extend their potential by exploring new applications.

Although some MXene/POM hybrid materials have been developed for energy storage, they are either applied in aqueous-electrolyte supercapacitors or batteries. None of them has been targeted for high-performance organic-electrolyte supercapacitors. This chapter will present our efforts to synthesize MXene/POM hybrid materials and investigate their capacitive behavior in a conventional organic electrolyte.

4.2 Direct anchoring: MXene/HPW12

Reduced graphene oxide has proved to be an excellent substrate to anchor POMs. Since MXene is another 2D material with polar functional groups on the surface we tried first to use the same approach used in the case of RGO (taking advantage of weak H-bonding interactions) to anchor POMs on MXene without any other bonding or linking molecule. The experimental details are presented in section 2.1.6, Chapter 2.

Fig. 4.1 shows the SEM images of pristine MXene and MXene/HPW12 hybrid materials. Both of them exhibit accordion-like morphology, which is typical for MXene. No aggregation nor any impurities can be discerned, implying that the POMs are either dispersed homogeneously in the nanoscale, or not absorbed at all. To confirm any assumptions, we carried out EDX semi-quantitative analysis and XRD, as shown in Fig. 4.2.

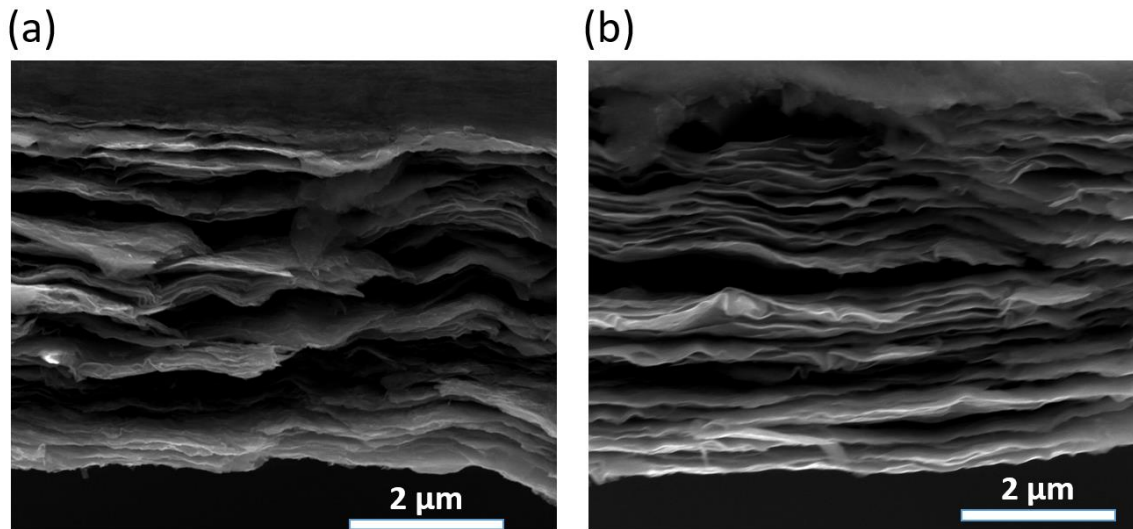


Fig. 4.1 SEM images of MXene and MXene/HPW12.

The EDX spectrum of MXene/HPW12 confirms the presence of W. And the semi-quantitative analysis results (Table 4.1) show that MXene/HPW12 contains 6 wt% W (0.84 at%). The loading mass of HPW12 on MXene is low. The XRD pattern of MXene/HPW12 does not present any diffraction peaks of crystallized HPW12. In principle this would suggest proper dispersion of nanoclusters within the sample (as opposed to microcrystals formation, but this conclusion is compromised by the low effective loading of HPW12.

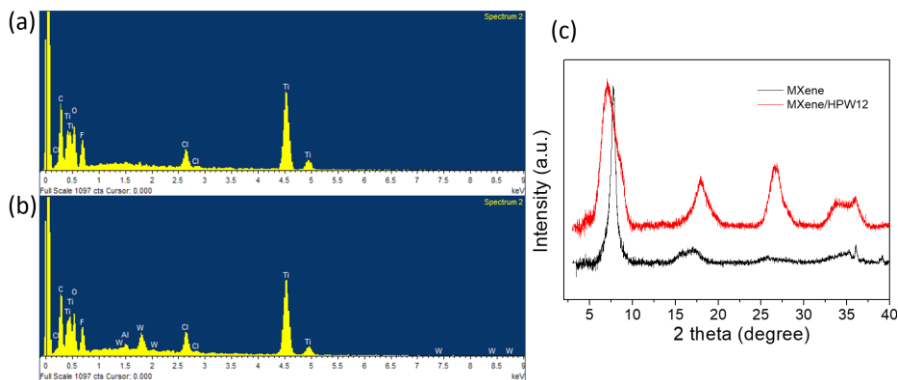


Fig. 4.2 EDX spectra of (a) MXene and (b) MXene/HPW12. (c) XRD patterns of MXene and MXene/HPW12.

Table 4.1 EDX semi-quantitative analyses of MXene and MXene/HPW12

Element	MXene		MXene/HPW12	
	Weight%	Atomic %	Weight%	Atomic %
C K	15.9	32.35	16.56	35.40
O K	14.5	22.14	11.86	19.03
F K	12.12	15.59	10.56	14.27
Cl K	3.35	2.31	4.07	2.95
Ti K	54.13	27.61	50.4	27.02
W M	0	0	6.04	0.84

The atomic ratio W:C 0.84:35.4 indicates the presence of one PW12 cluster per every 500 C atoms, approximately. Thus, although some clusters seem to have been incorporated to MXene, our conclusion is that MXene cannot anchor sizable amounts of POMs through sonication (Preparation of MXene/HPW12 MXene/HPW12, chapter 2) , like rGO does. The loaded quantity of HPW12 on MXene is very low. This little amount of HPW12 cannot make a difference in capacitive performance. Therefore, we decided to consider other methods to load more POMs on MXene.

4.3 Cation-assisted in-situ growth (Article 2)

Submitted article

Polyoxometalate Intercalated MXene with Enhanced Electrochemical Stability

Jun-Jie Zhu^a and Pedro Gomez-Romero^{a,b,}*

^a Catalan Institute of Nanoscience and Nanotechnology (ICN2), CSIC and
BIST, Campus UAB, Bellaterra, 08193 Barcelona, Spain.

^b Consejo Superior de Investigaciones Científicas (CSIC), Spain

*Corresponding Author

E-mail: pedro.gomez@icn2.cat, Tel: +34 937373608, Fax: +34 936917640,
ICN2, Campus UAB, 08193 Bellaterra (Barcelona) Spain

ABSTRACT

MXene/polyoxometalates (POMs) hybrids are useful target materials for a variety of applications. Yet, the goal to prepare simple binary hybrids by intercalation of POMs into MXene has not been achieved. We propose and demonstrate here a method to intercalate POMs (phosphotungstate, PW12) into $Ti_3C_2T_x$ MXene through the interaction between POM anions and pre-intercalated surfactant cations. A variety of quaternary ammonium cations have been used to

expand $Ti_3C_2T_x$ interlayer spacing. Cetyltrimethylammonium cations (CTA^+) lead to an expansion of 2 nm while allowing to intercalate a considerable load (10 wt%) thanks to its tadpole-like shape and size. CTAPW12 has a layered structure compatible with $Ti_3C_2T_x$. The CTA^+ -delaminated $Ti_3C_2T_x$ keeps the large interlayer spacing after being coupled with PW12. The PW12 clusters are dispersed and kept isolated thanks to CTA surfactant and the confinement into $Ti_3C_2T_x$ layers. The redox reactions in CTA^+ -delaminated $Ti_3C_2T_x/PW12$ are diffusion-controlled, which proves the well-dispersed PW12 clusters are not adsorbed on the surface of $Ti_3C_2T_x$ particles but within $Ti_3C_2T_x$ layers. The CTA^+ -delaminated $Ti_3C_2T_x/PW12$ shows superior electrochemical stability (peak currents remain unchanged after 100 cycles) over the other MXene/POMs hybrids prepared in this work (20% peak currents remain after 20 cycles). We associate this improved stability to the effective intercalation of PW12 within $Ti_3C_2T_x$ layers helped by the CTA cations, as opposed to the external aggregation of PW12 clusters into micro or nanocrystals taking place for the other cations. The results provide a solid guide to help develop high-performance MXene/POMs hybrid materials for a variety of applications.

Introduction

Since the discovery of $Ti_3C_2T_x$ --the first MXene--in 2011 by Naguib et al.,¹ the MXene family is flourishing. More than 30 new MXenes have been synthesized.² MXenes have a general formula $M_{n+1}X_nT_x$, where M is a transition metal, X is carbon and/or nitrogen, n is an integer between 1 and 3, and T_x represents surface functional groups. Due to their two-dimensional structure, high conductivity, redox activity and hydrophilicity, MXenes have shown great

potential in various applications, including energy storage,³ electromagnetic interference,⁴ sensors,⁵ water remediation,⁶ photocatalysis,⁷ radio-frequency antennas,⁸ etc.

Beyond the compositional richness of these MXene formulations, their anionic charge and layered structure have prompted the development of a variety of hybrids derived from them.⁹⁻¹³

Polyoxometalates (POMs) are a class of metal-oxide clusters consisting of multiple metal-oxide octahedra linked together by oxygen atoms to form nanoclusters with ordered and well-know structures. Their intrinsic nanosize, high surface to bulk ratio and fast and reversible redox activity have launched them for applications in various fields, such as energy storage,^{14, 15} catalysis,¹⁶ sensors,¹⁷ etc.

MXenes and POMs share some target applications while featuring complementary properties and dimensionalities which could lead to synergies. For example, 2D MXenes could provide an electronically conducting matrix whereas 0D POMs could provide a pillaring effect opening the resulting structure and facilitating ion transport. Thus, POM-intercalated MXene hybrids seem interesting on their own right. And several laboratories have tried to synthesize this type of hybrids, although intercalation has proven to be elusive. Chen et al. anchored POMs on the surface of $Ti_3C_2T_x$ with (ionic liquid) linkers. Their hybrid material was shown to deliver high specific capacitance for a long term in an aqueous electrolyte.¹⁸ Chao et al. reported the *in-situ* growth of 10-20 nm Mo and Fe-based POM nanoparticles on $Ti_3C_2T_x$ nanosheets. Their hybrid material showed excellent pseudocapacitive performance in lithium-ion capacitors and sodium-ion capacitors.⁹ Zhou et al. embedded phosphomolybdic acid and $Ti_3C_2T_x$

in polypyrrole and built an impedimetric aptamer biosensor for osteopontin with extremely low detection limit, high selectivity and stability.¹⁰ MXene/POMs hybrid materials not only show great potential in conventional fields, but also expand their application. For instance, Zong et al. developed GdW₁₀-based polyoxometalates/ Ti₃C₂T_x composite for contrast-enhanced computed tomography and magnetic resonance imaging.¹¹ Therefore, it is a good idea to develop MXene/POMs hybrid materials both to strengthen their properties and performance through synergies in conventional application as well as to explore new fields and extend their use to new applications.

MXene/POM hybrid materials reported until now, either deposit crystallised POM nanoparticles on the MXene surface or anchor POM nanoclusters on the MXene surface with linkers. It might seem that POMs can only adhere onto the MXene surface and not get intercalated.

The LiF/HCl-etched Ti₃C₂T_x has an interlayer spacing of ca. 1.2 nm.¹⁹ Using large cations during the delamination process can lead to an expansion of this interlayer distance. For instance, tetramethylammonium (TMA) treated Ti₃C₂T_x has an interlayer distance of around 1.5 nm.¹⁹ With extended time, even larger cations can intercalate MXene, resulting in a larger interlayer distance. Up to now, various cations, including tetraethylammonium (TEA),²⁰ tetrabutylammonium (TBA),²¹ 1-ethyl-3-methylimidazolium (EMIM),²² dodecyltrimethylammonium (DTA),²³ cetyltrimethylammonium (CTA)²³ etc. been shown to intercalate MXene. The resulting interlayer distance can be as large as 2.7 nm. The Keggin POMs clusters are around 1 nm; Thus, the interlayer space is large enough to accommodate POMs. However, this goal has not been accomplished yet due to several reasons.

The first obstacle is the electrostatic repulsion. Since MXene monolayers are terminated with negative-charged functional groups (e.g. OH^- , F^- , Cl^-), only cations can easily enter the interlayers. Even with the assistance of an electric field, small anions (like Cl^- , Br^-) can hardly intercalate.²⁴ Not to mention the much larger POMs which are all polyanions. On the other hand, POM salts in which the negative charge of these anions is balanced by a suitable amount of counter-cations do not suffer electrostatic repulsion but tend to crystallize. The crystallized POM nanoparticles are too large to enter MXene interlayers and can only be adhered onto its surface. Furthermore, crystallization packs POM clusters into extended arrays preventing the direct interaction of each cluster with a suitable substrate or electrolyte, which is the key to their success as catalysts or energy storage electrodes, respectively.

On the other hand, most of the cations used to expand the interlayer distance of MXenes can interact with POMs. And the fact that anionic POMs can interact with organic and inorganic cations, can be used advantageously to control POM self-assembly, stabilization, solubility, and function.²⁵ For example, Tetraethylammonium phosphotungstate (TEAPW₁₂) has been shown to improve the capacitive performance in organic electrolytes, where the activity of most inorganic POMs is less than optimal.²⁶ CTA^+ , DTA^+ and TBA^+ can induce the reversible self-assembly of Wells-Dawson POMs ($\text{P}_2\text{W}_{17}\text{MnO}_{62}$) into 1D nanowires and 2D superlattices with excellent catalytic activity.²⁷ It would be fascinating to design and develop this kind of self-assembly reactions between POMs and cationic surfactants within the interlayer space of MXene.

We report here for the first time a method to intercalate POM clusters into MXene ($\text{Ti}_3\text{C}_2\text{T}_x$) layers by utilizing the interactions between POM anions and

organic cations pre-intercalated into $Ti_3C_2T_x$. Thus, a variety of quaternary ammonium cations were used to expand the interlayer spacing and then react with POMs. The cations capable of expanding the interlayer space substantially enough to form nano lamellar structures, were finally able to anchor isolated POMs clusters in between layers. This POM-intercalated MXene hybrid outperforms the hybrid materials based on POM nanoparticles/MXene mentioned above in electrochemical stability owing to the superior interlayer hybridization. This study shows a new strategy to design and synthesize MXene/POMs hybrid materials to meet the demands for better performance in conventional applications (catalysts, sensors, energy storage) as well as to enable new uncharted ones.

Experimental

Synthesis of MXene ($Ti_3C_2T_x$, MX)

$Ti_3C_2T_x$ was synthesized through a LiF/HCl etching method. Thus, 1 g Ti_3AlC_2 (MAX phase) was added slowly into a Teflon-vessel containing 1 g LiF and 20 mL 9 M HCl solution, kept stirring for 24 h at 35 °C. The mixture was poured into a 50 mL centrifugation tube, centrifuged at 3500 rpm for 5 minutes, then washed with Milli-Q water. This process was repeated until the pH of the dark-green supernatant was >6. Finally, the mixture was centrifuged at 6000 rpm for 20 minutes. The sediment was collected and used in the following dispersion.

0.1 g $Ti_3C_2T_x$ sediment was dispersed in 50 mL Milli-Q water (shaken by hand), deaerated with Ar for 20 minutes, stored in the fridge for future use. 20 mL of the

$\text{Ti}_3\text{C}_2\text{T}_x$ colloid was filtered on Celgard 3501 membrane, rinsed, dried in vacuum oven at 60 °C and stored in an argon-filled glovebox, labeled as MX.

Synthesis of quaternary ammonium cations delaminated MXene (TMAMX, TBAMX, DTAMX and CTAMX)

0.1 g $\text{Ti}_3\text{C}_2\text{T}_x$ sediment was dispersed in each of four 50 mL 0.5 M quaternary ammonium solutions (tetramethylammonium hydroxide (TMAOH), tetrabutylammonium hydroxide (TBAOH), dodecyltrimethylammonium bromide (DTAB) and cetyltrimethylammonium bromide (CTAB)) (shaken by hand), deaerated with Ar for 20 minutes. The four mixtures were shaken by hand twice every day for four days. Four kinds of cation-exchanged $\text{Ti}_3\text{C}_2\text{T}_x$ colloids were obtained. 20 mL of each colloid was filtered on Celgard 3501 membrane, rinsed and dried with Ar flow. The films can be easily peeled off from the membrane, dried in vacuum oven at 60 °C and stored in an argon-filled glovebox. As-prepared samples are labeled as TMAMX, TBAMX, DTAMX and CTAMX, respectively.

Synthesis of MXene/POMs hybrids (TMAMX-PW12, TBAMX-PW12, DTAMX-PW12 and CTAMX-PW12)

20 mL of each cation-exchanged $\text{Ti}_3\text{C}_2\text{T}_x$ colloid was filtered on Celgard 3501 membrane, rinsed repeatedly. Then 20 mL of 20 mM phosphotungstic acid (PW12) was added on the filter cake, filtered, rinsed, and dried with Ar flow. The films were carefully peeled off, dried in vacuum oven at 60 °C and stored in an argon-filled glovebox. As-prepared samples are named as TMAMX-PW12, TBAMX-PW12, DTAMX-PW12 and CTAMX-PW12.

Material characterization

Powder XRD patterns were collected on a PANalytical X'pert Pro-MRD diffractometer with Cu K α radiation and PIXel detector. Scanning electron microscopy images were taken on a Quante 650 FEG microscope. High-resolution transmission electron images (HR-TEM) and high angle annular dark field scanning transmission electron microscopy (HAADF-STEM) images were taken on a FEI Tecnai G2 F20 microscope.

Electrochemical characterization

All the electrochemical characterizations were done in T-type Swagelok cells, in which Ag/Ag⁺ and overloaded activated carbon served as the reference electrodes and counter electrodes, respectively. 1 M TEABF₄ in acetonitrile was used as the electrolyte. The electrochemical tests were carried out in an Argon-filled glove box with the oxygen and water levels under 5 ppm.

Results and discussion

We carried out thermogravimetric analyses (TGA) to estimate the amount of the quaternary ammonium cations in MXenes, as shown in Fig. 1. The pristine Ti₃C₂T_x (MX) suffers a slight weight loss (3.2%) before 500°C, corresponding to the removal of some surface functional groups, e.g., -F, -OH and -O.^{28, 29} All the quaternary ammonium cation-exchanged MXenes undergo relatively drastic weight losses when heating up to 450°C, followed by a plateau. The quaternary ammonium cations can be completely removed before 450°C in nitrogen atmosphere.³⁰ Thus, the extra weight loss of quaternary ammonium cation-

exchanged MXenes is associated with the removal of these organic compounds.²⁸ Among them, CTAMX presents the greatest amount of intercalated organic cation (10 wt%), and DTAMX has the smallest (3.8 wt%), as determined by comparison with the loss associated to pristine MXene. Since the quaternary ammonium cations will serve as the anchor sites in the reactions with PW12, we normalize the weight percentage by molecular weight and calculate the concentration of quaternary ammonium cation (mmol g^{-1}) to estimate their potential capabilities of anchoring POMs. TMAMX has the highest concentration (0.83 mmol g^{-1}) of quaternary ammonium cation among the four samples, more than twice that of TBAMX (0.35 mmol g^{-1}) and three times that of CTAMX (0.27 mmol g^{-1}). DTAMX has the lowest as well (0.12 mmol g^{-1}). The different concentrations will lead to different morphologies and different PW12 loading masses once they interact with PW12.

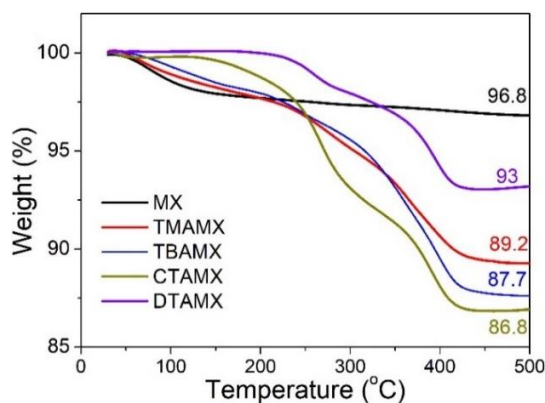


Fig. 1 Thermogravimetric curves of MX, TMAMX, TBAMX, DTAMX and CTAMX in nitrogen at a heating rate of 10 °C min^{-1} .

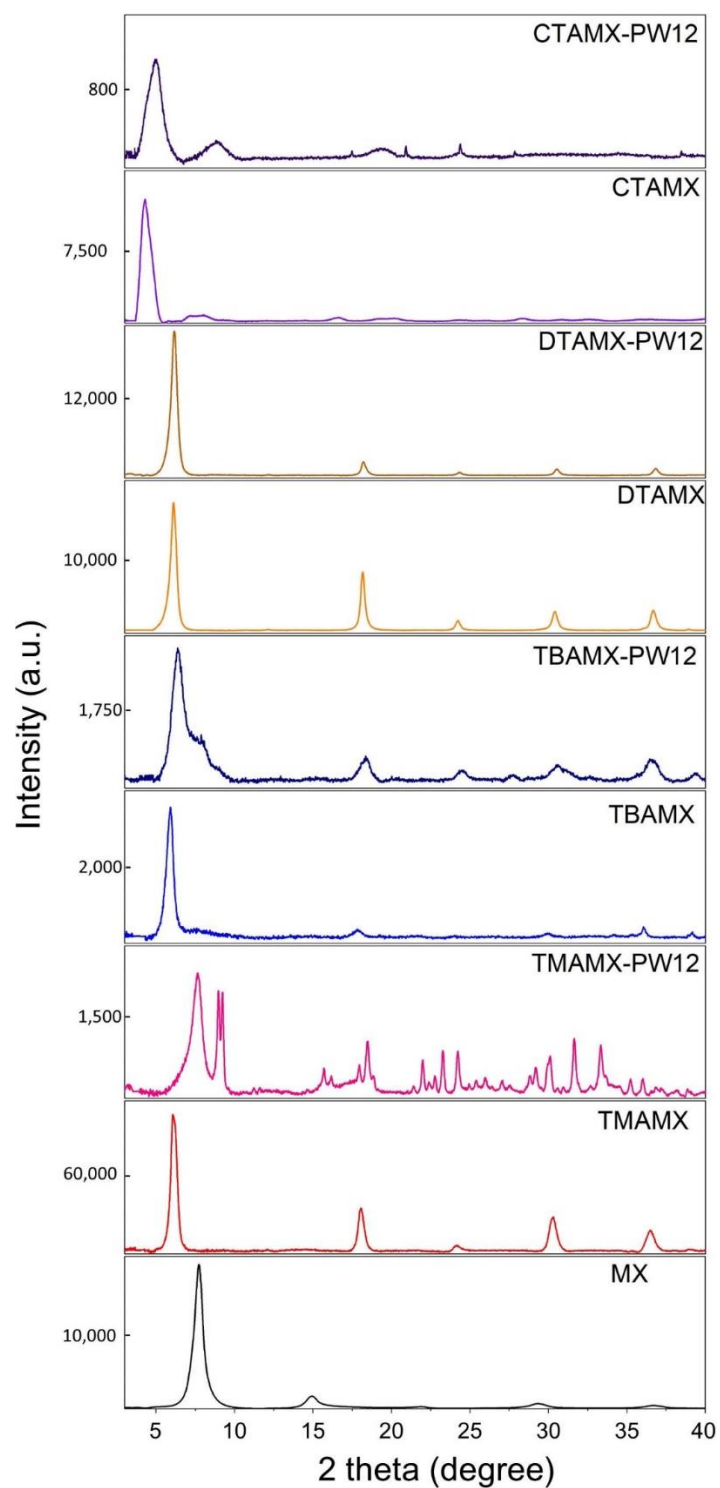


Fig. 2 XRD patterns of pristine MXene (MX), cations delaminated MXene (TMAMX, TBAMX, DTAMX, and CTAMX) and MXene/POMs hybrids (TMAMX-PW12, TBAMX-PW12, DTAMX-PW12, and CTAMX-PW12).

Table 1. Positions of (002) peaks and their corresponding interlayer spacings for pristine MXene, cation-exchanged MXene and MXene/POMs hybrids

	2 θ values for (002) diffraction peaks/ $^{\circ}$	Interlayer distance/ \AA
MX	7.76	11.39
TMAMX	6.08	14.53
TMAMX-PW12	7.62	11.58
TBAMX	5.90	14.95
TBAMX-PW12	6.38	13.84
DTAMX	6.10	14.48
DTAMX-PW12	6.16	14.34
CTAMX	4.26	20.70
CTAMX-PW12	4.96	17.80

We carried out powder XRD to characterize the crystal structure of the solid phases, as shown in Fig. 2. Table 1 presents the positions of (002) diffraction peaks and the interlayer distance. We can observe a significant expansion of the interlayer distance associated to large cations (TMA^+ , TBA^+ , DTA^+ and CTA^+) taking the place of Li^+ . Pristine $\text{Ti}_3\text{C}_2\text{T}_x$ (MX) has the (002) diffraction peak at 7.76° , corresponding to an interlayer distance of 11.39 \AA . TMA^+ and TBA^+ expand the interlayer distances to 14.53 \AA and 14.95 \AA , respectively. The degree of expansion agrees well with the size of the cations: TMA^+ has four methyl groups while TBA^+ has four butyls. Yet, both of them are isotropic.

In the expansion of the interlayer spacing we can distinguish two cases: isotropic and markedly anisotropic cations.

Thus, considering the shape of cations, TMA⁺ and TBA⁺ are spherical, while DTA⁺ and CTA⁺ are tadpole-like. The former only have one way to get intercalated whereas the latter can suffer certain degree of conformational variation. This could explain the relatively similar spacings of TBA and DTA intercalates. On the other hand, when we compare the cases of the two anisotropic cations we find the same trend. DTA⁺ and CTA⁺ both have three methyl groups and a long aliphatic chain. The tail of CTA⁺ (hexadecyl) is longer than DTA⁺ (dodecyl), leading to a larger interlayer distance (20.70 Å). It becomes more difficult for larger spherical quaternary ammonium cations to insert into the layers.¹⁹ Our TGA results also agree with that. Increasing spherical quaternary ammonium cation size can only expand interlayer space slightly since fewer cations get intercalated. By contrast, tadpole-like quaternary ammonium cations can easily insert the layers even with a long tail. Some studies have confirmed that the interlayer space gets expanded remarkably with the increase of tail length.^{28, 31} Indeed, the interlayer distance of CTAMX is 20.70 Å, larger than DTAMX (14.48 Å). It is the largest interlayer distance among all the samples.

After being coupled with PW12 clusters, the MXene/POMs hybrids show shrunk interlayer distance. The shrinkage of interlayer space must be associated with the extraction of cations during the reaction with PW12 and following washing procedure. Among all the MXene/POMs hybrids, only TMAMX-PW12 exhibits extra diffraction peaks. They match well with the XRD patterns of TMAPW12 (Fig. S1). It confirms that the pre-intercalated quaternary ammonium cations can fasten PW12 anions to form organic PW12 compounds. By contrast, the rest MXene/POMs hybrids do not show distinct extra peaks from POMs. It does not mean the absence of organic PW12 compounds. TMAMX has the

highest cation concentration, anchoring more PW12 clusters and forming big enough PW12 crystals to present diffraction patterns. The rest MXene/POMs hybrids do not present characteristic diffraction patterns from POMs. Several reasons can explain it: low loading mass, nanocrystals, intrinsic poor crystallinity nature (Fig. S1). Meanwhile, the interlayer distance of TMAMX-PW12 shrinks most significantly (from 14.53 Å to 11.58 Å), close to pristine MXene (11.39 Å), indicating that most of the TMA⁺ have been extracted. TBAMX-PW12 and DTAMX-PW12 only show a slight shrinkage of the interlayer distance. CTAMX-PW12 show a visible decrease in the interlayer space, but after that, its interlayer distance (17.80 Å) is still larger than the rest.

Electron microscopy and affiliated energy-dispersive X-ray spectroscopy can provide evidence to prove the existence as well as distribution of PW12 clusters. Fig. 3 presents the SEM images of the MXene/POMs hybrids. In TMAMX-PW12 (Fig. 3a), we can discern many tiny particles corresponding to TMAPW12, spread everywhere: among Ti₃C₂T_x flakes and on the surface. By contrast, in TBAMX-PW12 (Fig. 3b), DTAMX-PW12 (Fig. 3c) and CTAMX-PW12 (Fig. 3d), we can hardly discern any such particles. The existence of small particles and nanosheets can explain why the XRD pattern of TMAMX-PW12 is a combination of both TMAPW12 and Ti₃C₂T_x diffraction patterns. Due to the high concentration of TMA⁺ in TMAMX and most of TMA⁺ were extracted out when reacting with PW12, TMAPW12 have aggregated into micron-sized particles outside the Ti₃C₂T_x layers. The absence of such particles in the other MXene/POMs hybrids confirms that PW12 clusters have not been accumulated into extended (therefore diffracting) microcrystals. But this does not mean that PW12 clusters are not attached to MXene. EDX analyses can verify this.

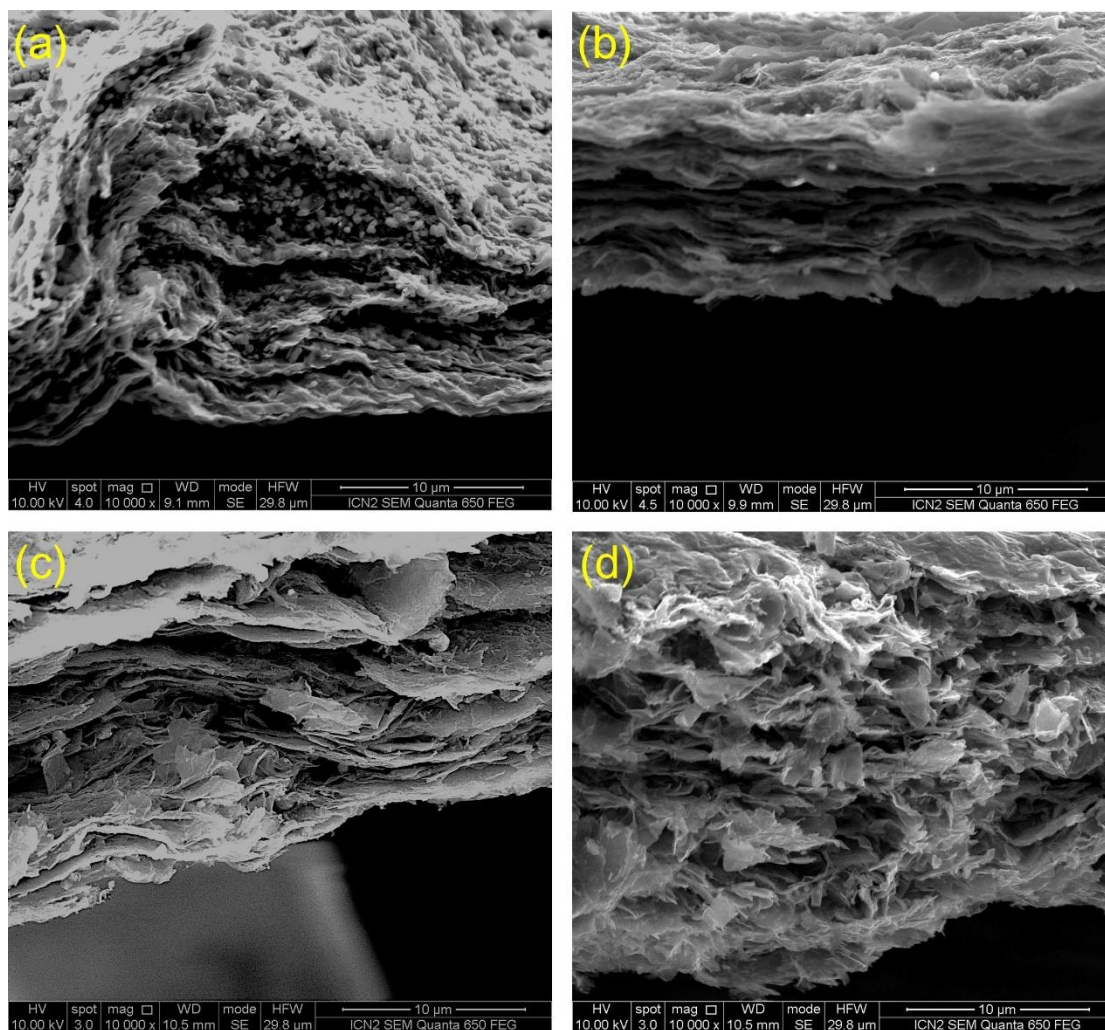


Fig. 3 SEM images of (a) TMAMX-PW12, (b) TBAMX-PW12, (c) DTAMX-PW12 and (d) CTAMX-PW12.

Table 2 lists the titanium and tungsten concentration of the MXene/POMs hybrids derived from EDX analysis. TMAMX-PW12 has the largest and DTAMX-PW12 has the smallest amount of W among the MXene/POMs hybrids. It agrees well with our expectation: the concentration of the intercalated quaternary ammonium cations affects the capability to fasten PW12 clusters. A considerable amount of W can be discerned in the TBAMX-PW12 and CTAMX-PW12, confirming the effective anchoring of PW12 clusters. In principle, such concentration of a constituent is high enough to present diffraction patterns if well-

crystallized. The absence of POMs diffraction patterns in TBAMX-PW12, DTAMX-PW12 and CTAMX-PW12 is related to poor crystallinity, such as nanocrystals and disorder in a long-range.

Table 2. EDX semi-quantitative analysis results

	W wt%	Ti wt%
TMAMX-PW12	27.31	28.93
TBAMX-PW12	15.93	53.50
DTAMX-PW12	7.540	55.77
CTAMX-PW12	19.01	41.45

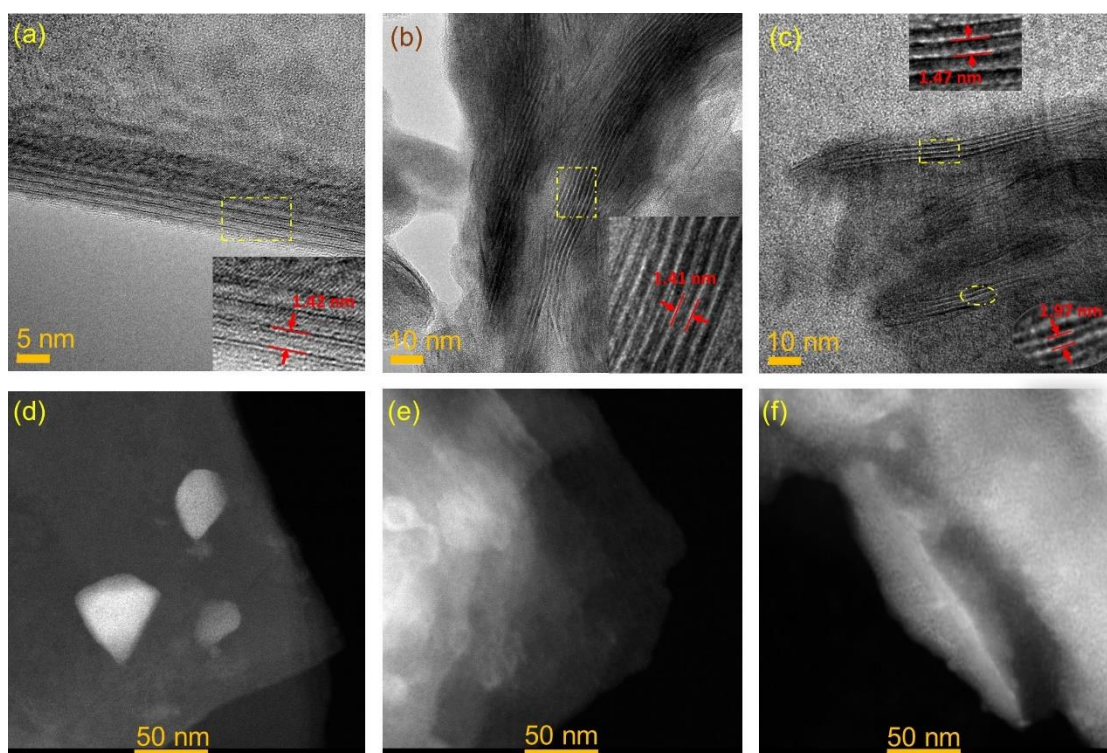


Fig. 4 HR-TEM images of (a) TBAMX-PW12, (b) DTAMX-PW12 and (c) CTAMX-PW12 (the inset images are zoom-in areas for observing interlayer distance). HAADF-STEM images of (d) TBAMX-PW12, (e) DTAMX-PW12 and (f) CTAMX-PW12.

To further investigate the distribution state of PW12 clusters in the MXene/POMs hybrids that we cannot discern in SEM, we characterize them in HR-TEM and HAADF-STEM, as presented in Fig. 4.

All the HR-TEM images feature a layered structure. We can estimate the interlayer distance through the zoom-in HR-TEM images. TBAMX-PW12 shows an interlayer distance of 1.42 nm (Fig. 4a inset), and DTAMX-PW12 shows an interlayer distance of 1.41 nm (Fig. 4b inset). Both of them agree well with the interlayer distance derived from the XRD patterns. However, in CTAMX-PW12 HR-TEM images, we can discern different interlayer distances (1.47 nm and 1.97 nm in Fig. 4c inset), which are either larger or smaller than the interlayer distance (1.78 nm) from XRD. We speculate that the two interlayer distances correspond to two intercalation.

The smaller interlayer distance corresponds to $Ti_3C_2T_x$ layers where a few CTA^+ are extracted, and no PW12 clusters get in, leading to an interlayer distance close to TBAMX-PW12 and DTAMX-PW12. The larger interlayer distance corresponds to $Ti_3C_2T_x$ layers with most CTA^+ remaining and PW12 clusters intercalating, reacting with these CTA^+ .

HAADF-STEM can provide Z-contrast imaging, in which W would be more visible. TBAMX-PW12 (Fig. 4d) show the $Ti_3C_2T_x$ nanosheets clearly, on which several small bright particles (<50 nm) are attached. These particles are TBAPW12 nanocrystals. Since the particles are much larger than the interlayer distance, they are impossible to insert within $Ti_3C_2T_x$ layers. DTAMX-PW12 (Fig. 4e) shows a similar morphology. We can discern the thin, semi-transparent $Ti_3C_2T_x$ nanosheets with the bright particles of 20 nm spreading. DTAPW12 must have aggregated outside of the $Ti_3C_2T_x$ layers too. CTAMX-PW12 (Fig. 4f)

exhibits a different morphology. Numerous tiny bright dots spread everywhere. The EDX spectrum in such an area reveals the coexistence of Ti and W, confirming it is hybridized (Fig. S2a-c). Meanwhile, these observed areas are still semi-transparent, meaning that they are still very thin. PW12 clusters do not form a continuous, dense aggregation; instead, a thin homogeneous discontinuous distribution.

The PW12 clusters are around 1 nm. If we only consider the size, the interlayer space around 1.4 nm can accommodate the PW12 clusters. However, TMAMX, TBAMX and DTAMX all fail to do that because of electrostatic repulsion among anions.²⁴ As a result, the organic PW12 compounds have to aggregate outside the layers. CTAMX with a larger interlayer space has a higher tolerance against electrostatic repulsion and the possibility to accommodate PW12 clusters. Since CTA⁺ is a surfactant, it can prevent POMs cluster from aggregation. In some cases, CTA⁺ even rearrange POMs clusters into isolated clusters.²⁷ Moreover, several studies have proven that CTA⁺ can interact with Keggin-POMs by self-assembly, and even electrostatic layer-by-layer self-assembly, resulting in well-ordered lamellar phases.³²⁻³⁴ The SEM image (Fig. S2d) confirms CTAPW12 layers-stacking morphology. We cannot rule out the possibility of the partial crystallization of CTAPW12. However, even CTAPW12 has formed single layer short-range orderly lamellas, the layers still can accommodate them thanks to their structural compatibility.

The observed isolated bright dots (PW12 clusters) have two possible locations: on the surface of Ti₃C₂T_x nanosheets; beneath the thin Ti₃C₂T_x layers. We speculate PW12 clusters are mostly beneath the Ti₃C₂T_x layers, because Ti₃C₂T_x layers can confine the growth of PW12 clusters, avoid forming thick

aggregates. Electrochemical characterization, capable of distinguishing whether the associated redox reactions are diffusion-controlled or surfacecapacitive, can help prove this hypothesis.

Dunn et al. have proposed a method to distinguish whether charge storage processes are diffusion-controlled or surface capacitive by carrying out CVs at various scan rates.³⁵ The dependence of the current response on the scan rate can provide insights into the charge-storage mechanism according to Eq1

$$i = av^b \quad \text{Eq1}$$

where i is the maximum peak current obtained at a specific scan rate v , and a and b are adjustable parameters. The current linear dependence on scan rate ($b = 1$) usually means charge is stored by a fast response mechanism, such as surface capacitive. If the current response follows a linear dependence on the square root of the scan rate ($b = 0.5$), it is a diffusion-controlled process. We can determine the b value by linear fitting the straight line of $\log i$ vs $\log v$, in which the slope is the b value.

Herein, we performed CVs from 1 mV s⁻¹ to 50 mV s⁻¹ on three MXene/POMs hybrids: TMAMX-PW12 (MXene with micro POMs aggregates), TBAMX-PW12 (MXene with nano POMs aggregates) and CTAMX-PW12 (MXene with homogeneously distributed POMs clusters), as shown in Figs. 5a, 5d and 5g. The electrochemical behaviors of the crystalized PW12 electrode are also characterized and presented in Fig. S4. Comparing the CVs of pristine Ti₃C₂T_x (Fig. S3a), PW12(Fig. S4a) and those of MXene/POMs hybrid materials (Fig. 5), we can classify the redox peaks in the MXene/POMs hybrid materials into two types: the peaks totally derived from PW12, corresponding to Re1-Re3 and Ox1 to Ox3; the overlapped peak contributed from PW12 and Ti₃C₂T_x corresponding

to the reduction peak at -1.8 V. The pairing of redox peaks is accomplished through carrying out CVs in various narrow potential range, as shown in Fig. S5. Re1 and Ox1 are a redox pair. Ox2 actually is an overlap of two oxidation peaks, pairing with Re2 and Re3. The Ox3 is associated with the reduction peak buried in the cation-intercalation peak of $Ti_3C_2T_x$ (at -1.8 V).

The energy storage mechanisms of pristine $Ti_3C_2T_x$ and crystallized PW12 are studied (Figs. S3 and S4). For pristine $Ti_3C_2T_x$, only the reduction peak, corresponding to the cation-intercalation, is in part diffusion-controlled ($b=0.75$). The rest rectangle shape mainly corresponds to surface capacitive process ($b=0.92$). For crystallized PW12, the redox pairs show various diffusion-controlled percentage. The Re1 and Ox1 redox pair, which presents the sharpest peaks, is mostly diffusion-controlled ($b = 0.6$). While the other peaks, especially the broad peaks, are less diffusion-controlled or even almost surface capacitive ($b = 1$ for Re2). This reveals the nature of the multi-step redox reaction of crystallized PW12 in the organic electrolyte: the first step are more diffusion-controlled.

We performed linear fit on the redox peaks of the three MXene/POMs hybrids, as shown in Figs. 5 (b-c), (e-f) and (h-l). The figures confirm the good fitting. The fitting results are listed in Table 3. The b-values of TMAMX-PW12 are close to 0.5, indicating the redox reactions are almost 100% diffusion-controlled. It is not surprising with such large crystallized POMs particles.³⁶ The b-values of TBAMX-PW12 increase. Several studies have pointed out that the energy storage mechanism shifts from diffusion-controlled to surface capacitive with decreasing particle size.³⁷ TMAMX-PW12 has PW12 microcrystals while TBAMX-PW12 has PW12 nanocrystals. The redox reaction in TBAMX-PW12 becomes less diffusion-controlled since PW12 crystals are smaller.

CTAMX-PW12 does not present larger b-values even though PW12 clusters dispersed homogeneously in nanoscale. It is quite surprising at first glance, because in other studies (such as activated carbon/POMs,^{26, 38} reduced graphene oxide/POMs,³⁹ polypyrrole hydrogel wrapped CNT/POMs,⁴⁰ metal-organic framework/POMs⁴¹⁻⁴³) where the POMs clusters are nano-dispersed (bright dots detected in HAADF-STEM), the b-values are close to 1, revealing that the redox reactions of the nano-dispersed PW12 clusters are surface capacitive. The electrochemical behaviours of CTAMX-PW12 seem to be contrary to these other studies. However, this is an evidence to prove those nano-dispersed PW12 clusters have intercalated in $Ti_3C_2T_x$ layers, not just spreaded on the $Ti_3C_2T_x$ surface. In the other nano-dispersed PW12 hybrid materials, the PW12 clusters are anchored on the surface of the substrates. Most of the active sites on PW12 are exposed to the electrolyte directly. Their redox reactions are surface capacitive. In the case of CTAMX-PW12, the PW12 clusters are dispersed homogeneously within $Ti_3C_2T_x$ layers where they are surrounded by large cationic surfactant molecules. The ions of the electrolyte have to diffuse along the slit between $Ti_3C_2T_x$ layers to reach the PW12 clusters, restricting the redox reactions under diffusion-controlled. Fig. 5(j) illustrates the fabrication process of the POMs intercalated MXene.

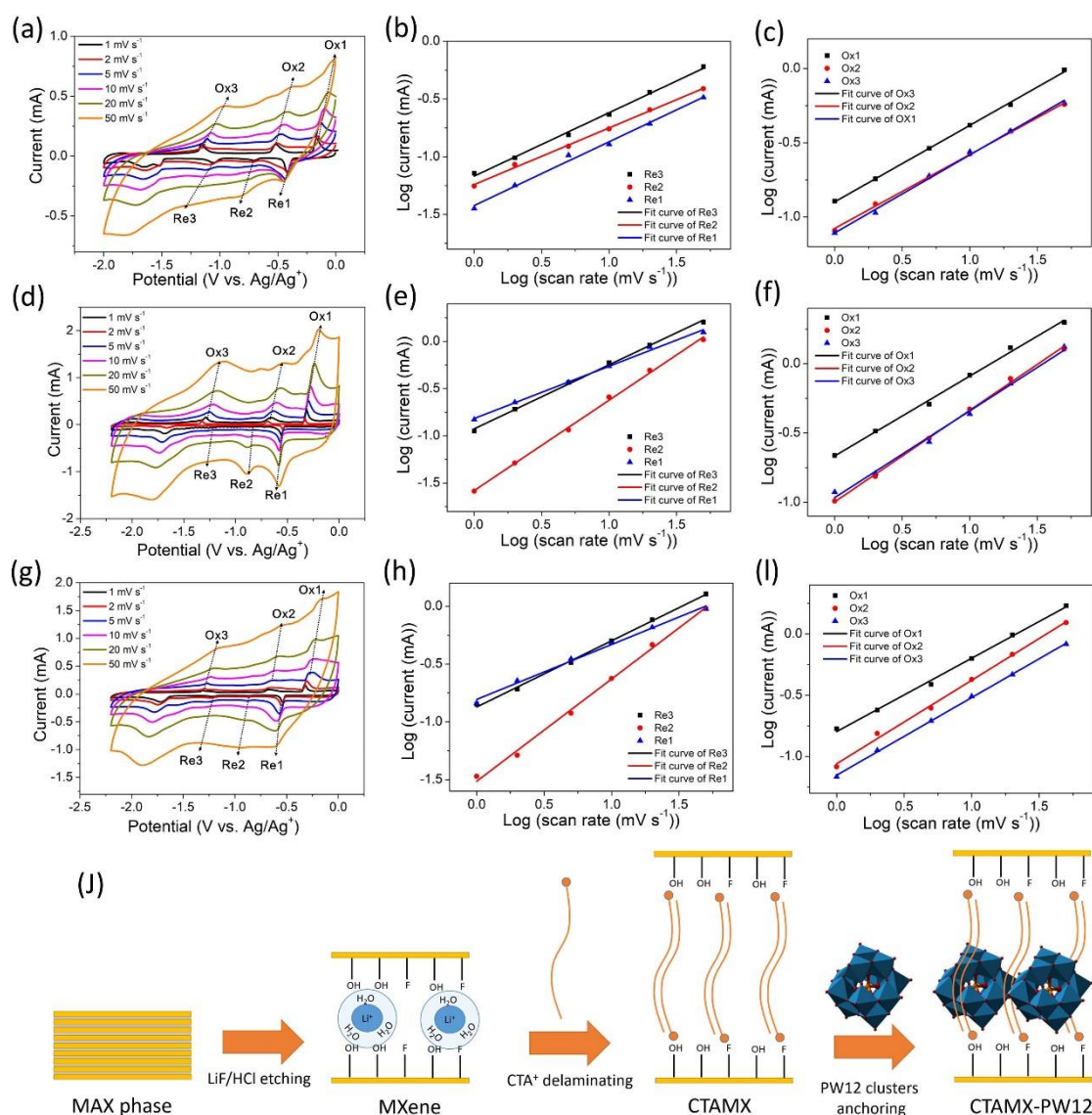


Fig. 5 CVs of (a) TMAMX-PW12 (d) TBAMX-PW12 and (g) CTAMX-PW12. Linear fitting of log currents versus log scan rates plots to determine b-values of reduction peaks and oxidation peaks: (b) and (c) for TMAMX-PW12; (e) and (f) for TBAMX-PW12; (h) and (i) for CTAMX-PW12. (j) Schematic illustration of the fabrication of POMs-intercalated MXene (CTAMX-PW12).

Table 3. b-values derived from fitting current of reduction peaks (Re) and oxidation peaks (Ox) at various scan rates.

	Ox1	Ox2	Ox3	Re1	Re2	Re3
TMAMX- PW12	0.51	0.50	0.52	0.54	0.50	0.55
TBAMX- PW12	0.66	0.57	0.62	0.55	0.96	0.67
CTAMX- PW12	0.58	0.66	0.63	0.51	0.88	0.57

Furthermore, we study the electrochemical stability to check if the PW12 clusters can be attached on $\text{Ti}_3\text{C}_2\text{T}_x$, keep redox active for long term. Actually, the pristine crystallized PW12 electrode undergoes severe redox activity loss upon cycling (Fig. S4). Some studies applying pristine POMs electrodes have reported the same phenomenon.⁴⁴ Therefore, most efforts have been made on developing POMs-based hybrid materials, whose nano-dispersion improve the cycling stability.

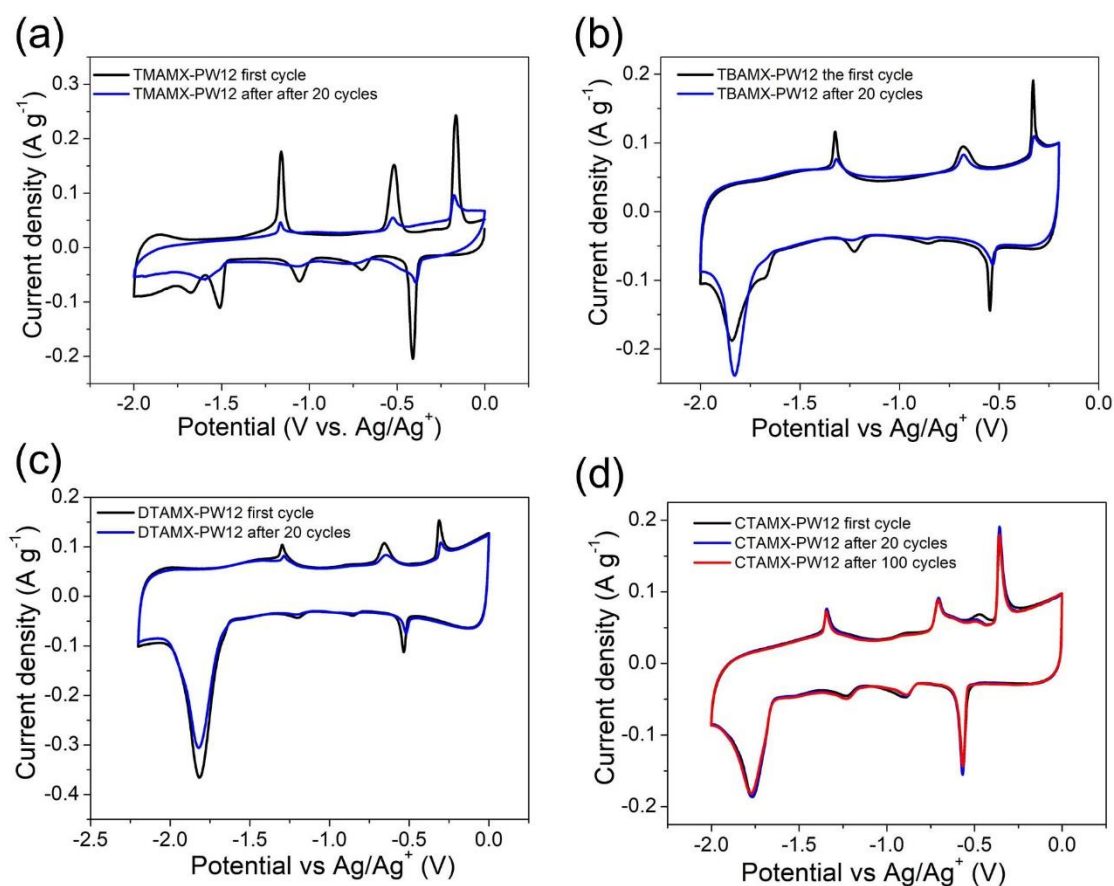


Fig. 6 CVs of (a) TMAMX-PW12, (b) TBAMX-PW12, (c) DTAMX-PW12 and (d) CTAMX-PW12 before and after a few cycles at 2 mV s^{-1} .

Fig. 6 presents CVs of MXene/POMs hybrids before and after the indicated number of cycles. Comparing the CVs before and after cycling, TMAMX-PW12 shows the most remarkable difference. All the peak currents drop dramatically. For instance, only 20% of the initial peak current of Ox1 remains after 20 cycles. In order to establish the reason for this decay we run EDX analyses of the electrode after cycling and found a very substantial decrease of W in the sample (Fig. S6 and Table S2). Thus, the most likely conclusion is that POMs are detached upon cycling. This, in turn, means that PW12 in the form of microcrystals attached onto $\text{Ti}_3\text{C}_2\text{T}_x$ nanosheets cannot stand cycling.

The situations for TBAMX-PW12 and DTAMX-PW12 are better than TMAMX-PW12, but still not good enough. TBAMX-PW12 maintains 21% of the initial peak current of Ox1 after 20 cycles, and DTAMX-PW12 has 35 % left. By analogy we can conclude that also PW12 nanocrystals are lost upon cycling in the organic electrolyte. Meanwhile, the quasi-rectangles derived from $Ti_3C_2T_x$ almost keep their initial shape, indicating the good stability of $Ti_3C_2T_x$ in the organic electrolyte. The cation-intercalation peaks (at around -1.8 V) sharpen after cycling, which must be associated to the activation process. In pristine $Ti_3C_2T_x$, this cation-intercalation peak is less intense than for TBA or DTA-intercalated MXenes. This suggests enhanced cation-intercalation processes associated to the larger interlayer spacing provided by pre-intercalated TBA and DTA cations. Indeed, MXenes pre-intercalated with organic cations have been reported to accommodate more cations from the electrolytes, resulting in increased capacities.^{23, 31, 45}

Unlike the other three MXene/POMs hybrid materials, the CVs of CTAMX-PW12 after 20 cycles almost overlaps the first one. Even after 100 cycles, the peak current of Ox1 is still 104% of the first cycle, revealing its excellent electrochemical stability. The difference between CTAMX-PW12 and the other MXene/POMs hybrids must be related to microstructure. This excellent electrochemical stability is usually found in well-dispersed and well-anchored POMs-based hybrid materials, such as activated carbon/POMs,²⁶ graphene/POMs³⁹ and metal-organic framework/POMs.⁴⁶ TMAMX-PW12, TBAMX-PW12 and DTAMX-PW12 behave like pristine crystallized PW12 electrode because the PW12 clusters have crystallized into micro or nanoparticles outside MXene layers. The micro or nanoparticles are attached to or surrounded by multilayer $Ti_3C_2T_x$ flakes. $Ti_3C_2T_x$ serves as both an active

component and the conductive substrate for PW12 anchoring. The conductivity within the PW12 particles is still poor.

On the contrary, in the case of CTAMX-PW12, PW12 clusters are nano-dispersed, rigidly intercalated within $Ti_3C_2T_x$ layers. Every PW12 cluster has direct access to the conductive $Ti_3C_2T_x$ substrate. And, last but not least, an EDX analysis of the electrode after 100 cycles showed only a minor loss of W in the sample, as compared with TMAPW12 (Fig. S6 and Tabs S2), all of which contribute to explain the cycling stability. Therefore, CTAMX-PW12 does not suffer the same detachment problem as crystallized PW12 does.

Conclusion

In summary, we successfully prepared a POM-intercalated MXene through the reaction between PW12 anions and the pre-intercalated CTA cations. Some small cations (TMA^+) can intercalate into $Ti_3C_2T_x$ layers easily, but their expansion of the interlayer spacing is not enough to accommodate PW12 anions. CTA^+ delaminated $Ti_3C_2T_x$ (CTAMX) works well thanks to its shape and interlayer spacing (2 nm). The XRD pattern confirms that POM-intercalated MXene (CTAMX-PW12) still keeps a relatively large interlayer distance (1.7 nm). HAADF-STEM shows the PW12 clusters spread homogeneously. The electrochemical analyses prove that the redox reactions of PW12 are still diffusion-controlled in CTAMX-PW12. Combining the information provided by XRD patterns, HR-TEM images, HAADF-STEM images, and electrochemical characterization, we can reach the following conclusion: Assisted by CTAB cations, PW12 clusters can be intercalated and spread homogeneously at the nanoscale within $Ti_3C_2T_x$ layers. Contrary to other POMs/MXene hybrids tested in this work, The CTAB-dispersed-

POMs intercalated MXene can be reversibly and sustainably cycled in a three-electrode cell, showing a superior performance compared to the other crystallized POM-MXene hybrids.

Thus, our work has shown how to intercalate and stabilize POMs within MXene, keeping the electroactivity of both in a synergic combination which could be used to harness the electrochemical activity of POMs in a variety of applications.

Acknowledgements

Partial funding from Ministerio de Ciencia Innovacion y Universidades (MCIU), the Agencia Estatal de Investigacion (AEI) and the European Regional Development Fund (FEDER) (grant RTI2018-099826-B-I00) is gratefully acknowledged. ICN2 is funded by the CERCA programme / Generalitat de Catalunya, and also supported by the Severo Ochoa Centres of Excellence programme, funded by the Spanish Research Agency (AEI, grant no. SEV-2017-0706). J.J Z. acknowledges his scholarship (No. 201806370211) under China Scholarship Council. This work has been carried out within the framework of doctoral program (PhD) of Material Science (Department of Physics) of Universitat Autònoma de Barcelona (UAB).

REFERENCES

1. M. Naguib, M. Kurtoglu, V. Presser, J. Lu, J. Niu, M. Heon, L. Hultman, Y. Gogotsi and M. W. Barsoum, *Adv. Mater.*, 2011, **23**, 4248-4253.
2. L. Verger, C. Xu, V. Natu, H.-M. Cheng, W. Ren and M. W. Barsoum, *Current Opinion in Solid State and Materials Science*, 2019, **23**, 149-163.
3. M. R. Lukatskaya, O. Mashtalir, C. E. Ren, Y. Dall'Agnese, P. Rozier, P. L. Taberna, M. Naguib, P. Simon, M. W. Barsoum and Y. Gogotsi, *Science*, 2013, **341**, 1502-1505.
4. F. Shahzad, M. Alhabeb, C. B. Hatter, B. Anasori, S. M. Hong, C. M. Koo and Y. Gogotsi, *Science*, 2016, **353**, 1137-1140.
5. S. J. Kim, H. J. Koh, C. E. Ren, O. Kwon, K. Maleski, S. Y. Cho, B. Anasori, C. K. Kim, Y. K. Choi, J. Kim, Y. Gogotsi and H. T. Jung, *ACS Nano*, 2018, **12**, 986-993.
6. K. Rasool, R. P. Pandey, P. A. Rasheed, S. Buczek, Y. Gogotsi and K. A. Mahmoud, *Materials Today*, 2019, **30**, 80-102.
7. P. Kuang, J. Low, B. Cheng, J. Yu and J. Fan, *Journal of Materials Science & Technology*, 2020, **56**, 18-44.
8. A. Sarycheva, A. Polemi, Y. Liu, K. Dandekar, B. Anasori and Y. Gogotsi, *Science Advances*, 2018, **4**, eaau0920.
9. H. Chao, H. Qin, M. Zhang, Y. Huang, L. Cao, H. Guo, K. Wang, X. Teng, J. Cheng, Y. Lu, H. Hu and M. Wu, *Adv. Funct. Mater.*, 2021, **31**, 2007636.
10. S. Zhou, C. Gu, Z. Li, L. Yang, L. He, M. Wang, X. Huang, N. Zhou and Z. Zhang, *Appl. Surf. Sci.*, 2019, **498**.
11. L. Zong, H. Wu, H. Lin and Y. Chen, *Nano Research*, 2018, **11**, 4149-4168.
12. J. Miao, Z. Lang, X. Zhang, W. Kong, O. Peng, Y. Yang, S. Wang, J. Cheng, T. He, A. Amini, Q. Wu, Z. Zheng, Z. Tang and C. Cheng, *Adv. Funct. Mater.*, 2018, DOI: 10.1002/adfm.201805893.
13. X. Yang, Q. Wang, K. Zhu, K. Ye, G. Wang, D. Cao and J. Yan, *Adv. Funct. Mater.*, 2021, **31**, 2101087.
14. M. R. Horn, A. Singh, S. Alomari, S. Goberna-Ferrón, R. Benages-Vilau, N. Chodankar, N. Motta, K. Ostrikov, J. MacLeod, P. Sonar, P. Gomez-Romero and D. Dubal, *Energy & Environmental Science*, 2021, **14**, 1652-1700.
15. M. Genovese and K. Lian, *J. Mater. Chem. A*, 2017, **5**, 3939-3947.
16. T. Kitano, K. Masuda, P. Xu and S. Kobayashi, *Chem Rev*, 2018, **118**, 679-746.
17. M. Sánchez, A. González, L. Sabio, W. Zou, R. Ramanathan, V. Bansal and J. M. Domínguez-Vera, *Materials Today Chemistry*, 2021, **21**, 100491.
18. S. Chen, Y. F. Xiang, M. K. Banks, C. Peng, W. J. Xu and R. X. Wu, *Nanoscale*, 2018, **10**, 20043-20052.
19. M. Alhabeb, K. Maleski, B. Anasori, P. Lelyukh, L. Clark, S. Sin and Y. Gogotsi, *Chem. Mater.*, 2017, **29**, 7633-7644.
20. Y. Dall'Agnese, P. Rozier, P.-L. Taberna, Y. Gogotsi and P. Simon, *J. Power Sources*, 2016, **306**, 510-515.
21. J. L. Hart, K. Hantanasirisakul, A. C. Lang, B. Anasori, D. Pinto, Y. Pivak, J. T. van Omme, S. J. May, Y. Gogotsi and M. L. Taheri, *Nat. Commun.*, 2019, **10**, 522.
22. S. Zheng, C. J. Zhang, F. Zhou, Y. Dong, X. Shi, V. Nicolosi, Z.-S. Wu and X. Bao, *J. Mater. Chem. A*, 2019, **7**, 9478-9485.
23. J. Luo, W. Zhang, H. Yuan, C. Jin, L. Zhang, H. Huang, C. Liang, Y. Xia, J. Zhang, Y. Gan and X. Tao, *ACS Nano*, 2017, **11**, 2459-2469.
24. N. Shpigel, A. Chakraborty, F. Malchik, G. Bergman, A. Nimkar, B. Gavriel, M. Turgeman, C. N. Hong, M. R. Lukatskaya, M. D. Levi, Y. Gogotsi, D. T. Major and D. Aurbach, *J. Am. Chem. Soc.*, 2021, **143**, 12552-12559.
25. A. Misra, K. Kozma, C. Streb and M. Nyman, *Angew. Chem. Int. Ed. Engl.*, 2020, **59**, 596-612.
26. J.-J. Zhu, R. Benages-Vilau and P. Gomez-Romero, *Electrochim. Acta*, 2020, **362**, 137007.
27. Q. Liu, H. Yu, Q. Zhang, D. Wang and X. Wang, *Adv. Funct. Mater.*, 2021, **31**.
28. J. Y. Si, B. Tawiah, W. L. Sun, B. Lin, C. Wang, A. C. Y. Yuen, B. Yu, A. Li, W. Yang, H. D. Lu, Q. N. Chan and G. H. Yeoh, *Polymers (Basel)*, 2019, **11**.
29. R. Liu and W. Li, *ACS Omega*, 2018, **3**, 2609-2617.
30. G. Sui, Y. Zhao, Q. Zhang and Q. Fu, *RSC Advances*, 2016, **6**, 54785-54792.

31. K. Liang, R. A. Matsumoto, W. Zhao, N. C. Osti, I. Popov, B. P. Thapaliya, S. Fleischmann, S. Misra, K. Prenger, M. Tyagi, E. Mamontov, V. Augustyn, R. R. Unocic, A. P. Sokolov, S. Dai, P. T. Cummings and M. Naguib, *Adv. Funct. Mater.*, 2021, **31**.
32. S. Liu, D. Volkmer and D. G. Kurth, *J. Cluster Sci.*, 2003, **14**, 405-419.
33. M. Nyman, D. Ingersoll, S. Singh, F. Bonhomme, T. M. Alam, C. J. Brinker and M. A. Rodriguez, *Chem. Mater.*, 2005, **17**, 2885-2895.
34. M. Nyman, M. A. Rodriguez, T. M. Anderson and D. Ingersoll, *Cryst. Growth Des.*, 2009, **9**, 3590-3597.
35. J. Wang, J. Polleux, J. Lim and B. Dunn, *The Journal of Physical Chemistry C*, 2007, **111**, 14925-14931.
36. S.-C. Huang, C.-C. Lin, C.-W. Hu, Y.-F. Liao, T.-Y. Chen and H.-Y. Chen, *J. Power Sources*, 2019, **435**, 226702.
37. Y. L. Shao, M. F. El-Kady, J. Y. Sun, Y. G. Li, Q. H. Zhang, M. F. Zhu, H. Z. Wang, B. Dunn and R. B. Kaner, *Chem. Rev.*, 2018, **118**, 9233-9280.
38. J.-J. Zhu, L. Martinez-Soria and P. Gomez-Romero, *Nanomaterials*, 2022, **12**.
39. D. P. Dubal, J. Suarez-Guevara, D. Tonti, E. Enciso and P. Gomez-Romero, *J. Mater. Chem. A*, 2015, **3**, 23483-23492.
40. M. Wang, Y. Zhang, T. Zhang, Y. Li, M. Cui, X. Cao, Y. Lu, D. Peng, W. Liu, X. Liu, T. Wang and Y. Huang, *Nanoscale*, 2020, DOI: 10.1039/d0nr01070g.
41. D. F. Chai, Y. Hou, K. P. O'Halloran, H. J. Pang, H. Y. Ma, G. N. Wang and X. M. Wang, *Chemelectrochem*, 2018, **5**, 3443-3450.
42. G. Wang, T. Chen, S. Li, H. Pang and H. Ma, *Dalton Trans.*, 2017, **46**, 13897-13902.
43. N. N. Du, L. G. Gong, L. Y. Fan, K. Yu, H. Luo, S. J. Pang, J. Q. Gao, Z. W. Zheng, J. H. Lv and B. B. Zhou, *Acs Applied Nano Materials*, 2019, **2**, 3039-3049.
44. H. Wang, S. Hamanaka, Y. Nishimoto, S. Irle, T. Yokoyama, H. Yoshikawa and K. Awaga, *Journal of the American Chemical Society*, 2012, **134**, 4918-4924.
45. M. Xu, S. Lei, J. Qi, Q. Dou, L. Liu, Y. Lu, Q. Huang, S. Shi and X. Yan, *ACS Nano*, 2018, **12**, 3733-3740.
46. Y. D. Zhang, B. P. Lin, J. C. Wang, P. Han, T. Xu, Y. Sun, X. Q. Zhang and H. Yang, *Electrochim. Acta*, 2016, **191**, 795-804.

Electronic Supplementary Material

Polyoxometalate Intercalated MXene with Enhanced Electrochemical Stability

Jun-Jie Zhu^a and Pedro Gomez-Romero^{a,b,*}

^a Catalan Institute of Nanoscience and Nanotechnology (ICN2), CSIC and BIST, Campus UAB, Bellaterra, 08193 Barcelona, Spain.

^b Consejo Superior de Investigaciones Científicas (CSIC), Spain

*Author to whom correspondence should be addressed

E-mail address: pedro.gomez@icn2.cat, Tel: +34 937373608, Fax: +34 936917640, ICN2, Campus UAB, 08193 Bellaterra (Barcelona) Spain

Synthesis of quaternary ammonium phosphotungstate derivatives

10 mL of each 30 mM quaternary ammonium (tetramethylammonium hydroxide (TMAOH), tetraethylammonium hydroxide (TEAOH), tetrabutylammonium hydroxide (TBAOH), dodecyltrimethylammonium bromide (DTAB) and cetrimonium bromide (CTAB)) solution was added in to 10 mL of 10 mM phosphotungstic acid drop by drop, stirred for 1 h, filtered and dried in vacuum oven at 120 for 6 h. Five types of the quaternary ammonium phosphotungstate salts (TMAPW12, TEAPW12, TBAPW12, DTAPW12 and CTAPW12) were collected.

Preparation of the pristine PW12 electrode

TEAPW12 powders, carbon superP and PVDF were mixed at a weight ratio of 70:20:10 in a mortar, grinded. A few drops of 1-Methyl-2-pyrrolidone were added into the mixture to form a slurry, coated on aluminum foil, dried at 120°C under vacuum.

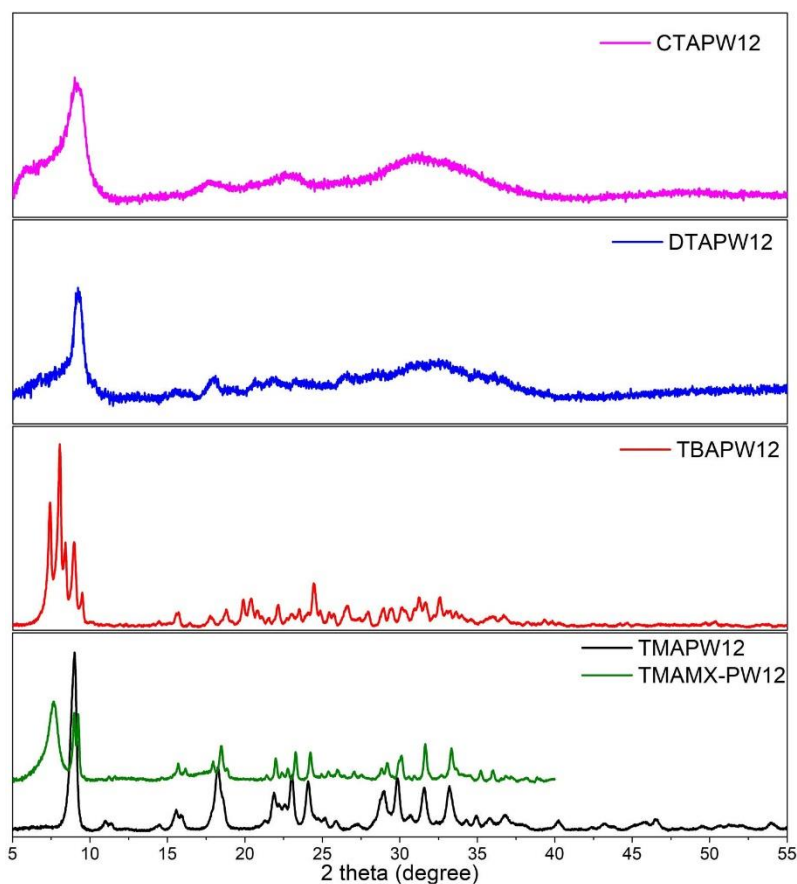


Figure S1. XRD patterns of pristine TMAPW12 (compared with TMAMX-PW12), TBAPW12, DTAPW12 and CTAPW12

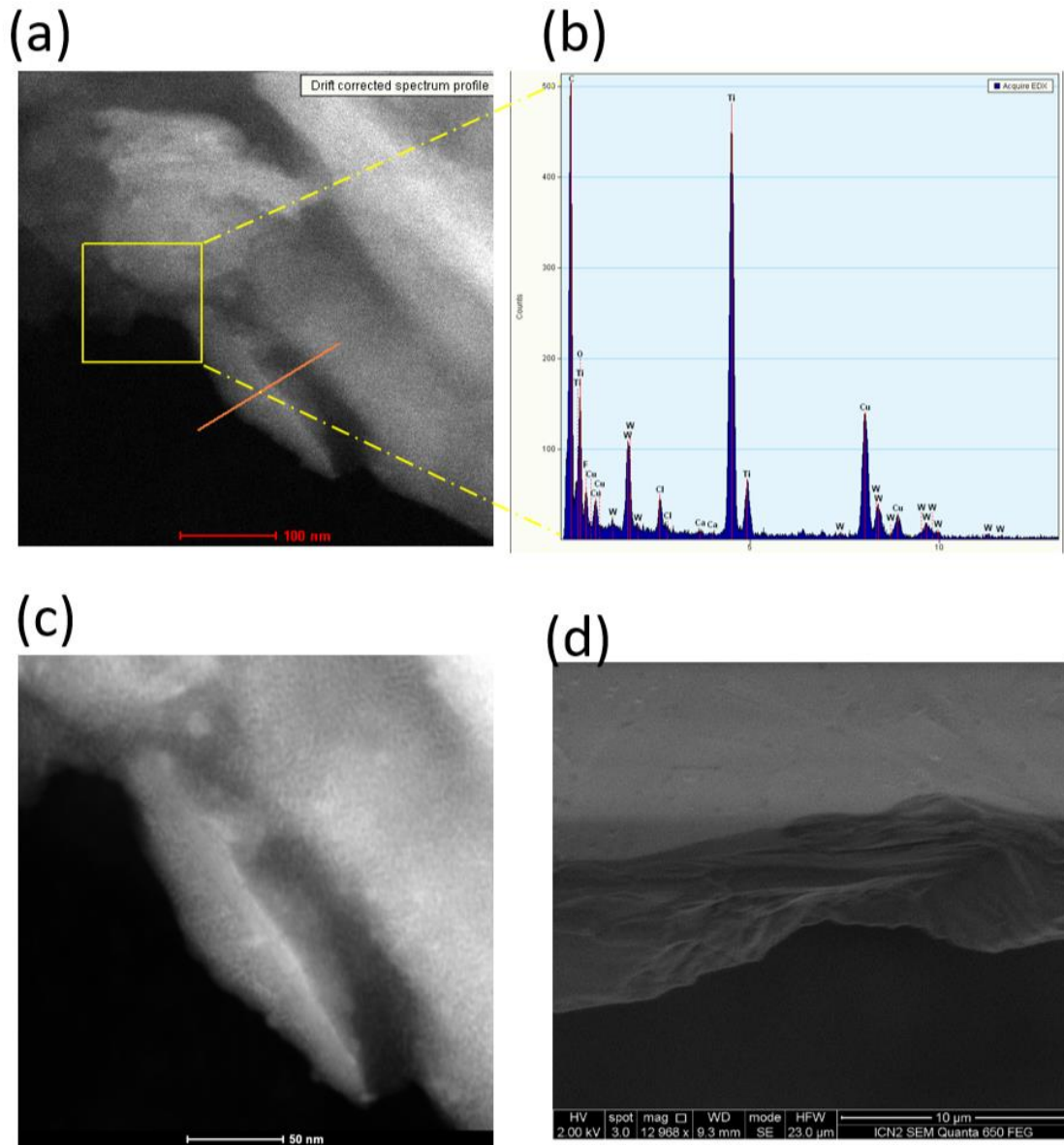


Figure S2. (a)The hybridized area and its (d) corresponding EDX spectrum in CTAPW12. (c)STEM images of the hybridized area. (d) SEM image of CTAPW12

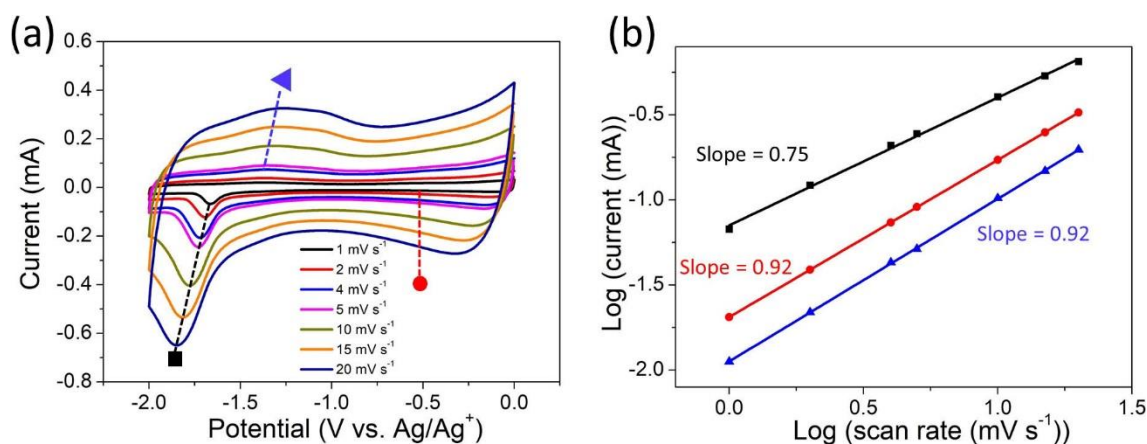


Figure S3. (a) CVs of $\text{Ti}_3\text{C}_2\text{T}_x$ in 1 M TEABF₄ in acetonitrile at various scan rates. (b) Linear fitting of log current versus log scan rate plot to determine b values (slopes) at the peaks (black and blue) or background rectangle (red).

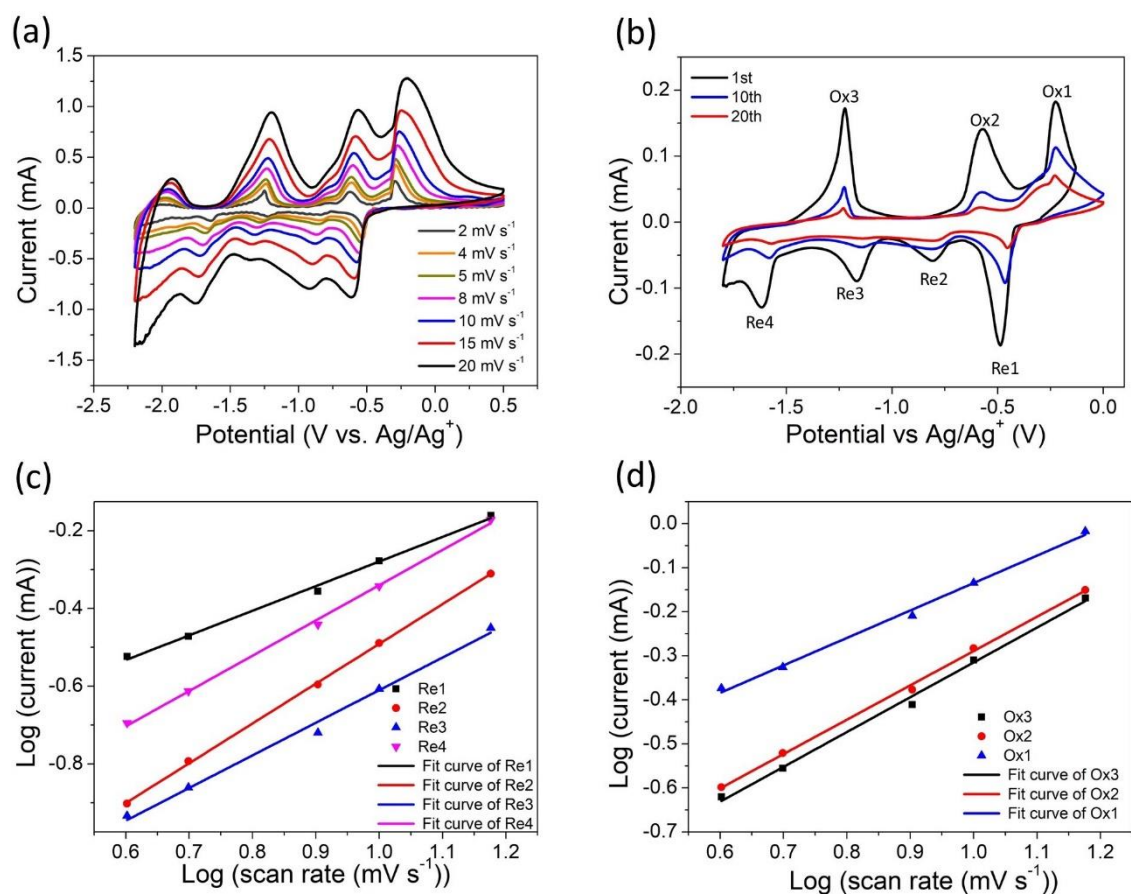


Figure S4. (a) CVs of the pristine PW12 solid electrode at various scan rates in 1 M TEABF₄ acetonitrile. (b) CVs of the pristine PW12 solid electrode at 2 mV s⁻¹

s^{-1} at the first, 10th and 20th cycles. Linear fitting of log current versus log scan rate plot to determine the b value of (c) reduction peaks and (d) oxidation peaks of PW12 electrode.

Table S1. b-values of the redox peaks of the pristine PW12 solid electrode.

	Re	Re	Re	Re	Re	Ox	Ox	Ox
	1	2	3	4	1	2	3	
crystalliz	0.6	1.0	0.8	0.9	0.6	0.7	0.7	
ed PW12	3	2	4	1	2	8	9	

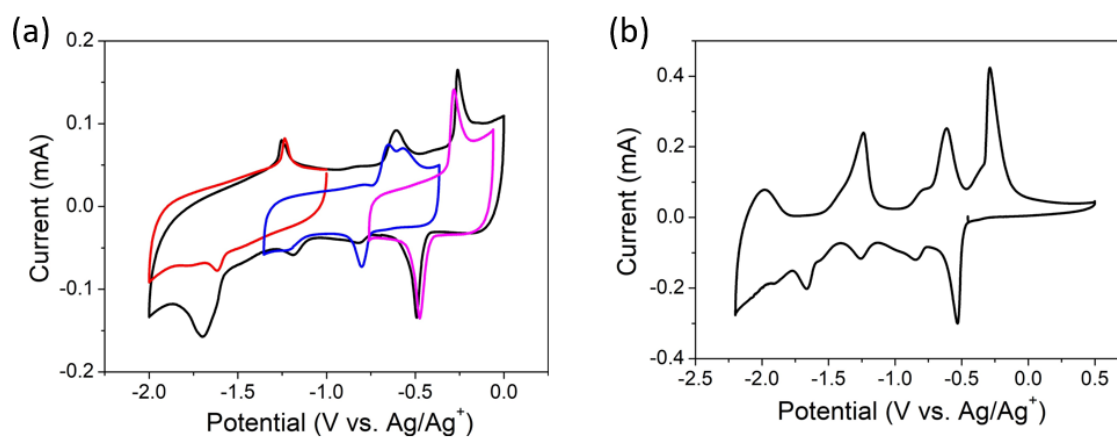


Figure S5. (a) CVs of CTAMX-PW12 at various potential range at 2 mV s^{-1} . (b) CV of pristine solid PW12 electrode (with PVDF binder and carbon black conducting additive) 2 mV s^{-1} .

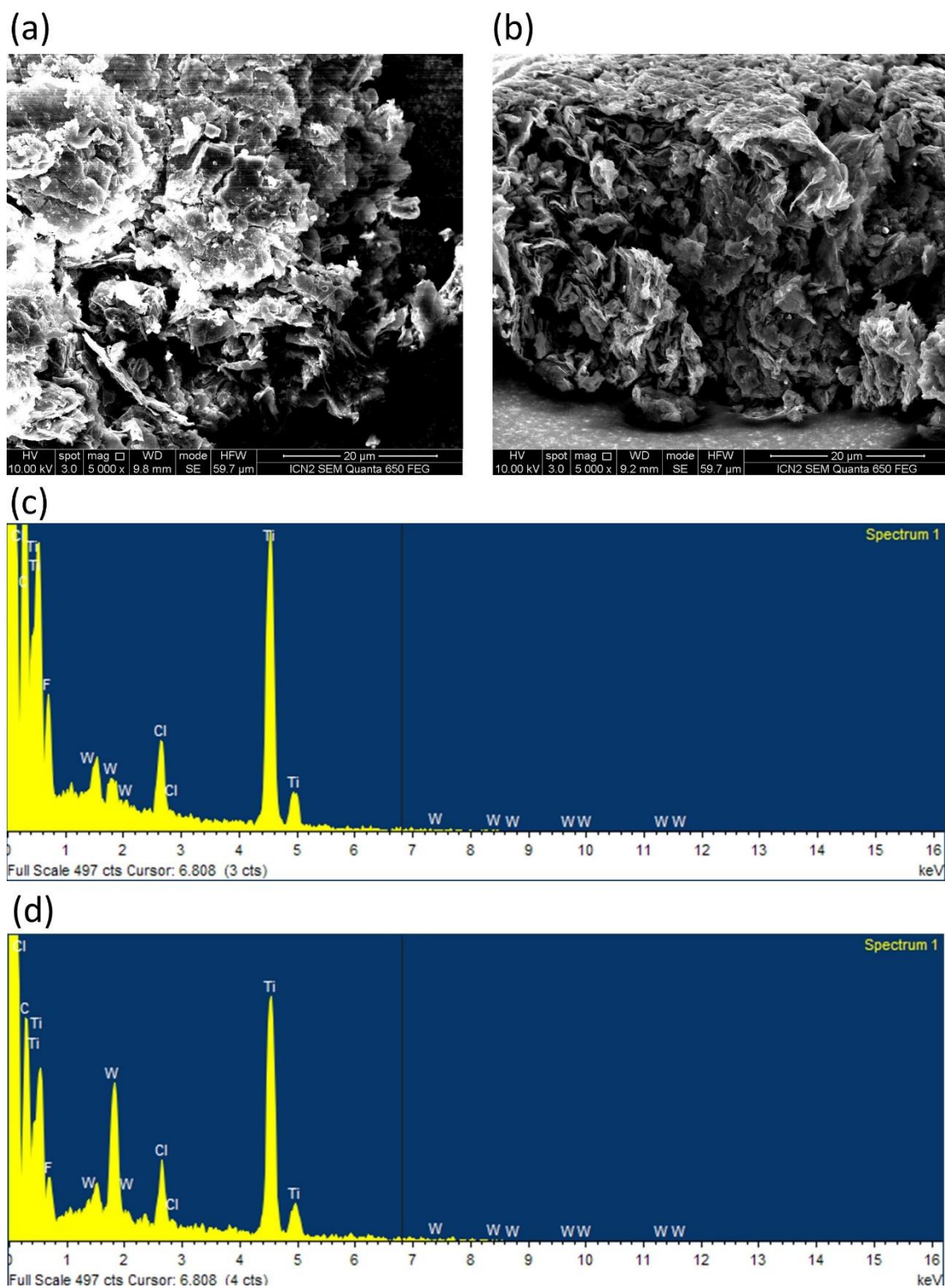


Figure S6. SEM images of cycled (a) TMAMX-PW12 (20 cycles) and (b) CTAMX-PW12 (100 cycles) electrodes. The corresponding EDX spectra of cycled (c) TMAMX-PW12 and (d) CTAMX-PW12.

Table S2. EDX semi-quantitative analysis results of cycled TMAMX-PW12 and CTAMX-PW12

	W wt%	Ti wt%
TMAMX-PW12	3.14	44.00
CTAMX-PW12	12.88	39.11

4.4 Capacitive performance of the POMs intercalated MXene

The research article described a method to synthesize hybrid materials with POMs truly intercalated into MXene and with enhanced electrochemical stability in the organic electrolyte. The capacitive performance of the POMs-intercalated MXene and the pristine MXene is compared in Fig. 4.1. The POMs intercalated MXene does not show a substantial improvement concerning capacitance performance. MXene/POM hybrid has slightly higher volumetric capacitance, but lower gravimetric capacitance. This is not surprising since both of the parent materials, POMs and MXene (and even more so for the W-containing POM) deliver high volumetric capacitance but low gravimetric capacitance. Thus, the combination of the two components does not lead to a synergy effect.

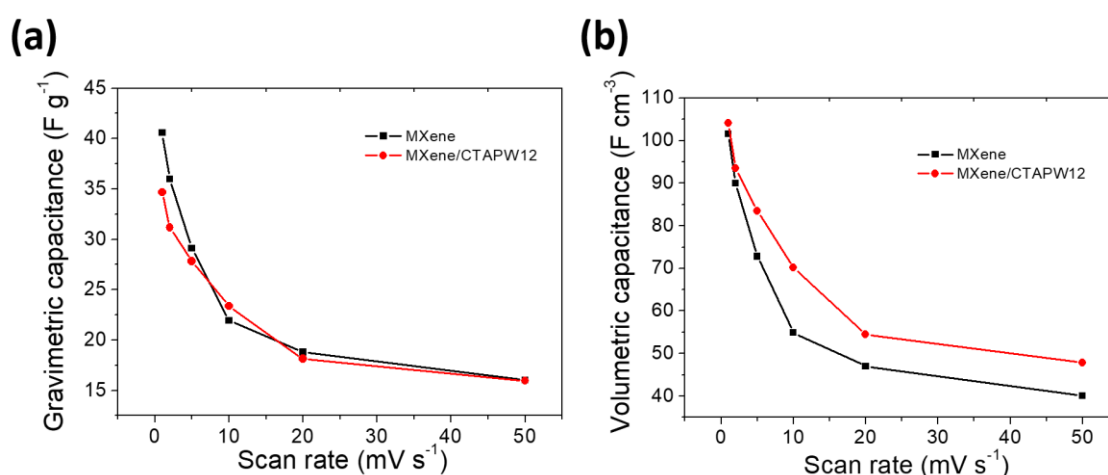


Fig. 4.1 (a) Gravimetric and (b) volumetric capacitance of MXene and MXene/CTAPW12 in 1 M TEABF₄ in acetonitrile at various scan rates.

4.5 Conclusion

This chapter presents two methods to synthesize MXene/POMs (Ti₃C₂T_x/PW12) hybrid materials: sonication-assisted dispersion and pre-

intercalated cations assisted growth. Unlike rGO which can anchor a large amount of POMs through simple adsorption with bath-sonication, MXene can only anchor very little POMs (< 1 at%). With the assistance of pre-intercalated cations, more POMs grew on MXene, but along with other problems. If the interlayer spacing is not expanded enough, the POMs aggregate outside of the MXene layers. This integration is unstable. POMs lose their redox activities during cycling.

With the large pre-intercalated cations (CTA⁺), POMs clusters can successfully be intercalated and immobilize within MXene layers. The POMs are also well-dispersed thanks to the surfactant cations. This MXene/POMs hybrid material maintain the redox activities after cycling in the organic electrolyte, revealing the superiority of this intercalated POMs/MXene structure. However, even though it has good cycle stability, its capacitance does not get substantially improved, because POMs and in particular PW12 feature the same characteristics as MXene: high volumetric capacitance and low gravimetric capacitance. Moreover, the redox reaction of these MXene/POM hybrid materials is diffusion-controlled, not well-suited to the fast-rate performance of supercapacitors. In order to develop MXene/POMs hybrid materials for high-performance organic-electrolyte supercapacitors, we need another solution: a truly synergic effect.

References to main text

- [1] M. Hu, R. Cheng, Z. Li, T. Hu, H. Zhang, C. Shi, J. Yang, C. Cui, C. Zhang, H. Wang, *Nanoscale*, 12 (2020) 763-771.
- [2] H. Chao, H. Qin, M. Zhang, Y. Huang, L. Cao, H. Guo, K. Wang, X. Teng, J. Cheng, Y. Lu, H. Hu, M. Wu, *Advanced Functional Materials*, (2021).
- [3] S. Zhou, C. Gu, Z. Li, L. Yang, L. He, M. Wang, X. Huang, N. Zhou, Z. Zhang, *Appl. Surf. Sci.*, 498 (2019).
- [4] L. Zong, H. Wu, H. Lin, Y. Chen, *Nano Research*, 11 (2018) 4149-4168.

Chapter 5 MXene/AC/POM triple hybrid materials

5.1 Context

The work reported in the previous chapter allowed us to show that the direct intercalation of POMs into MXenes is not straightforward. Even when it is accomplished, it cannot endow MXenes with new merits because both MXene and POMs feature high volumetric capacitance and relatively low gravimetric capacitance. Activated carbon is a microporous 3D framework, providing sites for POMs anchoring and promoting porous structure formation by hindering MXene restacking. The two binary hybrid materials: AC/POM and MXene/POM have already shown their unique characteristics compared to their parent materials[1, 2]. This chapter will present a rational design strategy to combine the merits of MXene, AC and POM in a single ternary hybrid electrode material for organic-electrolyte supercapacitors.

5.2 Rational Design of MXene/Activated Carbon/Polyoxometalate Triple Hybrid Electrodes with Enhanced Capacitance for Organic-Electrolyte Supercapacitors (Article 3)

<https://doi.org/10.1016/j.jcis.2022.04.170>



Contents lists available at ScienceDirect

Journal of Colloid and Interface Science

journal homepage: www.elsevier.com/locate/jcis

Rational design of MXene/activated carbon/polyoxometalate triple hybrid electrodes with enhanced capacitance for organic-electrolyte supercapacitors



Jun-Jie Zhu^{a,*}, Avireddy Hemesh^b, Jordi Jacas Biendicho^b, Luis Martinez-Soria^a, Daniel Rueda-Garcia^a, Joan Ramon Morante^{b,c}, Belen Ballesteros^a, Pedro Gomez-Romero^{a,d,*}

^a Catalan Institute of Nanoscience and Nanotechnology (ICN2), CSIC and BIST, Campus UAB, Bellaterra, 08193 Barcelona, Spain

^b Catalonia Institute for Energy Research (IREC), Jardins de les Dones de Negre 1, 08930, Sant Adrià de Besòs, Spain

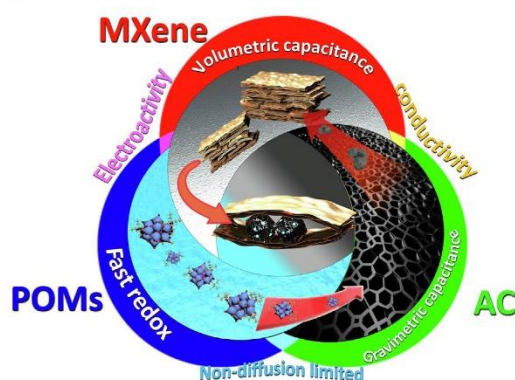
^c Faculty of Physics, University of Barcelona, Barcelona, Spain

^d Consejo Superior de Investigaciones Científicas (CSIC), Spain

HIGHLIGHTS

- POMs were nano-dispersed within MXene with assistance of AC matrix.
- The hybrid combined the merits and compensate for the demerits of each component.
- Gravimetric capacitance of the hybrid was 2.2 times that of MXene.
- POMs remained anchored in the long-term leading to great cycle stability.
- Hybrid's asymmetric cells outperformed AC/MXene cells by weight and volume.

GRAPHICAL ABSTRACT



ARTICLE INFO

Article history:

Received 13 January 2022

Revised 26 April 2022

Accepted 28 April 2022

Available online 5 May 2022

Keywords:

Hybrid electroactive materials

MXene

Polyoxometalates

Organic

Supercapacitors

ABSTRACT

We report a triple hybrid electrode (MXene/activated carbon (AC)/polyoxometalates (POMs)) combining the merits of three materials: MXene (high volumetric capacitance), AC (high gravimetric capacitance) and Phosphotungstate (fast redox). Phosphotungstic acid (HPW12) and tetraethylammonium phosphotungstate (TEAPW12) were the two POMs used to prepare MXene/AC/POMs triple hybrids. MXene/AC/TEAPW12 outperformed MXene/AC/HPW12 in 1 M tetraethylammonium tetrafluoroborate (TEABF₄)/acetonitrile. Nano-dispersion of POMs facilitates charge storage through surface capacitive processes (91% at 2 mV s⁻¹). MXene/AC/TEAPW12 delivered significantly higher gravimetric capacitance (87F g⁻¹ at 1 mV s⁻¹) than MXene (40F g⁻¹ at 1 mV s⁻¹) in the same organic electrolyte, without sacrificing much volumetric capacitance (less than 10%). The gravimetric capacitance of the triple hybrid was similar to that of MXene/AC, whereas its volumetric capacitance was 1.5 times higher. Replacing TEA cations with 1-ethyl-3-methylimidazolium cations (EMIM⁺), the capacitance improved by 21%. Coupled with AC positive electrodes in an asymmetric cell, MXene/AC/TEAPW12 delivered 4.6 times higher gravimetric energy density and 3.5 times higher volumetric energy density than a similar MXene asymmetric cell

* Corresponding authors at: ICN2, Campus UAB, 08193 Bellaterra (Barcelona), Spain.

E-mail addresses: zhu.junjie@icn2.cat (J.-J. Zhu), pedro.gomez@icn2.cat (P. Gomez-Romero).

<https://doi.org/10.1016/j.jcis.2022.04.170>

0021-9797/© 2022 The Author(s). Published by Elsevier Inc.

This is an open access article under the CC BY-NC-ND license (<http://creativecommons.org/licenses/by-nc-nd/4.0/>).

at relatively high-power densities. This study proves that MXene/AC/TEAPW12 combines the merits and compensates for the demerits of each component and is a promising electrode material for organic-electrolyte supercapacitors.

© 2022 The Author(s). Published by Elsevier Inc. This is an open access article under the CC BY-NC-ND license (<http://creativecommons.org/licenses/by-nc-nd/4.0/>).

1. Introduction

Energy storage devices with high energy density, power density and long lifespan are in urgent demand for a growing number of applications. Supercapacitors are a good starting point for this challenge since they feature intrinsically high power density and long cycle life. However, they run short of energy density. There are two main ways to increase the energy density of supercapacitors: i) increasing working voltage through the use of organic electrolytes, and ii) increasing storage capacity by a proper choice of electrode materials or through hybridization[1]. In this study, we followed both approaches based on the design of complex but unique hybrid materials leading to an optimal combination of charge storage capacity and high conductivity together with the high voltage range typical of organic electrolytes.

We first needed a material with a very high volumetric capacitance, and MXenes excel in this respect as they constitute a family of two-dimensional materials, usually containing one layer of transition metal and one layer of carbide. MXenes have a general formula $M_{n+1}X_nT_x$, where M is a transition metal, X is carbon and/or nitrogen, n is an integer between 1 and 3, and T_x represents surface functional groups[2]. A conductive inner transition metal carbide layer enables fast electron supply to electrochemically active sites, which makes of MXenes promising electrode materials for supercapacitors[3].

MXenes stand out from their competitors because of the high volumetric capacitance[4–6], the key parameter for the industry when compactness is required. In this scenario, titanium carbides ($Ti_3C_2T_x$) is the most widely studied and developed MXene, which has been found to deliver a volumetric capacitance as high as $900F\text{ cm}^{-3}$ in an aqueous electrolyte[3].

Conventional aqueous electrolytes allow for a stable potential window of less than 1.5 V. Since energy density is proportional to the square of the voltage, other electrolytes like “water-in-salt” electrolytes (with $V = 2.2\text{ V}$)[7], organic electrolytes (with $V = 2.7\text{ V}$)[8] or ionic liquids (with $V > 3\text{ V}$)[9,10] have been preferred for a rational optimized design. Indeed, several groups have already attempted to use MXene in organic electrolytes. Some examples include MXenes for lithium-ion capacitors [11,12], sodium-ion capacitors [13], or just supercapacitors with conventional organic electrolytes[8,13–15]. Some experimental drawbacks have already been described in these types of applications. For example, contrary to the previous hypothesis, $Ti_3C_2T_x$ MXene provides much lower specific capacitance in conventional organic electrolytes (less than 40 F g^{-1} or 70 F cm^{-3} in 1 M TEABF4 in acetonitrile[16]) than in aqueous electrolytes. Various approaches have been followed to enhance the energy storage capabilities of MXenes, including expanding interlayer distance by other nano-materials or functional groups[5,17–22], increasing active sites by making porous MXenes[23,24], or trying to introduce active materials[25–31], including polyoxometalates (POMs)[19,32]. However, these attempts have failed to intercalate POMs into MXenes and have led to mixed phases instead[32].

POMs constitute a family of nanometric metal oxide clusters, able to provide fast reversible multi-electron redox reactions not limited by diffusion[33–35]. As such, POMs have been used as active materials, just by themselves[35,36] or as active components in hybrid materials[33,35,37–41] in many kinds of energy

storage devices. In these devices, their proper dispersion at the nanoscale and long-term anchoring onto a conducting substrate are key issues for fully harnessing the fast reversible multi-electron redox activity characteristic of POMs. Several porous materials, such as activated carbon[39,41,42], and 2D materials, for example, reduced graphene oxide (rGO)[38,40], have been shown to effectively anchor POMs[39,40]. The resulting hybrid materials have shown enhanced performance, including capacitance[38–42], and even increased potential window[39].

The synthesis of hybrid materials made of MXenes and POMs has been tackled by various authors. For example, Chen et al.[25] modified $Ti_3C_2T_x$ MXene with Keggin-type POMs by ionic liquid polymer linker but used it in low voltage aqueous electrolytes. Chao et al.[32] proposed the in-situ growth of Keplerate-type POMs on $Ti_3C_2T_x$ MXene, leading to a hybrid material with interesting performance in lithium-ion capacitors and sodium-ion capacitors. However, in their study, the first report needed the use of a linker to bond the acid form of a POM to MXene and its use was restricted to aqueous electrolytes. And while the second used organic electrolytes they failed to disperse POMs, leading to a material made of a mixture of phases, namely, MXene and crystallized POM. Thus, in both cases there was a failure to harness the full potential of POMs combined with MXene while working in a high-voltage organic electrolyte.

Accordingly, this was our goal, and in order to achieve it, we made use of activated carbon (AC) as a “transporting” phase for POMs, since, in a previous study, we had shown that this dual hybrid material can work in organic solvents, with properly dispersed POMs with their electroactivity not limited by diffusion [33].

Our working hypothesis was supported by our earlier work on AC/POM hybrids, which showed proper dispersion of POM clusters through physical adsorption in micropores, leading to materials able to operate both in aqueous or organic electrolytes[39,42,43]. Likewise, “hybrid” MXene/AC flexible electrodes have also been reported, with activated carbon facilitating the charge transfer from the electrode[16].

With these considerations in mind, we decided that a triple hybrid material formed by MXene, AC and POM could provide a complex but versatile system, in a rational design to produce a multifunctional electrode for energy storage[44]. Herein, we report the results of our work, which demonstrate that the MXene/AC/POM system can be made to optimize the functionality of each of the three components, leading to enhanced volumetric and gravimetric capacitances in an organic electrolyte symmetric supercapacitor.

2. Experimental

2.1. Synthesis of MXene ($Ti_3C_2T_x$)

MXene ($Ti_3C_2T_x$) was synthesized through a LiF/HCl etching method[45]. Namely, 0.5 g MAX phase (Ti_3AlC_2 , 99%, Y-Carbon Ltd.) was added slowly into a mixture of 0.5 g LiF (>99.99%, Sigma-Aldrich) and 10 mL 9 M HCl solution (diluted from 37% HCl, Sigma-Aldrich). The etching process was carried out in a capped Teflon-vessel for 24 h at 35°C. For washing and delamination, the mixture was poured into a 50 mL centrifugation tube and

washed with deionized water by centrifugation at 3500 rpm for 5 min. The supernatant was discarded. This step was repeated for several cycles until the pH of the dark-green supernatant was > 6. The sediments at the bottom expanded upon washing, which indicated delamination. Finally, the sediments were dispersed in water by hand-shaking and deaerated with Ar for 20 min and stored in the fridge for future use. A certain amount of the MXene colloid was filtered-off on a Celgard 3501 membrane to determine the concentration and for further use. The as-prepared electrode had a thickness of $11 \pm 1 \mu\text{m}$ and an areal density of $3 \pm 0.3 \text{ mg}\cdot\text{cm}^{-2}$.

2.2. Synthesis of MXene/HPW12

20 mL MXene colloid (around 1 mg mL^{-1}) was mixed with 20 mL 10 mM phosphotungstic acid ($\text{H}_3\text{PW}_{12}\text{O}_{40}$ (HPW12), reagent grade, Sigma-Aldrich) solution, and probe-sonicated for 1 h under circulating cooling water at 10°C . The mixture was filtered-off and washed with Milli-Q water until the filtrate was neutral. The product was peeled off from the membrane, dried in a vacuum oven at 60°C and stored in an argon-filled glovebox. The as-prepared sample (MXene/HPW12) could serve as a free-standing electrode. The as-prepared electrode had a thickness of $13 \pm 1 \mu\text{m}$ and an areal density of $3.3 \pm 0.3 \text{ mg cm}^{-2}$.

2.3. Synthesis of MXene/AC/HPW12

0.05 g activated carbon (DLC Super 30 from Norit Chemical) and 1.44 g phosphotungstic acid (HPW12) were added into 50 mL MXene colloid (around 1 mg mL^{-1}) and kept in probe-sonication for 1 h under circulating cooling water to keep the temperature below 10°C . Subsequently, the mixture was filtered-off onto a Celgard 3501 membrane to get a free-standing electrode. The as-prepared electrode had a thickness of $24 \pm 2 \mu\text{m}$ and an areal density of $2.8 \pm 0.2 \text{ mg cm}^{-2}$.

2.4. Synthesis of MXene/AC/TEAPW12

AC/TEAPW12 was prepared following our previously reported method[33]. Then, 0.05 g AC/TEAPW12 was added into 50 mL MXene colloid (around 1 mg mL^{-1}) and kept in probe-sonication for 1 h under circulating cooling water to keep the temperature below 10°C . The mixture was filtered-off onto Celgard 3501 membrane to obtain a free-standing electrode. The as-prepared electrode had a thickness of $21 \pm 2 \mu\text{m}$ and an areal density of $2.4 \pm 0.2 \text{ mg cm}^{-2}$.

For comparison, MXene/TEAPW12 and MXene/AC were also prepared and characterized (Figs. S1, S2 and S10).

2.5. Material characterization

Powder X-ray diffraction (XRD) patterns were collected on a PANalytical X'pert Pro-MRD diffractometer with $\text{Cu K}\alpha$ radiation ($\lambda = 1.5406 \text{ \AA}$) and PIXel detector. The interlayer distance (d) of the (002) planes was determined by Bragg's law:

$$d = \frac{\lambda}{2\sin\theta} \quad (1)$$

where λ is the X-ray wavelength, θ is the the diffraction angle.

Scanning electron microscopy (SEM) images were taken on a Quante 650 FEG microscope. For energy-dispersion X-ray spectra (EDX) semi-quantitative analysis, we averaged the elemental analysis of five spectra to present the final results. High resolution transmission electron microscopy (HR-TEM) images, high angle annular dark field scanning transmission electron microscopy (HAADF-STEM) images, and selected area electron diffraction

(SAED) patterns were obtained from an FEI Tecnai G2 F20 microscope. Volumetric N_2 sorption isotherms were collected at 77 K (N_2) using an ASAP 2020 HD (Micromeritics). Pore size distribution was estimated using a density functional theory (DFT) model (N_2 -cylindrical pores-oxide surface) implemented in the Microactive 4.00 software with a regularization factor of 0.01. X-ray photoelectron spectra were collected on Phoibos 150 probe from SPECS. Peak fitting for the high-resolution spectra was performed using CasaXPS Version 2.3.1. Before the peak fitting, the background was subtracted using a Shirley function.

2.6. Electrochemical characterization

T-type Swagelok cells were applied to fabricate three-electrode configuration. The working electrodes were cut into 10 mm round pieces and the overloaded activated carbon counter electrodes were cut into 12 mm round pieces. 0.01 M Ag/Ag^+ served as the reference electrode. 1 M TEABF_4 in acetonitrile or 1 M EMIMTFSI in acetonitrile served as the electrolyte. CR2032 coin cells were used to fabricate asymmetric devices. The electrochemical tests were carried out in an argon-filled glove box with the oxygen and water lever under 5 ppm.

The gravimetric capacitance (C_m) and the volumetric capacitance (C_v) were calculated from cyclic voltammograms (CVs) according to the following equations:

$$C = \frac{\int I(V) \cdot dV}{2\nu\Delta V} \quad (2)$$

$$C_v = \frac{C}{V_e} \quad (3)$$

$$C_m = \frac{C}{m} \quad (4)$$

where $\int I(V) \cdot dV$ is the integral area of CVs, ν is the scan rate, ΔV is voltage window, V_e is the volume (cm^3) of the electrode and m is the mass (g) of the electrode.

The gravimetric energy density E_m (Wh kg^{-1}) and volumetric E_v energy density (Wh cm^{-3}), gravimetric power density P_m (W kg^{-1}) and volumetric power density P_v (W cm^{-3}) were calculated from the two-electrode cell discharge data using the following equations:

$$E_m = \frac{C\Delta V^2}{3.6 \times 2m_{total}} \quad (5)$$

$$E_v = \frac{C\Delta V^2}{3600 \times 2V_{total}} \quad (6)$$

$$P_m = \frac{1000 \times I\Delta V}{m_{total}} \quad (7)$$

$$P_v = \frac{I\Delta V}{V_{total}} \quad (8)$$

where m_{total} is the total mass (g) of the two electrodes, V_{total} is the total volume (cm^{-3}) of the two electrodes, and I is the discharging current (A).

3. Results and discussion

The crystal structure of the solid phases was characterized by XRD. Fig. 1 presents the XRD patterns of the pristine MXene and derived materials. Table 1 shows the positions of (002) diffraction peaks and the interlayer distance. All the XRD patterns confirm the

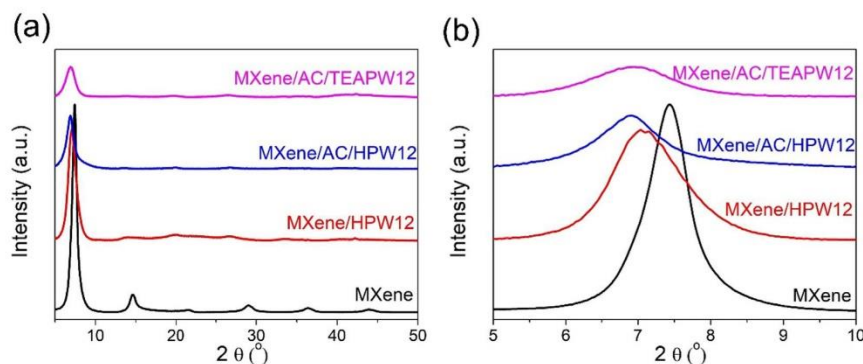


Fig. 1. (a) XRD patterns of pristine MXene, MXene/HPW12, MXene/AC/TEAPW12 and MXene/AC/HPW12. (b) Zoom-ins of (a) in the 5–10° 2 θ range showing (002) peaks.

layered structure of the pristine MXene and the hybrid materials but with different interlayer distances and various crystallinity.

As can be observed, the pristine MXene has its (002) peak centred at 7.44°, and an interlayer distance of 11.87 Å, which is in the typical range of LiF/HCl-etched Ti₃C₂T_x MXene[45]. The (002) peak of MXene/HPW12 is broader, revealing a poorer crystallinity, probably associated with the powerful probe-sonication that broke down large nanosheets. In this case, the peak shifts towards smaller two theta angles. On the other hand, the interlayer distance of 12.42 Å, is only slightly larger than that of the pristine MXene. Arup Chakraborty et al. have recently pointed out that even small anions such as Cl⁻ and Br⁻ are difficult to insert into MXenes[46]. Since PW12 anions are 1 nm in diameter, significantly larger than pre-intercalated Li⁺, we conclude that the PW12 clusters are not intercalated into MXene but are mainly anchored on the surface. The XRD pattern of MXene/AC/HPW12 presents a broad peak at around 6.91°, corresponding to a slightly larger interlayer distance (12.80 Å) compared with MXene. The AC particles are micron scale. Thus, neither AC nor PW12 clusters can insert MXene layers. The slight variation of interlayer distance is supposed to be associated with the fact that high-power sonication slightly increases interlayer distance[47]. Furthermore, the sonication during the preparation and the amorphous AC reduced the overall crystallinity of the final material. For the same reasons, the XRD pattern of MXene/AC/TEAPW12 presents a similarly broad peak, with minor shifting with respect to the pristine MXene. The XRD patterns of the hybrid materials (MXene/HPW12, MXene/AC/HPW12 and MXene/AC/TEAPW12) do not exhibit any other peaks corresponding to HPW12 nor TEAPW12. This is very significant since it rules out the inclusion of the POMs as crystallized extended phases. Instead, XRD results are consistent either with the absence of POMs in the hybrid or with POM clusters being dispersed individually or at most in groups small enough to prevent bulk diffraction. The fol-

lowing EDX analyses in Table 2, confirm the existence of tungsten (PW12).

In order to observe the morphology and evaluate the loading mass of PW12 clusters, the samples were characterized with energy-dispersive X-ray spectroscopy. The pristine MXene (Fig. 2a) exhibits an accordion-like structure, which remains even after suffering high-power probe-sonication (MXene/HPW12, Fig. 2b). For the MXene/HPW12 material, we cannot detect or discern any other heterogeneous aggregates, but the EDX spectrum confirms the presence of PW12 clusters, not apparent most likely due to the small nanosize of the PW12 clusters (1 nm). MXene/AC/HPW12 (Fig. 2c) and MXene/AC/TEAPW12 (Fig. 2d) exhibit a similar morphology, different from pristine MXene with the particles spreading on or surrounded by nanosheets. Since in the XRD patterns of MXene/AC/HPW12 and MXene/AC/TEAPW12 we cannot discern any diffraction peaks except those from MXene, we confirmed that the particles were amorphous AC, with dispersed, not well-crystallized PW12 clusters. We have previously shown that AC is an ideal matrix for absorbing PW12 and spreading them in nanopores[39]. We therefore propose that most PW12 clusters are adsorbed on AC in these triple hybrid materials, as proven in the EDX spectra and HAADF-STEM images, shown in the following Table 2 and Fig. 4.

Table 2 lists the weight percentage of tungsten and titanium derived from EDX spectra. MXene/HPW12 only contains 6 wt% tungsten even with the assistance of high-power sonication, revealing that MXene is not a good substrate for direct-anchoring of POMs. That is most likely the reason why most previous studies had to resort to linking groups[48,49] or in-situ synthesis[32]. Indeed, through the in-situ synthesis (synthesis of MXene/TEAPW12, in supplementary materials), we could load a large amount of TEAPW12 on MXene (Table S1). As for MXene/AC/HPW12, improvement in the loading mass of PW12 must be ascribed to the inclusion of AC in the material providing a microporous matrix for anchoring POMs. MXene/AC/TEAPW12 contains less W than MXene/AC/HPW12 because we carried out an ex-situ synthesis, in which TEAPW12 clusters had been already immobilized in AC accounting for 37.5 wt% in AC/TEAPW12 precursor.

Table 1

The positions of (002) peaks and their corresponding interlayer space derived from the XRD patterns.

Sample	2 θ values for (002) diffraction peaks/°	Interlayer distance/Å
MXene	7.44	11.87
MXene/HPW12	7.09	12.42
MXene/AC/TEAPW12	6.91	12.80
MXene/AC/HPW12	6.95	12.71

Table 2

Semi-quantitative analysis result from EDX spectra.

Sample	Ti/ wt. %	W/ wt. %
MXene/HPW12	51.2 ± 3.6	6.1 ± 1.1
MXene/AC/HPW12	31.4 ± 2.1	17.5 ± 2.0
MXene/AC/TEAPW12	39.7 ± 2.8	13.5 ± 1.8

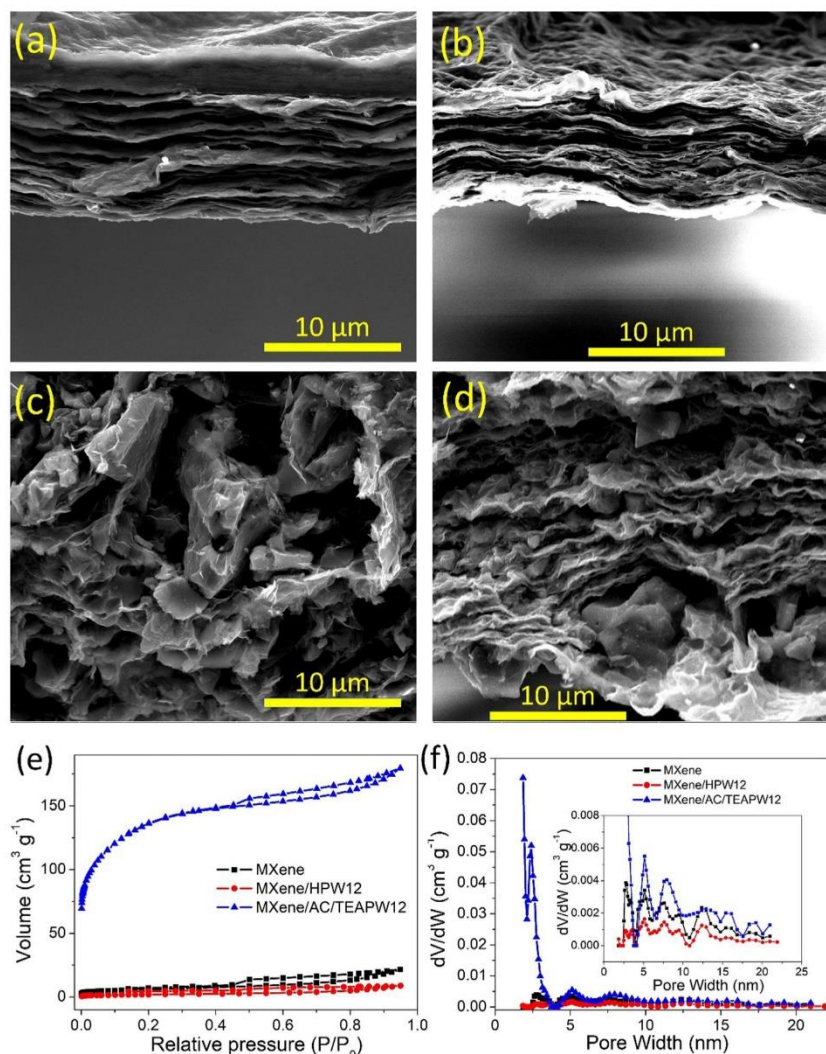


Fig. 2. SEM images of (a) MXene, (b) MXene/HPW12, (c) MXene/AC/HPW12 and (d) MXene/AC/TEAPW12. (e) N_2 sorption isotherms and (f) pore size distribution curves of MXene, MXene/HPW12 and MXene/AC/TEAPW12.

Since the SEM images reveal a remarkable expansion of the space among MXene nanosheets due to the AC particles, we carried out volumetric N_2 sorption experiments to investigate the influence of the inclusion of HPW12 or AC/TEAPW12 on the porous properties of MXene. Fig. 2e presents the nitrogen sorption isotherms of MXene, MXene/HPW12 and MXene/AC/TEAPW12. MXene/AC/TEAPW12 exhibits a significantly larger absorbed volume. The specific surface area of MXene/AC/TEAPW12 is $499 \text{ m}^2 \text{ g}^{-1}$, 30 times larger than pristine MXene ($15 \text{ m}^2 \text{ g}^{-1}$), which we ascribe to the microporous nature of AC/TEAPW12 (specific surface area = $1007 \text{ m}^2 \text{ g}^{-1}$) [33]. The pore-size distribution (Fig. 2f) reveals that MXene/AC/TEAPW12 exhibits a hierarchical porous structure characterized by the dominance of AC micropores and the development of the mesopores inherited from MXene. While the inclusion of AC/TEAPW12 promotes mesopore formation, the

addition of HPW12 leads to a decrease of specific surface area (from $15 \text{ m}^2 \text{ g}^{-1}$ to $7.8 \text{ m}^2 \text{ g}^{-1}$), the pore structure remains the same (Fig. 2f). This can be explained by the heavy molecular weight of HPW12 as well as the fact that HPW12 clusters occupy some mesopores.

In order to compare the surface composition, bonding forming and element valence, we carried out XPS analysis on the pristine MXene, the double hybrid (MXene/HPW12) and the triple hybrid material (MXene/AC/TEAPW12). The low-resolution survey spectra (Fig. 3a) show that in addition to elements Ti, C, F, Cl and O that compose MXene, the hybrid materials (MXene/HPW12 and MXene/AC/TEAPW12) contain element W (Fig. 3a inset, W 4d peaks). The elemental compositions calculated by XPS are presented in Table S2, which shows that MXene/AC/TEAPW12 has a higher W atomic ratio than MXene/HPW12.

Fig. 3b-d illustrate the C 1 s spectra of MXene, MXene/HPW12 and MXene/AC/TEAPW12. The pristine MXene and MXene/HPW12 show three peaks located at 281.85, 284.8 and 288.1 eV, which are matched to C-Ti, C-C and C-O, respectively. The MXene/AC/TEAPW12 shows an extra peak at 285.3 eV, which we attribute to the C-C bonds in AC. Fig. 3e-g depict the Ti 2p spectra of MXene, MXene/HPW12 and MXene/AC/TEAPW12, in which the Ti-C ($2p^{3/2}$ 455.0 eV, $2p^{1/2}$ 461.1 eV), Ti(II) ($2p^{3/2}$ 455.8 eV, $2p^{1/2}$ 461.5 eV), Ti(III) ($2p^{3/2}$ 457.0 eV, $2p^{1/2}$ 462.9 eV) and Ti(IV) ($2p^{3/2}$ 458.6 eV, $2p^{1/2}$ 464.4 eV) peaks agree well with results from previous research[50,51]. Ti(II) and Ti(III) are associated with surface terminating groups, while Ti(IV) is associated with TiO_2 . MXene/HPW12 presents less intensive Ti(II) peaks and more intensive Ti(III) peaks than MXene, implying the inclusion of the small amount of HPW12 changed the valence of Ti. HPW12 is anchored on MXene through chemical bonds. By contrast, the Ti 2p spectrum of MXene/AC/TEAPW12 does not show such significant change except for stronger Ti(IV) peaks, which should be ascribed to the fact that AC is just physically constrained among MXene nanosheets and TEAPW12 are pre-immobilized on AC. The stronger Ti(IV) peaks in MXene/HPW12 and MXene/AC/TEAPW12 must be associated with the slight oxidation due to the high-power probe-sonication. We also collected high-resolution spectra from 25 to 45 eV to investigate the W 4f orbital in hybrid materials. However, since the binding energy of Ti 3p is very close to W 4f, the W $4f^{7/2}$ and $4f^{5/2}$ peaks are deformed. Nonetheless, it is still possible to discern the two main peaks at 36.1 and 38.2 eV, agreeing well with W(VI) $4f^{7/2}$ and $4f^{5/2}$ peaks in PW12 (Fig. S2d).

HAADF-STEM is an effective method to investigate the dispersion of heavy atoms, particularly the PW12 clusters. Fig. 4a-d present HAADF-STEM images of pure MXene and these hybrid samples. The corresponding HR-TEM images are presented in Fig. S3. Under HAADF-STEM, MXene (Fig. 4a) presents a homogeneous texture, while MXene/HPW12 (Fig. 4b) is slightly different.

In some areas, the nanosheets are covered by a thin, bright layer, corresponding to PW12 confirmed by EDX (Fig. S4). We conclude that MXene is not an effective substrate for dispersing PW12 clusters because aggregation happens even in low loading mass. On the other hand, the dispersion states of PW12 clusters in triple hybrid materials MXene/AC/HPW12 (Fig. 4c) and MXene/AC/TEAPW12 (Fig. 4d) are quite different from the MXene/HPW12. The bright dots, around 1 nm (as confirmed by EDX element mapping and line scan in Fig. S5), spread homogeneously on the substrate, indicating that the PW12 clusters are well-dispersed at the nanoscale. Fig. 4e-f present the STEM image and the EDX element mapping in an extended area, in which we can discern the MXene nanosheets surrounding the AC particles loaded with PW12 clusters. The SAED patterns (Fig. S6) prove the triple hybrid materials have mixed phases: crystallized MXene, amorphous AC and uncrystallized PW12 clusters. This is in good agreement with the fact that MXene/AC/HPW12 and MXene/AC/TEAPW12 do not show any diffraction peaks other than those of MXene in XRD.

With the images of SEM and STEM, we illustrate how the three components combine in MXene/AC/TEAPW12 (Fig. 5). First, the PW12 nanoclusters are anchored on microporous AC matrix and dispersed at nanoscale. Then, the PW12-anchored AC particles mix with flexible MXene nanosheets and stack together under vacuum-assisted filtration. Finally, we obtain the PW12-anchored AC wrapped by MXene nanosheets.

Cyclic voltammograms were carried out to characterize the electrochemical properties of the materials, as well as to determine the capacitance of the various electrodes studied and to analyze the energy storage mechanisms. The CV of MXene in 1 M TEABF₄ in acetonitrile (Fig. 6a) is predominantly capacitive (ideally rectangular shape) but superposed a pair of broad redox waves. The reduction wave centred at -1.75 V vs. Ag/Ag⁺ must be ascribed to the intercalation of TEA⁺. The corresponding oxidation peak, centred at -1.48 V vs. Ag/Ag⁺, is broader and weaker, indicating the

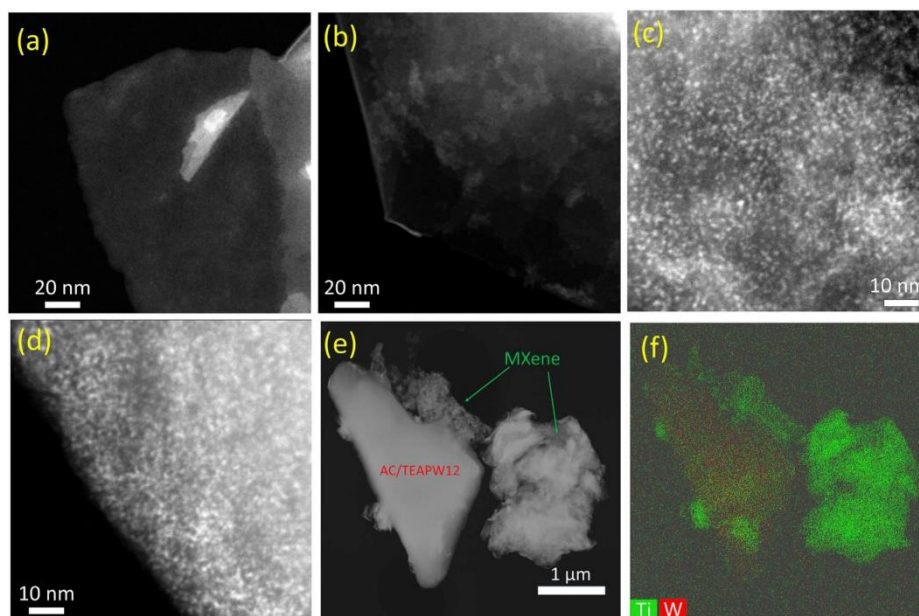


Fig. 4. HAADF-STEM images of (a) MXene, (b) MXene/HPW12, (c) MXene/AC/HPW12 and (d) MXene/AC/TEAPW12. (e) STEM image at low magnification and (f) the corresponding element mapping of MXene/AC/TEAPW12.

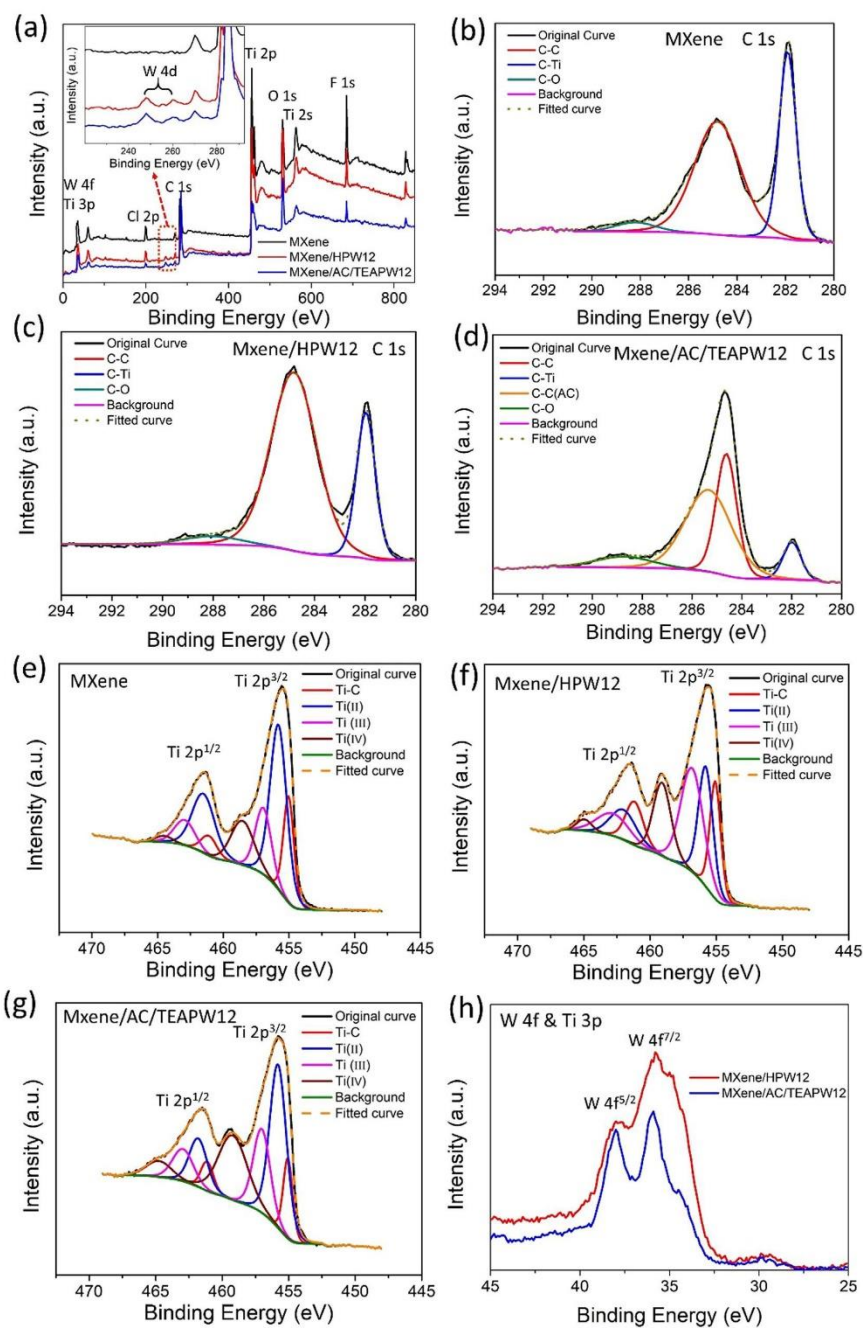


Fig. 3. (a) XPS full spectrum of MXene, MXene/HPW12 and MXene/AC/TEAPW12 (inset is the zoom-in area to discern W 4d peaks). C 1s spectra of (b) MXene, (c) MXene/HPW12 and (d) MXene/AC/TEAPW12. Ti 2p spectra of (e) MXene, (f) MXene/HPW12 and (g) MXene/AC/TEAPW12. (h) W 4f spectra of MXene/HPW12 and MXene/AC/TEAPW12 (Ti 3p overlap).

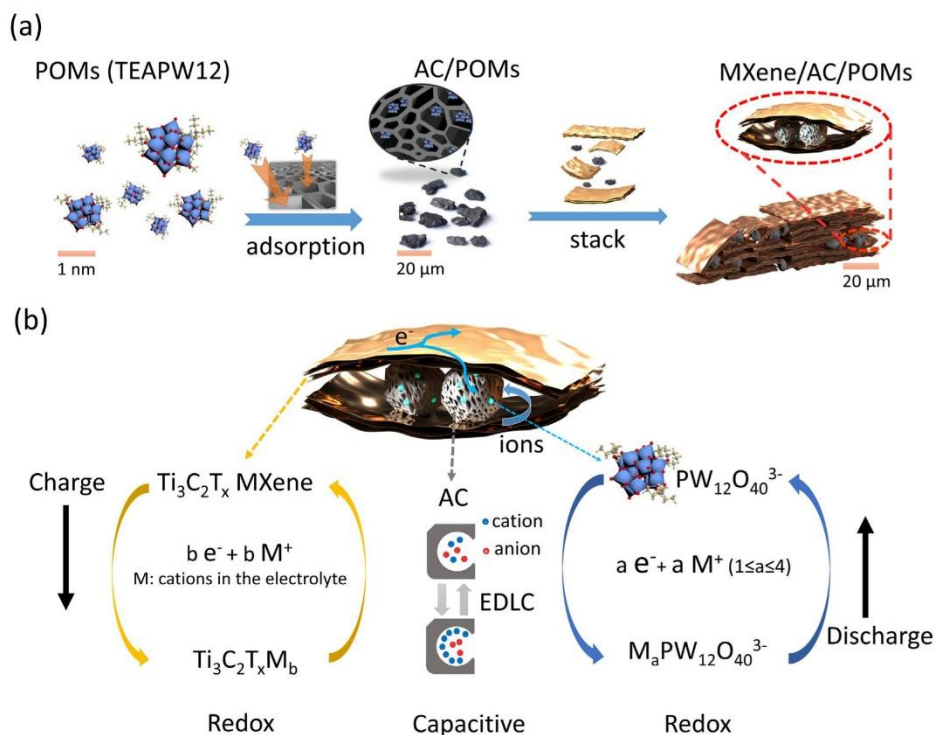


Fig. 5. Schematic illustration of the combination of TEAPW12, AC and MXene. (b) Schematic illustration of the working mechanism of MXene/AC/TEAPW12.

intercalation–deintercalation process is not 100% reversible. This agrees well with the XRD patterns of cycled MXene, in which we observe a significant shifting of (002) peak to low angle (Fig. S7). In the CV of MXene/HPW12 (Fig. 6a), besides the broad waves from MXene, we can discern some new small peaks from PW12 clusters. Since the loading mass of HPW12 is very low, these peaks are weak and their contribution to the capacitance is not very substantial.

The CV of MXene/AC/TEAPW12 (Fig. 6b) mainly shows four pairs of redox waves, similar to AC/TEAPW12[33]. Since TEAPW12 is immobilized on AC in advance, MXene/AC/TEAPW12 presents redox waves at the same positions. Fig. 5(b) illustrates how the triple hybrid MXene/AC/TEAPW12 works. The MXene nanosheets and porous AC particles construct the framework for electron flow. The hierarchical porous structure facilitates ion diffusion. As a result, all three components contribute to electrochemical energy storage: MXene and TEAPW12 store charges through reversible redox reactions; AC store charges through electric double-layer capacitance.

On the other hand, the situation is more complicated for MXene/AC/HPW12. The CV of MXene/AC/HPW12 (Fig. 6b) shows more than six pairs of redox waves. In principle, PW12 clusters only present three or four pairs of redox waves in this potential range (more redox pairs are possible in a wider potential range, but they are not 100% reversible). The extra redox waves must be associated with different anchoring states: PW12 clusters anchoring on AC; and PW12 clusters anchoring on MXene (The classification of these redox waves is presented in Fig. S8a-c).

To investigate the energy storage mechanism, we carried out CVs at various scan rates (Fig. S9). The dependence of the current response on the scan rate can provide insights into the charge-storage mechanism according to Eq9 as suggested by John Wang et al. [52]:

$$\frac{i(V)}{v^{1/2}} = k_1 v^{1/2} + k_2 \quad (9)$$

where $i(V)$ is the current at the given potential V , v is the scan rate. k_1 is a variable characterizing the contribution from surface capacitive processes (e.g. pseudocapacitance, electric double layer capacitance), and k_2 is the other variable representing the contribution from diffusion-controlled processes (e.g. intercalation–deintercalation, sluggish redox reactions) at a given potential. k_1 and k_2 can be determined by a linear fitting of Eq9.

Fig. 6c shows the contribution of the diffusion-controlled process versus the surface capacitive process to the overall capacitance of MXene/AC/TEAPW12 from 0.2 to 2 mV s^{-1} . The surface capacitive process dominates the energy storage process in the whole range. At 0.2 mV s^{-1} , the surface capacitive process accounts for 78.9% of total capacitance; when the scan rate rises to 2 mV s^{-1} , this ratio increases to 91%. With the rise of the scan rate, the contribution of surface capacitance increases, revealing that the surface capacitive process prevails at faster scan rates. This trend is common in many other hybrid materials[53,54]. MXene/AC/TEAPW12 maintains a higher surface capacitive contribution in the whole range, mainly benefiting from the excellent dispersion of PW12 clusters.

Fig. 6d presents the gravimetric capacitance of MXene, MXene/HPW12, MXene/AC/HPW12 and MXene/AC/TEAPW12 in 1 M TEABF4 in acetonitrile at various scan rates. MXene and MXene/HPW12 almost deliver the exact equivalent gravimetric capacitance because the loading of PW12 on MXene/HPW12 is very low. MXene/AC/HPW12 and MXene/AC/TEAPW12 exhibit significantly higher gravimetric capacitance, thanks to AC with high gravimetric capacitance. Compared with the hybrid material

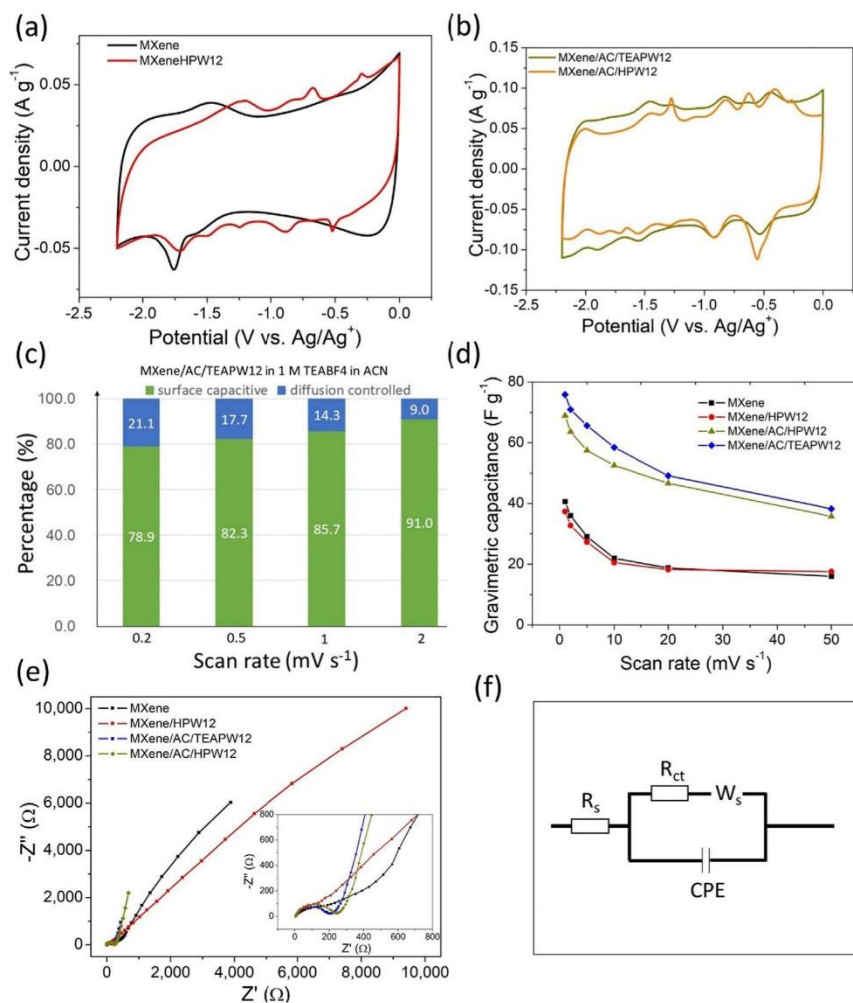


Fig. 6. (a) Cyclic voltammograms of MXene and MXene/HPW12 at 1 mV s⁻¹ in 1 M TEABF4 acetonitrile. (b) Cyclic voltammograms of MXene/AC/HPW12 and MXene/AC/TEAPW12 at 1 mV s⁻¹ in 1 M TEABF4 acetonitrile. (c) Surface capacitive contribution and diffusion-controlled contribution at various scan rates. (d) Gravimetric capacitance of MXene, MXene/HPW12, MXene/AC/HPW12 and MXene/AC/TEAPW12 at various scan rates. (e) Electrochemical impedance spectra of MXene, MXene/HPW12, MXene/AC/HPW12 and MXene/AC/TEAPW12. (f) Equivalent circuit for fitting impedance spectra.

MXene/AC of the same weight ratio (MXene/AC 1:1, 88F g⁻¹ at 0.1 A g⁻¹[16], or 77F g⁻¹ at 1 mV s⁻¹(Fig. S10)), MXene/AC/TEAPW12 could deliver the equivalent gravimetric capacitance. The addition of TEAPW12 does not improve the gravimetric capacitance due to the large molecular weight of PW12 clusters (>2800 g mol⁻¹). On the other hand, as other studies show, the anchoring of TEAPW12 can improve the volumetric capacitance, instead of the gravimetric capacitance in the same electrolyte[33]. Due to the porous nature of AC, MXene/AC delivers 33% lower volumetric capacitance than that of MXene[16]. In contrast, in our study, the volumetric capacitance of MXene/AC/TEAPW12 is only around 10% lower than pristine MXene (Fig. S10), but much higher than MXene/AC[16], AC/TEAPW12[33] and AC[33].

To investigate the electrochemical response as well as diffusion properties of the triple hybrids, we carried out impedance tests (Fig. 6e). All the spectra are fitted by a modified Randles circuit

(Fig. 6f). The fitted values are presented in Table S4. The intercepts at the very high-frequency region represent equivalent series resistance (R_s), which is a combination of the ionic resistance of the electrolyte, the intrinsic resistance of the active materials, and the contact resistance at the active material/current collector interface. Since all the electrodes were characterized in the same setup, their R_s are similar. The arc at high frequency represents charge-transfer resistance R_{ct}. The following transitory parts between the semicircles and the final linear parts represent the Warburg impedance, which is associated with mass transfer (diffusion). The R_{ct} of MXene and MXene/HPW12 are smaller (around 50%) than MXene/AC/HPW12 and MXene/AC/TEAPW12, but the diffusion impedance values are significantly larger (5 times), revealing that different steps restrict the charge store process. In MXene and MXene/HPW12, due to the high electronic conductivity of MXene nanosheets, the active sites which have already been

exposed to the electrolyte can carry out the charge transfer process quickly, leading to a relatively smaller R_{ct} . After that, ions have to diffuse through the slits between nanosheets, or even insert layers to reach the active sites. As a result, their diffusion impedance values are extremely large. By contrast, MXene/AC/HPW12 and MXene/AC/TEAPW12 have larger R_{ct} due to the inferior electronic conductivity of AC, but the diffusion is greatly promoted thanks to the hierarchical porous structure.

In general, the electrochemical performance of any electrode is related to its thickness, especially for MXenes. Normally, thicker MXene electrodes lead to remarkably lower volumetric capacitance [4]. In our case, on the contrary, the increased porosity of our hybrid material leads to a thicker electrode (as shown by SEM) but with improved capacitance. We chose to compare pristine MXene with hybrid electrodes keeping their masses (areal densities) comparable, rather than their thicknesses.

The combination of the three components has a synergistic effect in that several merits are merged in the MXene/AC/TEAPW12 triple hybrid. We attempted to estimate the overall capacitance contributed from each component according to the composition and individual specific capacitance. For instance, at 1 mV s^{-1} the gravimetric capacitance of MXene/AC/TEAPW12, MXene and AC/TEAPW12 is 76 F g^{-1} , 40 F g^{-1} and 90 F g^{-1} , respectively. Since MXene and AC/TEAPW12 each account for half the mass of MXene/AC/TEAPW12, a MXene/AC/TEAPW12 = 1:1 mixture would have a gravimetric capacitance of 65 F g^{-1} , lower than the MXene/AC/TEAPW12 hybrid material. The extra capacitance must be ascribed to the fact that AC/TEAPW12 promotes the porous properties of MXene, which is a part of the synergistic effect. Furthermore, the MXene provides a conductive substrate with high volumetric capacitance. AC provides a microporous matrix for TEAPW12 anchoring, and also contributes to high gravimetric capacitance. TEAPW12 clusters could be nanodispersed and durably anchored on AC, providing extra-fast reversible redox reactions not limited by diffusion, and compensating the sacrificed volumetric capacitance due to the addition of AC. Finally, we were able to obtain a well-balanced triple hybrid material with both high gravimetric and volumetric capacitances in a conventional organic electrolyte.

The capacitance of MXene in organic electrolytes can be improved by fine tuning of the ions used in the electrolyte. Thus, EMIMTFSI has flatter cations than TEABF4, and the cations could intercalate into MXene more easily. Accordingly, MXene can deliver higher capacitance in the EMIMTFSI/acetonitrile electrolyte [8]. We compared the electrochemical behaviors of MXene/AC/HPW12 and MXene/AC/TEAPW12 in 1 M EMIMTFSI in acetonitrile and 1 M TEABF4 in acetonitrile (Fig. 7a). The current densities of the CVs in 1 M EMIMTFSI in acetonitrile are remarkably higher than those in 1 M TEABF4 in acetonitrile, indicating a larger capacitance. The CVs of MXene/AC/HPW12 and MXene/AC/TEAPW12 show more than one pair of redox waves in 1 M EMIMTFSI in acetonitrile, implying the PW12 clusters are still redox active in this electrolyte. Fig. 7b presents the gravimetric capacitance of MXene, MXene/AC/HPW12 and MXene/AC/TEAPW12 at various scan rates. MXene/AC/TEAPW12 still delivers the largest gravimetric capacitance (102 F g^{-1} at 1 mV s^{-1}) among the three, almost double that of MXene (52 F g^{-1} at 1 mV s^{-1}), and also higher than the gravimetric capacitance of MXene/AC/TEAPW12 (76 F g^{-1} at 1 mV s^{-1}) in 1 M TEABF4 in acetonitrile. The enhancement of capacitance derives from the cation intercalation–deintercalation in the energy storage process. Since the cation intercalation–deintercalation is usually diffusion-controlled, we carried out the CVs at various scan rates to analyze the contribution from these two mechanisms.

Fig. 7c presents the contribution of the diffusion-controlled and surface capacitive processes from 0.2 mV s^{-1} to 2 mV s^{-1} . The surface capacitive process still dominates the energy storage in the

whole range, but the diffusion-controlled process starts to play a bigger role. At 0.2 mV s^{-1} , the diffusion-controlled process accounts for 43.5%, more than double that in 1 M TEABF4 in acetonitrile. The remarkably increased ratio of the diffusion-controlled contribution proves the deeper involvement of cation intercalation–deintercalation in MXene, thus, MXene and MXene/AC/TEAPW12 could deliver more capacitance in 1 M EMIMTFSI in acetonitrile.

We charge-discharged MXene/AC/TEAPW12 for 10,000 cycles in both electrolytes (Fig. 7d) and ran CVs before and after cycling (Fig. 7e and f). MXene/AC/TEAPW12 shows excellent cycle stability in 1 M TEABF4 acetonitrile. Its capacitance almost remains the same after 10,000 cycles. Furthermore, the CV after 10,000 cycles exhibits four pairs of redox waves. Their current densities even stay the same, indicating the anchoring and redox activities of PW12 clusters do not change. The excellent cycle stability and long-term anchoring of PW12 clusters must be ascribed to the AC matrix, which has been proved to be an ideal substrate for anchoring POMs [35,39,43]. In contrast, the in-situ growth MXene/TEAPW12 show much worse cycle stability (Fig. S8d) in the same electrolyte. The redox waves almost disappear after 1000 cycles (Fig. S8e). Other previously reported MXene/POM hybrid materials cannot give very long-term cycle stability [32]. Thus, AC is the key to the excellent cyclic performance of the triple hybrid materials. In 1 M EMIMTFSI in acetonitrile, the capacitance of MXene/AC/TEAPW12 increases by 7% after 10,000 cycles, which could be associated with the expanded interlayer distance due to cation intercalation during cycling [11,55]. However, the deep cation intercalation is not problem-free. Firstly, this cation intercalation–deintercalation is not 100% reversible, which is reflected by the fact that in 1 M EMIMTFSI in acetonitrile the Coulombic efficiency is lower because more cations involve in intercalation. Moreover, the long-term, repeating intercalation–deintercalation could damage the microstructure and worsen the conductivity, which is revealed by CVs (Fig. 7f). The electrode after 10,000 cycles suffers larger resistance. The electrochemical impedance spectra further confirm it.

Fig. 7g compares the impedance spectra of MXene/AC/TEAPW12 before and after cycled in 1 M TEABF4 in acetonitrile. The spectrum was fitted by the same equivalent circuit (Fig. 6f) and the fitting values are presented in Table S5. The two spectra almost overlap. The zoom-in figure (Fig. 7g inset) presents the slight different, in which we can only discern the slightly larger arc, corresponding to R_{ct} . By contrast, the impedance spectrum of MXene/AC/TEAPW12 cycled in 1 M EMIMTFSI in acetonitrile (Fig. 7h) is significantly different from the fresh one. The intercept on X-axis (representing R_s) stays the same, but the arc (R_{ct}) is remarkably larger and the followed linear transition zoom (related to diffusion impedance) is remarkably longer, revealing that the charge-transfer and diffusion processes are impeded in the cycled electrode. The impedance spectra confirm that long-term intercalation–deintercalation in 1 M EMIMTFSI in acetonitrile could damage the microstructure, hindering ion diffusion and leading to high resistance.

Table 3 compares the capacitive performance of the triple hybrid material MXene/AC/TEAPW12 and the double hybrid materials MXene/AC, AC/TEAPW12 and MXene/TEAPW12 in 1 M TEABF4 in acetonitrile, which demonstrates the superiority of the triple hybrid material over double hybrid materials. Compared with MXene/AC and AC/TEAPW12, MXene/AC/TEAPW12 shows enhanced volumetric capacitance without sacrificing gravimetric capacitance and cycle stability. Meanwhile, the defects of MXene/TEAPW12, i.e. poor cycle stability and low gravimetric capacitance, are overwhelmed in MXene/AC/TEAPW12.

We assembled asymmetric supercapacitors to compare the potential application of the MXene/AC/TEAPW12 triple hybrid

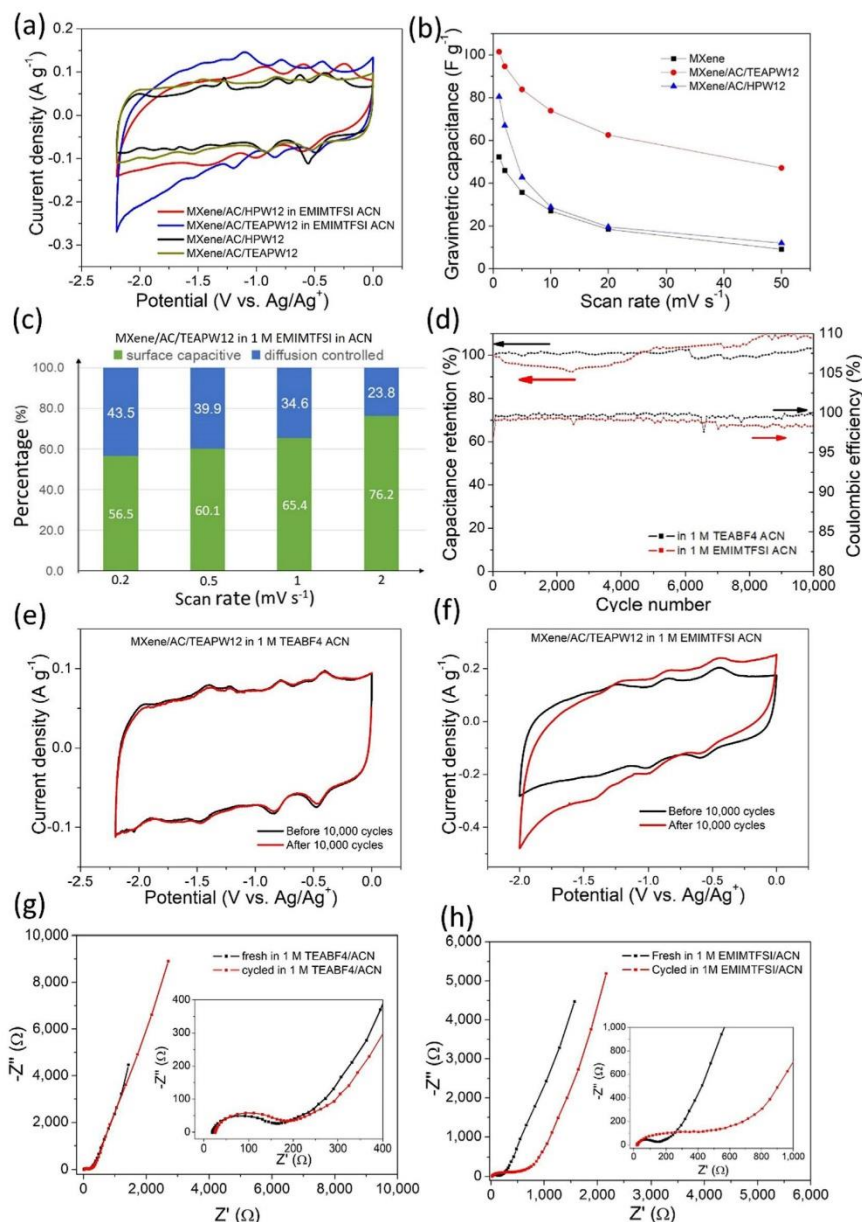


Fig. 7. (a) CVs of MXene/AC/HPW12 and MXene/AC/TEAPW12 at 1 mV s⁻¹ in 1 M TEABF4 in acetonitrile or 1 M EMIMTFSI in acetonitrile; (b) Gravimetric capacitance of MXene, MXene/AC/HPW12 and MXene/AC/TEAPW12 in 1 M EMIMTFSI in acetonitrile; (c) Diffusion-controlled contribution and surface capacitive contribution at various scan rates; (d) Cycling stability test: capacitance retention and Coulombic efficiency of MXene/AC/TEAPW12 in the two electrolytes (current density: 2 A g⁻¹). (e) CVs of MXene/AC/TEAPW12 in 1 M TEABF4 in acetonitrile before and after cycling; (f) CVs of MXene/AC/TEAPW12 in 1 M EMIMTFSI in acetonitrile before and after cycling. Electrochemical impedance spectra of MXene/AC/TEAPW12 before and after cycling in (g) 1 M TEABF4 in acetonitrile and (h) 1 M EMIMTFSI in acetonitrile.

materials (AC/MXene/AC/TEAPW12) and pristine MXene (AC//MXene) in full-cell. The conventional AC electrodes served as the positive electrode. 1 M TEABF4 in acetonitrile served as the electrolyte. The details about preparing AC electrodes and charge balance calculation are presented in [supplementary materials](#).

Fig. 8a presents the CVs of the positive (AC) and negative (MXene/AC/TEAPW12) electrodes in the respective potential range, in which the negative electrode is charged to -2.2 V, and the positive electrode is charged to +0.5 V. As a result, a voltage window of 2.7 V can be achieved in the full cell. Cyclic polarization (CP) was

Table 3

Comparison of the capacitive performance of the triple hybrid material MXene/AC/TEAPW12 and the double hybrid materials MXene/AC, AC/TEAPW12 and MXene/TEAPW12.

	Gravimetric capacitance	Volumetric capacitance	Capacitance retention	Reference
MXene/AC/TEAPW12	87F g ⁻¹ at 1 mV s ⁻¹	76F cm ⁻³ at 1 mV s ⁻¹	102% after 10,000 cycles	this work
MXene/AC ^a	88F g ⁻¹ at 0.1 A g ⁻¹	30F cm ⁻³ at 0.1 A g ⁻¹	92% after 10,000 cycles	[16]
AC/TEAPW12 ^b	92F g ⁻¹ at 1 mV s ⁻¹	64F cm ⁻³ at 1 mV s ⁻¹	93% after 10,000 cycles	[33]
MXene/TEAPW12	36F g ⁻¹ at 1 mV s ⁻¹	120F cm ⁻³ at 1 mV s ⁻¹	80% after 1,000 cycles	this work

a, MXene account for 50 wt% in MXene/AC. b, it is not a free-standing electrode, the mass of the binder, conductive additive and current collector are not included in calculating the gravimetric capacitance.

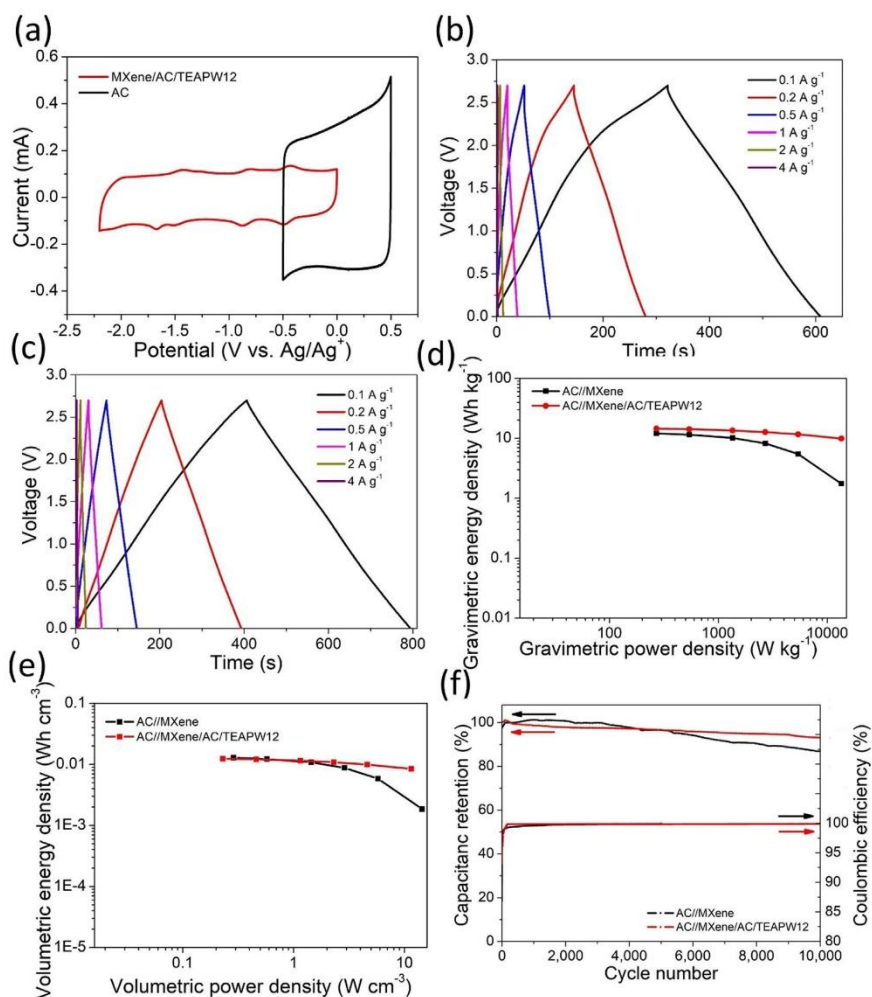


Fig. 8. (a) CVs of the positive and negative electrodes in AC//MXene/AC/TEAPW12 asymmetric cell. Galvanostatic charge–discharge curves of (b) AC//MXene and (c) AC//MXene/AC/TEAPW12 cells at various current densities. (d) Gravimetric and (e) volumetric Ragone plot of AC//MXene and AC//MXene/AC/TEAPW12 cell. (f) Cycling stability test: capacitance retention and Coulombic efficiency of AC//MXene and AC//MXene/AC/TEAPW12 cell during charge–discharge at 1 A g⁻¹ for 10,000 cycles.

carried out on both asymmetric cells at various scan rates (from 2 mV s⁻¹ to 1 V s⁻¹, Fig. S11a–d). The CP curves of AC//MXene/AC/TEAPW12 present several weak waves during the charging and discharging processes, deriving from the redox reaction of TEAPW12. At high scan rates (>100 mV s⁻¹), the CP curves of AC//MXene/AC/TEAPW12 remain rectangular while those of AC//MXene do not, indicating the better rate capability of AC//

MXene/AC/TEAPW12 cell. The specific capacitance normalized by the total mass of two electrodes at various scan rates is presented in Fig. S11e.

Galvanostatic charge–discharge (GCD) was carried out to evaluate the performance of the asymmetric cells in practical application. The GCD curves of AC//MXene (Fig. 8b) diverge from the ideal triangular shape due to the sluggish intercalation–deintercalation

tion of cations in MXene. In contrast, the GCD curves of AC//MXene/AC/TEAPW12 (Fig. 8c) are triangular, which agrees with the previous single electrode analysis: MXene/AC/TEAPW12 mainly stores charges through surface capacitive processes. The gravimetric capacitance of the asymmetric cells at various current densities or scan rates is presented in Fig. S11f. The AC//MXene/AC/TEAPW12 surpasses AC//MXene, especially at high rates.

Fig. 8d–e present Ragone plots normalized by the total mass or volume of two electrodes, respectively. The data in these plots demonstrate that the hybrid AC//MXene/AC/TEAPW12 features higher gravimetric energy densities as well as higher volumetric energy densities compared with AC//MXene. In the gravimetric Ragone plot, AC//MXene/AC/TEAPW12 delivers an energy density of 14.2 Wh kg^{-1} at a power density of 540 W kg^{-1} , 25% higher than AC//MXene. At high rates, the superiority of AC//MXene/AC/TEAPW12 is remarkable. The energy density of AC//MXene/AC/TEAPW12 is 5.6 times that of AC//MXene at 13.5 kW kg^{-1} . Meanwhile, even normalized by volume, AC//MXene/AC/TEAPW12 does not fall behind. At low power densities, AC//MXene/AC/TEAPW12 delivers almost equivalent volumetric energy densities (0.012 Wh cm^{-3} at 0.23 W cm^{-3}) compared with AC//MXene (0.013 Wh cm^{-3} at 0.29 W cm^{-3}). At high power densities, AC//MXene/AC/TEAPW12 outperforms AC//MXene significantly as well (8.5 mWh cm^{-3} at 11.5 W cm^{-3} for AC//MXene/AC/TEAPW12, 1.9 mWh cm^{-3} at 14.4 W cm^{-3} for AC//MXene). The advantage of AC//MXene/AC/TEAPW12 lies in its excellent rate capability of the asymmetric cell that must be associated with the merits of the hybrid MXene/AC/TEAPW12 electrode. That is, AC particles suppress restacking of MXene flakes, promoting ion diffusion and TEAPW12 clusters are dispersed homogeneously on AC, able to conduct fast reversible redox reaction. Both of them lead to excellent rate capability.

We also charge-discharged both asymmetric cells at 1 A g^{-1} for 10,000 cycles to evaluate their cycle stability (Fig. 8f). As we have proved the excellent cycle stability of MXene/AC/TEAPW12 single electrode in a wide potential range (Fig. 5d–e), the AC//MXene/AC/TEAPW12 cell is expected to have good cycle stability. After 10,000 cycles, 92% of its initial capacitance remained and although the AC//MXene cell also exhibits good cyclability, its cycle stability decreased faster (88% remaining after 10,000 cycles). The Coulombic efficiencies of both cells increased at the first few cycles, then stayed over 99.5%. We performed post-mortem analyses (Fig. S12) on the cycled MXene/AC/TEAPW12 electrode. The morphology of the cycled MXene/AC/TEAPW12 is as same as the fresh one, and the EDX spectrum indicates the existence of W. The long-term cycling did not damage the porous structure and the anchoring of POMs. The good cycle stability can be ascribed to both the stability of active materials and the proper charge balance and the fact that the potential of the two electrodes is not taken beyond the stable potential window of the electrolyte.

4. Conclusion

In this work, we did design and prepared for the first time a MXene/activated carbon (AC)/polyoxometalate(POM) hybrid material which shows synergic effects, making it possible an effective, functional and long-lasting incorporation of POMs to MXene. Our work also has shown how to modulate the properties of a final electrode by choosing wisely the properties of the components and the final composition. Thus, MXene plays the role of a conductive scaffold, provides high volumetric capacitance and allows for fabricating free-standing electrodes. AC serves as the matrix for anchoring POMs, provides high gravimetric capacitance and ensures good cyclic performance. POMs provide extra fast reversible redox activity and enhance volumetric capacitance. As-

prepared MXene/AC/TEAPW12 triple hybrid material delivered much larger gravimetric capacitance ($(87 \text{ F g}^{-1}$ at 1 mV s^{-1}) than MXene (40 F g^{-1} at 1 mV s^{-1}) in conventional organic electrolyte without sacrificing much volumetric capacitance (less than 10%). Even compared with MXene/AC of the same mass ratio, the gravimetric capacitance of MXene/AC/TEAPW12 was almost equivalent and the volumetric capacitance was 1.5 times higher. The capacitive performance can be further improved by replacing spherical TEA with flat EMIM cations in the electrolyte. The asymmetric cell AC//MXene/AC/TEAPW12 outperformed AC//MXene cell concerning both gravimetric (4.6 times higher at 13.5 kW kg^{-1}) and volumetric energy densities (3.5 times higher at around 13 W cm^{-3}) and featured very good cycle stability (92% after 10,000 cycles). The work shed light on the synergic effects in the triple hybrid materials. We can further improve gravimetric and/or volumetric capacitance by using other POMs, fine-tuning composition ratios, etc.

CRedit authorship contribution statement

Jun-jie Zhu: Methodology, Conceptualization, Formal analysis, Investigation, Writing – original draft. **Avireddy Hemesh:** Resources, Conceptualization, Formal analysis, Project administration. **Jordi Jacas Biendicho:** Software, Writing – review & editing. **Luis Martinez-Soria:** Resources, Data curation. **Daniel Rueda-Garcia:** Formal analysis, Resources. **Joan Ramon Morante:** Writing – review & editing, Funding acquisition. **Belen Ballesteros:** Formal analysis, Data curation. **Pedro Gomez-Romero:** Writing – review & editing, Supervision, Funding acquisition.

Declaration of Competing Interest

The authors declare that they have no known competing financial interests or personal relationships that could have appeared to influence the work reported in this paper.

Acknowledgements

Partial funding from Ministry of Science, Innovation and Universities (MCIU), the State Research Agency (AEI) and the European Regional Development Fund (FEDER) (grant RTI2018-099826-B-I00) and AGAUR (2017 SGR 00870, 2017 SGR 1246) are gratefully acknowledged. ICN2 and IREC are funded by the CERCA programme / Generalitat de Catalunya, and ICN2 is also supported by the Severo Ochoa Centres of Excellence programme, funded by the Spanish Research Agency (AEI, grant no. SEV-2017-0706). J.J. Z. acknowledges his scholarship (No. 201806370211) under China Scholarship Council. We thank Haizea Rodriguez Sagasti for help with the programming to calculate the contribution from different energy storage mechanisms. This work has been carried out within the framework of doctoral program (PhD) of Material Science (Department of Physics) of Universitat Autònoma de Barcelona (UAB).

Appendix A. Supplementary material

Supplementary data to this article can be found online at <https://doi.org/10.1016/j.jcis.2022.04.170>.

References

- [1] D.P. Dubal, O. Ayyad, V. Ruiz, P. Gomez-Romero, Hybrid energy storage: the merging of battery and supercapacitor chemistries, *Chem. Soc. Rev.* 44 (7) (2015) 1777–1790, <https://doi.org/10.1039/c4cs00266k>.
- [2] C.E. Shuck, Y. Gogotsi, Taking MXenes from the lab to commercial products, *Chem. Eng. J.* 401 (2020), <https://doi.org/10.1016/j.cej.2020.125786>.

- [3] M.R. Lukatskaya, S. Kota, Z. Lin, M.-Q. Zhao, N. Shpigiel, M.D. Levi, J. Halim, P.-L. Taberna, M.W. Barsoum, P. Simon, Y. Gogotsi, Ultra-high-rate pseudocapacitive energy storage in two-dimensional transition metal carbides, *Nat. Energy* 2 (8) (2017) 17105, <https://doi.org/10.1038/nenergy.2017.105>.
- [4] M. Ghidui, M.R. Lukatskaya, M.Q. Zhao, Y. Gogotsi, M.W. Barsoum, Conductive two-dimensional titanium carbide 'clay' with high volumetric capacitance, *Nature* 516 (7529) (2014) 78–81, <https://doi.org/10.1038/nature13970>.
- [5] M.Q. Zhao, C.E. Ren, Z. Ling, M.R. Lukatskaya, C. Zhang, K.L. Van Aken, M.W. Barsoum, Y. Gogotsi, Flexible MXene/carbon nanotube composite paper with high volumetric capacitance, *Adv. Mater.* 27 (2) (2015) 339–345, <https://doi.org/10.1002/adma.201404140>.
- [6] M.R. Lukatskaya, O. Mashtalir, C.E. Ren, Y. Dall'Agness, P. Rozier, P.L. Taberna, M. Naguib, P. Simon, M.W. Barsoum, Y. Gogotsi, Cation Intercalation and High Volumetric Capacitance of Two-Dimensional Titanium Carbide, *Science* 341 (6153) (2013) 1502–1505.
- [7] H. Avireddy, B.W. Byles, D. Pinto, J.M. Delgado Galindo, J.J. Biendicho, X. Wang, C. Flox, O. Crosnier, T. Brousse, E. Pomerantseva, J.R. Morante, Y. Gogotsi, Stable high-voltage aqueous pseudocapacitive energy storage device with slow self-discharge, *Nano Energy* 64 (2019), <https://doi.org/10.1016/j.nanoen.2019.103961>.
- [8] Y. Dall'Agness, P. Rozier, P.-L. Taberna, Y. Gogotsi, P. Simon, Capacitance of two-dimensional titanium carbide (MXene) and MXene/carbon nanotube composites in organic electrolytes, *J. Power Sources* 306 306 (2016) 510–515.
- [9] Z. Lin, D. Barbara, P.-L. Taberna, K.L. Van Aken, B. Anasori, Y. Gogotsi, P. Simon, Capacitance of Ti3C2Tx MXene in ionic liquid electrolyte, *J. Power Sources* 326 (2016) 575–579, <https://doi.org/10.1016/j.jpowsour.2016.04.035>.
- [10] Q. Fan, R. Zhao, M. Yi, P. Qi, C. Chai, H. Ying, J. Hao, Ti3C2–MXene composite films functionalized with polypyrrole and ionic liquid-based microemulsion particles for supercapacitor applications, *Chem. Eng. J.* 428 (2022), <https://doi.org/10.1016/j.cej.2021.131107>.
- [11] J. Luo, W. Zhang, H. Yuan, C. Jin, L. Zhang, H. Huang, C. Liang, Y. Xia, J. Zhang, Y. Gan, X. Tao, Pillared Structure Design of MXene with Ultralarge Interlayer Spacing for High-Performance Lithium-Ion Capacitors, *ACS Nano* 11 (3) (2017) 2459–2469, <https://doi.org/10.1021/acsnano.6b07668>.
- [12] X. Wang, T.S. Mathis, K. Li, Z. Lin, L. Vleck, T. Torita, N.C. Osti, C. Hatter, P. Urbankowski, A. Sarycheva, M. Tyagi, E. Mamontov, P. Simon, Y. Gogotsi, Influences from solvents on charge storage in titanium carbide MXenes, *Nat. Energy* 4 (3) (2019) 241–248, <https://doi.org/10.1038/s41560-019-0339-9>.
- [13] X. Wang, S. Kajiyama, H. Iinuma, E. Hosono, S. Oro, I. Moriguchi, M. Okubo, A. Yamada, Pseudocapacitance of MXene nanosheets for high-power sodium-ion hybrid capacitors, *Nat. Commun.* 6 (2015) 6544, <https://doi.org/10.1038/ncomms7544>.
- [14] J. Luo, C. Fang, C. Jin, H. Yuan, O. Sheng, R. Fang, W. Zhang, H. Huang, Y. Gan, Y. Xia, C. Liang, J. Zhang, W. Li, X. Tao, Tunable pseudocapacitance storage of MXene by cation pillaring for high performance sodium-ion capacitors, *J. Mater. Chem. A* 6 (17) (2018) 7794–7806, <https://doi.org/10.1039/c8ta02068j>.
- [15] S. Kajiyama, L. Szabova, H. Iinuma, A. Sugahara, K. Gotoh, K. Sodeyama, Y. Tateyama, M. Okubo, A. Yamada, Enhanced Li-Ion Accessibility in MXene Titanium Carbide by Steric Chloride Termination, *Adv. Energy Mater.* 7 (9) (2017) 1601873, <https://doi.org/10.1002/aenm.201601873>.
- [16] L.Y. Yu, L.F. Hu, B. Anasori, Y.T. Liu, Q.Z. Zhu, P. Zhang, Y. Gogotsi, B. Xu, MXene-Bonded Activated Carbon as a Flexible Electrode for High-Performance Supercapacitors, *ACS Energy Lett.* 3 (7) (2018) 1597–1603, <https://doi.org/10.1021/acsenerylett.8b00718>.
- [17] A.S. Levitt, M. Alhabeb, C.B. Hatter, A. Sarycheva, G. Dion, Y. Gogotsi, Electrospun MXene/carbon nanofibers as supercapacitor electrodes, *J. Mater. Chem. A* 7 (1) (2019) 269–277.
- [18] W. Zheng, P. Zhang, J. Chen, W.B. Tian, Y.M. Zhang, Z.M. Sun, In situ synthesis of CNTs@Ti3C2 hybrid structures by microwave irradiation for high-performance anodes in lithium ion batteries, *J. Mater. Chem. A* 6 (8) (2018) 3543–3551, <https://doi.org/10.1039/c7ta10394h>.
- [19] M. Hu, R. Cheng, Z. Li, T. Hu, H. Zhang, C. Shi, J. Yang, C. Cui, C. Zhang, H. Wang, B. Fan, X. Wang, Q.-H. Yang, Interlayer engineering of Ti3C2Tx MXenes towards high capacitance supercapacitors, *Nanoscale* 12 (2) (2020) 763–771.
- [20] S. Zheng, C.J. Zhang, F. Zhou, Y. Dong, X. Shi, V. Nicolosi, Z.-S. Wu, X. Bao, Ionic liquid pre-intercalated MXene films for ionogel-based flexible micro-supercapacitors with high volumetric energy density, *J. Mater. Chem. A* 7 (16) (2019) 9478–9485.
- [21] Y. Wen, R. Li, J. Liu, Z. Wei, S. Li, L. Du, K. Zu, Z. Li, Y. Pan, H. Hu, A temperature-dependent phosphorus doping on Ti3C2Tx MXene for enhanced supercapacitance, *J. Colloid Interface Sci.* 604 (2021) 239–247, <https://doi.org/10.1016/j.jcis.2021.06.020>.
- [22] Z. Zhao, X. Wu, C. Luo, Y. Wang, W. Chen, Rational design of Ti3C2Cl2 MXenes nanodots-interspersed MXene@NiAl-layered double hydroxides for enhanced pseudocapacitor storage, *J. Colloid Interface Sci.* 609 (2022) 393–402, <https://doi.org/10.1016/j.jcis.2021.12.041>.
- [23] Y. Zhu, K. Rajiou, S. Le Vot, O. Fontaine, P. Simon, F. Favier, Modifications of MXene layers for supercapacitors, *Nano Energy* 73 (2020), <https://doi.org/10.1016/j.nanoen.2020.104734>.
- [24] X. Yang, Q. Wang, K. Zhu, K. Ye, G. Wang, D. Cao, J. Yan, 3D Porous Oxidation-Resistant MXene/Graphene Architectures Induced by In Situ Zinc Template toward High-Performance Supercapacitors, *Adv. Funct. Mater.* 31 (20) (2021) 2101087, <https://doi.org/10.1002/adfm.202101087>.
- [25] S. Chen, Y.F. Xiang, M.K. Banks, C. Peng, W.J. Xu, R.X. Wu, Polyoxometalate-coupled MXene nanohybrid via poly(ionic liquid) linkers and its electrode for enhanced supercapacitive performance, *Nanoscale* 10 (42) (2018) 20043–20052, <https://doi.org/10.1039/c8nr05760e>.
- [26] H. Niu, Q. Yang, Q. Wang, X. Jing, K. Zhu, K. Ye, G. Wang, D. Cao, J. Yan, Oxygen vacancies-enriched sub-7 nm cross-linked Bi2.88Fe5O12-x nanoparticles anchored MXene for electrochemical energy storage with high volumetric performances, *Nano Energy* 78 (2020), <https://doi.org/10.1016/j.nanoen.2020.105360>.
- [27] Z. Zou, Q. Wang, J. Yan, K. Zhu, K. Ye, G. Wang, D. Cao, Versatile Interfacial Self-Assembly of Ti3C2Tx MXene Based Composites with Enhanced Kinetics for Superior Lithium and Sodium Storage, *ACS Nano* 15 (7) (2021) 12140–12150, <https://doi.org/10.1021/acsnano.1c03516>.
- [28] W. Wu, C. Wang, C. Zhao, D. Wei, J. Zhu, Y. Xu, Facile strategy of hollow polyaniline nanotubes supported on Ti3C2-MXene nanosheets for High-performance symmetric supercapacitors, *J. Colloid Interface Sci.* 580 (2020) 601–613, <https://doi.org/10.1016/j.jcis.2020.07.052>.
- [29] Y. Zhang, P. Chen, Q. Wang, Q. Wang, K. Zhu, K. Ye, G. Wang, D. Cao, J. Yan, Q. Zhang, High-Capacity and Kinetically Accelerated Lithium Storage in MoO3 Enabled by Oxygen Vacancies and Heterostructure, *Adv. Energy Mater.* 11 (31) (2021) 2101712, <https://doi.org/10.1002/aenm.202101712>.
- [30] H. Li, F. Musharavati, E. Zalenezhad, X. Chen, K.N. Hui, K.S. Hui, Electrodeposited NiCo layered double hydroxides on titanium carbide as a binder-free electrode for supercapacitors, *Electrochim. Acta* 261 (2018) 178–187, <https://doi.org/10.1016/j.electacta.2017.12.139>.
- [31] H. Li, X. Chen, E. Zalenezhad, K.N. Hui, K.S. Hui, M.J. Ko, 3D hierarchical transition-metal sulfides deposited on MXene as binder-free electrode for high-performance supercapacitors, *J. Ind. Eng. Chem.* 82 (2020) 309–316, <https://doi.org/10.1016/j.jiec.2019.10.028>.
- [32] H. Chao, H. Qin, M. Zhang, Y. Huang, L. Cao, H. Guo, K. Wang, X. Teng, J. Cheng, Y. Lu, H. Hu, M. Wu, Boosting the Pseudocapacitive and High Mass-Loaded Lithium/Sodium Storage through Bonding Polyoxometalate Nanoparticles on MXene Nanosheets, *Adv. Funct. Mater.* 31 (16) (2021) 2007636, <https://doi.org/10.1002/adfm.202007636>.
- [33] J.-J. Zhu, R. Benages-Vilau, P. Gomez-Romero, Can polyoxometalates enhance the capacitance and energy density of activated carbon in organic electrolyte supercapacitors?, *Electrochim. Acta* 362 (2020), <https://doi.org/10.1016/j.electacta.2020.137007>.
- [34] Y. Hou, D.F. Chai, B.A. Li, H.J. Pang, H.Y. Ma, X.M. Wang, L.C. Tan, Polyoxometalate-Incorporated Metallacalixarene@Graphene Composite Electrodes for High-Performance Supercapacitors, *ACS Appl. Mater. Interfaces* 11 (23) (2019) 20845–20853, <https://doi.org/10.1021/acsaami.9b04649>.
- [35] M.R. Horn, A. Singh, S. Alomari, S. Goberna-Ferrón, R. Benages-Vilau, N. Chodankar, N. Motta, K. Ostrikov, J. MacLeod, P. Sonar, P. Gomez-Romero, D. Dubal, Polyoxometalates (POMs): from electroactive clusters to energy materials, *Energy Environ. Sci.* 14 (4) (2021) 1652–1700, <https://doi.org/10.1039/d0ee03407j>.
- [36] S.-C. Huang, C.-C. Lin, C.-W. Hu, Y.-F. Liao, T.-Y. Chen, H.-Y. Chen, Vanadium-based polyoxometalate as electron/ion sponge for lithium-ion storage, *J. Power Sources* 435 (2019), <https://doi.org/10.1016/j.jpowsour.2019.226702>.
- [37] J. Vaillant, M. Lira-Cantu, K. Cuentas-Gallegos, N. Casañ-Pastor, P. Gómez-Romero, Chemical synthesis of hybrid materials based on PANi and PEDOT with polyoxometalates for electrochemical supercapacitors, *Prog. Solid State Chem.* 34 (2–4) (2006) 147–159, <https://doi.org/10.1016/j.progsolidstchem.2005.11.015>.
- [38] J. Suarez-Guevara, V. Ruiz, P. Gomez-Romero, Stable graphene-polyoxometalate nanomaterials for application in hybrid supercapacitors, *Phys. Chem. Chem. Phys.* 16 (38) (2014) 20411–20414, <https://doi.org/10.1039/c4cp03321c>.
- [39] J. Suárez-Guevara, V. Ruiz, P. Gomez-Romero, Hybrid energy storage: high voltage aqueous supercapacitors based on activated carbon-phosphotungstate hybrid materials, *J. Mater. Chem. A* 2 (4) (2014) 1014–1021, <https://doi.org/10.1039/c3ta14455k>.
- [40] D.P. Dubal, J. Suarez-Guevara, D. Tonti, E. Enciso, P. Gomez-Romero, A high voltage solid state symmetric supercapacitor based on graphene-polyoxometalate hybrid electrodes with a hydroquinone doped hybrid gel-electrolyte, *J. Mater. Chem. A* 3 (46) (2015) 23483–23492, <https://doi.org/10.1039/c5ta05660h>.
- [41] M. Genovese, K. Lian, Pseudocapacitive behavior of Keggin type polyoxometalate mixtures, *Electrochem. Commun.* 43 (2014) 60–62, <https://doi.org/10.1016/j.elecom.2014.03.014>.
- [42] V. Ruiz, J. Suarez-Guevara, P. Gomez-Romero, Hybrid electrodes based on polyoxometalate-carbon materials for electrochemical supercapacitors, *Electrochem. Commun.* 24 (2012) 35–38, <https://doi.org/10.1016/j.elecom.2012.08.003>.
- [43] M. Genovese, K. Lian, Polyoxometalate modified pine cone biochar carbon for supercapacitor electrodes, *J. Mater. Chem. A* 5 (8) (2017) 3939–3947, <https://doi.org/10.1039/c6ta10382k>.
- [44] S. Kumar, G. Saeed, L. Zhu, K.N. Hui, N.H. Kim, J.H. Lee, OD to 3D carbon-based networks combined with pseudocapacitive electrode material for high energy density supercapacitor: A review, *Chem. Eng. J.* 403 (2021), <https://doi.org/10.1016/j.cej.2020.126352>.
- [45] M. Alhabeb, K. Maleski, B. Anasori, P. Lelyukh, L. Clark, S. Sin, Y. Gogotsi, Guidelines for Synthesis and Processing of Two-Dimensional Titanium Carbide (Ti3C2Tx MXene), *Chem. Mater.* 29 (18) (2017) 7633–7644, <https://doi.org/10.1021/acs.chemmater.7b02847>.

- [46] N. Shpigel, A. Chakraborty, F. Malchik, G. Bergman, A. Nimkar, B. Gavriel, M. Turgeman, C.N. Hong, M.R. Lukatskaya, M.D. Levi, Y. Gogotsi, D.I. Major, D. Aurbach, Can Anions Be Inserted into MXene?, *J Am. Chem. Soc.* 143 (32) (2021) 12552–12559, <https://doi.org/10.1021/jacs.1c03840>.
- [47] M. Malaki, A. Maleki, R.S. Varma, MXenes and ultrasonication, *J. Mater. Chem. A* 7 (18) (2019) 10843–10857, <https://doi.org/10.1039/c9ta01850f>.
- [48] S. Zhou, C. Gu, Z. Li, L. Yang, L. He, M. Wang, X. Huang, N. Zhou, Z. Zhang, Ti₃C₂T_x MXene and polyoxometalate nanohybrid embedded with polypyrrole: Ultra-sensitive platform for the detection of osteopontin, *Appl. Surf. Sci.* 498 (2019) 143889.
- [49] L. Zong, H. Wu, H. Lin, Y. Chen, A polyoxometalate-functionalized two-dimensional titanium carbide composite MXene for effective cancer theranostics, *Nano Res.* 11 (8) (2018) 4149–4168, <https://doi.org/10.1007/s12274-018-2002-3>.
- [50] L.-Å. Näslund, P.O.A. Persson, J. Rosen, X-ray Photoelectron Spectroscopy of Ti₃AlC₂, Ti₃C₂T_x, and TiC Provides Evidence for the Electrostatic Interaction between Laminated Layers in MAX-Phase Materials, *The Journal of Physical Chemistry C* 124 (50) (2020) 27732–27742, <https://doi.org/10.1021/acs.jpcc.0c07413>.
- [51] C. Shen, L. Wang, A. Zhou, B. Wang, X. Wang, W. Lian, Q. Hu, G. Qin, X. Liu, Synthesis and Electrochemical Properties of Two-Dimensional RGO/Ti(3)C(2)Tx Nanocomposites, *Nanomaterials (Basel)* 8 (2) (2018), <https://doi.org/10.3390/nano8020080>.
- [52] J. Wang, J. Polleux, J. Lim, B. Dunn, Pseudocapacitive Contributions to Electrochemical Energy Storage in TiO₂ (Anatase) Nanoparticles, *The Journal of Physical Chemistry C* 111 (40) (2007) 14925–14931, <https://doi.org/10.1021/jp074464w>.
- [53] H. Huang, D. Kundu, R. Yan, E. Tervoort, X. Chen, L. Pan, M. Oschatz, M. Antonietti, M. Niederberger, Fast Na-Ion Intercalation in Zinc Vanadate for High-Performance Na-Ion Hybrid Capacitor, *Adv. Energy Mater.* 8 (35) (2018) 1802800, <https://doi.org/10.1002/aenm.201802800>.
- [54] L. Hu, R. Gao, A. Zhang, R. Yang, X. Zang, S. Wang, S. Yao, Z. Yang, H. Hao, Y.-M. Yan, Cu²⁺ intercalation activates bulk redox reactions of MnO₂ for enhancing capacitive performance, *Nano Energy* 74 (2020), <https://doi.org/10.1016/j.nanoen.2020.104891>.
- [55] J. Li, X. Yuan, C. Lin, Y. Yang, L.e. Xu, X. Du, J. Xie, J. Lin, J. Sun, Achieving High Pseudocapacitance of 2D Titanium Carbide (MXene) by Cation Intercalation and Surface Modification, *Adv. Energy Mater.* 7 (15) (2017) 1602725.

Supplementary materials

Rational design of MXene/Activated carbon/Polyoxometalates triple hybrid electrodes with enhanced capacitance for organic-electrolyte supercapacitors

Jun-Jie Zhu^{a,*}, Hemesh Avireddy^b, Jordi Jacas Biendicho^b, Joan Ramon Morante^{b,c}, Belen Ballesteros^a, Pedro Gomez-Romero^{a,d,*}

^a Catalan Institute of Nanoscience and Nanotechnology (ICN2), CSIC and BIST, Campus UAB, Bellaterra, 08193 Barcelona, Spain.

^b Catalonia Institute for Energy Research (IREC), Jardins de les Dones de Negre 1, 08930, Sant Adrià de Besòs, Spain.

^c Faculty of Physics, University of Barcelona, Barcelona, Spain

^d Consejo Superior de Investigaciones Científicas (CSIC), Spain

*Authors to whom correspondence should be addressed

* Corresponding author. E-mail address: pedro.gomez@icn2.cat (P. Gomez-Romero), zhu.junjie@icn2.cat (J.J. Zhu) Tel: +34 937373608, Fax: +34 936917640, ICN2, Campus UAB, 08193 Bellaterra (Barcelona) Spain

Synthesis of MXene/AC

0.05 g activated carbon was added into and 50 mL $\text{Ti}_3\text{C}_2\text{T}_x$ MXene colloid (around 1 mg mL^{-1}), kept in probe-sonication for 1 h under circulating cooling water to keep the temperature below $10 \text{ }^\circ\text{C}$. The mixture was filtered off onto Celgard 3501 membrane to get a free-standing electrode. The as-prepared electrode has a thickness of $36 \text{ }\mu\text{m}$ and an areal density of 1.8 mg cm^{-2} .

In-situ growth MXene/TEAPW12

Delamination of MXene with TEOAH

MXene was treated with tetrabutylammonium hydroxide (TEAOH) to replace Li^+ with TEA cation. Typically, 5 mL 40% TEOAH solution was mixed with 50 mL MXene colloid (around 1 mg mL^{-1}), and kept shaking overnight. A certain amount of this mixture was filtered, washed with water until the filtrate was neutral, dried at $60 \text{ }^\circ\text{C}$ under vacuum, named as MXene/TEAOH, for further characterization.

Synthesis of MXene/TEAPW12

After the washing process of preparing MXene/TEAOH (until the pH of filtrate < 8.5), 20 mL of 20 mM phosphotungstic acid was added on the residue, rest for 3 h, filtered it again and washed it until the filtrate was neutral ($\text{pH} > 5.5$). The MXene/POMs hybrid (MXene/TEAPW12) was obtained. The as-prepared free-standing electrode has a thickness of $10 \text{ }\mu\text{m}$ and an areal density of 3.5 mg cm^{-2} .

Preparation of activated carbon electrode for asymmetric capacitors

The activated carbon electrodes serve as the positive electrodes in the asymmetric capacitors. First, activated carbon, carbon black and poly(vinylidene fluoride) were mixed at a weight ratio of 85:5:10 and smashed in a mortar. A few drops of N-methyl-2-pyrrolidinone was added in the mixed powder to form a slurry, kept stirring for 6 h, then coated onto aluminum foil ($>99\%$, with the thickness of 0.018 mm) with doctor-blade method (RK PrintCoat, with the gap of $60 \text{ }\mu\text{m}$), and dried under vacuum at $120 \text{ }^\circ\text{C}$ for 12 h. The loading mass of each electrode is in the range of $1.5\text{-}2 \text{ mg cm}^{-2}$, the density of the AC electrode is 0.52 g cm^{-3} . The specific capacitance of this electrode is 82 F g^{-1} at 2 mV s^{-1} according to our previous study.

Charge balance of the asymmetric capacitors

The charge balance calculation was processed with the following equation

$$\frac{m_+}{m_-} = \frac{C_- \times \Delta E_-}{C_+ \times \Delta E_+}$$

where m_+ and m_- are the mass of the two electrodes, C_+ and C_- are the gravimetric capacitance of the active materials on the electrodes, ΔE_+ and ΔE_- are the variation ranges of the potential on the electrodes.

In our case, ΔE_- is 1.7 V (-2.2 to -0.5 V), and ΔE_+ is 1 V (-0.5 to 0.5 V), $m_{AC}: m_{MXene/AC/TEAPW12}=1.1$, and $m_{AC}: m_{MXene}=0.76$

After the mass balance, the asymmetric capacitors are assembled in CR2032 coin cells with a coin-cell crimper (TMAXCN).

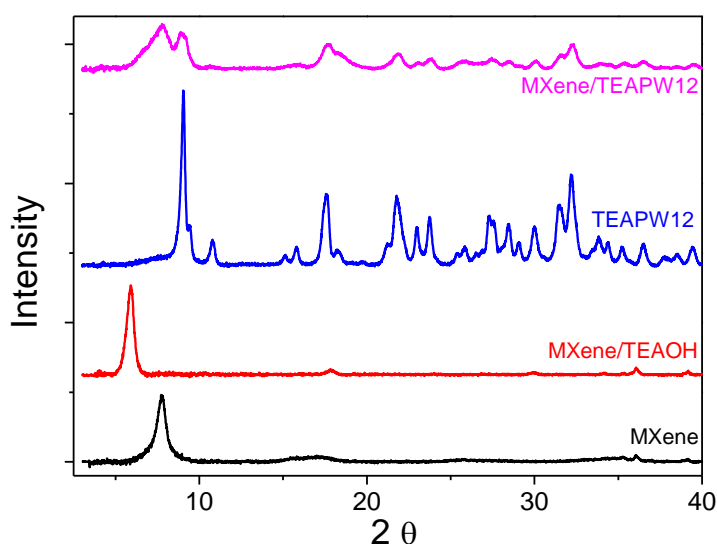


Fig. S1. XRD patterns of MXene/TEAPW12, TEAPW12, MXene/TEAOH and MXene

Discussion: The patterns of Mxene/TEAOH exhibits a peak at 5.896° , and the interlayer distance expands to 14.445 \AA , proving the successful replacement of Li^+ with TEA^+ because TEA^+ is larger than Li^+ . Alhabeab et al. prepared TMAOH(tetramethylammonium hydroxide) delaminated $\text{Ti}_3\text{C}_2\text{T}_x$ MXene, with the position of (002) peak at 6.0° [1]. They point out TEAOH could not delaminate $\text{Ti}_3\text{C}_2\text{T}_x$ MXene but do with V_2CT_x and Ti_3CNT_x MXenes. Herein, we get a different result because we use LiF/HCl-etched $\text{Ti}_3\text{C}_2\text{T}$ instead of HF-etched $\text{Ti}_3\text{C}_2\text{T}$. It is easier to exchange Li^+ than proton with TEA^+ because it needs smaller interlayer space expansion. Finally, we got a larger interlayer distance than TMAOH-delaminated $\text{Ti}_3\text{C}_2\text{T}_x$ MXene. MXene/TEAPW12 exhibits a little bit smaller interlayer distance, which must be due to partial removal of TEA^+ in the reaction between TEA^+ and PW12 anions. The non-expanded interlayer distance is evidence that the deposition of TEAPW12 clusters happened on the surface,

instead of in layers.

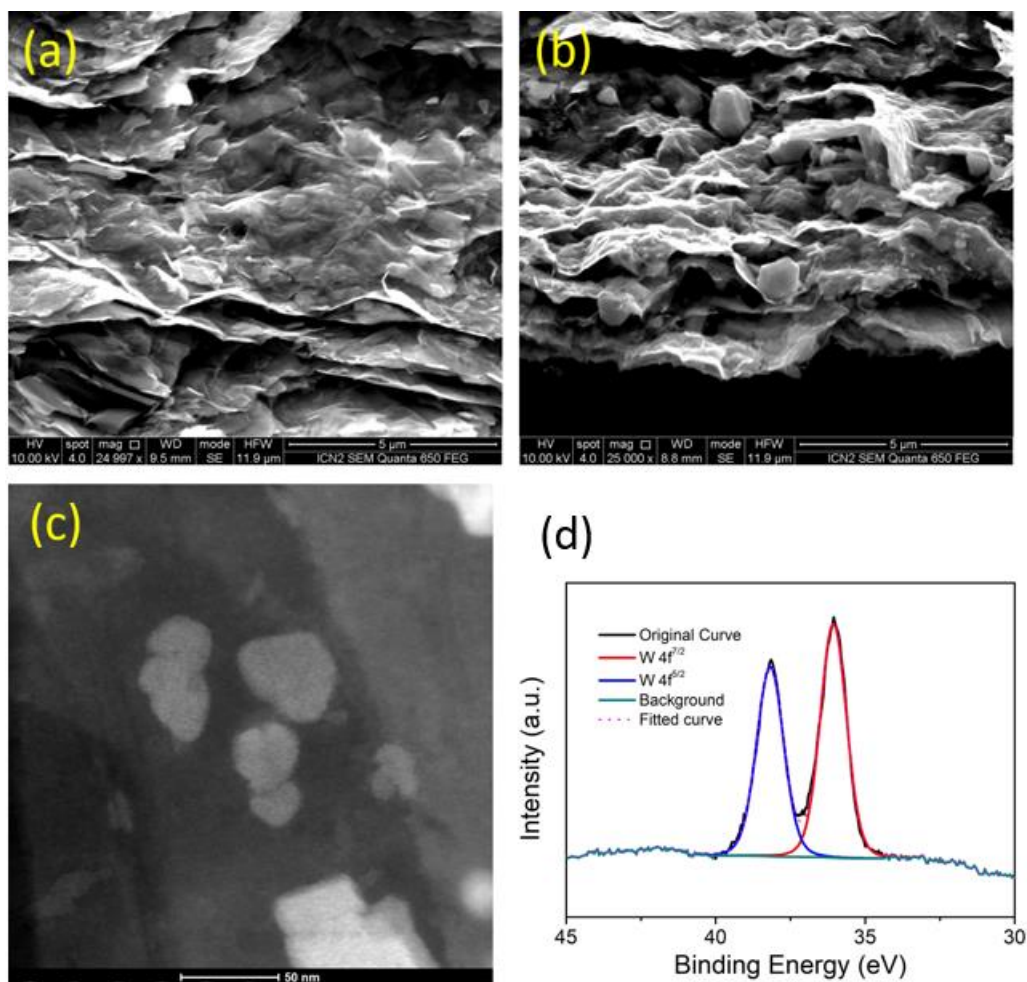


Fig. S2 SEM images of (a) MXene/TEAOH and (b) MXene/TEAPW12. (c) HAADF-STEM image of MXene/TEAPW12

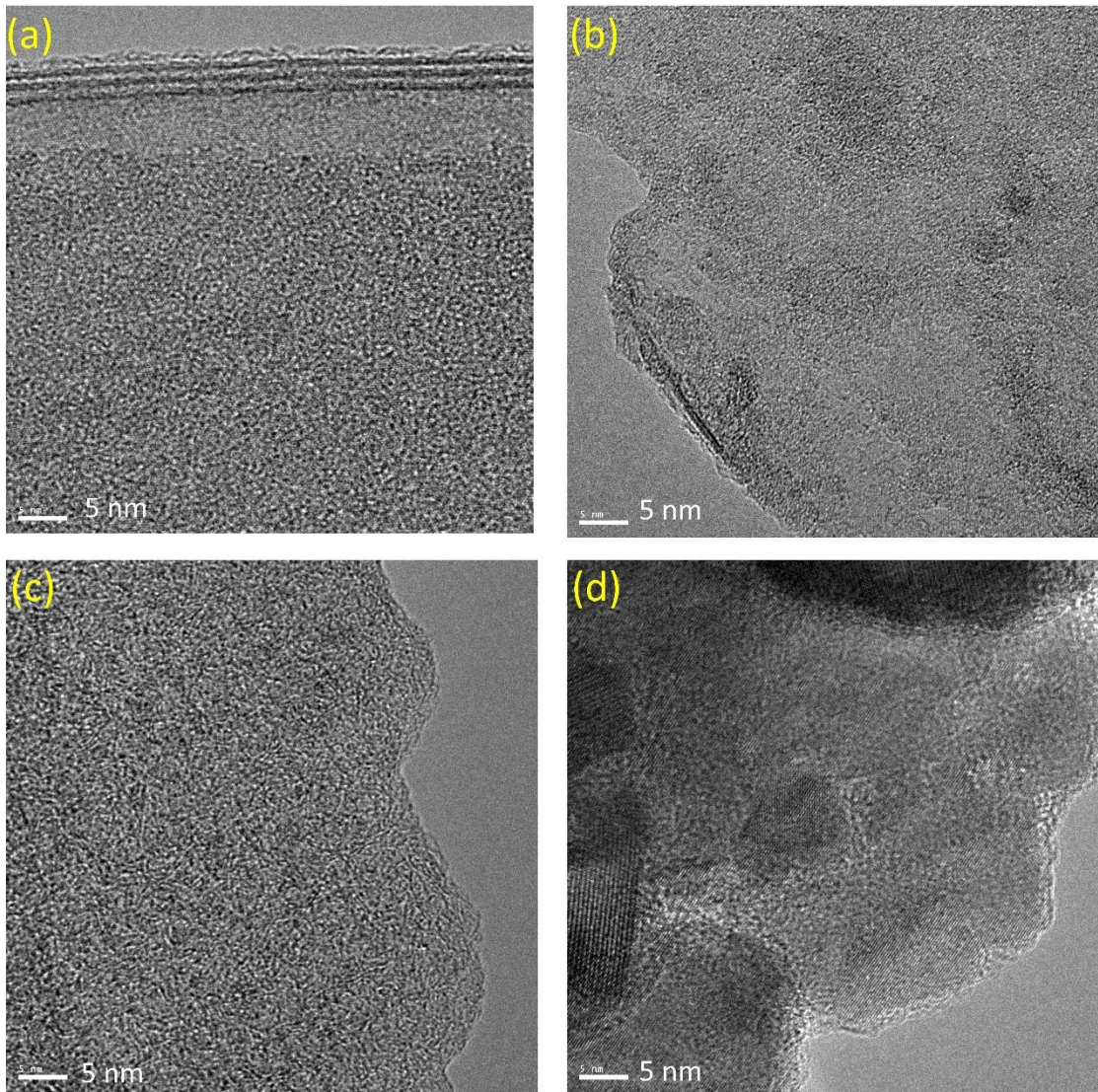


Fig. S3 HR-TEM images of (a) MXene, (b) MXene/HPW12, (c) MXene/AC/TEAPW12 and (d) MXene/AC/TEAPW12.

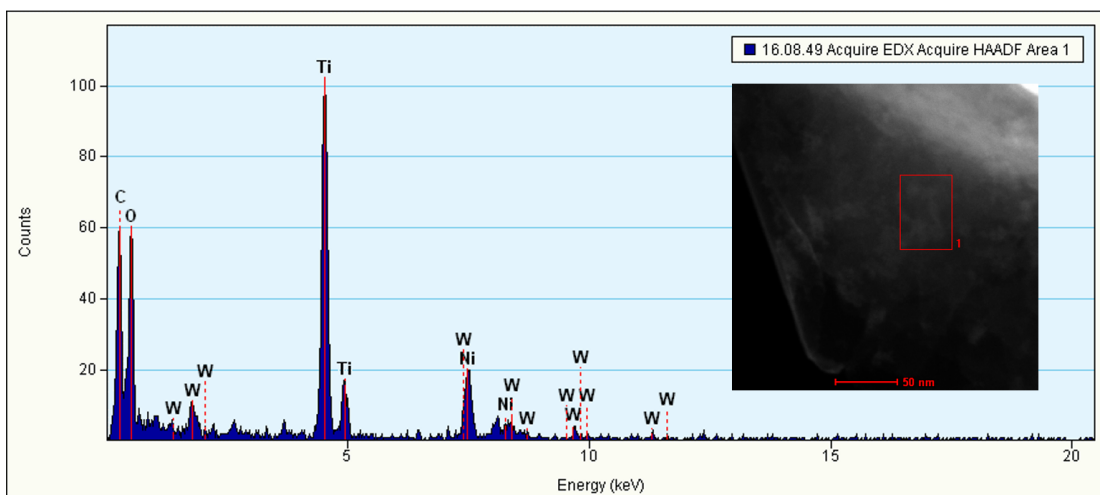


Fig. S4 EDX spectrum of MXene/HPW12.

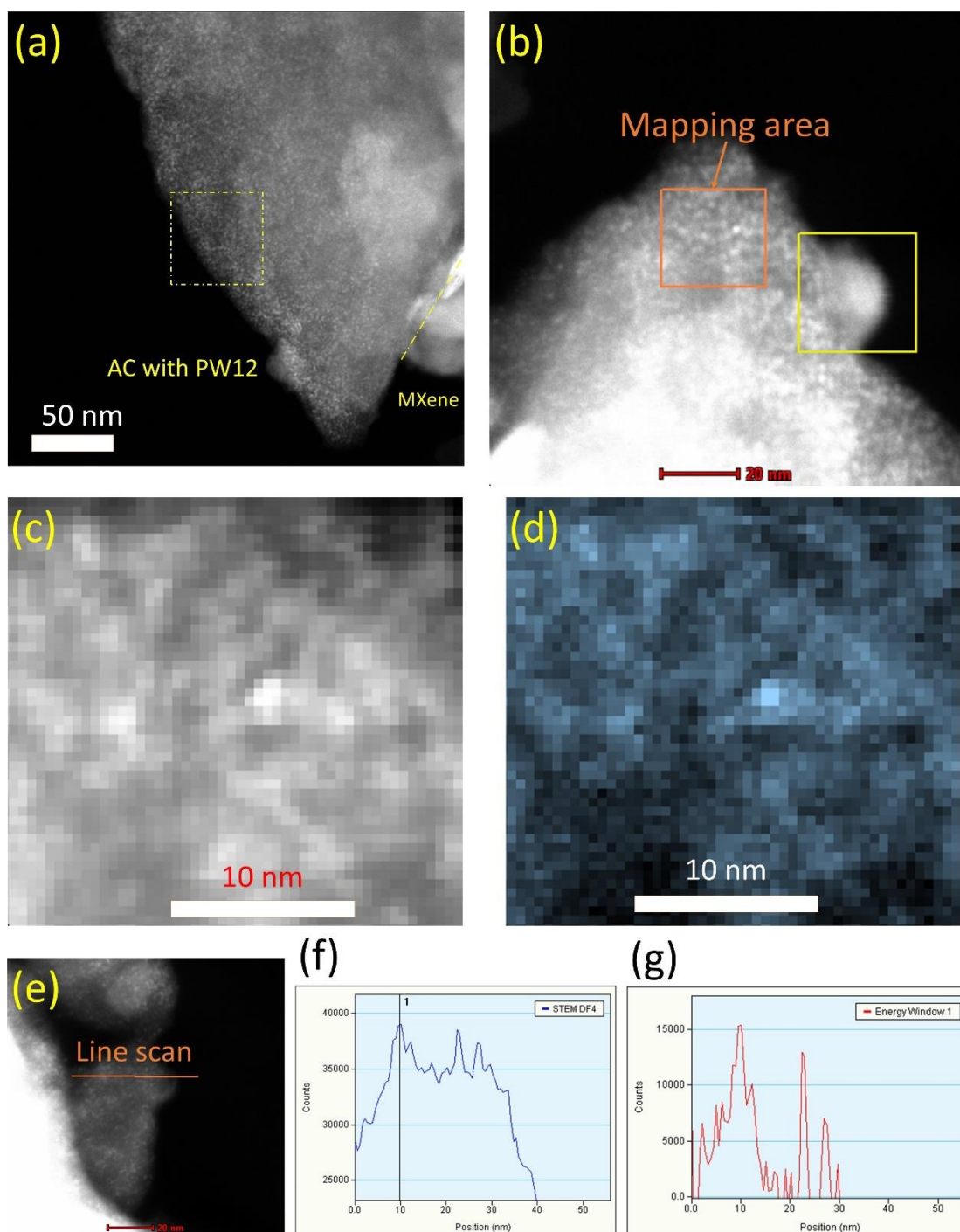


Fig. S5 (a) HAADF-STEM image of MXene/AC/TEAPW12, in which both MXene and AC/TEAPW12 are in horizon. (c) Mapping of HAADF-STEM signal. (d) Mapping of W. (e) Line scan range. (f) Line scan of STEM signal. (g) Line scan of W signal, whose fluctuation keeps pace with STEM signal.

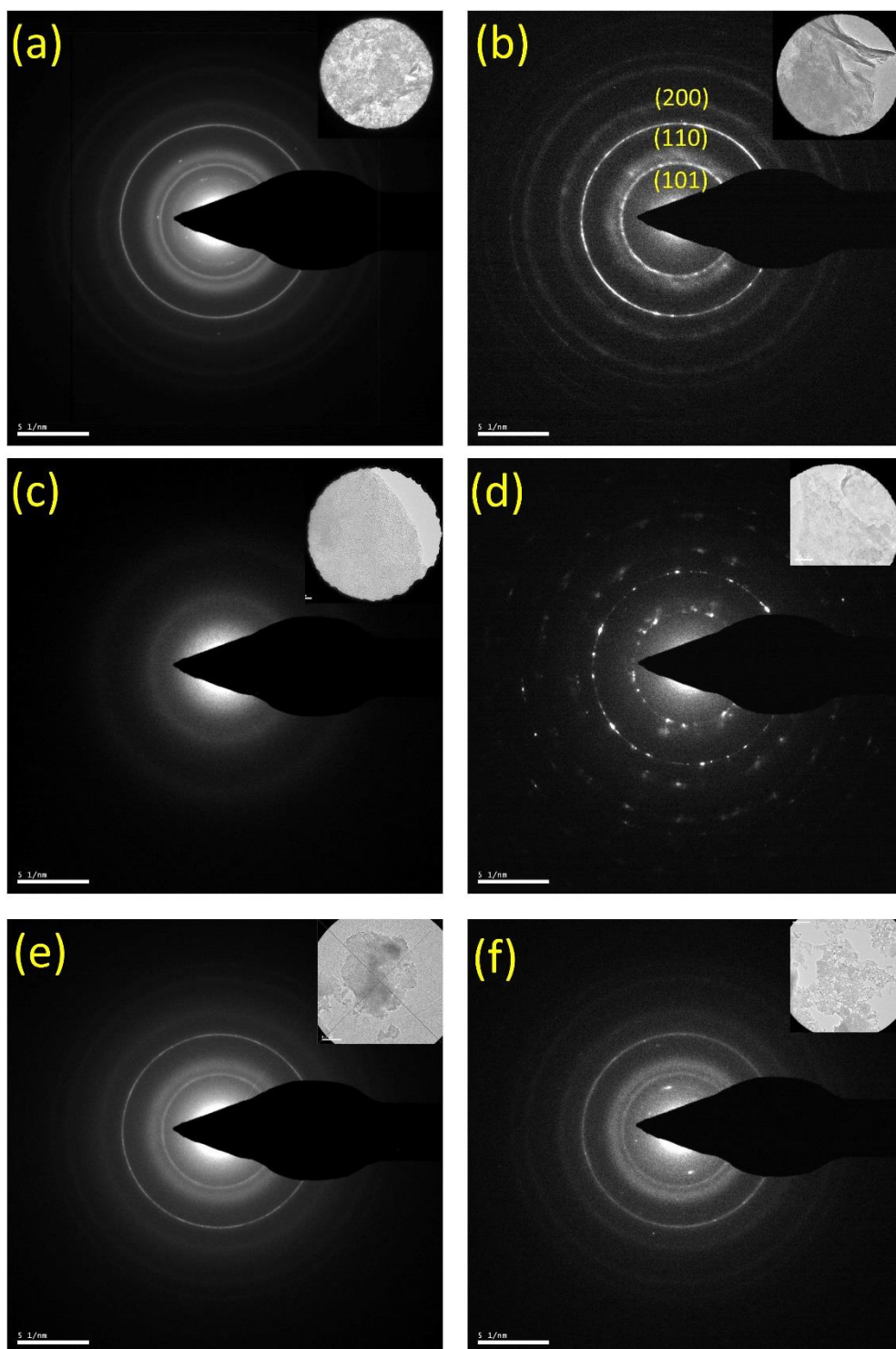


Fig. S6 Selected area electron diffraction patterns of (a) MXene, (b) MXene/HPW12, (c) AC/TEAPW12 area in MXene/AC/TEAPW12, (d) MXene area in MXene/AC/TEAPW12, (e) mixed area in MXene/AC/TEAPW12 and (f) mixed area in MXene/AC/HPW12

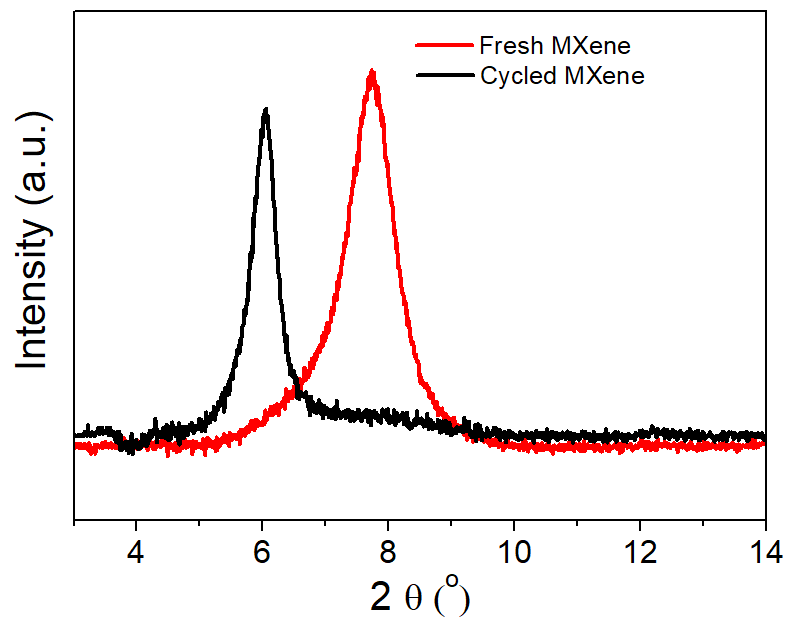


Fig. S7 XRD patterns of fresh MXene and cycled MXene

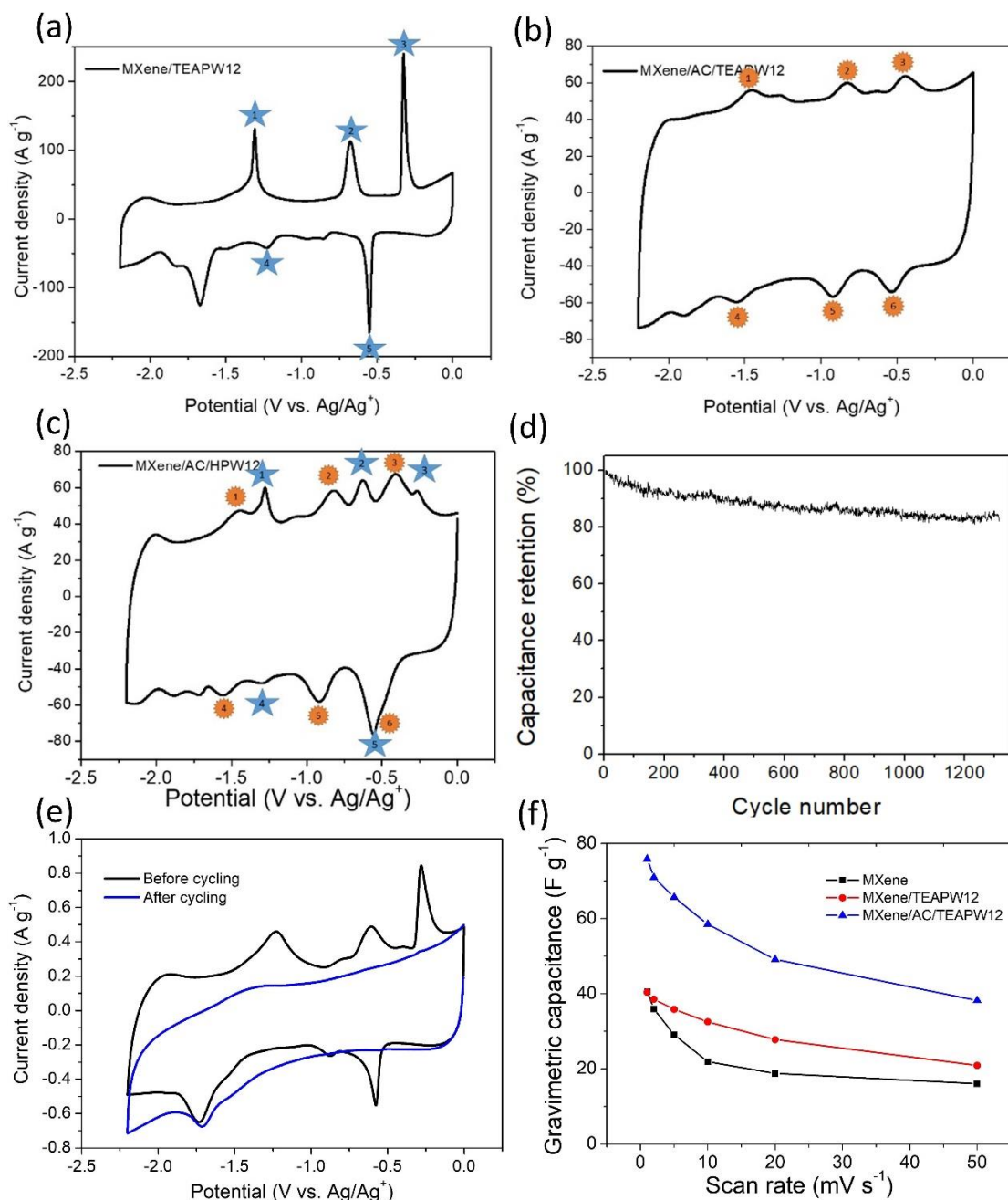


Fig. S8 CVs of (a) MXene/TEAPW12, (b) MXene/AC/TEAPW12 and (c) MXene/AC/HPW12. (The redox peaks in the CV of MXene/AC/HPW12 can be classified: the star-labelled peaks are from PW12 clusters on MXene, the circle-labelled peaks are from PW12 cluster on AC. (d) Cycling stability test of MXene/TEAPW12. (e) CVs of MXene/TEAPW12 at 10 mV s⁻¹ before and after 1000 cycles. (f) Gravimetric capacitance of MXene/TEAPW12, MXene and MXene/AC/TEAPW12.

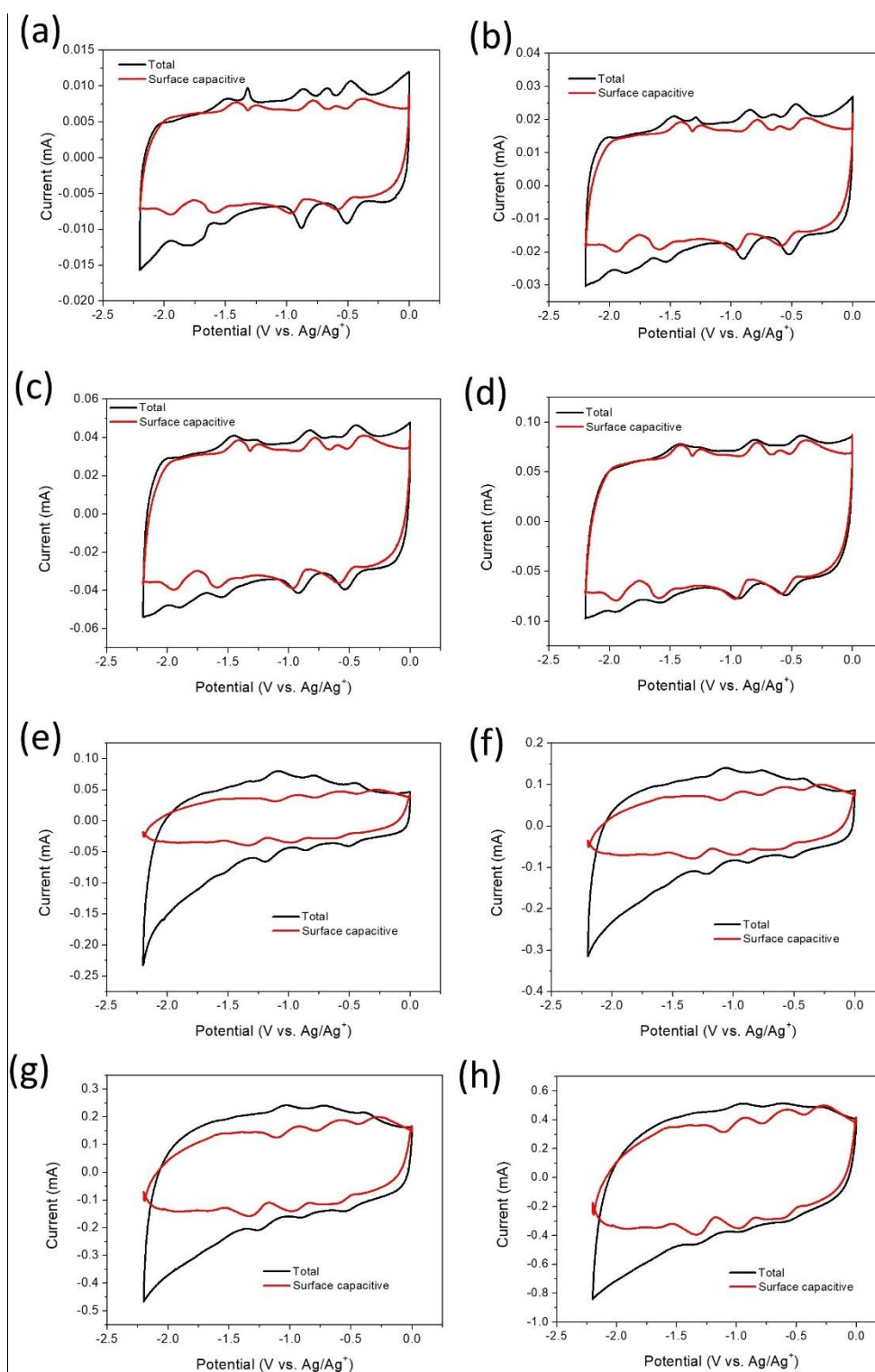


Fig. S9 CVs and the contribution from surface capacitive current of MXene/AC/TEAPW12 in 1 M TEABF4 in acetonitrile at (a) 0.2 mV s⁻¹, (b) 0.5 mV s⁻¹, (c) 1 mV s⁻¹ and (d) 2 mV s⁻¹. CVs and the contribution from non-diffusion controlled current of MXene/AC/TEAPW12 in 1 M EMIMTFSI in acetonitrile at (e) 0.2 mV s⁻¹, (f) 0.5 mV s⁻¹, (g) 1 mV s⁻¹ and (h) 2 mV s⁻¹.

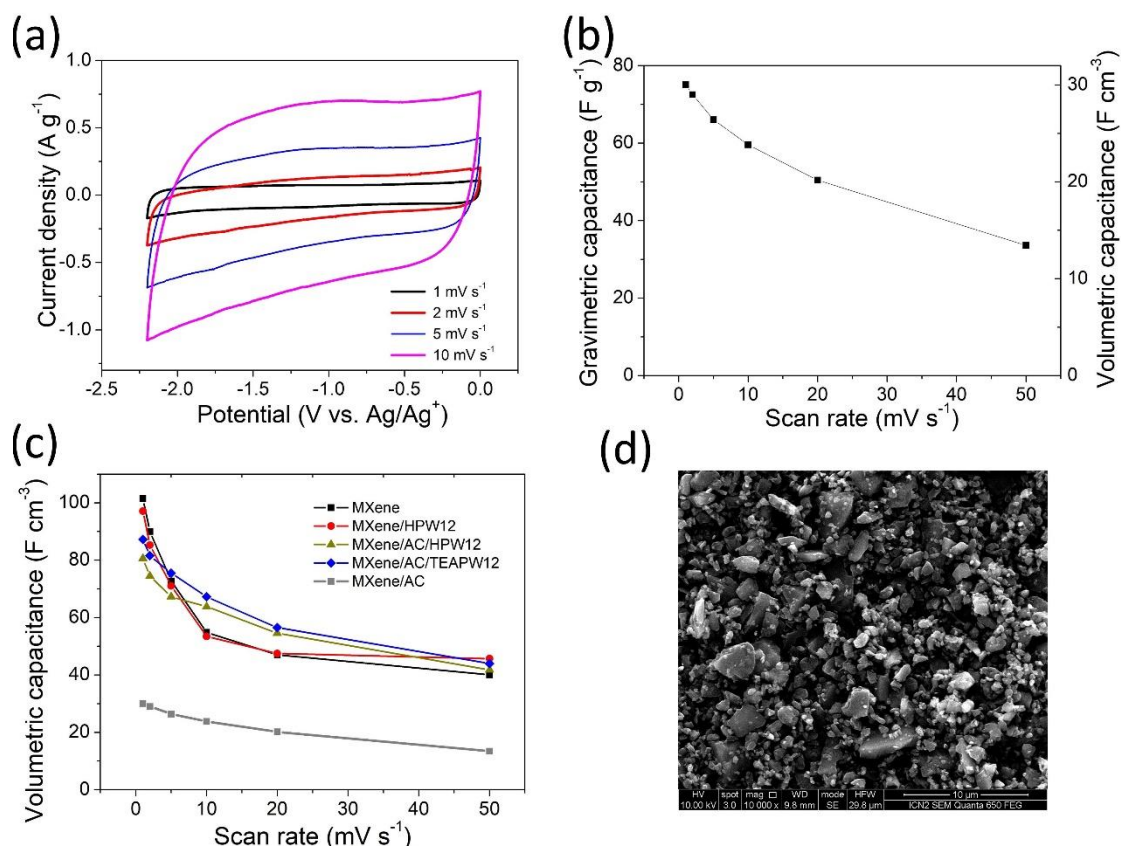


Fig S10 (a) CVs of MXene/AC at various scan rates. (b) Gravimetric capacitance and volumetric capacitance of MXene/AC at various scan rates. (c) Comparison of the volumetric capacitance of MXene, MXene/HPW12, MXene/AC/HPW12, MXene/AC/TEAPW12 and MXene/AC at various scan rates in 1 M TEABF₄ in acetonitrile. (d) SEM image of pristine AC.

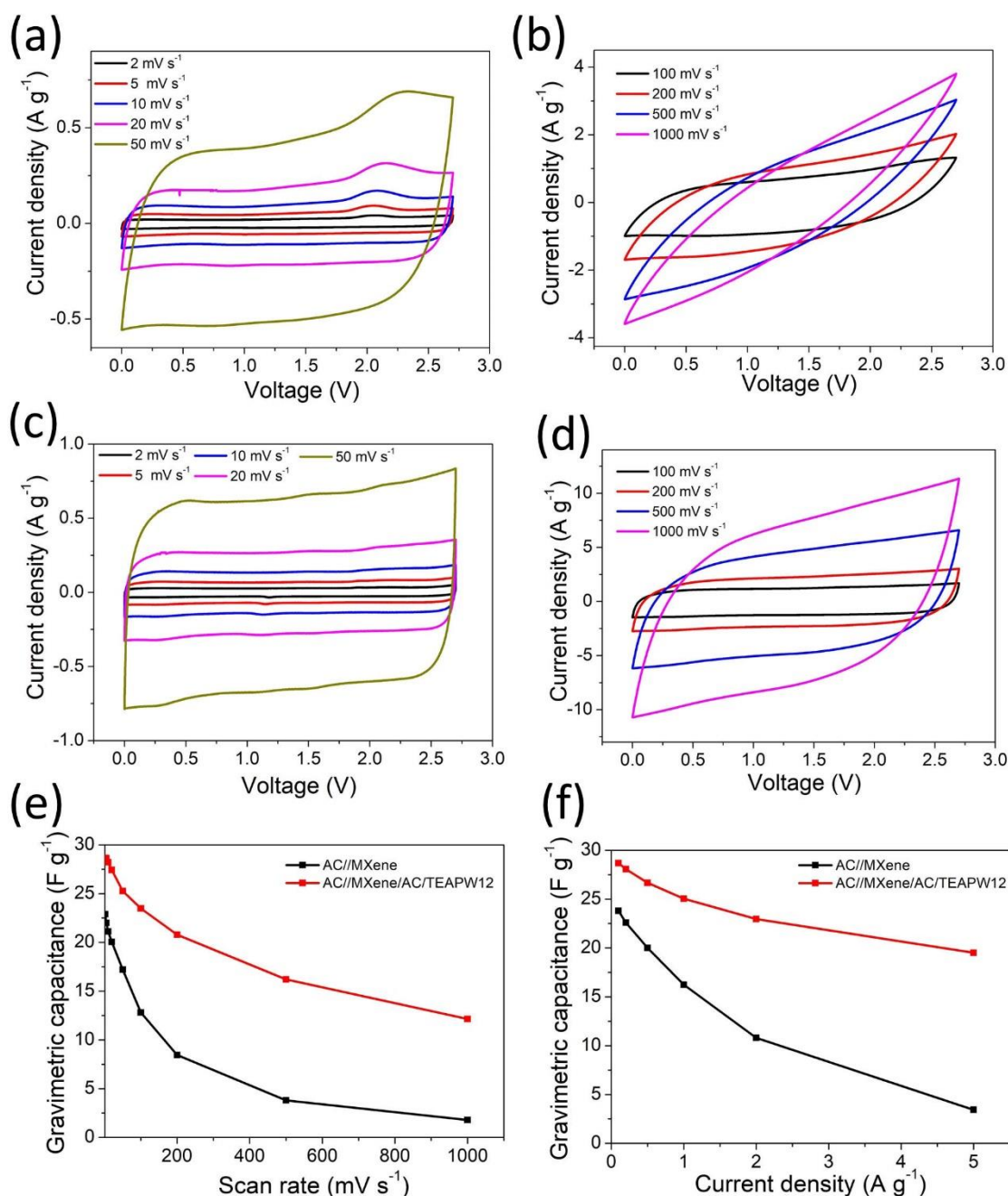


Fig. S11 Cyclic polarization curves of AC//MXene cell from (a) 2 to 50 mV s^{-1} and from (b) 100 to 1000 mV s^{-1} . Cyclic polarization curves of AC//MXene/AC/TEAPW12 cell from (c) 2 to 50 mV s^{-1} and from (d) 100 to 1000 mV s^{-1} . Gravimetric capacitance of AC//MXene and AC//MXene/AC/TEAPW12 cells derived from (e) cyclic polarization at various scan rates and (f) charge-discharge at various current densities. (Normalized by the total mass of two electrodes).

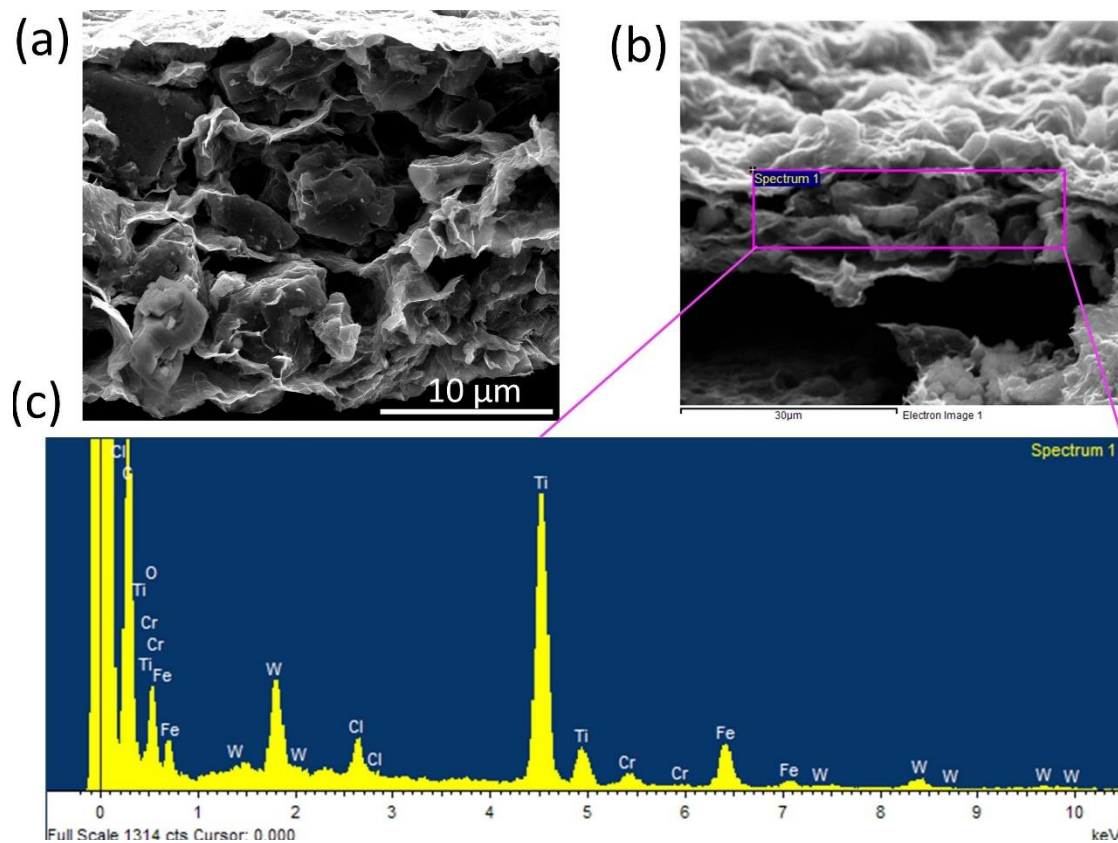


Fig. S12 SEM image of MXene/AC/TEAPW12 after 10,000 cycles. (b) the selected area and (c) the corresponding EDX spectrum of MXene/AC/TEAPW12 after 10,000 cycles (Fe and Cr are due to the contamination from stainless steel coin cell cases).

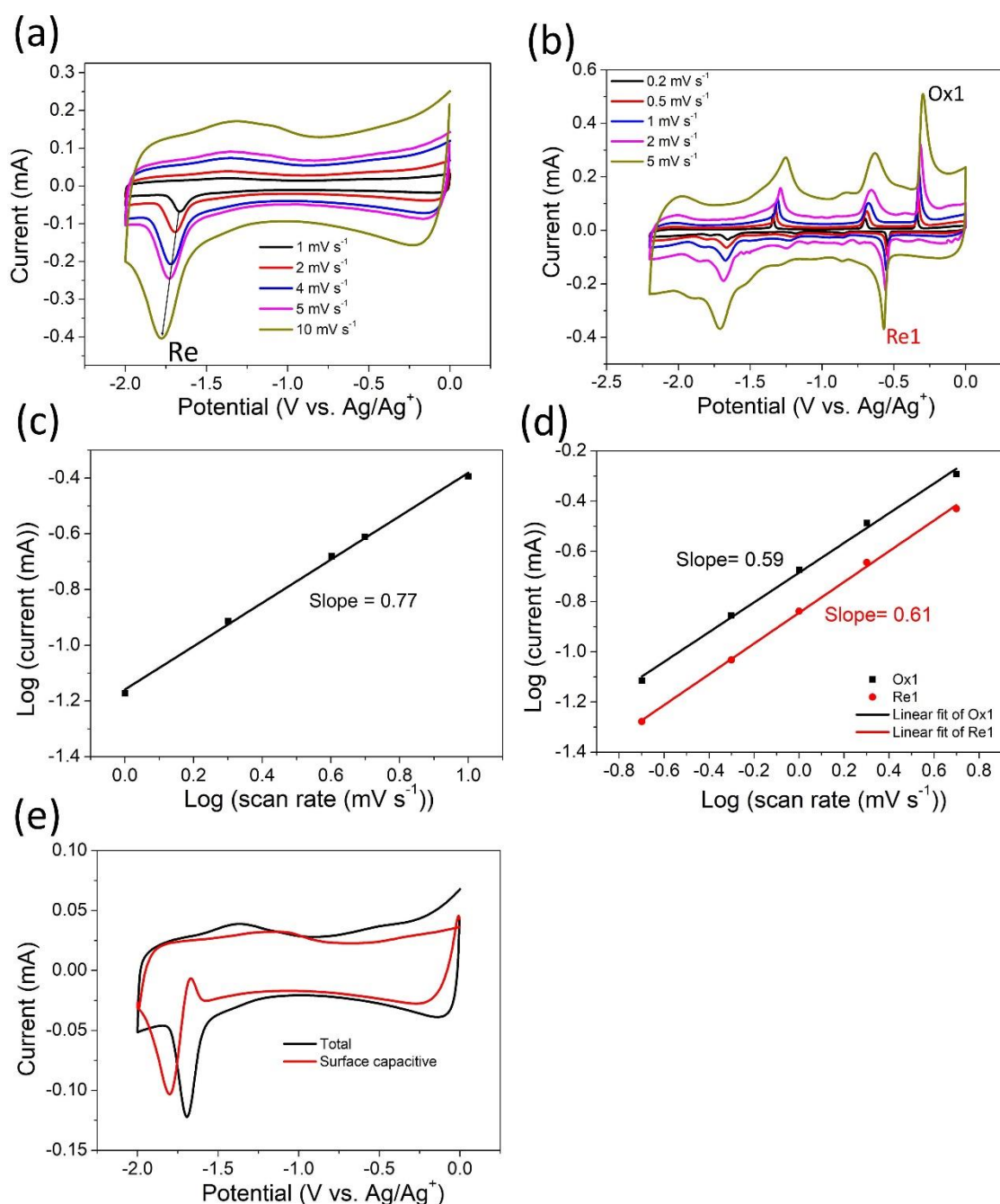


Fig. S13 CVs of (a) MXene and (b) MXene/TEAPW12 in 1 M TEABF4 in acetonitrile at various scan rates. (c) Linear fit of the reduction peak of MXene to determine the b-value. (d) Linear fit of the first redox pair of MXene/TEAPW12 to determine the b-value. (e) CV and the contribution from non-diffusion controlled current of MXene in 1 M TEABF4 in acetonitrile at 2 mV s^{-1} .

Note: We do not provide the CV and the contribution from non-diffusion controlled current of MXene/TEAPW12 because the positions of redox peaks are shifting with the increase of the scan rate, which means this analysis does not suit MXene/TEAPW12

Table S1 the EDX elemental analyses result of MXene/TEAPW12

Sample	Ti/ wt. %	W/ wt. %
Mxene/TEAPW12	35.4	19.4

Table S2 Elemental composition calculated from XPS

	Ti (at%)	C (at%)	O (at%)	F (at%)	Cl (at%)	W (at%)
MXene	21.74	43.62	18.73	10.77	5.14	
MXene/HPW12	19.09	49.95	22.32	5.27	3.14	0.23
MXene/AC/TEAPW12	11.76	63.92	18.83	3.49	1.68	0.31

Table S3 2 θ values for (002) diffraction peaks and interlayer distance of fresh and cycled MXene

Sample	2 θ values for (002) diffraction peaks/ $^{\circ}$	Interlayer distance/ \AA
Fresh MXene	7.75	11.39
Cycled MXene	6.07	14.54

Table S4 Fitting results of impedance sprctra

	R_s/Ω	R_{ct}/Ω	W_s-R/Ω	W_s-T/s	W_s-P	$Q/F s^{(a-1)}$	a
MXene	3.99	104	962	0.98	0.736	1.10E-05	0.798
MXene/HPW12	4.96	123	607	1.28	0.789	2.80E-06	0.877
MXene/AC/HPW12	5.12	198	154	0.83	0.86	3.50E-06	0.87
MXene/AC/TEAPW12	4.21	182	174	0.98	0.85	4.00E-06	0.856

Table S5 Fitting results of the impedance sprctra of MXene/AC/TEAPW12 before and after 10,000 cycles in 1 M EMIMTFSI in acetonitrile

	R_s/Ω	R_{ct}/Ω	W_s-R/Ω	W_s-T/s	W_s-P	$Q/F s^{(a-1)}$	a
Fresh	3.74	165.8	405.6	0.78	0.86	4.86E-06	0.87
Cycled	3.46	359.3	1350	2.82	0.79	3.82E-06	0.68

Reference to main text

[1] J.-J. Zhu, R. Benages-Vilau, P. Gomez-Romero, Can polyoxometalates enhance the capacitance and energy density of activated carbon in organic electrolyte supercapacitors?, *Electrochim. Acta* 362 (2020) 137007.

[2] L.Y. Yu, L.F. Hu, B. Anasori, Y.T. Liu, Q.Z. Zhu, P. Zhang, Y. Gogotsi, B. Xu, MXene-Bonded Activated Carbon as a Flexible Electrode for High-Performance Supercapacitors, *ACS Energy Lett.* 3(7) (2018) 1597-1603.

Chapter 6 Gel polymer Electrolytes integrated with POM electrodes

6.1 Context

In comparison with solid or gel electrolytes, conventional liquid electrolytes prevail in supercapacitors thanks to their relatively high ionic conductivity and good contact with thin electrodes. However, they have intrinsic drawbacks: high risk of leakage and flammability (organic electrolytes). Moreover, with the development of flexible devices, liquid electrolytes cannot meet the requirements anymore. Gel polymer electrolytes (GPEs) can simultaneously address many demanding challenges. They are fire-retardant, their geometry shape is variable, and they allow for fabricating safe, thin and flexible devices.

The integration of POMs with GPEs can date back to years ago[1]. POMs served as the plasticizer for the formation of GPEs and could be used to provide proton-conduction pathways[2]. And even though POMs are redox-active species, the POM-integrated GPEs did not provide extra capacitance. This chapter will present the efforts to incorporate POMs in GPEs as redox additives to improve capacitive performance. Two strategies were followed: 1) POMs serve as redox-active additives in GPEs; 2) POMs are incorporated in the electrode. The following two sections will deal with them, respectively.

6.2 Aqueous POM gel polymer electrolytes

Even though some previous studies have integrated POMs in aqueous GPEs, some issues have not been solved yet. They either cannot completely utilize the redox activity of POMs in full cells or work in a narrow voltage window. Thus, we first try to address these issues in aqueous POM GPEs.

6.2.1 Synthesis

1 g PVA was added into 10 mL hot Milli-Q water (85 °C) and kept stirring for 2 h in oil bath at 85 °C. Once PVA dissolved completely, 2.8 mL 85 wt% H₃PO₄ and 3 mL 0.18 M HSiW₁₂ were poured in the PVA solution and stirred for 2 h. The mixture was cooled down in ambient air and stayed still overnight. The phase separation happened. The top layer is a low-viscosity transparent solution; the bottom is a high-viscosity light yellow gel (Fig. 6.1(a)). We discarded the supernatant and kept the gel for coating.

A previously prepared AC electrode on a stainless steel substrate was coated with the gel to prepare the flexible free-standing electrodes (Fig. 6.1(b)). After 10 minutes, we fold the sheet in half. The AC electrodes can be easily peeled off. We obtained the flexible free-standing electrode/gel electrolyte/electrode sandwich (Fig. 6.1(c)). We can cut some round pieces and test them in coin cells.

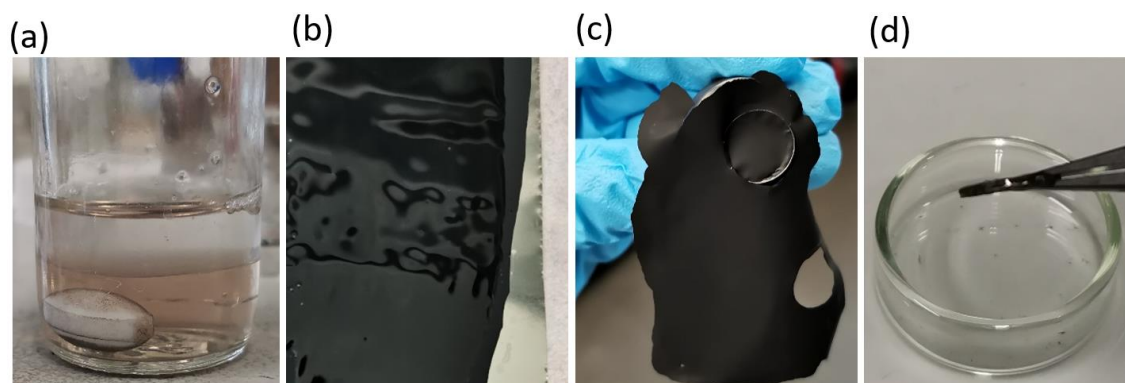


Fig. 6.1 Photos of (a) the phase separation of PVA/HSiW₁₂/H₃PO₄ solution, (b) gel-coated AC electrodes on SS substrate, (c) the top view of the flexible free-standing electrode/gel electrolyte/electrode sandwich, and (d) the cross-section flexible free-standing electrode/gel electrolyte/electrode sandwich sandwich.

6.2.2 Electrochemical behaviour of the electrolytes

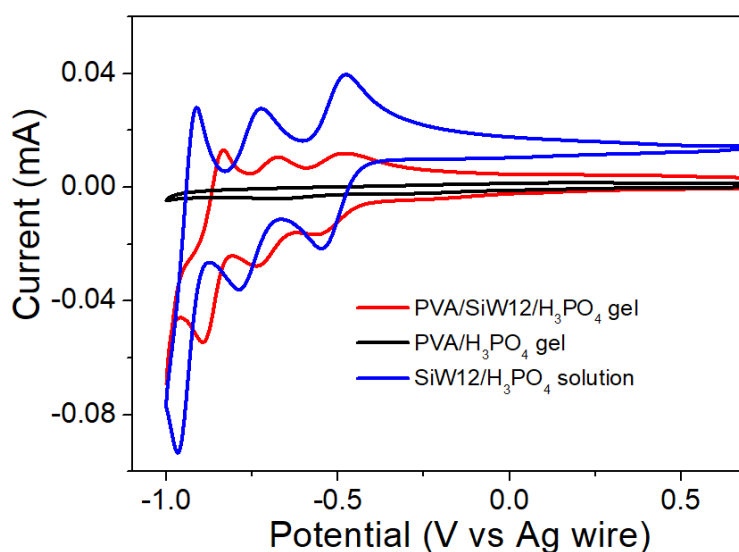


Fig. 6.2 Cyclic voltammetry at 10 mV s^{-1} in PVA/SiW12/ H_3PO_4 gel, PVA/ H_3PO_4 gel and SiW12/ H_3PO_4 solution.

Table 6.1 Potentials of redox peaks of glassy carbon electrode in in PVA/SiW12/ H_3PO_4 gel and SiW12/ H_3PO_4 solution at 10 mV s^{-1}

	1 st			2 nd			3 rd		
	Re	Ox	$E_{1/2}$	Re	Ox	$E_{1/2}$	Re	Ox	$E_{1/2}$
HSiW12/ H_3PO_4	0.55	0.47	0.51	0.79	0.72	0.76	0.97	0.91	0.94
PVA/HSiW12/ H_3PO_4	0.55	0.47	0.51	0.73	0.67	0.70	0.89	0.83	0.86

To compare the electrochemical behaviour of the gel polymer electrolytes and the liquid electrolyte, we used a three-electrode configuration in which glassy carbon, platinum plate and silver wire served as working, counter and pseudo-reference electrode, respectively. Fig. 6.2 shows the CVs. Table 6.1 lists the positions of the redox peaks. The CV of the glassy carbon electrode in PVA/ H_3PO_4 GPE has very small current ($< 2 \mu\text{A}$) and is almost featureless and with constant current, parallel to x-axis, indicating the absence of any redox behaviour. Like the other POMs/PVA GPEs [3, 4], the PVA/SiW12/ H_3PO_4 GPE show three pairs of redox peaks in the CV. The first redox

process at $E_{1/2} -0.51\text{V}$ takes place essentially at the same potential in the gel and in solution. On the other hand, the positions of subsequent redox peaks in the gel are different from $\text{SiW12}/\text{H}_3\text{PO}_4$ solution. The most negative redox pair is at around $E_{1/2} - 0.94\text{V}$, more negative than $\text{SiW12}/\text{H}_3\text{PO}_4$ solution. This agrees well with some previous study reporting that POMs-based aqueous GPEs can have a wider potential stability window because of the more negative potentials of the redox reactions[3].

6.2.3 Capacitive properties of AC in PVA/SiW12/H₃PO₄ GPE

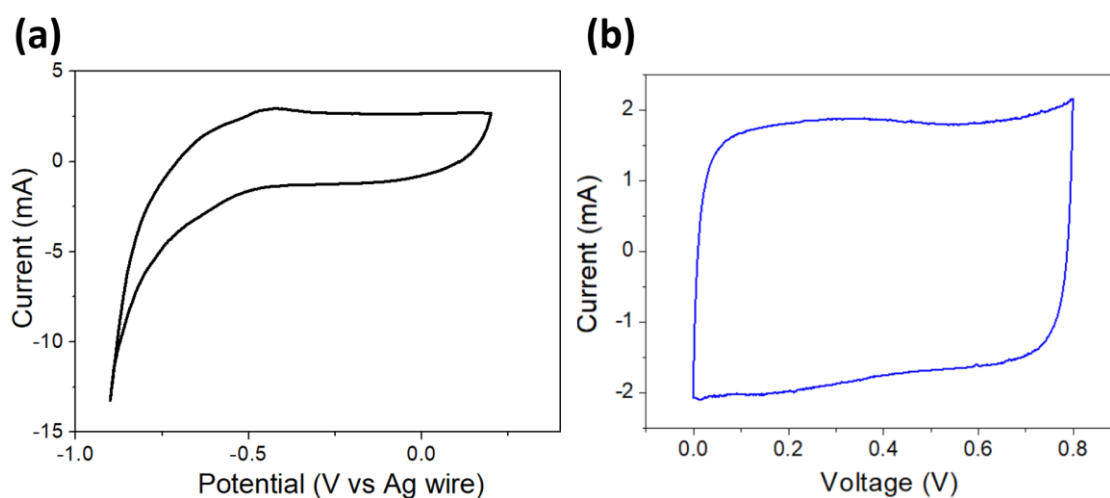


Fig. 6.3 (a) Cyclic voltammety of AC electrode at 10 mV s^{-1} in PVA/SiW12/H₃PO₄ gel. (b)

Cyclic polarization curve of flexible AC GPE cell 10 mV s^{-1} .

To investigate the feasibility to enhance the capacitive performance of conventional supercapacitors by using the redox active GPE (PVA/SiW12/H₃PO₄), a three-electrode cell, including an activated carbon working electrode, an over-sized activated carbon counter electrode and a silver wire quasi-reference electrode, was characterized with this GPE. The CV (Fig. 6.3a) of the activated carbon electrode does not present any redox peaks, revealing that the redox-active POMs contribute little to the capacitance of the whole system. It seems contrary to the behaviours when glassy carbon serves as the working electrode. However, after a careful examination of the working electrodes

and response currents in CVs, we came up with an explanation. The glassy carbon electrode has a planar electrode-electrolyte interface. The POMs in the electrolyte have easy access to the interface and exhibit redox activities. However, the interface area is relatively low, leading to a small response current. The activated carbon electrode has a very large surface derived from the micropores (pore size < 2 nm). Thus it delivers a high response current. However, since the POMs (cluster size around 1 nm) serve as the plasticizer in the GPE and are mostly confined in the polymer matrix, they cannot get into the micropores of AC to reach the interface. Most of the POMs cannot carry out their redox reaction.

Fig. 6.3(b) presents the CP curve of the full cell with AC electrodes and PVA/SiW₁₂/H₃PO₄ GPE. As expected, the CP curve is a rectangle and does not show any redox waves. Therefore, we conclude that the redox activities of POMs cannot be utilized in PVA-based aqueous GPEs when activated carbon serves as the active material because POMs are in the skeleton, cannot move to the reactive interface.

In order to fabricate high-performance POMs-based GPE supercapacitors, we decide to use pre-immobilized POMs electrodes (i.e. hybrid electrodes). Considering the high voltage window of organic electrolytes and the novel POMs-based hybrid materials compatible with the organic electrolytes, we developed organic GPEs to incorporate with our POMs-based hybrid materials as described in the following section.

6.3 Hybrid electrodes with organic GPE (Article 4)

<https://doi.org/10.3390/nano12030514>



Article

Coherent Integration of Organic Gel Polymer Electrolyte and Ambipolar Polyoxometalate Hybrid Nanocomposite Electrode in a Compact High-Performance Supercapacitor

Jun-Jie Zhu ^{1,*} , Luis Martinez-Soria ¹ and Pedro Gomez-Romero ^{1,2,*}

¹ Catalan Institute of Nanoscience and Nanotechnology (ICN2), CSIC and BIST, Campus UAB, Bellaterra, 08193 Barcelona, Spain; luis.martinezsoria@icn2.cat

² Consejo Superior de Investigaciones Científicas (CSIC), 28006 Madrid, Spain

* Correspondence: zhu.junjie@icn2.cat (J.-J.Z.); pedro.gomez@icn2.cat (P.G.-R.); Tel.: +34-937373608 (P.G.-R.); Fax: +34-936917640 (P.G.-R.)

Abstract: We report a gel polymer electrolyte (GPE) supercapacitor concept with improved pathways for ion transport, thanks to a facile creation of a coherent continuous distribution of the electrolyte throughout the electrode. Poly(vinylidene fluoride-co-hexafluoropropylene) (PVDF-HFP) was chosen as the polymer framework for organic electrolytes. A permeating distribution of the GPE into the electrodes, acting both as integrated electrolyte and binder, as well as thin separator, promotes ion diffusion and increases the active electrode–electrolyte interface, which leads to improvements both in capacitance and rate capability. An activation process induced during the first charge–discharge cycles was detected, after which, the charge transfer resistance and Warburg impedance decrease. We found that a GPE thickness of 12 μm led to optimal capacitance and rate capability. A novel hybrid nanocomposite material, formed by the tetraethylammonium salt of the 1 nm-sized phosphomolybdate cluster and activated carbon (AC/TEAPMo12), was shown to improve its capacitive performance with this gel electrolyte arrangement. Due to the homogeneous dispersion of PMo12 clusters, its energy storage process is non-diffusion-controlled. In the symmetric capacitors, the hybrid nanocomposite material can perform redox reactions in both the positive and the negative electrodes in an ambipolar mode. The volumetric capacitance of a symmetric supercapacitor made with the hybrid electrodes increased by 40% compared to a cell with parent AC electrodes. Due to the synergy between permeating GPE and the hybrid electrodes, the GPE hybrid symmetric capacitor delivers three times more energy density at higher power densities and equivalent cycle stability compared with conventional AC symmetric capacitors.

Keywords: gel polymer electrolytes; polyoxometalates; supercapacitors; hybrid electrodes; organic electrolytes; impedance spectroscopy



Citation: Zhu, J.-J.; Martinez-Soria, L.; Gomez-Romero, P. Coherent Integration of Organic Gel Polymer Electrolyte and Ambipolar Polyoxometalate Hybrid Nanocomposite Electrode in a Compact High-Performance Supercapacitor. *Nanomaterials* **2022**, *12*, 514. <https://doi.org/10.3390/nano12030514>

Academic Editors:
Antonio Guerrero-Ruiz and
Inmaculada Rodriguez-Ramos

Received: 28 December 2021
Accepted: 27 January 2022
Published: 1 February 2022

Publisher's Note: MDPI stays neutral with regard to jurisdictional claims in published maps and institutional affiliations.



Copyright: © 2022 by the authors. Licensee MDPI, Basel, Switzerland. This article is an open access article distributed under the terms and conditions of the Creative Commons Attribution (CC BY) license (<https://creativecommons.org/licenses/by/4.0/>).

1. Introduction

Portable/wearable electronic devices (e.g., mobile phones, laptops, cameras, smart-watch, activity trackers, and many more) are flourishing and demanding improved energy storage devices: small, thin, lightweight, flexible, fire-retardant, etc. [1]. Gel polymer electrolytes can simultaneously address many of these demanding challenges. They are fire-retardant, their geometry shape is variable, and they allow for fabricating safe, thin, and flexible devices.

Gel polymer electrolytes (GPE) are composed of polymer matrices and supporting electrolytes. Many polymers could serve as the matrices, such as poly(vinyl alcohol) (PVA), poly(methyl methacrylate) (PMMA), poly(ethylene oxide) (PEO), and copolymer poly(vinylidene fluoride-hexafluoro propylene) (PVDF-HFP) [2]. Depending on their hydrophilic or hydrophobic nature, these polymers are suitable for aqueous or nonaqueous

electrolytes. Compared to the conventional cell configuration consisting of liquid electrolytes and separators (e.g., cellulose membrane, Celgard membrane), polymer matrices in GPEs play several roles: as an effective separator, a reservoir for electrolytes, and pathways for ion diffusion. Due to the integrated functions and merits, GPE has widely substituted liquid electrolytes in a variety of energy conversion and storage devices, including solar cells [3], lithium-ion batteries [4,5], supercapacitors [6,7], etc.

Supercapacitors possess a high power density and long cycle life, but their energy density has yet to be improved compared with batteries. Electrodes, more specifically, the active materials on electrodes, are the critical components of supercapacitors, which could determine the intrinsic capacitance. Carbon-based materials can store energy in the electric double layer and have become the widest studied and commercialized active material for supercapacitors. The capacitance of carbon-based materials can gain more capacitance by introducing the other energy storage mechanism: redox reaction. Decorating with heteroatoms [8,9], incorporating redox-active materials could take the capacitance of carbon-based hybrid materials to the next level.

Polyoxometalates (POMs) are transition metal oxide clusters of around 1 nm in size, capable of delivering fast reversible multi-electron redox reactions, making them a competitive candidate in various energy storage devices [10]. For supercapacitors, POMs usually do not act as the active materials alone since the ion diffusion rate in crystallized POMs is sluggish, contrary to the high-power characteristic of supercapacitors. On the other hand, POMs can carry out their fast reversible redox reaction when they are well-dispersed. Thus, spreading or anchoring POMs on other materials, including activated carbon [11,12], reduced graphene oxide [13–15], carbon nanotubes [16,17], and a metal–organic framework [18] would be a solution. POMs-based hybrid materials have already shown their potential in supercapacitors to enhance capacitance and energy densities.

Since energy density is proportional to the square of the operating voltage window, using the nonaqueous electrolytes of the larger stable potential window is always favorable. The copolymer PVDF-HFP is compatible with many nonaqueous electrolytes, and so could serve as the matrix for nonaqueous gel polymer electrolytes. Conventional organic electrolytes [19], redox-active electrolytes [20], and ionic liquids [21,22] have already been incorporated with PVDF-HFP matrix to fabricate flexible supercapacitors with high energy density and safety.

Compared with liquid electrolytes, gel polymer electrolytes composed of the same liquid electrolytes typically show lower ionic conductivity because the polymer matrix impedes free ion movement [23,24], which affects the rate capability of supercapacitors. The rate performance of GPE supercapacitors can hardly exceed that of liquid-electrolyte supercapacitors.

Nonetheless, we can tackle this problem from an engineering perspective. Besides the nature of active materials and electrolytes, designing specific pathways for ion diffusion to reduce the diffusion route can improve the electrochemical performance of energy storage devices.

Herein, we introduce a well-engineered coherent electrode–electrolyte interface by integrating the copolymer PVDF-HFP throughout electrodes and the electrolyte. We obtain the thin gel polymer electrolyte once we soak the PVDF-HFP matrix in 1 M TEABF₄/acetonitrile. The coherent PVDF-HFP matrix provides a highway for ion movement throughout the electrodes and the electrolyte. This structure enhances the rate capability and the capacitance, which, in turn, allows for both high power densities and energy densities. Furthermore, we fabricate a symmetric supercapacitor with high energy density and power density thanks to the novel activated carbon/polyoxometalates hybrid material coupled with the gel polymer electrolyte.

2. Experimental Section

2.1. Materials

Activated carbon was purchased from Cabot Corporation, Alpharetta, GA, USA. Aluminium foil (>99%, 18 µm) was purchased from Goodfellow, Hamburg, Germany. Acetoni-

trile (electronic grade), N-methyl-2-pyrrolidone (anhydrous, $\geq 99.5\%$), dimethylformamide (anhydrous, $\geq 99.8\%$), tetraethylammonium tetrafluoroborate ($\geq 99\%$), Poly(vinylidene fluoride-co-hexafluoropropylene) (average molecule weight $\approx 400,000$), poly(vinylidene fluoride) (average molecule weight $\approx 534,000$), phosphomolybdic acid (HPMo12), and tetraethylammonium chloride ($\geq 98\%$) were from Sigma-Aldrich without additional purification. Nitrocellulose filter membranes (pore size = 0.025 μm , thickness = 0.17 mm) were purchased from MF-Milipore, Merck, Madrid Spain. Celgard 2400 membranes were purchased from Celgard, LLC, Charlotte, NC, USA.

2.2. Preparation of Gel Electrolytes

First, 2 g of PVDF-HFP was added in 10 mL acetone with vigorous stirring at 50 °C until a transparent viscous solution formed. Subsequently, the solution was cast on a glass plate using the doctor-blade method. After a few minutes, the acetone evaporated, and a white, half-transparent film was obtained. The film can be easily peeled off by a spatula and stored in an argon-filled glove box for further use. We can obtain PVDF-HFP films of different thicknesses by selecting separate doctor-blade bars, ranging from 2 μm to 36 μm . The film would be soaked in the liquid electrolyte just before assembling the devices.

2.3. Synthesis of Hybrid Materials

The organic-inorganic POM salt (TEAPMo12) was synthesized through metathesis reaction, as our previous literature reported. Typically, 100 mL of a 20 mM aqueous solution of phosphomolybdic acid was added to 100 mL of a 70 mM aqueous solution of tetraethylammonium chloride. The slight yellow precipitate appeared immediately. The suspension was kept stirring for 6 h, filtered, washed with DI water, collected, and dried at 120 °C overnight. Tetraethylammonium phosphomolybdate (TEAPMo12, $[(\text{C}_2\text{H}_5)_4\text{N}]_3\text{PMo}_{12}\text{O}_{40}$) was obtained.

The hybrid material AC/TEAPMo12 were prepared by sonicating 0.5 g AC in 100 mL of 10 mM TEAPMo12 in DMF for 6 h. The samples were collected by filtration and dried at 120 °C overnight.

2.4. Preparation of Electrodes

The conventional electrodes were fabricated by mixing the active material (AC), carbon black and poly(vinylidene fluoride) at a weight ratio of 85:5:10. The mixture was first formed as a slurry by adding a few drops of N-methyl-2-pyrrolidone (NMP) and then coated onto 18 μm aluminum foil and dried under vacuum at 120 °C for 12 h.

The gel-polymer-contained electrodes were prepared by dispersing the active materials, carbon black and PVDF-HFP (pre-dissolved in NMP), at a weight ratio of 85:5:10. The slurry was stirred for 6 h and then coated onto aluminum foil and dried under vacuum at 120 °C for 12 h. The thickness of the coated AC layer on Al foil was around 47 μm , and the thickness of coated AC/TEAPW12 was around 36 μm . The loading masses of both electrodes were around 2.4 $\text{mg}\cdot\text{cm}^{-2}$.

2.5. Characterization

Thermogravimetric analyses were carried out with NETZSCH-STA 449 F1 Jupiter thermal analysis system under oxygen flow with a heating rate of 10 °C min^{-1} from room temperature to 900 °C. Scanning electron microscopy images were taken on Quante 650 FEG microscopy. High angle annular dark field scanning transmission electron microscopy (HAADF-STEM) images were taken on FEI Tecnai G2 F20 microscopy.

Three types of cells were fabricated for different characterization. T-type stainless steel Swagelok® cells were used to characterize the materials in the three-electrode configuration. Ag/Ag⁺ (0.01 M AgNO₃) was used as the reference electrode. An electrode loaded with the treble weight of the AC active material was used as the counter electrode. CR2032 coin cells were used to fabricate symmetric supercapacitors. All the electrodes were pressed at 3 MPa before assembling. Additionally, 1 M tetraethylammonium tetrafluoroborate (TEABF₄)

in acetonitrile served as the electrolyte. All the cells were assembled in an argon-filled glovebox (Jacomex GP with $O_2 < 5$ ppm and $H_2O < 5$ ppm). Cyclic voltammetry (CV) was performed in a three-electrode configuration at various scan rates to investigate the capacitive behavior of individual electrodes. Cyclic polarization (CP), electrochemical impedance spectra (EIS), and galvanostatic charge–discharge (GCD) were performed in a two-electrode cell to evaluate the capacitive performance in devices and cycling stability. All the electrochemical tests were conducted on Biologic VMP3 multi-channel potentiostat. The calculation of capacitance, power densities and energy densities are presented in Supplementary Materials 1, Equations S1–S5.

3. Results and Discussion

3.1. Evaluation and Optimization of GPE

We prepared PVDF-HFP films of various thicknesses, ranging from 2 to 36 μm . Figure 1a presents photographs of the dry PVDF-HFP films. The thinnest film (2 μm) is transparent, and the rest are translucent. The Fourier-transform infrared spectra of PVDF-HFP films are presented in Supplementary Materials 2, Figure S2a. All the films turned to transparent gel after being soaked in 1 M TEABF₄ acetonitrile electrolyte (Figure 1b). After that, we obtained gel polymer electrolytes.

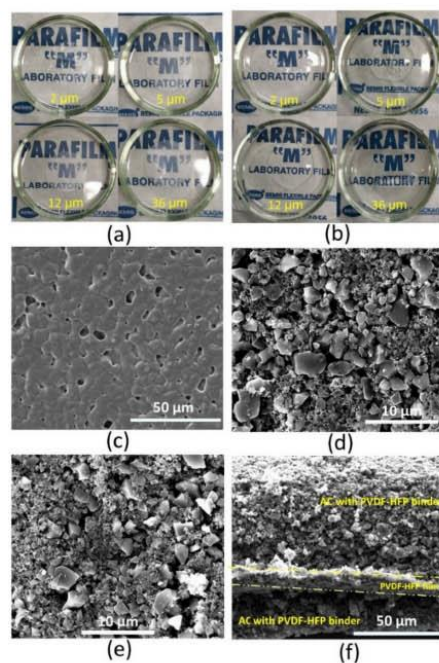


Figure 1. Photographs of PVDF-HFP films of various thicknesses: (a) dry films and (b) films soaked with 1 M TEABF₄ in acetonitrile. SEM images: (c) 12 μm PVDF-HFP film, (d) activated carbon electrodes with PVDF binder, (e) activated carbon electrodes with PVDF-HFP binder and (f) cross-section of the electrode/PVDF-HFP film/electrode sandwich (PVDF-HFP as the binder in the electrodes).

To construct a coherent electrode–electrolyte interface, PVDF-HFP serves as the binder in the electrodes. Figure 1c presents the morphology of PVDF-HFP film. We can discern micro-scale PVDF-HFP crystals connecting. The pores among PVDF-HFP crystals serve as the reservoir for the electrolyte and pathway for ion migration. Figure 1d,e present the AC electrode with PVDF and PVDF-HFP, respectively. The two kinds of electrodes show a similar morphology: AC particles dispersed and connected by Carbon SuperP (Csp)

tiny particles. We did not find any agglomeration of PVDF-HFP in Figure 1e. PVDF-HFP is soluble in NMP, which allows it to be dispersed homogeneously in the whole slurry before coating the electrodes. After drying the electrodes, PVDF-HFP covers the AC and Carbon SuperP particles, serving as an effective binder. Figure 1f presents the cross-section SEM image of the electrode–electrolyte interface. Many AC and Csp particles stick on the PVDF-HFP film after cutting, indicating the excellent compatibility between the electrodes and the films.

To evaluate the influence of GPE on capacitive performance, we built AC symmetric supercapacitors and performed electrochemical characterization. The electrochemical impedance analysis could give us some insight into the electrode/electrolyte interface, capacitive behaviors, ion diffusion, etc. Figure 2a,b present the Nyquist plots of the fresh and activated AC symmetric supercapacitors. The 2 μm PVDF-HFP film device is not included because the 2 μm PVDF-HFP film could not separate the two electrodes effectively. The thickness threshold for this kind of effective gel polymer electrolyte and separator would be around 5 μm .

All the spectra are fitted by an equivalent circuit shown in Figure 2c. At the very high-frequency region, the intercepts at real part Z, represented by R_s , provide the combined effect of the ionic resistance of the electrolyte, the intrinsic resistance of the active materials, and the contact resistance at the active material/current collector interface. Since all the cells have the same active material, the current collector and the liquid electrolyte, the intercepts are roughly the same at very high frequency. The semicircles at high frequency represent a parallel combination of charge-transfer resistance R_{ct} and the double layer capacitance C_{dl} . The following transitory parts between the semicircles and the final linear parts represent the Warburg impedance. This relates to the diffusive resistance of the electrolyte in the electrodes. Considering the different slopes of the final linear parts, we apply a modified restricted diffusion element W_s for fitting [25]. It has three parameters (Equations S6 and S7 in Supplementary Materials 1). W_s -R represents the diffusion impedance; W_s -T represents the diffusion time; W_s -P is an exponential factor: the number 0.5 means the infinite Warburg diffusion (slope = 1), and 1.0 means finite Warburg diffusion (vertical line) [26,27].

Table 1 lists the fitting results of the impedance spectra. The diameter of the compressed semicircle (R_{ct}) shows a significant difference among the cells. For the fresh cells with GPE, R_{ct} increases with the increase in the thickness of PVDF-HFP films. The R_{ct} values are in this order: 5 μm < cellulose (thickness = 170 μm and pore size = 25 μm) < 12 μm < 36 μm < celgard (thickness = 25 μm). R_{ct} normally involves the charge transfer process stem from redox-active materials. However, in AC supercapacitors, many studies found the R_{ct} exists too [24,28,29]. Since the pseudocapacitance in the activated carbon is insignificant, the R_{ct} is mainly dominated by the adsorption/desorption of ions, or in other words, pore accessibility [29]. The R_{ct} of the cells with the liquid electrolyte and the conventional separators (Celgard membrane and cellulose paper) do not change significantly after cycling. By contrast, R_{ct} of GPE cells decreased remarkably after cycling. The R_{ct} of the cell with 12 μm GPE decreases from 31 Ω to 2.8 Ω . This phenomenon implies an activation process at the electrode–electrolyte interface. The electrolyte has easier access to the pores after the activation. The PVDF-HFP serves as both the binder and the matrix for the gel electrolyte. At first, the TEABF₄ in acetonitrile only wet the PVDF-HFP film, not the PVDF-HFP in the electrodes. With the charge–discharge process ongoing, the PVDF-HFP in the electrodes infuses with TEABF₄, facilitating adsorption/desorption of ions in pores, and the porous structure remains.

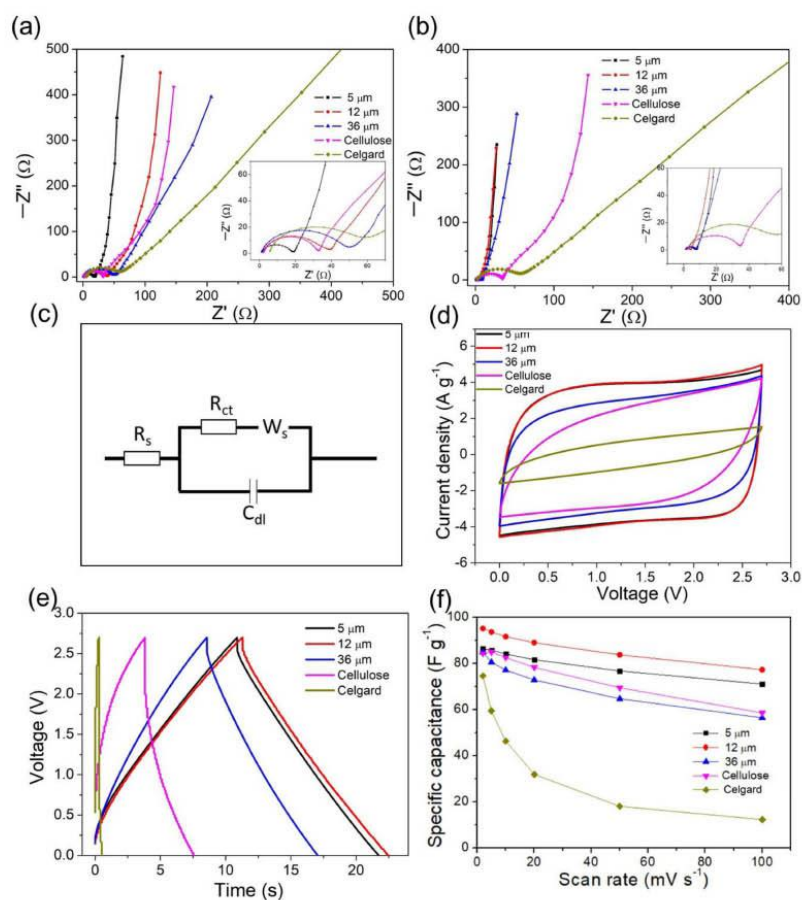


Figure 2. Nyquist plot of the cells with 5 μm , 12 μm , and 36 μm PVDF-HFP gel polymer electrolyte, or cellulose and Celgard separator in the liquid electrolyte: (a) the fresh cell, (b) the activated cells. (the intercepts and semicircles in the high-frequency range are zoomed in the inset graphs). (c) The equivalent circuit for fitting the impedance spectra. (d) Cyclic polarization curves at 100 $\text{mV}\cdot\text{s}^{-1}$ and (e) Galvanostatic charge–discharge curves at 8 $\text{A}\cdot\text{g}^{-1}$ of the cells with 5 μm , 12 μm , and 36 μm , PVDF-HFP gel polymer electrolyte, or cellulose and Celgard separator in the liquid electrolyte. (f) The specific capacitance of the cell at various scan rates.

Table 1. Some fitting results of impedance spectra.

Cells	State	R_s/Ω	C_{dl}/mF	R_{ct}/Ω	$W_s\text{-R}/\Omega$	$W_s\text{-T}/\text{s}$	$W_s\text{-P}$
5 μm	fresh	1.12	1.83	15.78	10.03	0.21	0.85
	activated	1.08	3.76	6.51	1.46	0.04	0.87
12 μm	fresh	1.87	1.93	32.16	22.01	0.32	0.74
	activated	0.83	4.17	3.23	2.10	0.06	0.83
36 μm	fresh	0.89	2.32	44.24	29.7	0.42	0.74
	activated	1.08	3.54	6.53	1.63	0.03	0.84
Cellulose	fresh	2.13	2.81	29.44	7.60	0.04	0.69
	activated	2.14	4.36	28.83	9.48	0.06	0.66
Celgard	fresh	2.09	1.55	31.23	91.56	0.13	0.58
	activated	2.23	1.19	42.62	45.47	0.05	0.54

Moreover, the Warburg impedance (both W_s -R and W_s -T) of GPE cells decreases after cycling, too, further confirming an improved ion-diffusion process. By contrast, W_s -R and W_s -T of Celgard membrane and cellulose paper cells do not show as significant a change as GPE cells do after cycling, revealing that the decrease in W_s -R and W_s -T is mainly associated with PVDF-HFP gel. The activation process happens when PVDF-HFP either exists in the electrodes or gel electrolytes (Supplementary Materials 3, Figure S3 and Table S3). W_s -P is an indicator to distinguish whether the diffusion is finite. The W_s -P of the Celgard cell is close to 0.5, corresponding to an infinite diffusion that mainly happens in the bulk electrolyte. For 12 μm and 36 μm GPE-based cells, we discern a clear increase (from 0.7 to 0.8) in W_s -P after cycling, revealing that the diffusion behavior changes during cycling. It agrees well with the deduction derived from R_{ct} . With charge–discharge going, more electrolytes permeate the pores in the PVDF-HFP, and the diffusion behavior shifts from infinite diffusion in bulk electrolyte to finite diffusion in the porous structure. Additionally, 5 μm GPE cells exhibit a slighter change in W_s -P after activation, which must relate to their thinnest thickness. The porous structure of 5 μm GPE cells is permeated quickly; thus, the diffusion behavior is mainly finite initially. The variations of these parameters (the decrease in R_{ct} , W_s -R and W_s -T; the increase in W_s -P) increase with the thickness of GPEs, revealing that the thicker GPE cells undergo a more remarkable activation.

The impedance analysis confirms the existence of the activation process in GPE cells. The diffusion is promoted after the activation, and more pores become accessible to the electrolyte. Concerning R_{ct} and W_s , the GPE cells are superior to the conventional configuration cells. Next, we compare their capacitive performance.

Figure 2d shows the cyclic polarization curves of the cells at $100 \text{ mV}\cdot\text{s}^{-1}$. The CP curves of the cells with cellulose or Celgard separator in the liquid electrolyte are not perfectly rectangular in shape. Their parallelogram shape implies their resistive nature. By contrast, the cells of 5 μm and 12 μm present the CP curves of the ideal rectangle shape, indicating their pure capacitive behavior even at the high scan rate of $100 \text{ mV}\cdot\text{s}^{-1}$. The difference among the CP curves agrees with the previous impedance analyses: GPE cells have smaller R_{ct} and Warburg impedance; thus, they remain capacitive at high scan rates.

Figure 3e presents galvanostatic charge–discharge curves at $8 \text{ A}\cdot\text{g}^{-1}$ of the cells. All the curves give a triangle shape, indicating the cells' capacitive nature. The GPE cells have much smaller IR drops, which is another indicator of low resistance in GPE cells. Figure 2f lists the specific capacitance of the cells at various scan rates. The specific capacitance of the GPE cells is almost equivalent to or slightly higher than that in the conventional configuration cell (a cellulose separator and the liquid electrolyte) at low scan rate ($2 \text{ mV}\cdot\text{s}^{-1}$). It reveals that the PVDF-HFP in electrodes and separators has no detriments on the capacitive performance. Instead, the capacitance of the 12 μm GPE cell is improved. We speculate that the PVDF-HFP on the active material allows the electrolyte to pass through, and some PVDF-HFP-covered areas are still active, while PVDF-covered areas are mostly inert. Even though the cells show only a slight difference in specific capacitance at the low scan rate ($2 \text{ mV}\cdot\text{s}^{-1}$), the difference between the GPE cells and the cells with conventional separators and liquid electrolyte becomes remarkable the increase in scan rates. The excellent rate capability of the GPE cells must be ascribed to the coherent integration of PVDF-HFP at the electrode–electrolyte interface.

Considering the capacitance and rate capability, we select the 12 μm GPE as the best option. The as-prepared PVDF-HFP film is much thinner than PVDF-HFP GPE in other studies [4–6,22], which implies its potential for compact devices. Our previous study has proved that the organic–inorganic POM salt can enhance the volumetric capacitance of activated carbon in the organic electrolyte, suitable for compact devices. Thus, in the following part, we develop a novel AC/POMs hybrid material (AC/TEAPMo12) to enhance the volumetric capacitive performance of the device further.

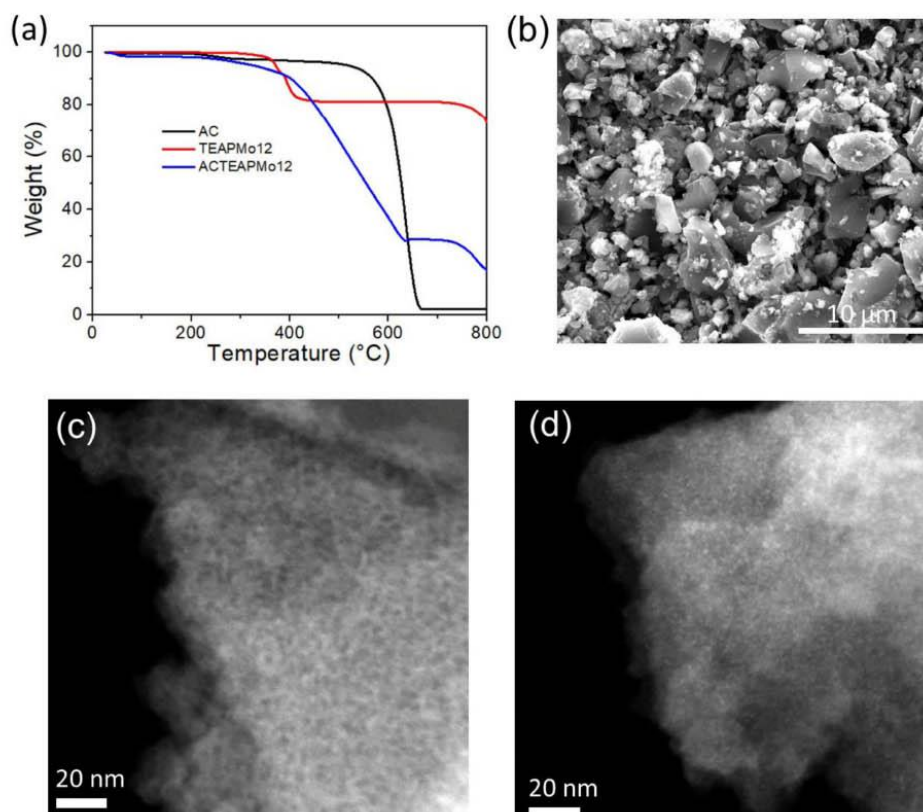


Figure 3. (a) The thermogravimetric curves of AC, TEAPMo12 and AC/TEAPMo12. (b) SEM image of AC/TEAPMo12. HAADF-STEM images of (c) AC and (d) AC/TEAPMo12.

3.2. Evaluation of the Hybrid Material

XRD patterns confirm the AC/TEAPMo12 contains TEAPMo12 (Supplementary Materials 2, Figure S2b). The composition of the hybrid materials AC/TEAPMo12 was determined by thermogravimetric analyses (Figure 3a). The pristine AC suffers a dramatic weight loss since 600 °C, which refers to the combustion of carbon in the air. Finally, 2.12 wt% of its initial weight remains as ashes. Pure TEAPMo12 undergoes a significant weight loss between 300 °C to 400 °C due to the decomposition of tetraethylammonium moieties. Subsequently, its weight stays relatively stable (81.1 wt% of the initial weight) until 730 °C. The hybrid AC/TEAPMo12 shows a weight loss before 620 °C, followed by a plateau that covers the range from 630 °C to 730 °C. At this plateau, 28.5 wt% of the initial weight remains. Therefore, we can estimate that AC/TEAPMo12 contains 33.3 wt% of TEAPMo12. TEAPMo12 possesses a large proportion in AC/TEAPMo12, but the XRD pattern of AC/TEAPMo12 only presents weak peaks from TEAPMo12 because TEAPMo12 clusters are not well crystallized, but nanocrystals are.

Figure 3b presents the SEM images of AC/TEAPMo12, from which we cannot see any aggregation of TEAPMo12. (The transmission electron microscopy images of AC and AC/TEAPMo12 are presented in Figure S2c,d) We expect the TEAPMo12 clusters to spread homogeneously on AC substrate as other keggin-type POMs do [11,12,30]. To study the distribution characteristics of TEAPMo12, we observe the samples under scanning transmission electron microscopy in the high angle annular dark field (HAADF-STEM). Figure 3c

shows the HAADF-STEM image of pristine AC. It reveals the porous nature of AC. Plenty of micropores (pore size < 2 nm) and mesopores (pore size from 2 to 50 nm), corresponding to the dark areas in the image, can be discerned. By contrast, in the HAADF-STEM image of AC/TEAPMo12 (Figure 3d), we cannot distinguish the pores. Instead, numerous bright dots around 1 nm spread on the sample, corresponding to Mo in TEAPMo12 clusters. It confirms that the TEAPMo12 clusters are dispersed homogeneously in nanoscale on AC substrate, agreeing with the speculation from XRD patterns. Indeed, the anchoring of TEAPMo12 clusters on AC would lead to a slight decrease in pore volume and surface area of the hybrid materials [11], and the bright dots make the contrast between pores and matrix less visible.

This hybrid material is characterized in three-electrode configurations to study its electrochemical behaviors and two-electrode symmetric cells to explore its performance in practice. Figure 4a compares the CVs of AC and AC/TEAPMo12 at $5 \text{ mV}\cdot\text{s}^{-1}$ in the full potential range. The CV of AC/TEAPMo12 exhibits four pairs of redox waves in addition to the rectangle shape of AC, confirming the electrochemical activities of TEAPMo12 clusters.

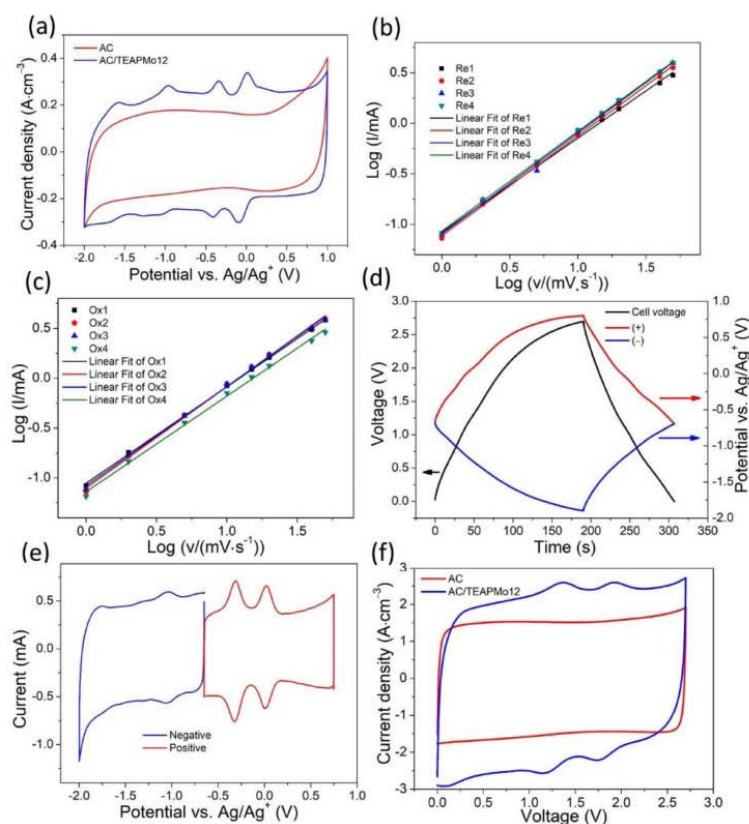


Figure 4. (a) CVs of AC and AC/TEAPMo12 at $20 \text{ mV}\cdot\text{s}^{-1}$ in three-electrode configuration. b-value determination for (b) oxidation peaks and (c) reduction peaks of CVs of AC/TEAPMo12. (d) The variation of the potential of the positive electrode, the negative electrode, and the voltage of the symmetric capacitor during galvanostatic charging–discharging. (e) CVs of the positive and the negative electrodes in their potential range. (f) Cyclic polarization curves of AC and AC/TEAPMo12 at $100 \text{ mV}\cdot\text{s}^{-1}$.

The charge-storage mechanism of AC/TEAPMo12 was analyzed by discriminating the non-diffusion-controlled contribution and diffusion-controlled contribution to the total charges stored in AC/TEAPMo12 electrodes. The dependence of the current response on the scan rate reveals the charge-storage mechanism, as shown in Equation (1)

$$i = av^b \quad (1)$$

where i is current obtained at a specific scan rate v , and a and b are adjustable parameters. The current response of linear dependence on scan rate ($b = 1$) usually means the charge is stored by a fast response mechanism, such as surface capacitive mechanism and redox reactions that could perform fast rate [31]. Otherwise, if any slow diffusion of ion or electron transfer limits the reaction, the dependence could deviate from linearity ($b < 1$). We performed CVs at various scan rates (Supplementary Materials 4 and Figure S4a) and ran the linear fitting at the potentials where the redox reactions happen according to Equation (2)

$$\log i = \log a + b \log v \quad (2)$$

Figure 4b,c show the fitting curves. Table 2 lists the b values at the redox potentials. All the R^2 are close to 1, revealing the effective fitting. The b values at all the redox potentials are close to 1, which means the non-diffusion-controlled process dominates the charge storage. It might seem surprising for redox-active materials, but this phenomenon happens when the redox-active species are well-dispersed, such as POMs on 3D framework [31], AC/TEAPW12 hybrids [11]. The contribution of the non-diffusion-controlled process and the diffusion-controlled process to the capacitance in the whole potential is analyzed and presented in Supplementary Materials 4, Figure S4(b–f). We conclude that the non-diffusion-controlled process dominates the energy storage in the whole potential range at any scan rate.

Table 2. Values of b Equations (1) and (2) and regression coefficients (R^2) derived from the fitting current of reduction peaks (Re) and oxidation peaks (Ox) at various scan rates.

	Re1	Ox1	Re2	Ox2	Re3	Ox3	Re4	Ox4
b	0.932	0.967	0.990	1.000	0.999	0.998	0.988	0.960
R^2	0.997	0.999	0.997	0.999	0.997	0.999	0.998	0.999

3.3. Evaluation of Symmetric Devices

We put two identical hybrid electrodes and a Ag/Ag^+ reference electrode in a T-type Swagelok cell to explore its behaviors in symmetric capacitors. After activation, the electrodes in the symmetric capacitor deliver a potential of zero-charge (when the voltage of the cell is zero) around -0.65 vs. Ag/Ag^+ during galvanostatic charging–discharging from 0 – 2.7 V (Figure 4d). The variation of the potential of the positive electrode is from -0.65 V to 0.75 V. That of the negative electrode is from -0.65 V to -1.9 V. This potential of zero-charge is in the middle of the four pairs of redox waves, which means the positive and the negative electrodes can carry out two redox reactions, respectively. The cyclic voltammograms of the two electrodes in their working potential range exhibit two redox pairs, respectively (Figure 4e). It confirms that all the redox reactions in Figure 4a participate in energy storage in the symmetric capacitor. Figure 4f compares the cyclic polarization curves of AC and AC/TEAPMo12 in two-electrode symmetric capacitors. The integrated area of the AC/TEAPMo12 cell curve is larger than that of AC cell, indicating the volumetric capacitance (Y -axis in Figure 4f is normalized by volume). The CP curve exhibits two redox waves because some redox waves on the positive and negative electrodes overlap and merge into one wave. It is further evidence that redox reactions are involved in the energy storage process of the symmetric capacitor. The CP curves of AC-Cellulose, AC-GPE and AC/TEAPMo12-GPE symmetric capacitors at various scan rates are presented in

Supplementary Materials 5, Figure S5(a–c), and the capacitance calculated from the CP curves are presented in Supplementary Materials 6, Figure S6.

We perform galvanostatic charging–discharging at various current densities to explore the capacitive performance of the conventional AC symmetric capacitor (AC-Cellulose), the GPE AC symmetric capacitor (AC-GPE), and the GPE AC/TEAPMo12 symmetric capacitor (AC/TEAPMo12-GPE) for practice use. The charging–discharging curves are presented in Supplementary Materials 5, Figure S5(d–f). Figure 5a presents the gravimetric capacitance of the symmetric capacitors. The gravimetric capacitance of AC-GPE and AC/TEAPMo12-GPE are almost equivalent at various current densities. It is not surprising that the hybrid material AC/TEAPMo12 does not enhance the gravimetric capacitance because the TEAPMo12 molecule has a large weight ($>2000 \text{ g}\cdot\text{mol}^{-1}$). Since POMs are compact nanoclusters, they are more effective in improving volumetric capacitance. At high current densities, the enhancement of capacitance in GPE cells is significant and must be assigned to the coherent integration between the electrode–electrolyte interfaces as we mentioned above. The volumetric capacitance of AC/TEAPMo12 is remarkably improved (Figure 5b). At $0.5 \text{ A}\cdot\text{g}^{-1}$, AC/TEAPMo12 delivers a volumetric capacitance of $74.6 \text{ F}\cdot\text{cm}^{-3}$, 41% larger than AC with the same gel polymer electrolyte. At any current densities, the volumetric capacitance of AC/TEAPMo12 gains more than 40 % improvement. The POMs clusters are mainly absorbed in pores and contribute little to the whole volume but a lot to the total weight [11]. Thus, the gravimetric capacitance improves only slightly, but the volumetric capacitance improves significantly. The hybrid material is suitable for compact devices.

The Ragone plot (Figure 5c) compares the energy densities and power densities of the three symmetric capacitors. To better view the practical application, we normalize the densities by the total volume of the electrodes (including current collectors), the separators, and the electrolytes. Since the thin PVDF-HFP film serves as both the electrolyte and the separator after soaking, the AC-GPE capacitor deliver two times more densities energy ($2.86 \text{ mWh}\cdot\text{cm}^{-3}$ at $1.77 \text{ W}\cdot\text{cm}^{-3}$ compared with $0.87 \text{ mWh}\cdot\text{cm}^{-3}$ at $0.68 \text{ W}\cdot\text{cm}^{-3}$) at even high power densities. The energy densities and power densities are further improved once AC/TEAPMo12 serves as the active material in the electrodes. It could deliver energy densities as high as $3.88 \text{ mWh}\cdot\text{cm}^{-3}$ at $2.39 \text{ W}\cdot\text{cm}^{-3}$. Thanks to the gel polymer electrolyte and the hybrid active material, compared with the conventional configuration, the AC/TEAPMo12-GPE symmetric capacitor exhibits superior energy densities and power densities.

Figure 5d shows the cycle stability of the three capacitors. All the cells suffer a slight drop in capacitance for the first few cycles, followed by a steady and prolonged loss in capacitance. After 10,000 cycles, all the cells have more than 90% of their initial capacitance. It proves that the PVDF-HFP gel polymer electrolyte and the AC/TEAPMo12 active material do not have detrimental effects on their cycle stability. Finally, coulombic efficiency of our AC/TEAPMo12-GPE cell in the first cycle was 97%, went up to 99.0% in the third cycle, and eventually stayed steady at 99.5% until the end of the 10,000 cycles.

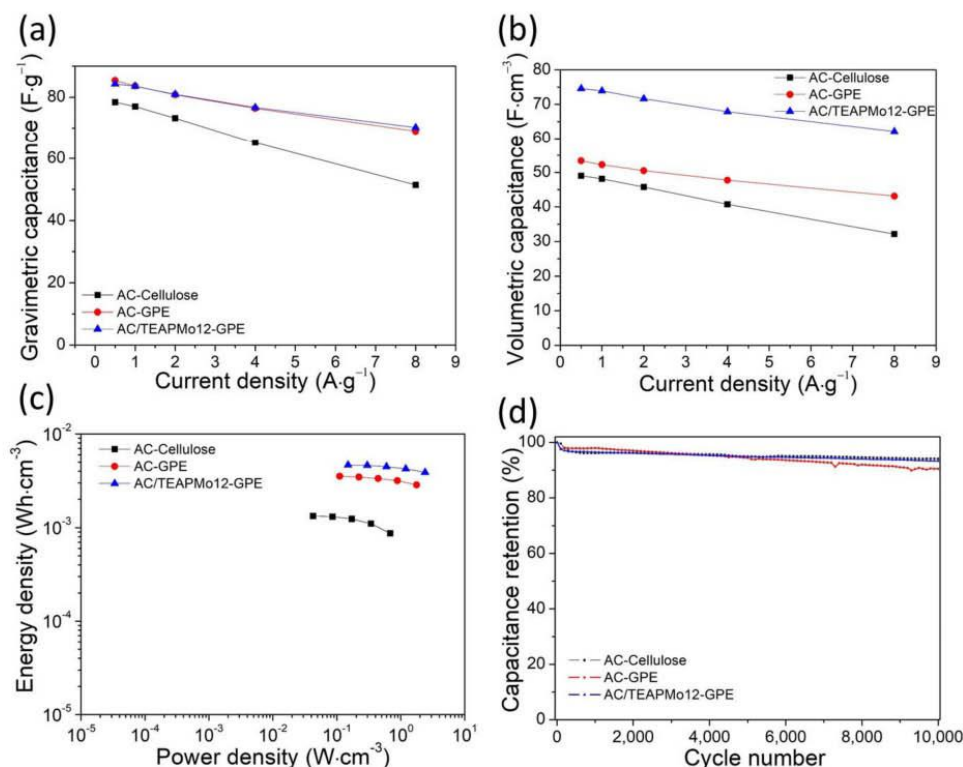


Figure 5. (a) Gravimetric capacitance, (b) volumetric capacitance, (c) ragone plot, and (d) cycle stability of AC-cellulose (with the cellulose separator and the liquid electrolyte), AC-GPE (AC with the 12- μm gel polymer electrolyte), and AC/TEAPMo12-GPE (AC/TEAPMo12 with the 12 μm gel polymer electrolyte) symmetric cells.

4. Conclusions

In this work, we developed a facile way to build coherent pathway throughout the electrodes and the gel polymer electrolyte (separator) by applying PVDF-HFP both in electrodes and electrolyte. The AC symmetric capacitor with GPE show that 5 μm GPE is the threshold as effective separator, and 12 μm GPE is the optimized thickness with regard to the capacitance and rate capability. Compared with the AC symmetric capacitors of conventional configuration, the GPE-based AC symmetric capacitors exhibit slightly larger capacitance and much better rate capability, which must be assigned to the coherent integration throughout the electrode and the electrolyte.

To further improve the capacitive performance of this GPE-based symmetric capacitor, we hybridize AC with TEAPMo12 and apply this hybrid material in a symmetric capacitor. TGA confirms that the AC/TEAPMo12 contains 33.3 wt% of TEAPMo12. HAADF-STEM show that TEAPMo12 clusters are dispersed homogeneously at nanoscale. Owing to the good dispersion, the redox reactions of TEAPMo12 are non-diffusion controlled, favoring high rate capability. The zero-charge potential of the AC/TEAPMo12 is in the middle of the four pairs of redox wave, which allows the positive and negative electrode in symmetric capacitor to perform two redox waves, respectively. The AC/TEAPMo12 symmetric capacitor could deliver a much higher energy (around 4.5 times) at a much higher power density (around 3.5 times) compared with the AC symmetric capacitor of the conventional configuration without sacrificing any cycle stability.

Supplementary Materials: The following supporting information can be downloaded at: <https://www.mdpi.com/article/10.3390/nano12030514/s1>, Figure S2: (a) FT-IR spectra of the pristine PVDF-HFP pellets and the as-prepared PVDF-HFP film. (b) XRD patterns of AC, AC/TEAPMo12 and TEAPMo12. TEM images of (c) AC and (d) AC/TEAPMo12; Figure S3 EIS spectra of AC symmetric (a) AC symmetric capacitor with PVDF binder/PVDF-HFP gel polymer electrolyte, (b) AC symmetric capacitor with PVDF-HFP binder/Cellulose separator/Liquid electrolyte; Figure S4 (a) CVs of AC/TEAPMo12 at various scan rates. Non-diffusion current vs. total current in CVs at (b) $4 \text{ mV}\cdot\text{s}^{-1}$, (c) $8 \text{ mV}\cdot\text{s}^{-1}$, (d) $10 \text{ mV}\cdot\text{s}^{-1}$ and (e) $15 \text{ mV}\cdot\text{s}^{-1}$. (f) Non-diffusion-controlled process contribution vs. diffusion-controlled process contribution to the capacitance at various scan rates. Figure S5 Cyclic polarization curves of (a) AC-Cellulose, (b) AC-GPE and (c) AC/TEAPMo12-GPE at various scan rates. Galvanostatic charging-discharging curves of (d) AC-Cellulose, (e) AC-GPE and (f) AC/TEAPMo12-GPE at various current densities. Figure S6 (a) Gravimetric and (b) volumetric capacitance of AC-Cellulose, AC-GPE and AC/TEAPMo12-GPE at various scan rates. Table S3 the fitting results of impedance spectra; Equations for calculating capacitance, power density, energy density and the modified restricted Warburg diffusion element in impedance analysis.

Author Contributions: Conceptualization, J.-J.Z. and P.G.-R.; methodology, J.-J.Z. and P.G.-R.; validation, J.-J.Z.; L.M.-S. and P.G.-R.; formal analysis, J.-J.Z.; investigation, J.-J.Z. and P.G.-R.; resources, L.M.-S.; data curation, J.-J.Z.; writing—original draft preparation, J.-J.Z.; writing—review and editing, P.G.-R.; visualization, J.-J.Z.; supervision, P.G.-R.; project administration, P.G.-R.; funding acquisition, P.G.-R. All authors have read and agreed to the published version of the manuscript.

Funding: This research was funded by Ministerio de Ciencia Innovacion y Universidades (MCIU) grant number RTI2018-099826-B-I00, Spanish Research Agency (AEI) grant number SEV-2017-0706 and China Scholarship Council grant number 201806370211. And The APC was funded by CSIC.

Institutional Review Board Statement: Not applicable.

Informed Consent Statement: Not applicable.

Data Availability Statement: The data presented in this study are available on request from the corresponding authors.

Acknowledgments: Partial funding from Ministerio de Ciencia Innovacion y Universidades (MCIU), the Agencia Estatal de Investigacion (AEI) and the European Regional Development Fund (FEDER) (grant RTI2018-099826-B-I00) is gratefully acknowledged. ICN2 is funded by the CERCA programme/Generalitat de Catalunya, and also supported by the Severo Ochoa Centres of Excellence programme, funded by the Spanish Research Agency (AEI, grant no. SEV-2017-0706). J.J.Z. acknowledges his scholarship (No. 201806370211) under China Scholarship Council. This work has been carried out within the framework of doctoral program (PhD) of Material Science (Department of Physics) of Universitat Autònoma de Barcelona (UAB).

Conflicts of Interest: The authors declare no conflict of interest.

References

1. Dubal, D.P.; Chodankar, N.R.; Kim, D.-H.; Gomez-Romero, P. Towards flexible solid-state supercapacitors for smart and wearable electronics. *Chem. Soc. Rev.* **2018**, *47*, 2065–2129. [[CrossRef](#)] [[PubMed](#)]
2. Dai, H.; Zhang, G.; Rawach, D.; Fu, C.; Wang, C.; Liu, X.; Dubois, M.; Lai, C.; Sun, S. Polymer gel electrolytes for flexible supercapacitors: Recent progress, challenges, and perspectives. *Energy Storage Mater.* **2021**, *34*, 320–355. [[CrossRef](#)]
3. Vinoth, S.; Kanimozhi, G.; Narsimulu, D.; Kumar, H.; Srinadhu, E.; Satyanarayana, N. Ionic relaxation of electrospun nanocomposite polymer-blend quasi-solid electrolyte for high photovoltaic performance of Dye-sensitized solar cells. *Mater. Chem. Phys.* **2020**, *250*, 122945. [[CrossRef](#)]
4. Xu, P.; Chen, H.; Zhou, X.; Xiang, H. Gel polymer electrolyte based on pvdf-hfp matrix composited with rGO-PEG-NH₂ for high-performance lithium ion battery. *J. Membr. Sci.* **2021**, *617*, 118660. [[CrossRef](#)]
5. Jie, J.; Liu, Y.; Cong, L.; Zhang, B.; Lu, W.; Zhang, X.; Liu, J.; Xie, H.; Sun, L. High-performance PVDF-HFP based gel polymer electrolyte with a safe solvent in Li metal polymer battery. *J. Energy Chem.* **2020**, *49*, 80–88. [[CrossRef](#)]
6. Yadav, N.; Hashmi, S.A. Energy enhancement of quasi-solid-state supercapacitors based on a non-aqueous gel polymer electrolyte via a synergistic effect of dual redox additives diphenylamine and potassium iodide. *J. Mater. Chem. A* **2020**, *8*, 18266–18279. [[CrossRef](#)]

7. Fan, L.-Q.; Tu, Q.-M.; Geng, C.-L.; Huang, J.-L.; Gu, Y.; Lin, J.-M.; Huang, Y.-F.; Wu, J.-H. High energy density and low self-discharge of a quasi-solid-state supercapacitor with carbon nanotubes incorporated redox-active ionic liquid-based gel polymer electrolyte. *Electrochim. Acta* **2020**, *331*, 135425. [[CrossRef](#)]
8. Peng, H.; Yao, B.; Wei, X.; Liu, T.; Kou, T.; Xiao, P.; Zhang, Y.; Li, Y. Pore and Heteroatom Engineered Carbon Foams for Supercapacitors. *Adv. Energy Mater.* **2019**, *9*, 9. [[CrossRef](#)]
9. Chulliyote, R.; Hareendrakrishnakumar, H.; Joseph, M.G. Template free one pot synthesis of heteroatom doped porous Carbon Electrodes for High performance symmetric supercapacitor. *Electrochim. Acta* **2020**, *337*, 135698. [[CrossRef](#)]
10. Horn, M.R.; Singh, A.; Alomari, S.; Goberna-Ferrón, S.; Benages-Vilau, R.; Chodankar, N.; Motta, N.; Ostrikov, K.K.; MacLeod, J.; Sonar, P.; et al. Polyoxometalates (POMs): From electroactive clusters to energy materials. *Energy Environ. Sci.* **2021**, *14*, 1652–1700. [[CrossRef](#)]
11. Zhu, J.-J.; Benages-Vilau, R.; Gomez-Romero, P. Can polyoxometalates enhance the capacitance and energy density of activated carbon in organic electrolyte supercapacitors? *Electrochim. Acta* **2020**, *362*, 137007. [[CrossRef](#)]
12. Suárez-Guevara, J.; Ruiz, V.; Gomez-Romero, P. Hybrid energy storage: High voltage aqueous supercapacitors based on activated carbon–phosphotungstate hybrid materials. *J. Mater. Chem. A* **2014**, *2*, 1014–1021. [[CrossRef](#)]
13. Dubal, D.P.; Rueda-García, D.; Marchante, C.; Benages, R.; Gomez-Romero, P. Hybrid Graphene-Polyoxometalates Nanofluids as Liquid Electrodes for Dual Energy Storage in Novel Flow Cells. *Chem. Rec.* **2018**, *18*, 1076–1084. [[CrossRef](#)]
14. Dubal, D.P.; Chodankar, N.R.; Vinu, A.; Kim, D.-H.; Gomez-Romero, P. Asymmetric Supercapacitors Based on Reduced Graphene Oxide with Different Polyoxometalates as Positive and Negative Electrodes. *ChemSusChem* **2017**, *10*, 2742–2750. [[CrossRef](#)]
15. Dubal, D.P.; Suarez-Guevara, J.; Tonti, D.; Enciso, E.; Gomez-Romero, P. A high voltage solid state symmetric supercapacitor based on graphene–polyoxometalate hybrid electrodes with a hydroquinone doped hybrid gel-electrolyte. *J. Mater. Chem. A* **2015**, *3*, 23483–23492. [[CrossRef](#)]
16. Wang, M.; Zhang, Y.; Zhang, T.; Li, Y.; Cui, M.; Cao, X.; Lu, Y.; Peng, D.; Liu, W.; Liu, X.; et al. Confinement of single polyoxometalate clusters in molecular-scale cages for improved flexible solid-state supercapacitors. *Nanoscale* **2020**, *12*, 11887–11898. [[CrossRef](#)]
17. Hu, J.; Ji, Y.; Chen, W.; Streb, C.; Song, Y.-F. “Wiring” redox-active polyoxometalates to carbon nanotubes using a sonication-driven periodic functionalization strategy. *Energy Environ. Sci.* **2016**, *9*, 1095–1101. [[CrossRef](#)]
18. Cui, L.; Yu, K.; Lv, J.; Guo, C.; Zhou, B. A 3d pomof based on a {asw12} cluster and a Ag-MOF with interpenetrating channels for large-capacity aqueous asymmetric supercapacitors and highly selective biosensors for the detection of hydrogen peroxide. *J. Mater. Chem. A* **2020**, *8*, 22918–22928. [[CrossRef](#)]
19. Osaka, T.; Liu, X.; Nojima, M.; Momma, T. An Electrochemical Double Layer Capacitor Using an Activated Carbon Electrode with Gel Electrolyte Binder. *J. Electrochem. Soc.* **1999**, *146*, 1724–1729. [[CrossRef](#)]
20. Martins, V.L.; Rennie, A.J.R.; Lesowiec, J.; Torresi, R.M.; Hall, P.J. Using Polymeric Ionic Liquids as an Active Binder in Supercapacitors. *J. Electrochem. Soc.* **2017**, *164*, A3253–A3258. [[CrossRef](#)]
21. Fan, L.-Q.; Tu, Q.-M.; Geng, C.-L.; Wang, Y.-L.; Sun, S.-J.; Huang, Y.-F.; Wu, J.-H. Improved redox-active ionic liquid-based ionogel electrolyte by introducing carbon nanotubes for application in all-solid-state supercapacitors. *Int. J. Hydrog. Energy* **2020**, *45*, 17131–17139. [[CrossRef](#)]
22. Bhat, M.; Yadav, N.; Hashmi, S. Pinecone-derived porous activated carbon for high performance all-solid-state electrical double layer capacitors fabricated with flexible gel polymer electrolytes. *Electrochim. Acta* **2019**, *304*, 94–108. [[CrossRef](#)]
23. Zhong, C.; Deng, Y.; Hu, W.; Qiao, J.; Zhang, L.; Zhang, J. A review of electrolyte materials and compositions for electrochemical supercapacitors. *Chem. Soc. Rev.* **2015**, *44*, 7484–7539. [[CrossRef](#)]
24. Yong, H.; Park, H.; Jung, C. Quasi-solid-state gel polymer electrolyte for a wide temperature range application of acetonitrile-based supercapacitors. *J. Power Sources* **2020**, *447*, 227390. [[CrossRef](#)]
25. Diard, J.-P.; Montella, C. Diffusion-trapping impedance under restricted linear diffusion conditions. *J. Electroanal. Chem.* **2003**, *557*, 19–36. [[CrossRef](#)]
26. Jacobsen, T.; West, K. Diffusion impedance in planar, cylindrical and spherical symmetry. *Electrochim. Acta* **1995**, *40*, 255–262. [[CrossRef](#)]
27. Huang, J. Diffusion impedance of electroactive materials, electrolytic solutions and porous electrodes: Warburg impedance and beyond. *Electrochim. Acta* **2018**, *281*, 170–188. [[CrossRef](#)]
28. Cheng, F.; Yang, X.; Zhang, S.; Lu, W. Boosting the supercapacitor performances of activated carbon with carbon nanomaterials. *J. Power Sources* **2020**, *450*, 450. [[CrossRef](#)]
29. Gamby, J.; Taberna, P.; Simon, P.; Fauvarque, J.; Chesneau, M. Studies and characterisations of various activated carbons used for carbon/carbon supercapacitors. *J. Power Sources* **2001**, *101*, 109–116. [[CrossRef](#)]
30. Suárez-Guevara, J.; Ruiz, V.; Gómez-Romero, P. Stable graphene–polyoxometalate nanomaterials for application in hybrid supercapacitors. *Phys. Chem. Chem. Phys.* **2014**, *16*, 20411–20414. [[CrossRef](#)]
31. Chai, D.; Hou, Y.; O’Halloran, K.P.; Pang, H.; Ma, H.; Wang, G.; Wang, X. Enhancing Energy Storage via TEA-Dependent Controlled Syntheses: Two Series of Polyoxometalate-Based Inorganic-Organic Hybrids and their Supercapacitor Properties. *ChemElectroChem* **2018**, *5*, 3443–3450. [[CrossRef](#)]

Supplementary materials

Coherent integration of organic gel polymer electrolyte and ambipolar polyoxometalate hybrid nanocomposite electrode in a compact high-performance supercapacitor

Jun-Jie Zhu,^{a*} Luis Martinez-Soria^a and Pedro Gomez-Romero^{a,b*}

^a Catalan Institute of Nanoscience and Nanotechnology (ICN2), CSIC and BIST, Campus UAB, Bellaterra, 08193 Barcelona, Spain.

^b Consejo Superior de Investigaciones Científicas (CSIC), Spain

* Corresponding author. E-mail address: pedro.gomez@icn2.cat (P. Gomez-Romero), zhu.junjie@icn2.cat (J.J. Zhu) Tel: +34 937373608 (P. Gomez-Romero), Fax: +34 936917640 (P. Gomez-Romero), ICN2, Campus UAB, 08193 Bellaterra (Barcelona) Spain

Supplementary materials 1

Calculation methods for gravimetric capacitance C_m ($F g^{-1}$), volumetric capacitance C_v ($F cm^{-3}$), volumetric energy density E_v ($Wh cm^{-3}$) and power density P_v ($W cm^{-3}$) are calculated according to the following equation:

For cyclic voltammograms or cyclic polarization:

$$C_{cell} = \frac{\int I(V) \cdot dV}{2\nu\Delta V} \quad (S1)$$

For galvanostatic charging and discharging (GCD):

$$C_{cell} = \frac{I \int V(t) \cdot dt}{\Delta V^2} \quad (S2)$$

$$C_m = \frac{2C_{cell}}{m} \quad (S3)$$

$$C_v = \frac{2C_{cell}}{V_e} \quad (S3)$$

$$E_v = \frac{C\Delta V^2}{3600 \times 2V_{total}} \quad (S4)$$

$$P_v = \frac{I\Delta V}{V_{total}} \quad (S5)$$

Where I is the discharge current of GCD, C_{cell} is the capacitance of the device, ΔV is voltage window, ν is the scan rate of CVs, V_e is the volume (cm^3) of the electrode after subtracting Al foil, m is the mass of active materials on one electrode, V_{cell} is the volume of the two electrode (including the current collector) and the separator.

The modified restricted Warburg diffusion element (W_s) is defined by the following equation.

$$Z(f) = \frac{R \coth(\tau i 2\pi f)^{\frac{a}{2}}}{(\tau i 2\pi f)^{\frac{a}{2}}} \quad (S6)$$

where R is the diffusion impedance (W_s -R), τ is the diffusion time (W_s -T), and a is the exponential factor (W_s -P). τ relates to the effective diffusion thickness (L) and the

diffusion coefficient (D), as show below:

$$\tau = \frac{L^2}{D} \quad (S7)$$

Supplementary materials 2

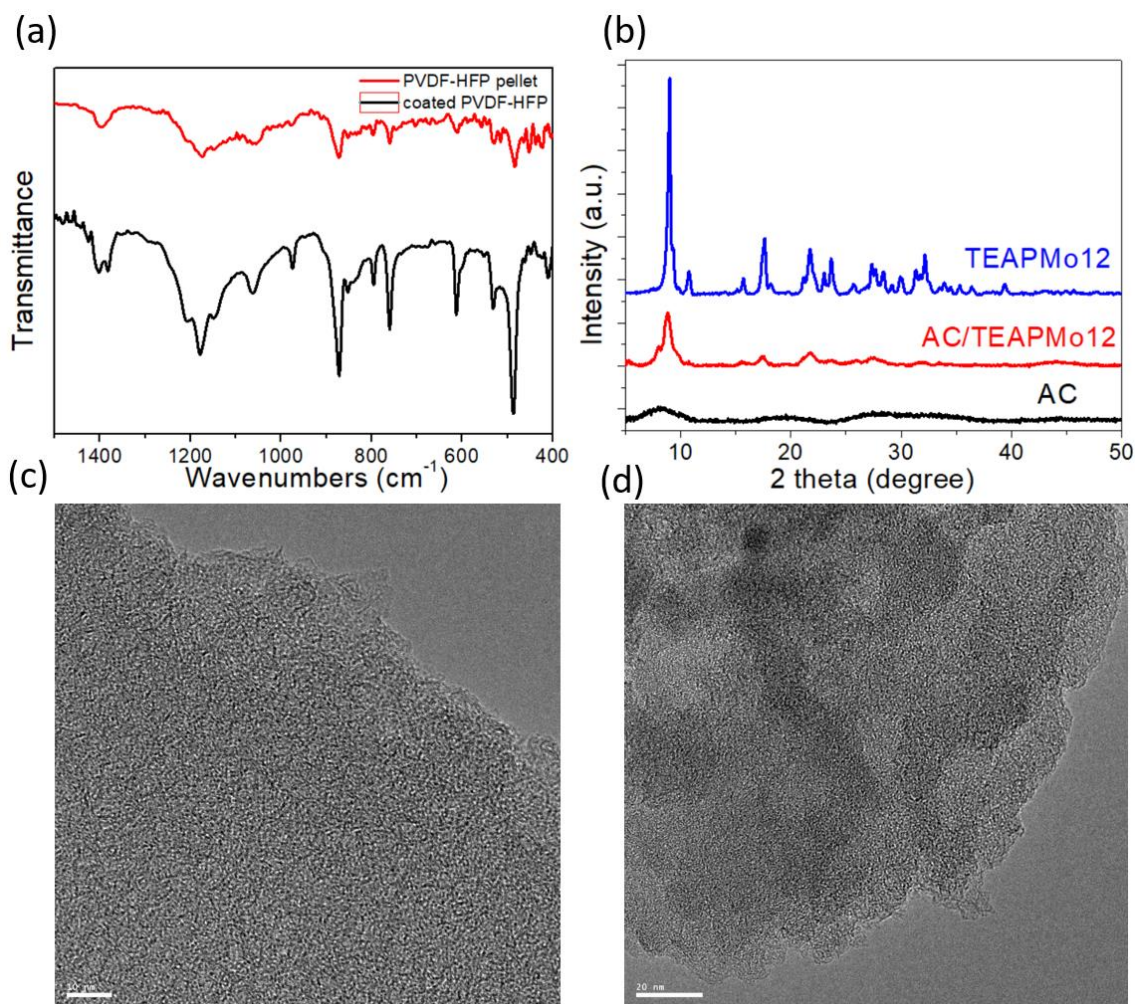


Figure S2 (a) FT-IR spectra of the pristine PVDF-HFP pellets and the as-prepared PVDF-HFP film. (b) XRD patterns of AC, AC/TEAPMo12 and TEAPMo12. TEM images of (c) AC and (d) AC/TEAPMo12.

Supplementary materials 3

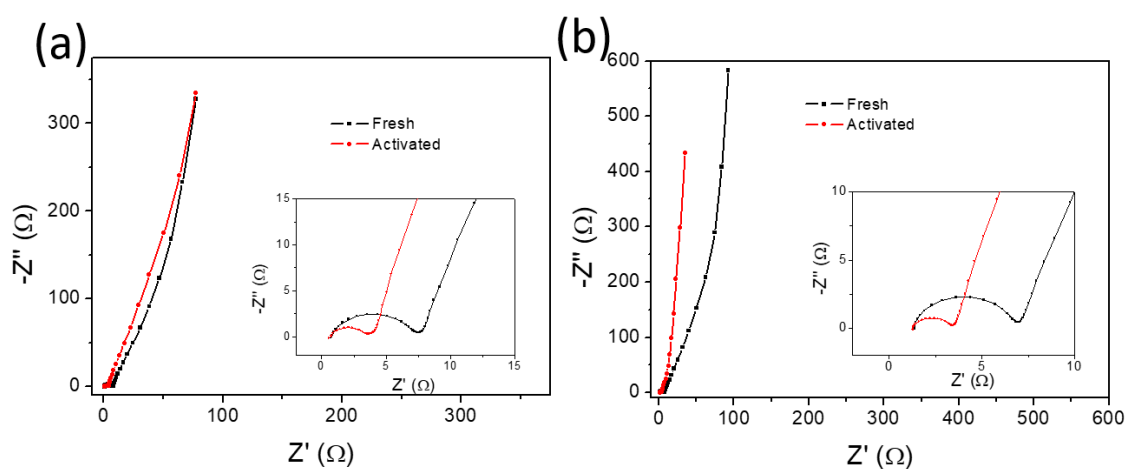


Figure S3 EIS spectra of AC symmetric (a) AC symmetric capacitor with PVDF binder/PVDF-HFP gel polymer electrolyte, (b) AC symmetric capacitor with PVDF-HFP binder/Cellulose separator/Liquid electrolyte

Table S3 the fitting results of impedance spectra

Cells	state	R_s/Ω	C_{dl}/mF	R_{ct}/Ω	W_{s^-}	W_{s^-}	W_{s^-}
					R/Ω	T/s	P
PVDF	fresh	0.857	1.739	5.85	2.83	0.04	0.80
binder/PVDF- HFP gel polymer electrolyte	cycled	0.744	2.512	2.58	1.72	0.03	0.84
PVDF-HFP binder/Cellulose separator/Liquid electrolyte	fresh	1.425	2.956	4.91	1.57	0.01	0.81
	cycled	1.364	5.291	1.79	0.76	0.01	0.86

Supplementary materials 4

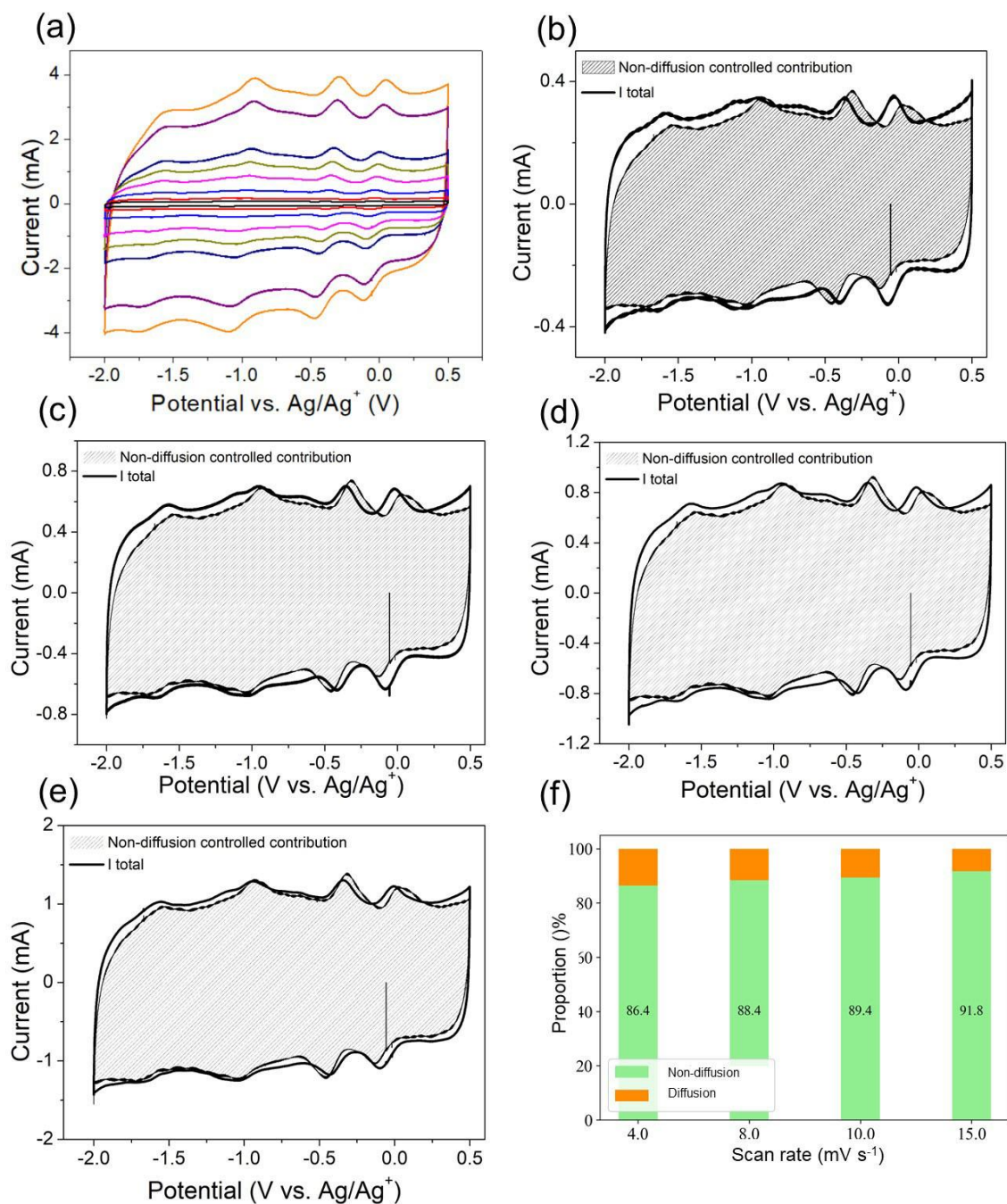


Figure S4 (a) CVs of AC/TEAPMo12 at various scan rates. Non-diffusion current vs. total current in CVs at (b) 4 mV s⁻¹, (c) 8 mV s⁻¹, (d) 10 mV s⁻¹ and (e) 15 mV s⁻¹. (f) Non-diffusion-controlled process contribution vs. diffusion-controlled process contribution to the capacitance at various scan rates.

Supplementary materials 5

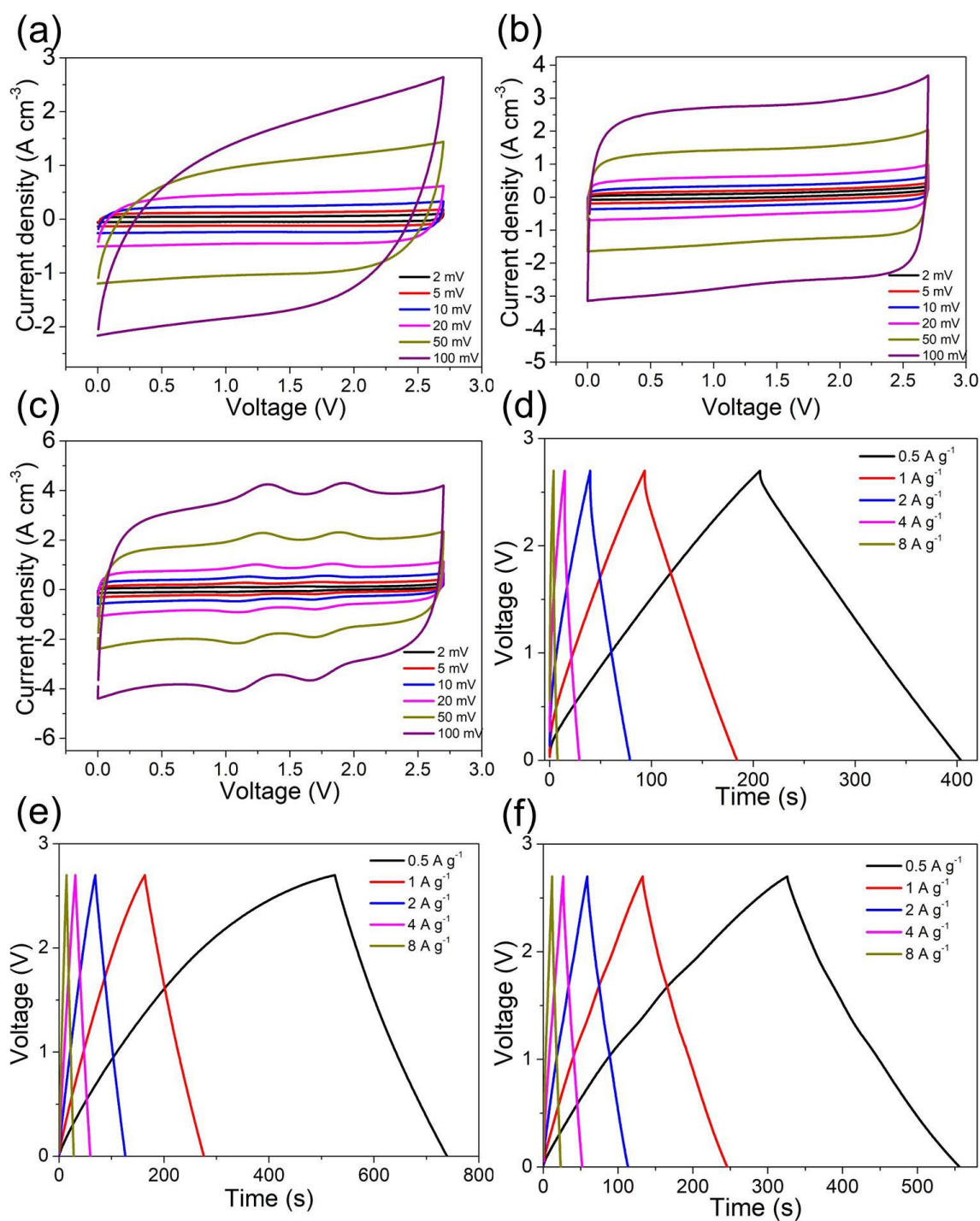


Figure S5 Cyclic polarization curves of (a) AC-Cellulose, (b) AC-GPE and (c) AC/TEAPMo12-GPE at various scan rates. Galvanostatic charging-discharging curves of (d) AC-Cellulose, (e) AC-GPE and (f) AC/TEAPMo12-GPE at various current densities.

Supplementary materials 6

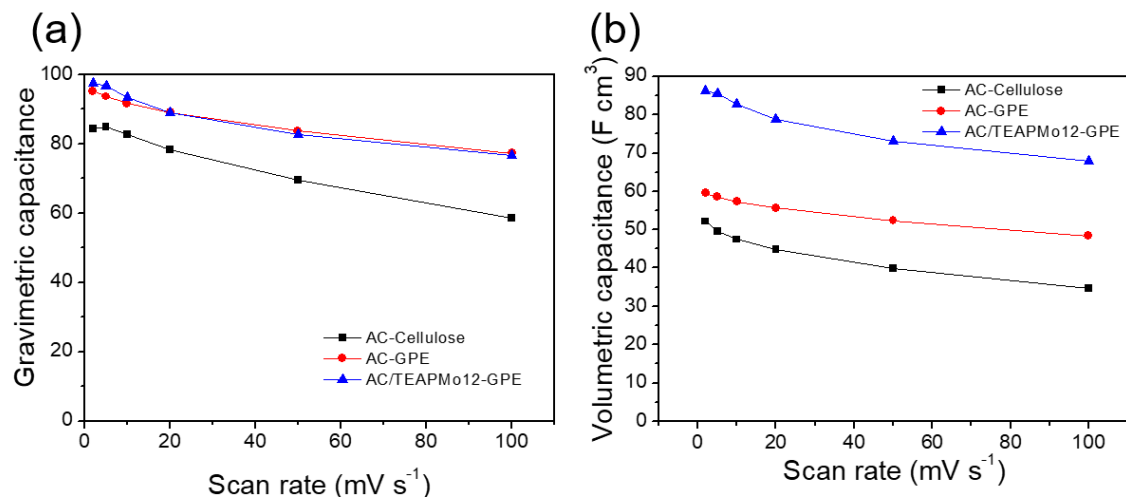


Figure S6 (a) Gravimetric and (b) volumetric capacitance of AC-Cellulose, AC-GPE and AC/TEAPMo12-GPE at various scan rates.

References to main text

- [1] K. Lian, Q. Tian, *Electrochemistry Communications*, 12 (2010) 517-519.
- [2] H. Gao, K. Lian, *Journal of The Electrochemical Society*, 160 (2013) A505-A510.
- [3] H. Gao, A. Virya, K. Lian, *J. Mater. Chem. A*, 3 (2015) 21511-21517.
- [4] H. Gao, K. Lian, *J. Electrochem. Soc.*, 160 (2013) A505-A510.

Chapter 7 Conclusions and perspectives

7.1 Thesis overview and final conclusions

This thesis has presented different but complementary approaches to enhance the performance of conventional organic-electrolyte supercapacitors. The central approach used has been the integration of electroactive polyoxometalates (POMs) in various hybrid electrode materials to increase capacity storage. Yet, in addition to this major topic, our work has also dealt with the optimization of electrolytes (including gel electrolytes) and the configuration of the devices.

The following are the main conclusions of the thesis:

Concerning POM-based hybrid materials, AC/POM hybrid materials were systematically studied first.

1.- Hybrids made of activated carbon and various polyoxometalates in their acid form (AC/HPW12, AC/HPMo12, AC/HSiW12) were unable to enhance the capacitance of AC in the organic electrolyte used (1 M TEABF₄/ACN).

2.- On the other hand, tetraethylammonium polyoxometalate derivatives were synthesized and coupled with AC. This organic-inorganic POMs salt was nano-dispersed homogeneously in an AC matrix.

3.- The electrochemical study of current as a function of scan rate in CVs demonstrated a linear dependence, indicative of a non-diffusion-limited storage mechanism of the AC/PW12 hybrid in organic electrolytes (typical of surface capacitive processes). This allowed for the kinetic matching of the fast reversible redox activities of POMs vs. capacitive electrodes.

4.- As a result, a symmetric supercapacitor with two identical AC/TEAPW12 electrodes showed enhanced volumetric capacitance (+36%), equivalent gravimetric capacitance and excellent cycle stability compared with a symmetrical supercapacitor with pristine AC electrodes.

Furthermore, a new 2D material-Ti₃C₂T_x MXene was studied to serve as the substrate to anchor POMs (PW12). This line of work led to the following conclusions:

5.- Elemental analysis proved that MXene could not directly anchor a substantial amount of PW12 clusters.

6.- Instead, an in-situ growth method was developed to load a large amount of PW12 on MXene. Several quaternary ammonium cations (TMA, TBA, DTA and CTA) were pre-intercalated into MXene layers to expand the interlayer distance and reacted with PW12 anions. Among the various quaternary ammonium cations, only CTA, which expanded the interlayer distance large enough (> 1.9 nm), allowed for the co-intercalation of PW12 within the interlayers.

7.- In all other cases, the POMs extracted the quaternary ammonium cations and crystallized outside the MXene phase.

8.- The POM-intercalated MXene showed remarkably improved electrochemical stability (100% after 100 cycles) in comparison with other in-situ growth MXene/POM hybrid materials (21% after 20 cycles).

9.- We assign this difference to the truly dispersed nature of our hybrid, compared with the crystallization of POMs on the surface of the other materials.

10.- This kind of MXene/POM hybrid materials is promising for various applications, including energy storage, catalyst and sensors. However, due to the large molecular weight of POMs, the POMs-intercalated MXene does not show higher volumetric nor gravimetric capacitance in a conventional organic-electrolyte supercapacitors.

11.- MXene/AC/POMs triple hybrid materials were designed to fabricate high-performance capacitive materials. The three components play different and complementary roles, and show synergic effects. MXene plays the role of a conductive scaffold, provides high volumetric capacitance and allows for fabricating free-standing electrodes. AC is the matrix for anchoring POMs, providing high gravimetric capacitance and ensuring good cycling performance. POMs provide extra fast reversible redox activity and enhance volumetric capacitance.

12.- The as-prepared MXene/AC/TEAPW12 showed a combination of the merits of each components: enhanced gravimetric capacitance (87 F g^{-1} at 1 mV s^{-1}), high volumetric capacitance (76 F g^{-1} at 1 mV s^{-1}) and good cycle stability (92% after 10,000 cycles) in the conventional organic electrolyte.

Concerning the development of electrolytes and the configuration of devices, POMs or POM-based hybrid materials were coupled with gel polymer electrolytes to fabricate quasi-solid devices.

13.- Acidic POMs (HPW12, HPMo12 and HSiW12) were investigated as the plasticizer and redox additives in aqueous PVA-based gel polymer electrolytes. However, since the POMs are trapped in the polymer matrix, the redox activities of POMs contribute little to the capacitance. The POM/PVA aqueous GPEs do not outperform the conventional aqueous GPE (e.g. $\text{H}_2\text{SO}_4/\text{PVA}$) with respect to voltage window and capacitance.

14.- On the other hand, 1 M TEABF₄/ACN/PVDF-HFP organic gel polymer electrolyte was developed. The symmetric capacitors with 1 M TEABF₄/ACN/PVDF-HFP GPE and activated carbon electrodes exhibit slightly larger capacitance and much better rate capability compared with symmetric activated carbon supercapacitors with 1 M TEABF₄/ACN liquid electrolyte.

15.- We propose that this improved performance is due to the growth of a coherent pathway for ion transport through the matrix of PVDF-HFP throughout the electrodes (PVDF-HFP as the binder) connected to the gel polymer electrolyte.

16.- The symmetric supercapacitor with AC/TEAPMo12 hybrid electrodes and 1 M TEABF₄/ACN/PVDF-HFP GPE can deliver much higher energy (around 4.5 times) at a much higher power density (around 3.5 times) compared with the AC symmetric capacitor with 1 M TEABF₄/ACN liquid electrolyte without sacrificing any cycle stability. This GPE as well as the coherent integration of electrode/electrolyte provides a new concept for designing compact, high-performance supercapacitors.

7.2 Perspective

This thesis has demonstrated the capability of POMs to enhance the capacitive performance of conventional double-layer supercapacitor electrodes in organic electrolytes and has also developed an organic gel polymer electrolyte compatible with these POMs-based hybrid materials. Abounding the diversity and versatility of POMs, these results show a further improvement of POM-based hybrid materials and devices and expand their potential modes of application. In this particular case, in organic electrolytes.

If we analyze possible ways to keep improving, we should consider that only some molybdenum or tungsten POMs with the Keggin structure have been used here to explore their integration in hybrid materials. All of them were commercial and therefore easy to use, but all of them have high molecular weight, which restricts their ability to enhance gravimetric capacitance. Other kinds of POMs with lighter molecular weight but still with reversible redox reactions (e.g. vanadates) can be studied to synthesize hybrid materials to enhance gravimetric capacitance.

The POM(PW12)-intercalated $Ti_3C_2T_x$ MXene does not show enhanced capacitive performance but has been proven to have much better electrochemical stability in the organic electrolyte with large cations (TEA). Other POMs can be intercalated within MXene to exploit the application in other fields, such as Li-ion storage, catalysis, sensing etc.

The formulation of our GPE (1 M TEABF₄/ACN/PVDF-HFP) has allowed the fabrication of high-performance compact devices. Since MXene-based hybrid materials are binder-free and flexible, it is promising to integrate PVDF-HFP GPE with MXene-based hybrid materials to manufacture flexible quasi-solid devices in the near future.

In summary, we would like to underscore the few negative results and the many positive results coming out of the work carried out in this thesis. Both are very important for understanding the mechanisms and factors that allow the design of high-performance energy storage devices. We will keep working along that path.